Dynamics of Bose-Einstein condensates near a Feshbach resonance in ^{85}Rb

by

Neil Ryan Claussen

B.S., Wake Forest University, 1996

A thesis submitted to the

Faculty of the Graduate School of the

University of Colorado in partial fulfillment

of the requirements for the degree of

Doctor of Philosophy

Department of Physics

2003

This thesis entitled:
Dynamics of Bose-Einstein condensates near a Feshbach resonance in ^{85}Rb
written by Neil Ryan Claussen
has been approved for the Department of Physics

Carl Wieman

Eric Cornell

Date

The final copy of this thesis has been examined by the signatories, and we find that both the content and the form meet acceptable presentation standards of scholarly work in the above mentioned discipline.

Claussen, Neil Ryan (Ph.D., Physics)

Dynamics of Bose-Einstein condensates near a Feshbach resonance in ^{85}Rb

Thesis directed by Distinguished Professor Carl Wieman

I describe experiments with Bose-Einstein condensates (BEC) of ^{85}Rb near a Feshbach resonance. The Feshbach resonance affects the collisions between atoms, allowing us to change the self-interaction energy of the BEC by applying a magnetic field. We used the Feshbach resonance to study the startling details of the BEC collapse after we abruptly switched the self-interaction from repulsive to attractive. This change caused a supernova-like implosion/explosion cycle, leaving behind a small remnant BEC. We also applied short magnetic field pulses toward the resonance to investigate the possibility of collisional coupling between atoms and diatomic molecules. We later created an atomic and molecular BEC superposition state and probed this state's coherence by applying two rapid magnetic field pulses. Careful measurements of the atom-molecule oscillation frequency allowed us to dramatically improve our determination of the Feshbach resonance parameters. All of these experiments have stimulated new theoretical work and have improved our understanding of the physics of resonant BEC.

Dedication

This work is dedicated to my wife, Lisa, and to the rest of my family: Susie, Pete, Eric, Grant, and Craig.

Acknowledgements

My time working at JILA has been greatly enriched by a number of people. First, I want to acknowledge my advisor, Carl Wieman. Carl has taught me a great deal about experimental physics and how to attack the many complex, real-world problems that occur in physics research. Carl's experimental skills and intuition are really amazing. Also, Carl nearly always has an optimistic viewpoint and his enthusiasm for exploring new areas is infectious. Another professor who has provided much advice and feedback is Eric Cornell. Eric was very involved in our experiments with ^{85}Rb from the beginning. He took an active interest in our results, even when they seemed bizarre and hard to understand, as in our initial studies of BEC collapse. Eric often startles you with great ideas and insights into the BEC physics. I am impressed that Carl and Eric have continued to pursue their research goals so diligently despite the many other commitments they now possess after receiving the 2002 Nobel prize.

There are a number of other professors I would like to thank. On the experimental side of things, Debbie Jin has been a wonderful source for ideas and suggestions. Debbie has a cheerful attitude and she has a knack for asking questions that expose the holes in your thinking. Chris Greene has greatly improved my knowledge of physics. I really enjoyed his Math Physics course, which gave me my first and only taste of the fascinating aspects of group theory. I also appreciate Chris' patience with my seemingly endless questions about the scattering theory and Feshbach resonances. Murray Holland has shown similar patience with me as we discussed the intricacies of the pairing theory

he developed (with Servaas Kokkelmans) to explain our experimental data. Outside of work, I had a lot of fun as a soccer teammate of Murray's in the Boulder city recreational league, where Murray proved a very enthusiastic and agile striker. Another person I want to thank is John Bohn. In the times I saw him giving talks and in class, I really enjoyed John's sense of humor. I also had fun working with John on the written QM comps exam, even though no one decided to take our test!

The graduate students at JILA are a fantastic bunch of people. I especially enjoyed working "in the trenches" with Jake Roberts and Sarah Thompson. Jake taught me a lot about good experimental techniques — especially how to think about error bars. He was an excellent teacher in the lab and from what I have heard, also as a TA in the classroom. In addition, Jake has been a good friend of mine and we shared many trials and tribulations during the course of the first experiments with ^{85}Rb. I hope that he will enjoy CSU and Rams football. Sarah Thompson joined our experiment shortly after Jake graduated. I've really enjoyed working with her for the past few years. She has a very strong aptitude for experimental physics and communicating with others. I am confident that she will continue to do great research in the future (hopefully the lab computers will stop crashing!) I have also learned a lot about exotic pets from Sarah.

Although I have not worked directly with them, there are many other grad students that I should acknowledge. Mike Matthews and Jason Ensher were fun to talk with and they were always full of laughs. Kristan Corwin was a good friend and a very enjoyable person to work with. Kurt Miller has always been ready to lend an ear to my comments and complaints. I appreciate his friendship and advice. I had a great time visiting Corsica for a BEC summer school with Heather Lewandowski and Paul Haljan. I think the tastes of the infamous "charcuterie du Corse" and fish soup will always stick with me, as will the sea-kayaking expedition. Brian DeMarco and Dirk Mueller were classmates of mine at JILA. I was always inspired by how well Brian spoke about physics and by his enthusiasm and skill for research. Dirk was a great

guy with a strong determination to succeed. He always seemed cheerful, no matter what the circumstances (except maybe at the end of our hike up Long's Peak). Brian, Dirk, and I had a tradition that I miss now — we would occasionally go out for a beer (preferably Guinness stout) and talk about practically everything under the sun. I have really enjoyed getting to know Scott Papp and Josh Zirbel after they took up residence across the hall on the new ^{85}Rb experiment. I am excited to see what interesting results will come out of their 2nd generation BEC experiment. I also enjoyed all of the rock climbing expeditions with Josh and the planning for the ascent of Devil's Tower (Oh yeah!) Other grad students that I was privileged to know while at JILA are Chris Myatt, Rich Ghrist, Kurt Vogel, Ian Coddington, David Harber, Peter Schwindt, Ying-ju Wang, Jonathan Goldwin, Josh Dunn, and Cindy Regal.

The post-docs that I worked closely with at JILA were Simon Cornish and Elizabeth Donley. Simon was a very careful experimentalist who devised several ingenious tools to make our lives easier in the lab. He was fun to work with and he advanced the progress of the experiment immensely. I also had fun skiing with Simon and his wife. Elizabeth was a real inspiration for me. She provided a lot of energy to explore new research directions after Jake graduated and Simon returned to Britain. I was privileged to work with Liz and also to rock climb with her on several occasions. I acknowledge another post-doc, Servaas Kokkelmans, who help me greatly during the process of studying the weakly bound state of the Feshbach resonance. Servaas performed very intricate calculations to allow us to use our measurements of the molecular binding energy to constrain the Feshbach resonance parameters. He worked with Murray Holland to develop a theoretical model for our atom-molecule oscillation data. Servaas also cheerfully answered a huge number of my questions about the Feshbach resonance and scattering theory. I am very grateful for his friendship and help. Another post-doc that I would like to thank is Brian Anderson. I met Brian at DAMOP in 1998 and was thrilled to discover that he could image around 100 atoms in a BEC (we wanted to do similar

things with ^{85}Rb). After Brian came to JILA, he helped us out with some clever image processing tools and lots of helpful questions about our data. Brian was also a master hiker who helped me broaden my horizons for exploring the mountains around Boulder. Recently, I met Eleanor Hodby after she joined our experiment. Although I have not had the opportunity to work with her very much, I am very glad for the chance to know her. I can see that Eleanor is quite talented and will make many exciting discoveries with ^{85}Rb. I should also acknowledge several other post-docs, including Eric Burt, who taught me to optimize the experiment "from soup to nuts"; Stefan Dürr, for his great physics knowledge and help with interpreting our results; David Hall, Simon Kuppens, Dwight Whittaker, and Peter Engels.

There were a large group of undergraduate students that I worked with during my time at JILA. Whether they were summer REU students or regular CU students, the undergrads performed a great deal of hard work for us. They built useful electronic circuits, analyzed data, and worked with diode lasers. I would like to acknowledge the people who worked in our lab: Carter Hand, Ryan Epstein, Jeff Collins, Nick Cizek, John Obrecht, Margaret Harris, and Alex Kane. I would also like to thank Estelle Andrews for her friendship and help with various projects.

It is hard to say enough about the JILA staff members. The fact that so many talented and bright people have chosen to work at JILA is a very large reason for the successful research that goes on here. I am thankful for the electronics shop staff, particularly Terry Brown, James Fung-a-Fat, Mike Whitmore, and David Tegart. The computing staff — in particular, Joel Frahm, Peter Ruprecht, and Jim McKown — have been indispensable. In addition, I want to thank several members of the instrument shop for their help: Blaine Horner, Hans Green, Seth Wieman, Hans Rohner, and Todd Asnicar.

I acknowledge my excellent undergraduate advisor, Keith Bonin, for encouraging me to pursue experimental physics. Keith was a wonderful person to work for. He always

had time to chat in his office about physics and many other interesting things. I really enjoyed working in the lab at Wake Forest — learning about diode lasers, atomic clusters, and basic machining. Keith found my passion for turkey hunting very entertaining and he actually made an effort to understand the basic principles. I really appreciate the advice Keith gave me about where to look for good experimental programs in AMO physics.

I also thank my good friends, the Swartz family. I have really enjoyed getting to know them during the past couple of years. Their children are truly wonderful and fun to hang out with. My parents and brothers have been very loving and supportive of my efforts in graduate school. I have been blessed to have such a close relationship with them, despite the fact that we live far apart. Finally, I want to thank my wife, Lisa Courtney. Lisa has supported me throughout my time here. She has been remarkably understanding of the long hours and occasional frustration that I felt. She encouraged me to do my best.

Contents

Chapter

Tables

Table

Figures

Figure

Chapter 1

Introduction

1.1 Breakdown of the thesis

This thesis describes experiments with a novel state of matter that only exists at very low temperature, known as a Bose-Einstein condensate or BEC. The different atoms in a BEC are so cold and slow-moving that they cannot be distinguished from one another. Using Heisenberg's uncertainty principle, one finds that in a BEC, the uncertainty in the position of each atom is comparable to the average spacing between the atoms. Thus, it is almost meaningless to talk about individual atoms anymore — the BEC is a kind of "super-atom". The task of creating a condensate is very difficult and depends on a number of fairly exotic experimental techniques that were developed quite recently (in the past 10 to 15 years). To make a BEC, one usually starts with a room temperature sample of alkali atoms, such as lithium, sodium, rubidium, or cesium. These atoms are confined in a vacuum chamber and then cooled to a few 100 μK using laser-cooling and trapping techniques. Although the laser cooling can dramatically reduce the temperature of the atoms, this type of cooling is not sufficient for creating a condensate. To achieve the conditions for BEC, the atoms must be further cooled (to 50-100 nK) using evaporative cooling — a method for selectively removing only the hottest atoms from the sample.

After forming a BEC, one may study a wealth of different quantum-mechanical phenomena. One of the most interesting properties of an alkali atom BEC is the presence

of inter-atomic interactions in the condensate, which are mediated by elastic collisions between the atoms. Due to a fortuitous internal atomic structure, the collisions of ^{85}Rb atoms can be strongly affected by applying an external magnetic field. This magnetic field dependence is known as a Feshbach resonance. The existence of the Feshbach resonance allows one to change the BEC interaction in a highly controlled fashion. We took full advantage of the tunable interaction to study a number of interesting behaviors of ^{85}Rb BEC. These experiments are discussed at length in the present thesis.

Before conducting the experiments described in this thesis, I worked with Jake Roberts on the first experiments with ^{85}Rb Bose-Einstein condensates [1]. Initially, we developed techniques to cool and magnetically trap the rubidium atoms. We used cold samples of atoms to locate the Feshbach resonance by studying the effects of a variable magnetic field on the elastic scattering of the trapped atoms. The discovery of the ^{85}Rb Feshbach resonance allowed us to improve the efficiency of evaporative cooling so that we were eventually able to create condensates. This achievement marked the first time that the ^{85}Rb isotope was cooled to quantum degeneracy. After forming condensates in 1999, we utilized the Feshbach resonance to control the atomic interactions in the BEC. This control allowed us to study a number of fascinating effects, including an adjustable size and shape for the quantum-mechanical wavefunction of the BEC. By changing the sign of the interaction from repulsive to attractive, we induced an implosion or "collapse" of the condensate.

The collapse experiments mark the point in time when Jake's thesis ends and my thesis begins. The present thesis begins with a detailed description of the dynamics of collapse in a BEC with attractive interactions. We also describe a series of new experiments involving time-varying magnetic fields applied to the BEC near the Feshbach resonance. By improving our magnetic field control apparatus, we were able to probe the response of the condensate to B-field changes on time scales as short as 10 microseconds. Surprisingly, the rapid magnetic field changes caused significant number loss from

the BEC, which implied the presence of microscopic dynamics occurring between the BEC atoms. We later showed that the mysterious BEC loss resulted from non-adiabatic transitions to another state — a diatomic molecular state that was nearly degenerate with the initial BEC state due to the Feshbach resonance. We observed evidence for atom-molecule coherence in the BEC and we used this coherence to precisely determine many detailed properties of the Feshbach resonance and interatomic interactions.

In the rest of the Chapter, we outline each of the subsequent parts of the thesis.

1.1.1 The 155 G ^{85}Rb Feshbach resonance (Chapter 2)

This Chapter provides a brief description of the Feshbach resonance that was so important for our experiments. We motivate the importance of the Feshbach resonance by showing how it affects the interactions in a BEC. Some discussion of the two-body scattering physics is given, and we show how the elastic scattering length varies as a function of magnetic field near the resonance. We also explain the most important properties of the weakly bound molecular state that causes the Feshbach resonance. The magnetic field dependence of the both the energy and spatial size of the molecular state can be adjusted via the applied B-field.

1.1.2 The ^{85}Rb experimental apparatus: new tools and upgrades (Chapter 3)

Here we explain new techniques and additions to the experiment that allowed us to collect the data described in Chapters 4-7. The first part of the Chapter describes a high-power laser upgrade to the experiment. We used the new laser to improve the process of collecting rubidium atoms from a room temperature vapor. We also devised a greatly improved method to measure the magnetic field on short time scales using short pulses of rf radiation. The new B-field measurement technique was essential for characterizing the magnetic field produced by another addition to the experiment — an

auxiliary magnetic field coil. We built the auxiliary coil to apply rapid B-field changes to the BEC. By varying the current through the auxiliary coil, we could precisely control the magnetic field on short time scales. The final part of the Chapter discusses our improved methods for measuring the most important properties of the condensed atoms — their number and temperature. We used the variable interaction strength afforded by the Feshbach resonance to change the BEC size and shape, which enhanced our ability to determine the BEC characteristics.

1.1.3 Dynamics of collapsing and exploding ^{85}Rb Bose-Einstein condensates (Chapter 4)

In this Chapter, we describe the startling response of a BEC to a change in the condensate self-interaction from repulsive to attractive. The sudden change caused a variety of unusual effects in the condensate. After a short delay that followed the change in the interaction, the BEC abruptly began to lose atoms. The atoms disappeared from the condensate over a time scale of a few milliseconds. During the same time period, an explosion of hot atoms was emitted from the collapsing condensate. We also observed strange features in the BEC density distribution. After the completion of the number loss, part of the initial condensate remained visible in a highly excited state of motion. We discuss the detailed behavior of the BEC collapse dynamics and summarize these results. At the end of the Chapter, the prominent features of the data are compared to theory.

1.1.4 Microscopic dynamics in a strongly-interacting Bose-Einstein condensate (Chapter 5)

Here we discuss condensate number dynamics resulting from rapid changes to the magnetic field. Using the auxiliary coil, we applied a short B-field pulse toward the Feshbach resonance to the condensate. The condensate responded to the pulse

by losing a large fraction of its initial number. Some of the atoms that left the BEC were visible in an explosion that was quite similar to the explosion seen in the collapse experiments of Chapter 4. We studied the dependences of both the BEC loss and the explosion characteristics on the exact shape and size of the magnetic field pulse. The time dependence of the loss suggested the presence of non-adiabatic transitions of the condensate atoms to the molecular state associated with the Feshbach resonance. We give some justification for this claim using a simple avoided crossing model for the Feshbach resonance.

1.1.5 Atom–molecule coherence in a Bose-Einstein condensate (Chapter 6)

This Chapter is an extension of the work in Chapter 5. Rather than using a single pulse, here we applied two magnetic field pulses to the condensate. The pulses approached the Feshbach resonance and were separated in time by a variable delay. As a function of the delay time between pulses, we observed oscillations in the number of BEC atoms. The oscillation frequency matched the binding energy for the molecular state of the Feshbach resonance. We also observed oscillations in the population of atoms in the explosion that resulted from the B-field pulses. These atom-molecule coherence data inspired a flurry of theoretical activity. We present a comparison of the data and theory at the end of the Chapter.

1.1.6 Very high precision bound state spectroscopy near a ^{85}Rb Feshbach resonance (Chapter 7)

The atom-molecule oscillations observed in Chapter 6 allowed us to dramatically improve our knowledge of the Feshbach resonance. We made very precise measurements of the oscillation frequency corresponding to the molecular binding energy. The frequency measurements were combined with precise measurements of the magnetic field

using a new experimental technique from Chapter 3. We fit the frequency and magnetic field data to a theoretical model of the scattering physics. The best fit to the data allowed us to extract greatly improved values for the Feshbach resonance properties, including its position and width in magnetic field. We improved the precision of the position and width determinations by more than a factor of 20. In addition, we used our data to obtain new values for several important parameters of the interatomic potentials for ^{85}Rb. Our results for the potential parameters had comparable precision to those of other recent high-precision experiments in rubidium. The agreement between our results and the results of the other analysis was very good.

1.1.7 Prior publication of our work

Most of the experiments described in this thesis were previously published in scientific journals. The experiments of Chapter 4 appeared in Ref. [2], while Chapter 5 was published in Ref. [3]. The work in Chapter 6 appeared in Ref. [4]. The observations of Chapter 7 were submitted but not yet published at the time of writing the thesis.

Chapter 2

The 155 G ^{85}Rb Feshbach resonance

2.1 Introduction

This Chapter provides a brief overview of a Feshbach resonance in the collisions of ^{85}Rb atoms. In addition to allowing the creation of ^{85}Rb Bose-Einstein condensates, the Feshbach resonance also made possible a variety of experiments involving changes to the self-interaction of the BEC. The effects of this variable self-interaction were numerous and they form the subject matter for the rest of this thesis.

2.2 Atomic interactions in a BEC

One of the most interesting properties of Bose-Einstein condensates in dilute atomic gases is the existence of interactions between the constituent atoms. Although the BEC is typically 5 orders of magnitude less dense than air, the interatomic interactions strongly affect a number of the properties of the condensate. The interactions in a BEC have been successfully described by mean-field theory [5], in which each BEC atom moves in an effective mean-field due to the other atoms. The mean-field interaction is mediated by the elastic collisions between atoms.

The well-known Gross-Pitaevskii (GP) equation can be used to describe a condensate in the limit of zero temperature and neglecting all correlations between the

atoms. The GP equation for a trapped BEC has the form

$$i\hbar\frac{\partial}{\partial t}\Phi(\vec{r},t) = \left[-\frac{\hbar^2\nabla^2}{2m} + V_{\text{ext}}(\vec{r}) + g|\Phi(\vec{r},t)|^2\right]\Phi(\vec{r},t), \tag{2.1}$$

where Φ is the BEC order parameter, V_{ext} is the trap potential energy, and the coefficient $g = \frac{4\pi\hbar^2 a}{m}$ characterizes the pair-wise interatomic interactions in the BEC through the s-wave elastic scattering length, a. The solution to the GP equation (2.1) is the condensate order parameter, Φ, which for most purposes can be regarded as the macroscopic wavefunction of the BEC atoms. The GP equation has the form of a nonlinear Schrodinger equation, where the nonlinear term arises from the mean-field interaction of one atom with all of the others. The mean-field interaction term, often called the self-interaction energy of the condensate, depends on the density of atoms and the scattering length. Thus, the GP equation predicts that the sign and magnitude of a determine the strength of the self-interaction and whether this interaction is attractive or repulsive.

For controlling the BEC self-interaction, it would clearly be desirable to find some method to change the scattering length. Almost one decade ago, it was suggested that the scattering length could be influenced using an external magnetic field [6]. The magnetic field would allow one to shift the energy of a molecular bound state to near-degeneracy with the energy of a colliding pair of atoms, thereby altering the elastic scattering properties. Such an effect is called a Feshbach resonance and was first studied in nuclear scattering. The physics of Feshbach resonances will be discussed in the rest of this Chapter.

2.3 Feshbach resonance

2.3.1 Simple picture of the resonance

In a simplified picture, a Feshbach resonance occurs when the energy of a bound state of the interatomic potential is equal to the kinetic energy of a colliding pair of atoms. Assuming a finite kinetic energy, such a degeneracy can occur only when the

bound state exists in a potential that has a higher threshold energy than that of the colliding atom pair. This condition can be satisfied in ultracold gases of alkali atoms, due to the low collision energy of the atoms and the existence of atomic hyperfine structure. Since the different hyperfine states generally possess different spin configurations and magnetic moments, one can sometimes tune the bound state energy into resonance with the colliding atom energy via the different Zeeman shifts in an external magnetic field. Assuming that both colliding atoms are in the lower hyperfine state, it may happen that an interatomic potential associated with the upper hyperfine state supports a bound state nearby in energy, as shown schematically in Figure 2.1.

The schematic curves in Figure 2.1 show the potential energy of the atoms as a function of their internuclear separation, R. Neglecting the Zeeman interaction, the large R asymptotic energy is determined entirely by the sum of the hyperfine energies for the colliding atoms. Each asymptote is called a collision channel and different channels are labeled by the hyperfine quantum numbers (F,m_F) for the atom pair.

If two atoms begin an elastic collision in the lower channel with kinetic energy much smaller than the hyperfine splitting, ΔE_{HF}, the atoms cannot exit the collision in the upper channel because of energy conservation. Thus, the upper channel is energetically "closed", while the lower channel is "open". In the case of ^{85}Rb experiments, the hyperfine splitting of 140 mK greatly exceeds the kinetic energy of the degenerate gas sample, which is <10 nK. This means that the Feshbach resonance will be "well-resolved" because the energy spread of the BEC atoms is far smaller than the energy difference between the two hyperfine states.

In addition to low collision energy and hyperfine structure, another requirement for the existence of a Feshbach resonance is a coupling between the open and closed channels. The coupling is provided by the Coulomb (or exchange) interaction, which couples together different hyperfine states at short internuclear distance [7]. As the atoms move together during a collision, the strong electrostatic interaction between the

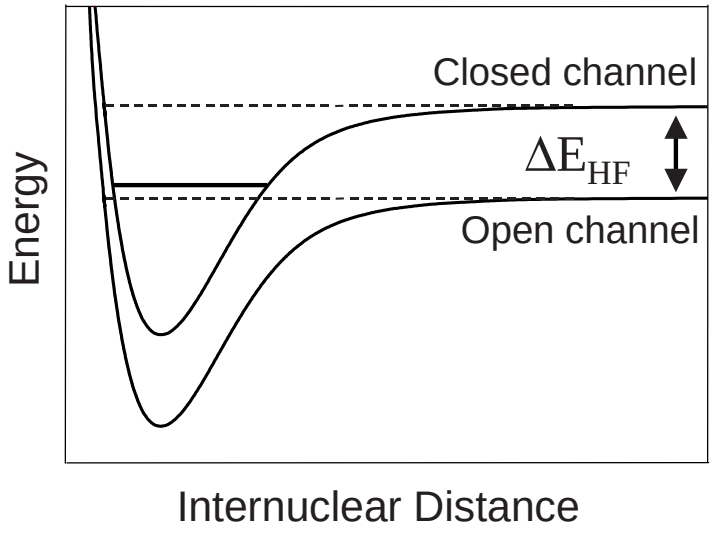

Figure 2.1: A simplified representation of the interatomic potentials involved in a Feshbach resonance. The solid lines represent the potential energy versus internuclear separation for the colliding atoms. The dashed lines show the threshold or asymptotic energies of the potential curves, which are separated by the hyperfine splitting, ΔE_{HF}. A bound state of the upper potential, shown by the short horizontal line, is nearly degenerate with the threshold energy of the lower potential. The definition of energetically open and closed channels is given in the text.

nuclei and the electron clouds overwhelms the relatively weak hyperfine interaction, allowing a spin flip to occur. Due to the symmetry of the binary system, the total spin projection quantum number $m_{F(tot)}=m_{F(1)}+m_{F(2)}$ is conserved, but the total spin $F_{tot}=F_1+F_2$ is not. The symmetry requirement determines whether a given closed channel can couple to the open channel.

2.3.2 Real ^{85}Rb Feshbach resonance

It turns out that the idealized picture of the Feshbach resonance caused by the interaction of a *single* closed channel with the open channel is too simplistic. Because of the complicated hyperfine structure of alkali atoms, any real resonance must involve coupling of the open channel to a number of different closed channels. As discussed in section 2.3.1, the symmetry of the Hamiltonian describing the colliding atoms dictates that only those channels with the same total spin projection as the open channel can be coupled. For the 155 G ^{85}Rb Feshbach resonance, the open channel is $|F_1, m_{F(1)}\rangle + |F_2, m_{F(2)}\rangle = |2,-2\rangle + |2,-2\rangle$. The symmetry requirement that $m_{F(tot)} = -4$ restricts the number of closed channels to four. We list the relevant ^{85}Rb closed channels in order of increasing threshold energy in Table 2.1.

Table 2.1: Closed channels involved in the ^{85}Rb Feshbach resonance. Each channel is a sum of two different hyperfine states, as indicated by the quantum numbers in the second column. The threshold energies and magnetic moments of the closed channels relative to the open channel are calculated using the Breit-Rabi equation at a magnetic field of 175 G. Note that $\Delta E_{\mathrm{HF}} = 3.036$ GHz.

Label	Closed channel	Energy/ΔE_{HF} at B=175 G	Magnetic moment (MHz/G)
(a)	$\|2,-1\rangle + \|3,-3\rangle$	0.840	-2.72
(b)	$\|2,-2\rangle + \|3,-2\rangle$	0.900	-1.57
(c)	$\|3,-1\rangle + \|3,-3\rangle$	1.799	-3.22
(d)	$\|3,-2\rangle + \|3,-2\rangle$	1.800	-3.14

All of these closed channels can potentially interact with the open channel. There-

fore the simplified picture of a Feshbach resonance given in Figure 2.1 is inadequate. In fact, to describe the resonance when the magnetic field approaches the resonance value, one must include the effects of multi-channel coupling [7, 8, 9]. In a coupled-channels approach, the wavefunction of the colliding atom pair is expanded as a sum of the open channel state and the four closed channel states. The expansion coefficients are dependent on collision energy, magnetic field, and the internuclear separation of the colliding atoms. When one substitutes the expanded wavefunction into the Schrodinger equation containing an approximate Hamiltonian for the interatomic interactions, one obtains a set of coupled equations that describe the elastic collision. By solving these equations, one can accurately determine the most important property of the elastic collision – the scattering length, a. The existence of the Feshbach resonance profoundly affects the scattering length by introducing a magnetic field dependence to a.

2.3.3 Variable scattering length

A well-known feature of low energy scattering from an attractive potential well is resonance scattering [10, 11]. Resonance scattering occurs when a bound state of the potential is very close to the collision energy of the atoms. The presence of the bound state near zero energy profoundly affects the scattering physics. This is because the colliding atoms can make a transition to the bound state and dwell there briefly before moving apart again after the collision. The biggest effect on the scattering occurs when the two levels have exactly the same energy, which causes the elastic cross section and scattering length to reach infinite values. In a Feshbach resonance, one can adjust the energy of a bound state relative to the collision energy by tuning the magnetic field. Even though the bound state exists in a different interatomic potential from that of the colliding atoms, the variable bound state energy can still dramatically alter the scattering length.

From the coupled-channels scattering theory of Feshbach resonances, one can

derive an approximate analytic expression for the variation of the scattering length with magnetic field [7]. In terms of the Feshbach resonance parameters, the scattering length is [7, 12]

$$a = a_{\rm bg}\left(1 - \frac{\Delta}{B - B_{\rm peak}}\right), \tag{2.2}$$

where $\rm B_{peak}$ is the resonance position and is defined to be the magnetic field where the magnitude of a becomes infinite, $a_{\rm bg}$ is the background scattering length, and Δ is the resonance width in magnetic field. Although equation (2.2) is only approximate, we have found that the analytic expression works very well. In fact, the scattering length from equation (2.2) agrees with a calculated from a full coupled-channels theory to better than 1% percent from 155 G to 250 G [13]. Figure 2.2 displays the scattering length predictions from equation (2.2).

2.3.4 Bound state properties for the ^{85}Rb Feshbach resonance

Very near the ^{85}Rb Feshbach resonance on the high B-field side, the scattering length is large and positive. From zero-energy scattering theory [10, 11], we know that when a is much bigger than the effective range of the attractive potential well ($a >> R_{\rm eff}$ ~25 $\rm a_0$), there must exist a weakly bound state just below the threshold energy. The binding energy of the weakly bound state bears a simple relationship to the scattering length:

$$\epsilon_{\rm bind} = -\hbar^2/(ma^2), \tag{2.3}$$

where m is the atomic mass. The arguments leading to this result are very general, so the equation must be valid as long as a is big. It is therefore not necessary to deal with a complicated coupled-channels calculation of $\epsilon_{\rm bind}$ in the large scattering length regime, provided that the parameters of the Feshbach resonance are well known and one can use equation (2.2) to determine the scattering length.

However, to obtain the full magnetic field dependence of the molecular binding

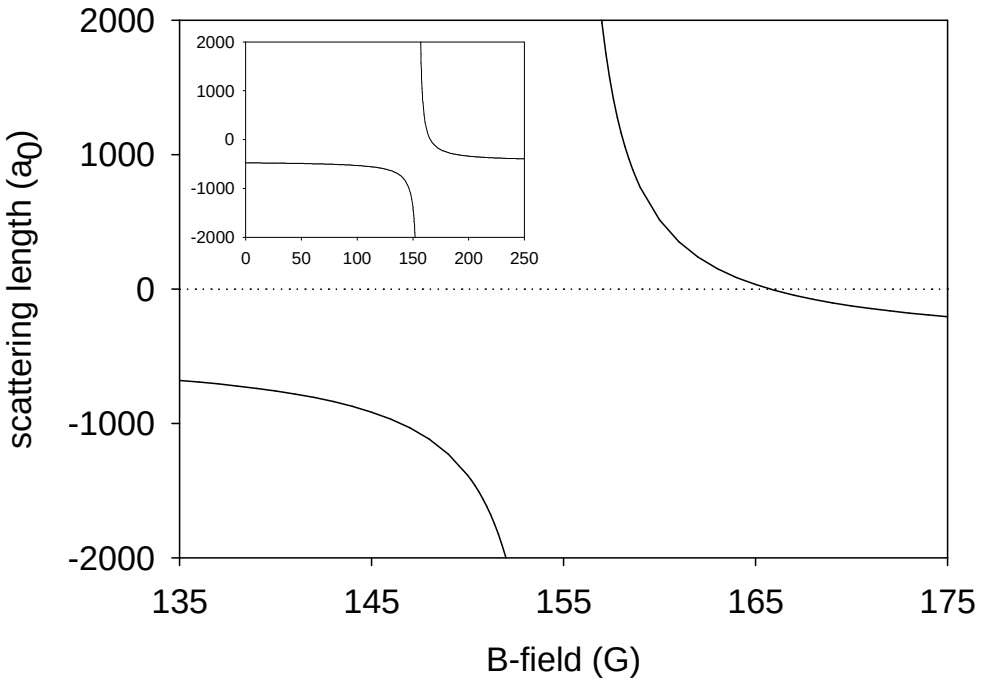

Figure 2.2: Magnetic field dependence of scattering length near the Feshbach resonance. The solid line is the scattering length calculated from equation (2.2) with the current best values for the resonance parameters (see Chapter 7). For the resonance position and width, we have B_{peak}=155.041 G and Δ=10.709 G, respectively. The value of the background scattering length is -443 a_0. The horizontal dashed line indicates zero scattering length, which occurs at B_{zero}=165.75 G. In the inset, we show the scattering length variation over a larger range of B-field.

energy, a coupled-channels calculation is needed [9]. When the interactions between all of the channels are accounted for, one obtains a rather complicated magnetic field dependence in ϵ_{bind}. The coupling matrix element between the open channel and each closed channel varies strongly with B-field, which leads to a nonlinear magnetic field dependence of the binding energy. Figure 2.3 shows this dependence along with the scattering length variation for magnetic fields above the ^{85}Rb Feshbach resonance.

In addition to the binding energy, another important property of the molecular state is the spatial size of the wavefunction. Zero-energy scattering theory provides a useful prediction for the shape of the molecular state wavefunction. Outside the effective range of the potential, the wavefunction for the molecular state can be shown to have the form [10]

$$\phi(r) \sim \frac{\exp\left(-r/a\right)}{r}, \tag{2.4}$$

where $a >> R_{\text{eff}}$ is the large, positive scattering length and R_{eff} is the range of the potential. Equation (2.4) shows that the decay of the bound state occurs over a length scale equal to the scattering length, which can easily exceed the potential range by several orders of magnitude. This behavior is possible because of the proximity of the bound state to zero energy. The elongated spatial size of the molecule has some bizarre consequences. For instance, when the scattering length is very large, the atoms in the weakly bound molecule spend the majority of their time at internuclear separations that are best described by the hyperfine basis. The molecular state is far too large to be labeled according to the conventional singlet/triplet molecular quantum numbers.

It is worth emphasizing that the characteristics of the weakly bound molecular state are completely different from those of the single closed channel state of conventional Feshbach theory. For instance, the weakly bound state extends far past the short-range part of the interatomic potential. The size of the weakly bound state is basically given by the scattering length when $a >> 0$. In contrast, the closed channel bound state

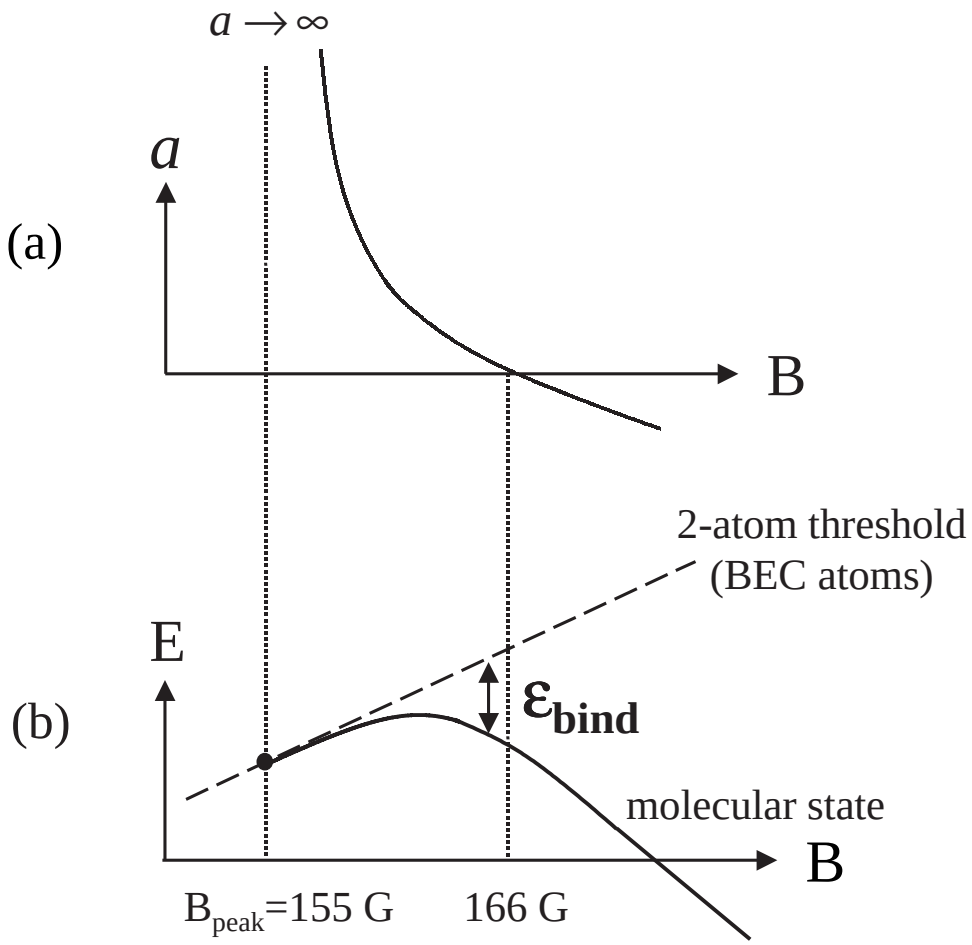

Figure 2.3: Schematic representation of the Feshbach resonance in ^{85}Rb. **(a)** Variation of scattering length for B>B_{peak}. The two vertical dotted lines indicate the range of magnetic field where $a > 0$. **(b)** Dependence of atomic and molecular energies on B-field. The dashed line shows the colliding atom threshold energy, while the solid curve is the molecular state energy, which intersects the atomic threshold at B_{peak}. For magnetic fields significantly above resonance, the molecular energy decreases linearly with B-field at a rate that is very similar to the magnetic moments of closed channels (c) and (d), as listed in Table 2.1.

is confined to the part of the interatomic potential where molecular forces dominate, which is roughly 25 a_0 in extent. Another property of the weakly bound state that sets it apart from the closed channel state is the magnetic field dependence. While the closed channel state exhibits a linear variation of energy versus B-field, the weakly bound state shifts in a highly nonlinear fashion (see Figure 2.3).

2.3.5 Physical relevance of weakly bound state

Prior to the publication of our recent measurements of the molecular state binding energy (see [4] and also Chapters 6-7), the existing theoretical descriptions of alkali atom Feshbach resonances [14, 15] were mostly based on the simple picture of a single closed channel coupled to the open channel (see section 2.3.1). In the course of our studies of ^{85}Rb condensates, we found that the simple picture was totally incorrect — it failed to describe the atom-molecule oscillation data in Chapter 6. Our measurements clearly demonstrated the physical relevance of the weakly bound molecular state. Several new theoretical models for the ^{85}Rb Feshbach resonance are currently being developed [9, 16, 17, 18] to describe the data.

Chapter 3

The ^{85}Rb experimental apparatus: new tools and upgrades

3.1 Overview

This chapter explains new features added to the original ^{85}Rb experimental apparatus. The vast majority of the apparatus and techniques that we used to produce ^{85}Rb Bose-Einstein condensates were already carefully documented by Jake Roberts [1]. I refer the reader to Ref. [1] for a more comprehensive picture of the ^{85}Rb machine and the actual BEC production process. In the first part of the chapter, I give a general overview of our recipe for BEC. The last part of the chapter contains much more detailed descriptions of several new experimental techniques and additions to the apparatus that were used to conduct the experiments described in Chapters 4-7. The detailed descriptions begin with an explanation of general physical principles and conclude with the practical details.

Our procedure for BEC production depends on two cooling techniques — laser cooling and evaporative cooling — to lower the temperature of a confined gas of atoms from room temperature (300 K) to a few billionths of a degree ($\sim$10 nK). We accomplish this cooling without any conventional cryogenic methods; the only cold part of the system is the trapped atom cloud itself. This is possible because the rubidium atoms are trapped in a "thermos bottle" of confining optical and magnetic fields that are housed inside an ultra-low pressure vacuum system. When the ^{85}Rb atom cloud cools to 10 nK, the quantum behavior of the atoms in the gas becomes apparent and they all

pile up in the ground state of the trap, forming a Bose-Einstein condensate. The BEC is remarkable — it is described by a macroscopically-sized quantum wavefunction that we can observe directly with a suitable microscope.

In our apparatus, we use a pair of magneto-optical traps (MOTs) to laser-cool and trap a few hundred million ^{85}Rb atoms. One MOT, called the "collection" MOT, has the important task of cooling the atoms down to roughly 100 μK from a room temperature vapor. We transfer these collected cold atoms to another ("science") MOT by pushing them through a narrow tube that connects the two MOT vacuum chambers. The chamber that encloses the science MOT is only weakly coupled to the collection MOT chamber containing the rubidium vapor, so the science chamber has roughly 100$\times$ lower pressure ($\sim 10^{-11}$ torr). This low pressure is crucial for the cooling efficiency of the next experimental stage — evaporative cooling.

Before starting the evaporative cooling process, we first illuminate the atoms with an optical pumping laser to force them into a particular internal hyperfine state, then we load the atoms into a purely magnetic trap. The magnetic trap confines the atoms spatially and has a much longer storage time than the MOT due to the absence of laser light, which continually excites the atoms and leads to trap loss. However, the magnetic trap has the disadvantage of being much more shallow than the MOT and lacking the capability to cool the atoms (because the magnetic trapping potential is conservative, there is no dissipation and this trap has no intrinsic cooling ability). In our system, we typically load the magnetic trap with 6×10^8 ^{85}Rb atoms in the $|F, m_F\rangle = |2, -2\rangle$ hyperfine state at a temperature of 40 μK.

We evaporatively cool the sample by applying a radio-frequency (rf) radiation field that selectively removes the hottest atoms from the magnetic trap. The removal is accomplished by inducing $\Delta m_F = +1$ transitions to an untrapped spin state. After making such a transition, an atom falls away from the trapped cloud, thereby removing energy from the sample. The most important feature of evaporative cooling in the

magnetic trap is the energy selectivity of the rf transitions. Due to the Zeeman energy shift of the trapped atoms, the most energetic atoms spend the greatest time in higher magnetic field regions of the trap, where the rf transition frequency is largest. By lowering the rf radiation frequency in a time-dependent fashion, one can gently lower the temperature of the trapped atom cloud. The optimal procedure for evaporative cooling is quite complex and we devoted a great deal of time to studying this process.

If the cooling process can be made efficient enough so that the number of atoms removed per unit time is relatively low and the energy removed per time is relatively high, then the phase space density (PSD) of the atom cloud will increase as evaporation continues. Eventually the PSD approaches unity, which means that the average inter-particle separation in the gas becomes equal to the deBroglie wavelength of an atom. Because ^{85}Rb atoms are bosons, their position space wavefunctions overlap with one another and the system undergoes a transition to a new "superatom" state, the Bose-Einstein condensate. In our system, we typically see a BEC begin to form at $\sim$15 nK. We continue to evaporate the cloud to further lower the temperature until we obtain condensates of 20,000 atoms at T$\sim$5 nK. Thus, the evaporative cooling process leads to PSD$\sim$1 after reducing N by four orders of magnitude and reducing T by ten orders of magnitude.

The resulting ^{85}Rb BEC is a fascinating object. It is a dilute, weakly-interacting, ultracold gas of atoms whose behavior is entirely quantum-mechanical. The interactions between atoms in the condensate are mediated by low energy collisions and can be fairly simply described in terms of the s-wave scattering length, a. Since the scattering length can be varied near a Feshbach resonance (see Chapter 2) by changing the magnitude of the magnetic field, our ^{85}Rb BEC in a magnetic trap offers a wealth of possibilities for studying the atom-atom interactions. In fact, the formation of the condensate at B=162.3 G (a=210 a_0) is only possible because of the proximity of the B-field to the Feshbach resonance at 155 G. At magnetic fields more than 11 G away from resonance,

the scattering length is large and negative, so the BEC self-interaction is attractive and only ∼80 atoms can exist in the BEC ground state (attractive interactions are discussed in Chapter 4).

After creating a stable ^{85}Rb BEC, we generally change the magnetic field and study the effect on the condensate. Depending on the details of the B-field change — its time-dependence and magnitude, one can observe very complex BEC dynamics, including implosions and explosions of the wavefunction, collision-induced losses, and coherent transfer between a single atom state and a diatomic molecular state. Our studies of these phenomena comprise the subject matter for Chapters 4-7 of this thesis.

3.2 New collection MOT laser

3.2.1 General discussion of collection MOT

Perhaps the most important step on the road to BEC is laser cooling and trapping of the atoms in a magneto-optical trap (MOT). We utilize a double MOT system [19] consisting of a collection MOT for gathering the atoms from a room temperature vapor and a science MOT for further cooling and transfer of the atoms into a magnetic trap. The double MOT apparatus allows us to collect and transfer multiple bunches of atoms from the collection chamber to the science chamber. After a capturing a sufficient number of atoms in the science MOT, we load them into the magnetic trap and proceed to evaporative cooling.

The collection MOT has the important task of cooling a fraction of the atoms in the room temperature vapor to roughly 100 μK. The fraction that is cooled is determined [20] by the velocity distribution in the gas and the capture velocity of the MOT, v_c, which is the maximum velocity that an atom can have and still be slowed enough to become trapped in the MOT. When an atom with larger velocity than v_c enters the trapping region, it slows down but does not remain in the MOT volume. The number

of atoms in the MOT depends strongly on v_c: $N_{MOT} \propto (v_c/v_{therm})^4$, where v_{therm} is the average velocity of the atoms in the vapor. The capture velocity increases with increasing laser intensity in the MOT beams because v_c depends on the photon scattering rate from the laser beam(s) that oppose the atom's motion. It is therefore desirable to use a relatively high power laser to maximize both loading rate and the number of atoms trapped in the MOT.

3.2.2 High power MOPA system

In our early work with ^{85}Rb, we used a Hitachi diode laser to supply the trapping light for the collection MOT. After stabilization with grating feedback, this laser produced roughly 20 mW of laser power, which was then divided into three retro-reflected beams. More recently we switched to a much higher power laser system, called a master-oscillator-power-amplifier (MOPA). The MOPA is capable of producing a power of several hundred mW and allows us to significantly increase the number of atoms in the collection MOT.

The MOPA consists of a frequency-stabilized master laser that sends its light into the power amplifier. The amplifier is a single-pass semiconductor device with a tapered shape to maximize the gain while reducing the power density inside the medium. The PA has high gain and very low reflectivity (<0.1%) on the input/output facets. The power amplifier thus has a wide (∼10 nm) gain spectrum limited only by the gain bandwidth of the semiconductor material. This makes the PA flexible enough for a variety of experiments with different alkali atoms. In addition, one can send multiple frequencies of laser light into a single PA — either by combining two laser beams or by simply modulating the MO laser. Modulation is a particularly attractive approach that allows one to simultaneously trap two different isotopes in overlapping MOTs (we originally designed our MOPA to trap ^{85}Rb and ^{87}Rb). Another possibility is to generate trapping light and repump light from the same MOPA.

One of the nicest features of the MOPA is its adjustable gain. By adjusting the current flowing through the PA one can vary the gain of the amplifier. The maximum gain for our PA is ∼100 for a 1.8 A current and an input power from the MO laser of 5 mW. We typically operate at much lower PA gain because we do not need such high power levels for the collection MOT and also to lengthen the lifetime of the PA.

Our MOPA system is based on Brian DeMarco's design [21], which was widely copied at JILA until the manufacturer (SDL) abruptly ceased to make the amplifiers. However, a similar PA chip is now available from TUI optics that can be used as a replacement for the SDL chip. Figure 3.1 displays the basic optical setup for our MOPA and Figure 3.2 shows the beam-shaping optics needed to correct the large astigmatism and ellipticity of the output from the PA. The PA output is ultimately sent through a fiber to spatially filter the beam and transport the light from one optical table to another.

3.2.3 Transfer of atoms between MOTs

After collecting 10^{10} atoms in the collection MOT, we push a small fraction of them down the transfer tube to the science MOT. This transfer is accomplished by turning off the collection MOT beams with a mechanical shutter while leaving on a fixed-power push beam that is directed along the transfer tube axis. Because the transfer velocity of 12 m/s is less than the capture velocity of the science MOT, all of the atoms that successfully travel down the tube without sticking to the stainless steel walls are trapped again by the second MOT. The sticking probability is reduced by a set of permanent guide magnets arranged in a hexapole configuration around the transfer tube.

Defining the efficiency of the transfer as the fraction of the initial collection MOT number that ends up in the science MOT, we find that our efficiency is quite low (0.1 to 0.2 %). Thus, to fill the lower MOT to our typical value N=6×10^8 requires 25 to 50

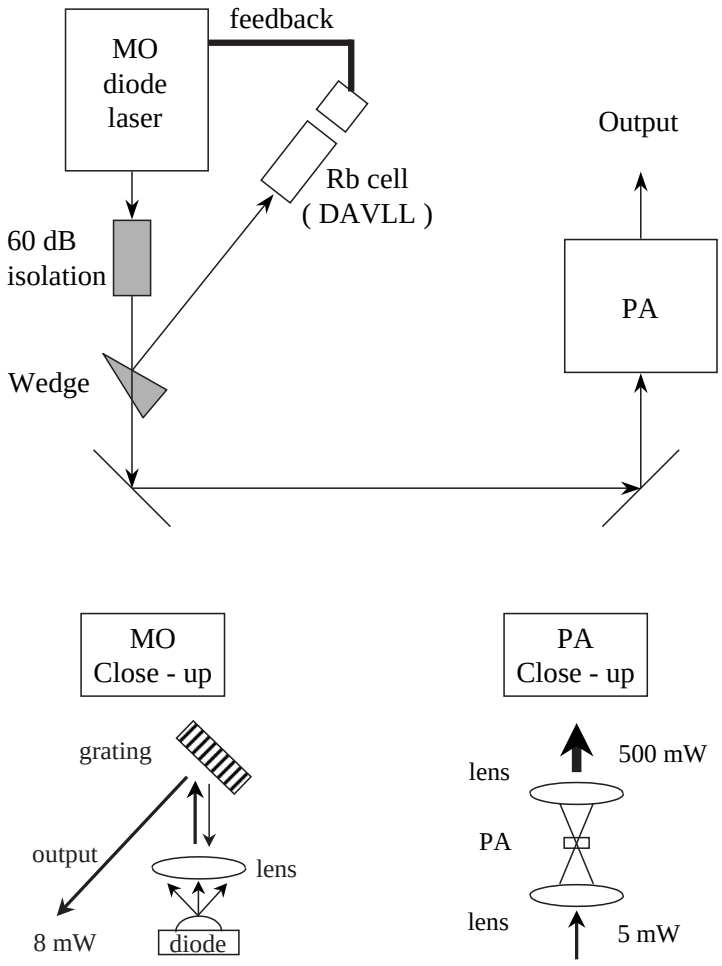

Figure 3.1: Schematic of MOPA. At top is the overall design of the MOPA, while the bottom part of the figure shows more of the details of the master oscillator and the power amplifier. We stabilize the MO using a DAVLL lock [22] and a rubidium cell. The output beam of the PA is shaped by the optical system shown in Figure 3.2.

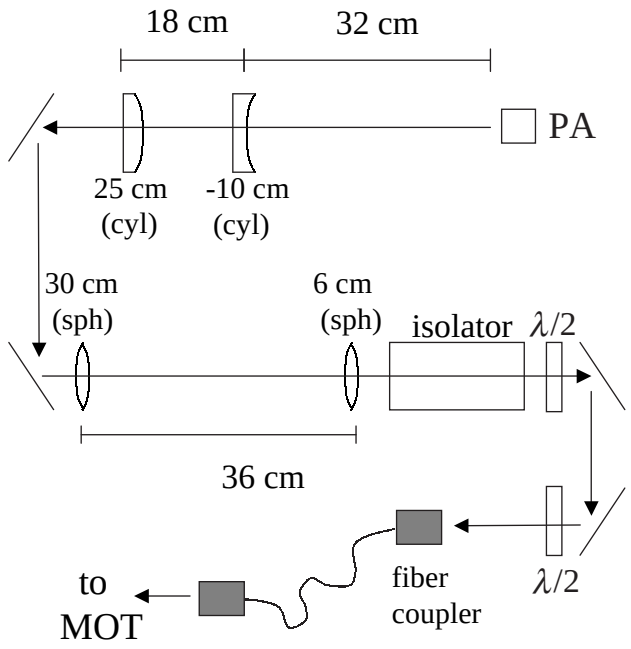

Figure 3.2: Schematic of MOPA beam-shaping optics. The first two lenses are cylindrical and only affect the vertical axis of the PA beam. After the second lens, the PA beam is roughly collimated with a square shape (∼1.5 cm on a side). The second pair of lenses form a telescope to shrink the beam until it will pass through the isolator aperture. Finally the beam travels through an optical fiber with 60% coupling efficiency before traveling to the collection MOT chamber. The collection MOT beams are 1" in diameter and each of the three retroreflected beams contains ∼20 mW for a MOPA current of 0.875 A. An additional pushing beam (with 5 to 10 mW power) is split from the main MOPA beam and is used to transfer atoms to the science MOT.

pushes. Since we actually do not allow the collection MOT to completely refill between pushes, the real number of transfers can be somewhat higher. In fact, a better figure of merit for the atom transfer is the total number transferred per unit time. For our typical repetition rate of 0.3 s and loading time of 20 to 40 s, we obtain a total transfer rate of 1 to 3×10^7 atoms/s.

I speculate that the primary bottleneck in the transfer process is going from the collection MOT to the transfer tube itself. The push beam that accelerates the atoms toward the science MOT causes a large amount of transverse heating of the atoms before they enter the tube. Only a small fraction of the collection MOT atoms near the center of the MOT may have a significant probability of successfully entering the tube.

This picture of the transfer process as being limited by the poor efficiency of pushing the collection MOT atoms into the transfer tube is supported by experimental data. We made measurements of the single load size as a function of power in the science MOT, for a fixed number of atoms in the collection MOT. The power variation was accomplished by picking off some of the MOPA laser light to supply the science MOT. Our measurements showed that we could reduce the number of atoms captured in the science MOT by turning down the beam power until the capture velocity dropped below 12 m/s. However, as long as we kept the power above this critical value, we could not further increase the number captured in the science MOT by increasing the power. The single-load number of atoms saturated as the science MOT power increased, despite the fact that the overall transfer efficiency from collection MOT to science MOT was very low ($\sim$0.2 %). This implies that we can capture all of the atoms that enter the transfer tube in the science MOT, but the number entering the tube must be far below the number in the collection MOT.

We have also observed that the number of atoms transferred to the science MOT in a single load is directly proportional to the number in the collection MOT. Using the MOPA laser for the collection MOT allowed us to increase the single load size by a

factor of 2 or more, depending on the laser power. In addition, we took advantage of the higher collection efficiency of the MOPA-powered MOT by decreasing the temperature of the Rb ampoule by several degrees yet maintaining the same MOT fill rate (1/e time of 2 s) and maximum build (N_{max}=10^{10}). This allows for a lower overall rubidium pressure in the vacuum system, which improves the magnetic trap lifetime.

3.3 Improved magnetic field measurement technique

3.3.1 Introduction

Studies of the ^{85}Rb Feshbach resonance depend critically on knowledge of the magnetic field strength. To measure the B-field, we developed a simple, precise method that relies on the Zeeman effect in a trapped cloud of atoms. In our technique, which is related to early NMR experiments [23], we induce spin-flip transitions in the atoms with a short ($\sim$10 μs) pulse of radio frequency (rf) radiation. The rf pulse coherently drives atoms from the original $|F, m_F\rangle = |2, -2\rangle$ hyperfine state to the $|2, -1\rangle$ state, which is weakly confined in the B-field range of interest ($\sim$160 G). Due to the weak confinement of the $|2, -1\rangle$ state, atoms that undergo a Δm_F=+1 transition find themselves far from their equilibrium position in the magnetic trap. These atoms experience a force that pushes them out of the original cloud of $|2, -2\rangle$ atoms. Thus, spin-flip transitions lead to the loss of atoms from the sample. The loss is frequency dependent; the rf frequency that maximizes the loss corresponds to the energy splitting between the Zeeman states. After the energy splitting is inferred from the rf frequency, we use the known hyperfine and Zeeman Hamiltonians in ^{85}Rb to extract the magnetic field. This B-field determination can be quite precise ($\pm$ 10 mG) due to the inherently narrow (Fourier transform-limited) linewidth of the rf pulse transition lineshape.

The short rf pulse method described here has several important advantages over our earlier method for magnetic field measurement by rf "carving" [1]. In the carving

technique, the frequency of the rf "knife" ramps down in ∼10 s from a chosen start value to a stop value. By varying the stop value and also the direction of the rf ramp, one can find the frequency at the center of the cloud and the corresponding magnetic field. Although the precision of such a B-field measurement can be even better than the precision yielded by the short rf pulse technique, the rf carving method has limited utility because of its long integration time. The rf carving averages the B-field during a 10 s window; in contrast, the rf pulse method averages the magnetic field for a time period equal to the pulse length, which can easily be as short as 10 μs. Clearly, measuring B-field with an rf pulse is well-suited to studies of the response of a BEC to rapid B-field changes — as discussed extensively throughout this thesis.

An additional advantage of the rf pulse method is its simple theoretical description using two-level quantum theory [24]. Although the ^{85}Rb atom is definitely *not* a spin-1/2 system, the simple two-level theory is still quite valid because of the typical magnetic field strengths used. At relatively strong magnetic fields, the Zeeman shift for a given spin state is not linear with B. Also, the splitting between a pair of adjacent spin states is not degenerate with the splitting of the next closest pair. For example, at B=162 G, the m_F=-2 → m_F=-1 transition frequency is 81.1 MHz while the m_F=-1 → m_F=0 transition frequency is 76.8 MHz. Hence, if the rf radiation is in resonance with the (-2 → -1) transition, the radiation is blue-detuned from the next closest transition (-1 → 0) by 4.3 MHz. This means that the short rf pulse cannot couple together more than one pair of spin states, provided that the spectral width of the pulse is sufficiently narrow. The spectral width for a typical 10 μs rf pulse is 89 kHz FWHM (full-width at half-maximum of Fourier transform), easily satisfying the conditions for the applicability of two-level theory. It is important to note that the different spin states are stable against spontaneous decay, so the intrinsic energy width of a given state is less than 1 Hz.

3.3.2 Rf apparatus

To utilize our new rf pulse method, we needed precise and repeatable timing control of the rf radiation. The apparatus for controlling rf and delivering it to the atoms is shown schematically in Figure 3.3. Continuous wave rf radiation is created by an HP8656B frequency synthesizer. The synthesizer output frequency and power is controlled via a GPIB computer interface.

The radiation was truncated into a short pulse with a Mini-Circuits rf switch (SPDT), model ZASWA-2-50DR. The switch was controlled by a variable pulse generator (Wavetek model 801) that could be externally triggered via a TTL signal from the computer TTL board. Finally, the rf pulse was amplified and applied to the atoms through a coil situated very near the magnetic trap.

Using our apparatus, we developed a simple procedure to drive rf transitions in a trapped cloud of cold atoms. First we load the atom cloud into the magnetic trap and evaporatively cool it to a given temperature (T$\leq$60 nK). Next we apply a short pulse of rf radiation from the rf coil. After the pulse, the trap remains on for 10-20 ms to allow the spin-flipped atoms to fall away, then the trap is switched off (B$\rightarrow$0) and the remaining $|2,-2\rangle$ atoms are imaged 12.8 ms later. We count the number of atoms in the absorption image, then repeat the procedure multiple times with different rf pulse frequencies to obtain a transition lineshape, as shown in Figure 3.4.

3.3.3 Lineshape measurements

The theory describing the response of the atom cloud to an rf pulse was derived in the early studies of magnetic dipole transitions in molecular beams [24]. When a two-level atom is subjected to a pulsed oscillatory coupling field, the probability of making a transition from the initial state (a) to the final state (b) is given by

$$P_{a\rightarrow b} = \frac{\Omega_0^2}{\delta^2+\Omega_0^2}\sin^2\left(\frac{\sqrt{\delta^2+\Omega_0^2}\tau}{2}\right), \tag{3.1}$$

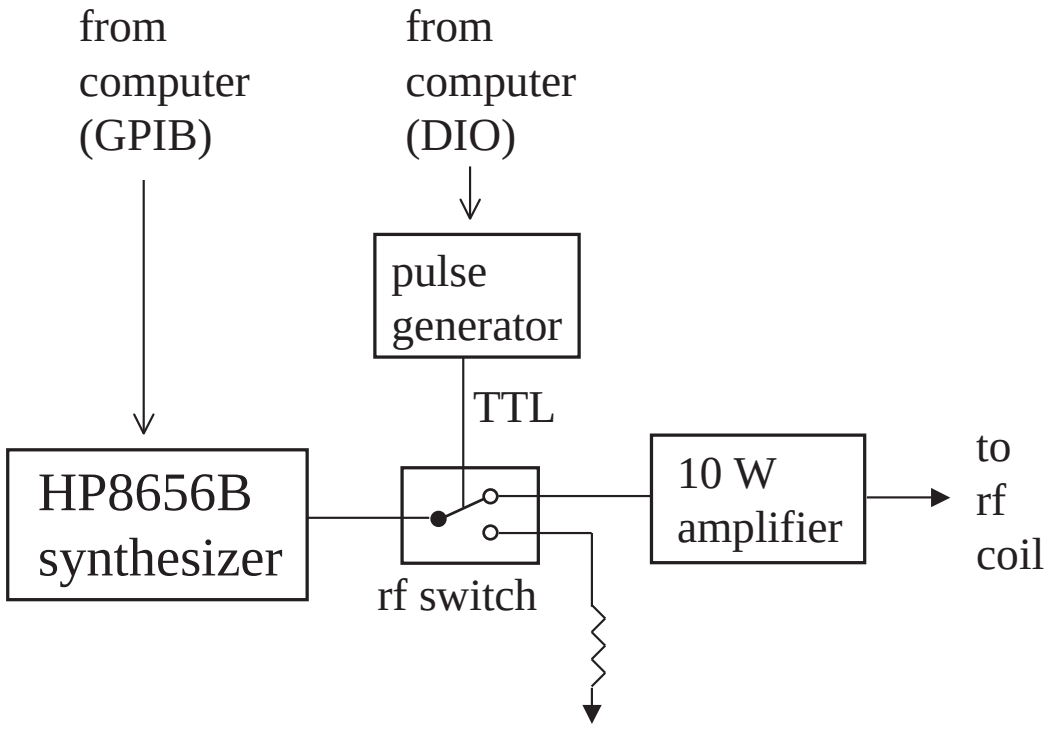

Figure 3.3: Schematic of apparatus used to control the rf radiation. A GPIB-controlled frequency synthesizer produces the rf at a fixed frequency and power. To truncate the rf wave into a pulse, we use a pulse generator and rf switch. Due to the extreme sensitivity of the atoms to rf fields, we chose a switch with very high isolation (-90 dB) and good switching characteristics (10%-90% rise/fall time=5 ns). From the measured rf transition linewidths (see section 3.3.3), we conclude that the spectral purity of the frequency synthesizer and the switching behavior of the rf switch are nearly ideal.

where τ is the pulse length, $\delta = (\omega_{rf} - \omega_0)$ is the detuning of the rf pulse from the resonance frequency, ω_0, and Ω_0 is the Rabi-flopping frequency at zero detuning. The Rabi frequency is proportional to the atom's magnetic moment and to the amplitude of the oscillating magnetic field: $\Omega_0 = \mu B/(2\hbar)$. In a typical lineshape measurement, τ is fixed and we tune δ until the transition probability reaches a maximum at δ=0. This detuning causes the maximum loss from the atom cloud in the experiment. To ensure that $P_{a\to b}(\delta = 0)$ is reasonably large (roughly 0.5), we adjust the rf power and pulse length to achieve $\Omega_0\tau \sim \pi/2$.

The predictions of equation (3.1) agree quite well with experimental data. Figure 3.4 shows lineshape data and theory for a particular choice of magnetic field, rf power, and (fixed) rf pulse length. We also varied the pulse length with fixed rf frequency to map out coherent Rabi oscillations (see Figure 3.5).

For most of our magnetic field measurements, we found that using cold thermal clouds was more convenient than using a condensate. Since a BEC can undergo huge number losses when the magnetic field is changed in the vicinity of the Feshbach resonance (see chapter 5), a BEC cloud is not suitable for measuring the field during our fast B-field pulse sequence. With a BEC cloud, it is difficult to separate the Feshbach resonance-induced number loss from the rf pulse-induced number loss. We therefore measure the magnetic field with cold, low-density thermal clouds. The low density prevents density-dependent losses from occurring during our rapid B-field changes, while the cold temperatures allow for fairly narrow rf transition linewidths. Thermal clouds have the additional advantage of being simpler and faster to produce than BECs. The cycle time for producing ∼60 nK, low density thermal clouds is roughly 40% shorter than the time to make a condensate.

There is one disadvantage to using thermal clouds, however. Since thermal clouds are hotter than condensates, they experience a larger magnetic field variation. The B-field variation arises from gravitational "sag" in the magnetic trap. Due to our rather

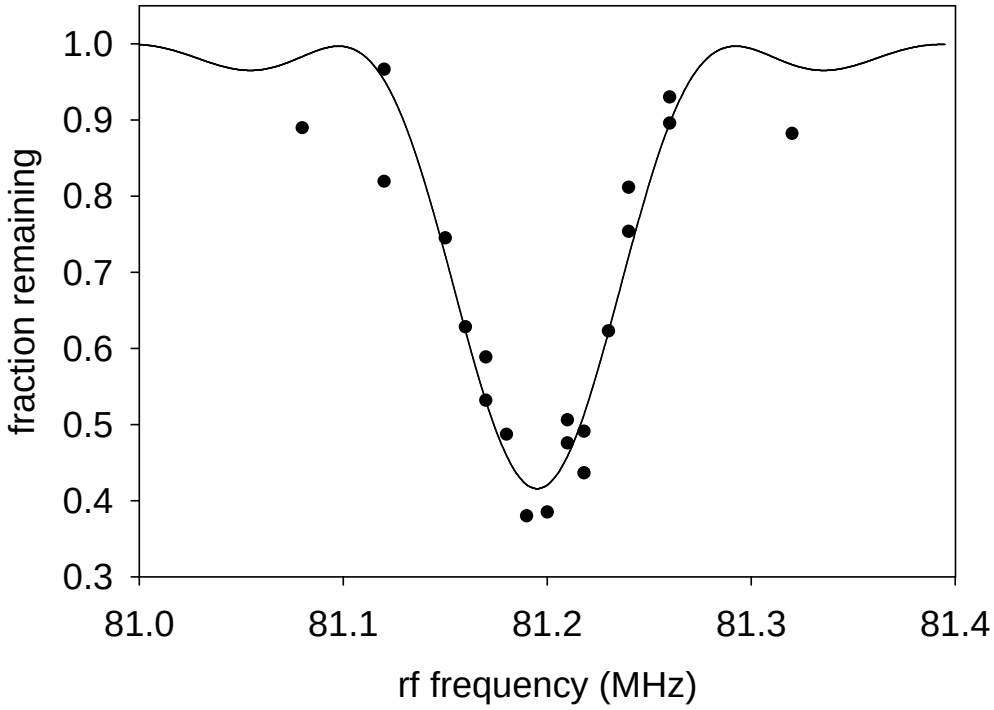

Figure 3.4: Comparison of lineshape data to theory for a sample of BEC atoms. The points are the fraction of atoms remaining after the rf pulse. The line shows the quantity (1-$P_{a\to b}$) computed from equation (3.1), with τ=10 μs and $\Omega_0 = 2\pi \times 28$ kHz (the RF synthesizer power was +5 dBm). These conditions correspond to a $\Omega_0\tau=\pi/1.9$ pulse. We used a BEC cloud at T$\sim$3 nK for the lineshape, so there is no indication of any linewidth broadening beyond the Fourier transform-limited theory (FWHM=89 kHz).

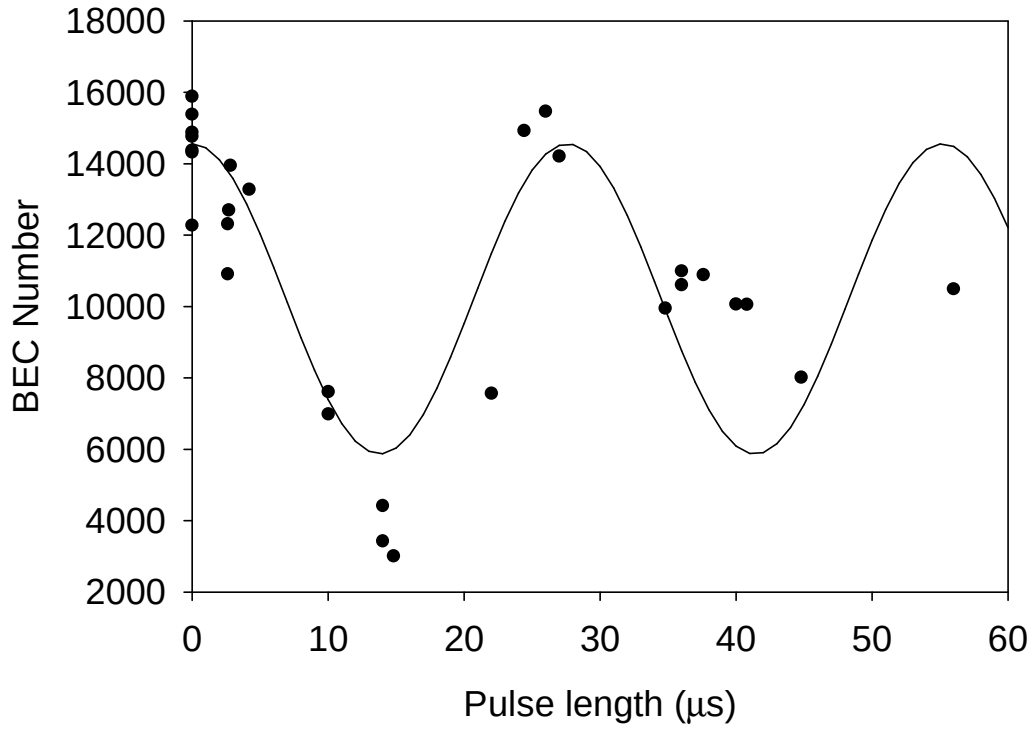

Figure 3.5: Rabi-flopping in a BEC. The points are the number of BEC atoms remaining after the RF pulse, while the line is given by equation (3.1) with $\Omega_0 = 2\pi \times 28$ kHz and $\delta = 2\pi \times 23$ kHz. The data set is somewhat undersampled, but it seems consistent with the theory at short times. However, at longer times, the Rabi flopping seems to damp out. This could be related to the large negative scattering length of the $|2, -1\rangle$ state, which does not have a nearby Feshbach resonance like the initial $|2, -2\rangle$ state. In addition, gravity should lead to decoherence because the $|2, -1\rangle$ state has a factor of 3 weaker magnetic moment than the initial state.

weak trapping potential, the atoms sag downward, away from the position of the B-field minimum, until the force from the (increasing) magnetic field gradient becomes strong enough to counteract gravity. In equilibrium, this leads to an approximately linear gradient of 26 G/cm along the vertical direction. Thus, the spread in B-field across the cloud is simply determined by the cloud's vertical width, σ_r, which depends on temperature as $\sigma_r \propto \sqrt{T}$.

The magnetic field width of the cloud translates directly into a spread in rf transition frequency, which leads to inhomogeneous broadening of the rf lineshape. The broadening is very simple to model as long as the rf pulse length is much less than a trap period because the atoms do not move during the pulse. To first order, each atom experiences a constant magnetic field with a magnitude that depends on the position of the atom when the pulse begins. One can calculate the correct transition probability by averaging over the distribution of transition frequencies along the vertical direction of the thermal cloud. The average probability is

$$\langle P_{a\to b}\rangle = \frac{1}{N}\int_{-\infty}^{\infty} P_{a\to b}(\omega_0,\omega_{rf})\frac{N}{(2\pi)^{3/2}\sigma_r\alpha\delta}\exp\left[-\frac{1}{2}\frac{(\omega_0-\omega_{rf})^2}{\sigma_r^2\alpha^2(2\pi\delta)^2}\right]d\omega_0, \tag{3.2}$$

where $P_{a\to b}(\omega_0,\omega_{rf})$ is the single atom probability from equation (3.1), ω_0 is the angular transition frequency at a given position, ω_{rf} is the angular rf frequency, N is the number of atoms in the thermal cloud, σ_r is the rms radial width of the gaussian density distribution, α=2600 G/m is the magnitude of the B-field gradient, and δ is the slope of transition frequency versus B-field, which is 530 kHz/G near 160 G.

Typically, we observed thermal cloud linewidths (FWHM) of ∼100 kHz with 10 μs pulses and T∼60 nK. To look for effects of inhomogeneous "thermal broadening" in the lineshapes, we increased the pulse length. For example, a pair of thermal cloud lineshapes measured with different rf pulse lengths are shown in Figure 3.6. These data show a significant amount of inhomogeneous broadening from the finite temperature of the clouds.

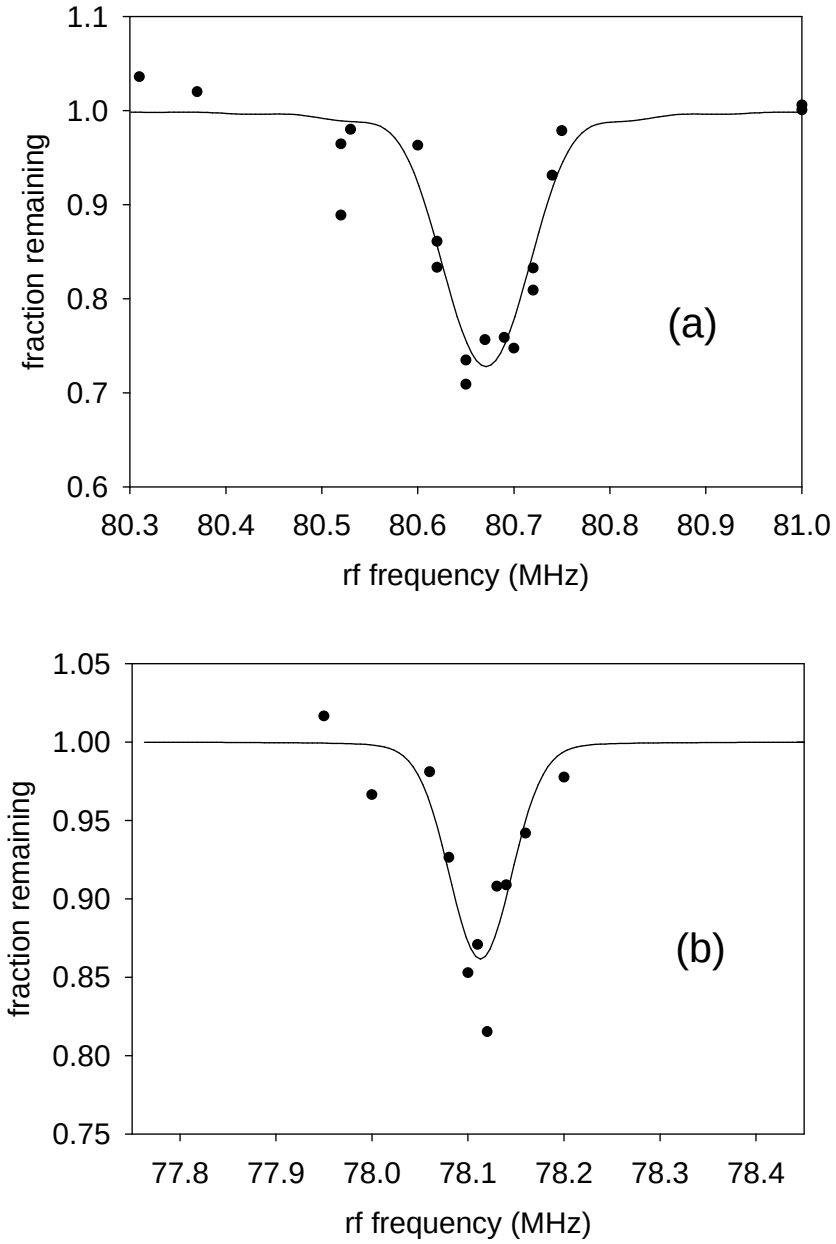

Figure 3.6: Lineshape data and theory for a thermal cloud. The points are the fraction of atoms remaining after the rf pulse and the lines are predictions from equation 3.2. The average thermal cloud density is 10^{11} cm^{-3}. **(a)** Data and theory for rf pulse length τ=10 μs, temperature T=50 nK, and Rabi frequency $\Omega_0 = 2\pi \times 20$ kHz. Here the Fourier transform limited linewidth is 89 kHz; however, thermal broadening increases the FWHM above the transform limit by 30%. **(b)** In this case, we have τ=50 μs, temperature T=60 nK, and Rabi frequency $\Omega_0 = 2\pi \times 6$ kHz. Although the transform limit decreases to 18 kHz, thermal broadening causes the linewidth from equation (3.2) to be 82 kHz. The lineshapes in **(a)** and **(b)** were measured at slightly different magnetic fields, so the center frequencies for the lineshapes are different.

The total width of a thermal cloud rf lineshape depends primarily on the pulse length (through the Fourier transform limit) and inhomogeneous broadening from spatial magnetic field differences across the cloud. Another potential source of line-broadening is time variations of the B-field during the rf pulse. We sometimes observed broadening that was larger than expected from the transform limit and finite temperature alone. In fact, one can use the observed linewidth to estimate the magnitude of B-field noise during a rf pulse. The noise can only be estimated in this way if it causes significant broadening beyond that due to the transform limit and finite temperature of the atom sample.

As an aside, it is worth mentioning that for the majority of our lineshape measurements, we fit the data to a Lorentzian function. Although this simple function does not capture the details of the full lineshape described by equation (3.2), the Lorentzian fit provides a good estimate of the linewidth and center frequency. In general, the data were not sufficiently precise to distinguish differences between the chosen fit function and the theoretical form discussed here.

3.3.4 Obtaining the B-field from lineshape data

Once the center frequency for the rf lineshape is measured, we calculate the magnetic field with the Breit-Rabi equation [24]. The form of this equation for ^{85}Rb is described in Ref. [1] and will not be repeated here. Since the Breit-Rabi equation is an exact analytical result for the B-field dependence of the energies of the various hyperfine states, we simply insert the measured energy difference between two states (the center frequency from the rf lineshape) and then invert the equation to obtain the magnetic field. The B-field determination has a precision limited only by the precision of the rf frequency measurement.

In principle, the accuracy of this B-field determination should also be very good. However, the measurement is distorted by one significant systematic effect from finite rf

power. The rf power systematic is a shift to the magnetic field due to interference of the rf radiation with the magnetic field control circuitry. The current sensor for the auxiliary coil current servo (described in section "aux-coil hall probes") detects the rf radiation and filters it, leading to a change in the current and a "DC" shift to the field. Examples of rf power shifts to the Hall probe current sensors are displayed in Figure 3.7. We used the Hall probe signals, which were previously calibrated with respect to magnetic field (see section 3.4.6), to correct for the rf power shift to the B-field.

We have an additional, independent way to determine the size of the rf power shift. In this method, we vary the power of the rf pulse and measure a lineshape for each value of power. The rf power shift causes the center frequency of the lineshape to decrease linearly with rf power (see Figure 3.8). By extrapolating to zero rf power, we obtain another estimate of the true rf transition frequency (B-field).

The rf power shift discussed here is only present due to interference of the rf radiation with the auxiliary coil current servo. There is no noticeable effect of a short rf pulse on the magnetic field produced by the baseball and bias coil currents, which provide the majority of the B-field experienced by the atoms.[1] Thus, in experiments where we change the magnetic field slowly, without using the auxiliary coil, there is no rf power shift to the measured B-field.

Because ^{85}Rb is not a two-level atom, the rf radiation causes another (small) power shift to the measured rf transition frequency. The shift arises because the rf radiation — tuned near the $|2,-2\rangle \rightarrow |2,-1\rangle$ resonance — simultaneously couples the $|2,-1\rangle$ and $|2,0\rangle$ states. This latter coupling leads to a small AC Stark shift of the m_F=-1 state. The Stark shift is equal to $\Omega_0^2/|4\delta| \simeq$0.3 kHz, where δ=4.3MHz is the relevant detuning at 162 G (see section 3.3.1). Of course, the calculated shift is totally

[1] The absence of an effect is due to two things: the servo that controls the current for the trapping coils (baseball and bias coils) has much lower bandwidth than the auxiliary coil servo, so it is not able to respond to the rf pulse during the time of the pulse. Also, the trapping coils have a larger inductance than the auxiliary coil and thus they offer a larger impedance to high frequency current changes.

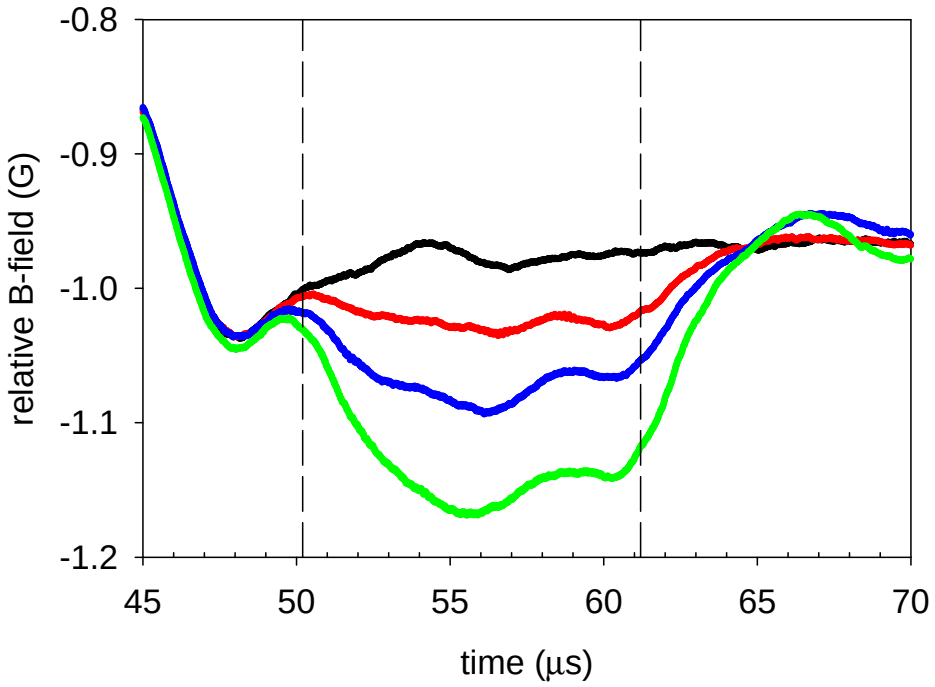

Figure 3.7: B-field shifts due to finite rf pulse power. Solid lines are the B-fields versus time calculated from the calibrated auxiliary coil current sensor. Vertical dotted lines show the 11 μs duration of an applied rf pulse. Each solid line corresponds to a different rf pulse power. From top to bottom, the rf power from the frequency synthesizer is -120 dBm, -1 dBm, 2 dBm, and 5 dBm. The current sensor output signals are filtered using a 2 μs averaging window, so there is no indication of oscillations at the rf frequency of $\sim$80 MHz. To estimate the B-field shift, we calculate the average difference between the line with -120 dBm and the line with a given rf power, *within the time window for the rf pulse*. We estimate the uncertainty on the B-field shift from the standard deviation of the average field difference.

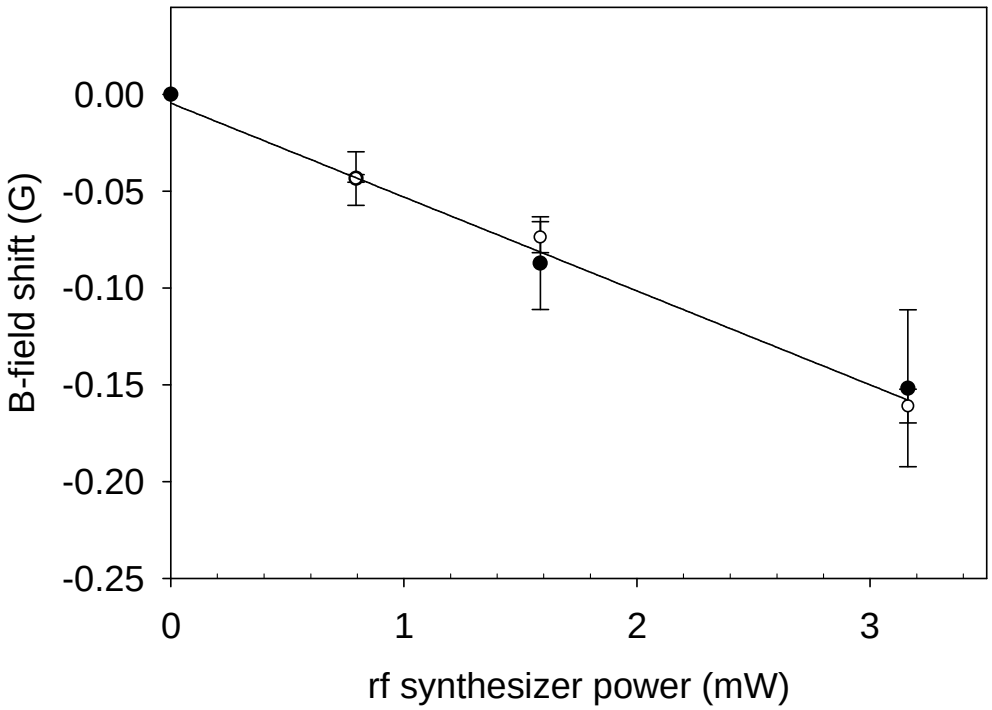

Figure 3.8: Comparison of two methods to measure rf power shift. Black points with error bars are B-field shifts as measured by the auxiliary coil current sensor as a function of rf pulse power (see caption to Figure 3.7). White points with error bars are B-field shifts determined directly from rf lineshape data. An arbitrary offset was added to the lineshape data to make the point at ∼0.8 mW overlap the corresponding current sensor measurement. The solid line is a weighted fit to the lineshape data, showing that the extrapolation to zero rf power agrees well with the current sensor data. The slope from the fit is -49(4) mG/mW.

negligible compared to a typical rf linewidth of 100 kHz, so we can safely ignore it. Ignoring the shift is reasonable as long as the magnetic field is large enough to break the degeneracy between adjacent Δm=+1 spin-flip transitions.

3.3.5 Outlook for rf lineshape measurements

The present technique for measuring the magnetic field made possible the precise characterization of the ^{85}Rb Feshbach resonance discussed in chapter 7. This method was also essential for understanding the time-variations of the B-field produced by the auxiliary coil (see section 3.4). There are at least two other possible experimental applications for the rf lineshape technique, although we have not fully explored them.

First, one can use the rf lineshapes to determine the nature of magnetic field noise in the experiment. By increasing the length of the rf pulse (and thereby decreasing the linewidth due to the Fourier transform limit), one can look for a linewidth "floor" corresponding to time variations in the B-field. The magnitude of these field variations could be explored by careful study of the lineshapes.

Second, the rf lineshape technique might be used to measure the average mean-field energy of a BEC. After subjecting a condensate to a rapid change in magnetic field (and scattering length), one could then measure an rf lineshape and look for a shift or broadening of the lineshape from the BEC self-interaction. Perhaps it would be possible to measure a beyond mean-field energy shift in this way [1]. Unfortunately, such a measurement would be difficult because condensate atoms experience non-adiabatic transitions to a molecular state when the B-field is changed quickly near the Feshbach resonance, as noted in chapter 5. Since the BEC loss occurs on a time scale ($\sim$10 μs) that is comparable to the minimum rf pulse length needed for a precise frequency measurement, interpetation of the rf lineshape would likely be very complicated. However, a compromise might be found in which the B-field change was slow enough to avoid non-adiabatic transitions but fast enough to prevent changes to the condensate density

(see section 3.5.3).

3.4 New auxiliary coil for rapid B-field pulses

3.4.1 Motivation for auxiliary coil

To study the response of a ^{85}Rb BEC to rapid magnetic field changes near the Feshbach resonance, we developed a specialized "auxiliary" magnetic field coil. This coil and its accompanying electronics were designed to provide controlled B-field pulses toward the resonance, allowing us to explore the resulting BEC dynamics over a wide range of time scales. In the following sections, the details of the auxiliary coil design and characterization are given.

Before building the auxiliary coil, we made some preliminary attempts to pulse the magnetic field quickly by rapidly changing the reference voltage used in the current servo for our main "baseball" (BB) trap coil. This is the same method we used to study condensate collapse dynamics, as described in Chapter 4. By using short magnetic field pulses, we hoped to avoid the issues of condensate heating and 3-body collisional losses that we previously observed with slower B-field ramps [1]. However, the BB coil ramping scheme had limited utility. Due to the 8 kHz bandwidth of the BB current control servo, a 10 G B-field pulse toward the Feshbach resonance from the initial field of 166 G required a total time of $\sim$250 μs. Surprisingly, we observed large BEC number loss under these conditions, with most of the loss occurring during the ramp itself. This evidence for rapid condensate number variations prompted us to explore even shorter time scales, so we developed a fast, high current control circuit that drives a separate auxiliary coil.

We decided there were at least two good reasons to start from scratch and build a separate coil rather than modifying the existing BB trap/servo system. Most importantly, the current control for the trap coils was previously optimized to give good

stability during rf evaporation and BEC production [1]. We wished to avoid the possibility of messing up one of the best parts of the apparatus and/or tying up the experiment during the extensive debugging process that would follow a change to the trap. In addition, we realized that we could carefully design the auxiliary coil to meet the specialized requirements for rapid B-field ramps, including low coil inductance and high bandwidth for the servo.

3.4.2 Auxiliary coil design

We designed the auxiliary coil to give a relatively large magnetic field at the position of the trapped atom cloud and to have a low self-inductance, L. Since the inductance for a solenoid is proportional to the area and the number of turns squared, we constructed the auxiliary coil with only 3 turns of square magnet wire with a coil diameter barely big enough to fit over the glass science cell. The coil is placed as close as possible to the trapped atoms and is oriented coaxially with the BB and bias trap coils, so that the B-fields in the z-direction add linearly. The position of the auxiliary coil with respect to the trapped atoms and the other major magnet coils is shown in Figure 3.9. For this geometry, the self-inductance of the auxiliary coil is $\sim$2 μH and the coil produces a magnetic field at the trap center of 10G when driven by a current of 167A.

3.4.3 Capacitor bank for auxiliary coil current

To switch such large currents rapidly, we built a circuit analogous to a short-pulse flashlamp driver [25]. We first charge a 170μF capacitor bank to 580V, then discharge it through the auxiliary coil at a rate determined by a transistor. The large capacitor bank at high voltage allows for large amounts of stored charge and also a large current ramp rate, dI/dt. From Faraday's law, $V = L\frac{dI}{dt}$, the maximum ramp rate is 2.9×10^8 A/s! In practice however, the transistor resistance limits the actual value of dI/dt to the more

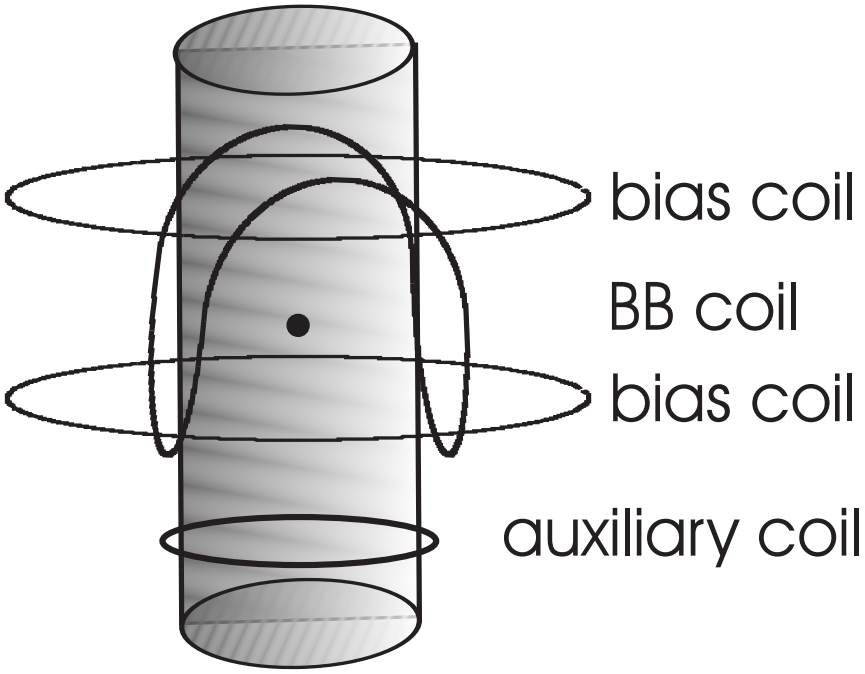

Figure 3.9: Schematic of the main magnetic coils. The shaded grey tube represents the glass cell and the black dot shows the position of the trapped atom cloud. The bias coils have average radii of 4.5 cm and are separated by 4 cm. The BB coil has a radius of 3.2 cm. The auxiliary coil barely fits over the cell with its 1.6 cm radius, and it is located 4 cm from the atoms.

modest value of 2.6×10^7 A/s.

In the course of testing the discharge rates of various capacitors, we learned that all capacitors are not created equal. In fact, different types of capacitors with the same values for C do not necessarily discharge at the same rates. For rapid discharge, i.e., ideal capacitor performance, one needs a capacitor with low effective series resistance (ESR). The ESR of a capacitor depends strongly on its innards — the materials used to store the charge. For example, electrolytic capacitors have very large ESR compared to metal film or oil-filled capacitors. To form our capacitor bank, we dug up several ancient, toxic, PCB-filled capacitors from the JILA electronics shop and also bought some new paper/polyester film capacitors from CSI Technologies ($100 per 50 μF capacitor). The capacitor bank voltage is limited by the finite capacitor working voltage of 600 V, which leads to a total stored charge Q=CV=0.1 Coulombs.

3.4.4 Servo electronics and transistor

To regulate the discharge rate of the capacitor bank, we use a negative-feedback current servo and a transistor. The servo compares the output of a fast Hall-effect current sensor (Hall probe model CLN-300) with a reference voltage and sends the difference signal to the transistor, as displayed schematically in Figure 3.10. The Hall probe used in this circuit is identical to those used for sensing the BB and bias coil currents [1]. These current sensors have excellent dynamic range and linearity, as well as a large bandwidth (150 kHz specification). We verified that the Hall probe was linear up to dI/dt values of 4×10^7 A/s by using a silicon-controlled rectifier (SCR) to discharge the capacitor bank very quickly.

The auxiliary coil current servo is quite simple — a single op-amp compares the hall probe signal to the reference voltage, producing an output proportional to the difference voltage. We chose the feedback loop using a variable RC click-box, also known as “Terry’s Magic Box”, to optimize the transient response of the servo to an input step

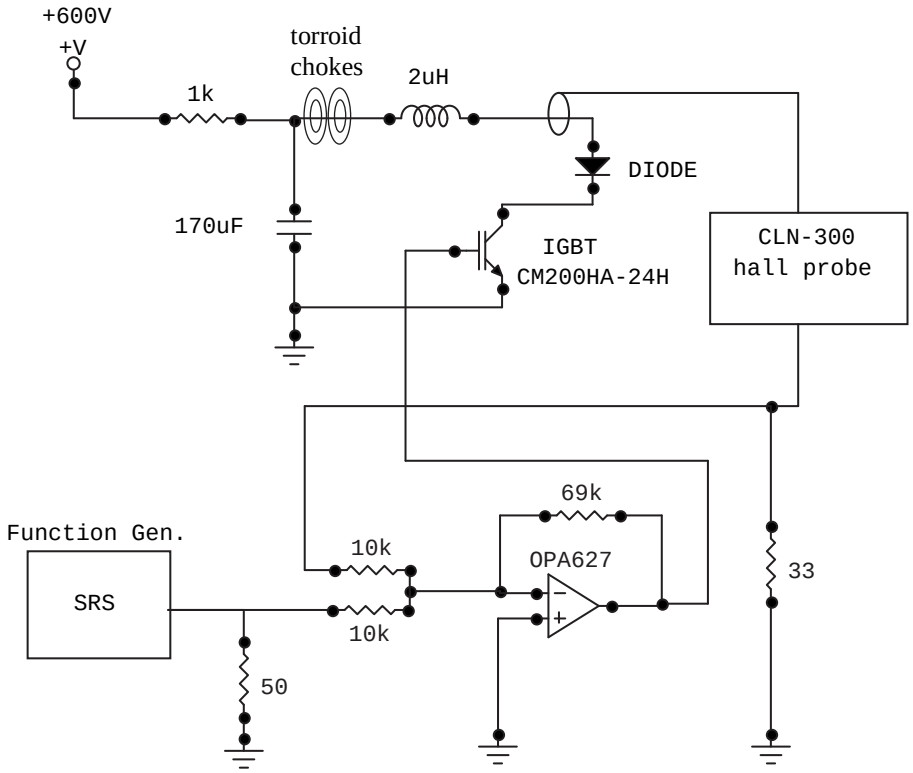

Figure 3.10: Circuit schematic for the auxiliary coil current control. The auxiliary coil is shown as the 2 μH inductor and the capacitor bank is the 170 μF capacitor. An important part of the circuit is the SRS function generator (model DS345), which was programmed via a GPIB interface with our Labview computer. The function generator allowed us to apply very precisely-tailored magnetic field pulses to the BEC atoms. The torroid chokes between the capacitor bank and the auxiliary coil prevent "parasitic" oscillations, which are created by miniature LC oscillators from the finite inductance and capacitance of the various circuit elements.

function pulse on the reference voltage. The best behavior was obtained with a simple proportional gain of ∼7. Terry's box allowed us to sidestep the calculation of the complicated frequency response of various circuit elements, including the Hall probe and transistor. We empirically determined the best feedback loop by examining the servo behavior for various R, C, and RC combinations.

The transistor used to control the capacitor discharge is an insulated-gate-bipolar-transistor (IGBT): Powerex model CM200HA-24H. This device has the useful property of a very large maximum voltage rating for the collector-emitter voltage (1200 V), which far exceeds the capacitor bank working voltage of 600 V. The IGBT has a maximum average power dissipation of 1.5 kW, which is generally not exceeded during our typical few hundred Amp current pulses. To ensure that we do not kill the transistor during a given current pulse, we use the minimum capacitor bank voltage necessary to supply the pulse. In this way we can minimize the voltage drop across the transistor (and therefore the power dissipation) during the discharge process. The most important advantage of the IGBT is that it can be used alone; there is no need to put several such devices in parallel. We found that using multiple transistors in parallel caused massive oscillations in the current due to competition between the devices. One disadvantage of the IGBT relative to a more common MOSFET is the higher ON resistance. The ON resistance of the transistor limits the maximum discharge rate of the capacitor bank — the auxiliary coil circuit can be modeled as a LCR damped oscillator, where the R value of the transistor determines the damping rate. Although the IGBT resistance is higher than a MOSFET, the IGBT is still preferable due to its better voltage and power ratings.

3.4.5 Auxiliary coil interferes with magnetic trap servo

In our initial attempts to pulse the magnetic field with the auxiliary coil circuit, we discovered that the auxiliary coil magnetic field change induced a corresponding

magnetic field change in the BB and bias coils. Mutual inductance between the various coils causes this effect, which forces the BB and bias servos to oscillate for several milliseconds. To avoid this undesirable interference of the auxiliary coil with the magnetic trap servos, we devised a scheme to briefly decouple the BB and bias servos from their respective FETs during the auxiliary coil pulse. We built a sample-and-hold circuit for the BB and bias coil servos, as shown in Figure 3.11. The operation of the circuit is as follows. Just before the beginning of the auxiliary coil pulse, we send a HOLD TTL signal to the LF398 sample-and-hold chip, instructing it to start holding the voltage constant. Soon afterward, we send a SWITCH TTL signal to the DG201 switches, causing one switch to open and one to close. Now the servo is decoupled from the FET gate and the sample-and-hold controls the FET. After the auxiliary coil pulse ends, we switch back to servo control and allow the LF398 to start sampling the input voltage. Of course, the sample-and-hold circuit cannot prevent the auxiliary coil from inducing currents in the other coils, but the circuit does remove the unwanted transient response to the induced currents.

3.4.6 Calibrating the total magnetic field

Before attempting any experiments to study condensate loss, we had to calibrate the auxiliary coil. We made a simple estimate of the magnetic field experienced by the trapped atoms for a given auxiliary coil current using the solenoid equation:

$$B(z) = \frac{\mu_0 N I}{2R} \left[1 + z^2/R^2\right]^{-3/2}, \tag{3.3}$$

where B(z) is the z-component of the magnetic field evaluated on the axis of the solenoid, μ_0=$4\pi \times 10^{-7}$ N/A^2 is the free-space permeability, N is the number of turns in the solenoid, I is the current, and R is the radius. Using the measured coil radius and position (see Figure 3.9), the solenoid equation predicts a B-field to current ratio of -0.06 G/A, or -3.57 G/V$_{Hall}$, where V$_{Hall}$ is the Hall voltage — the voltage produced

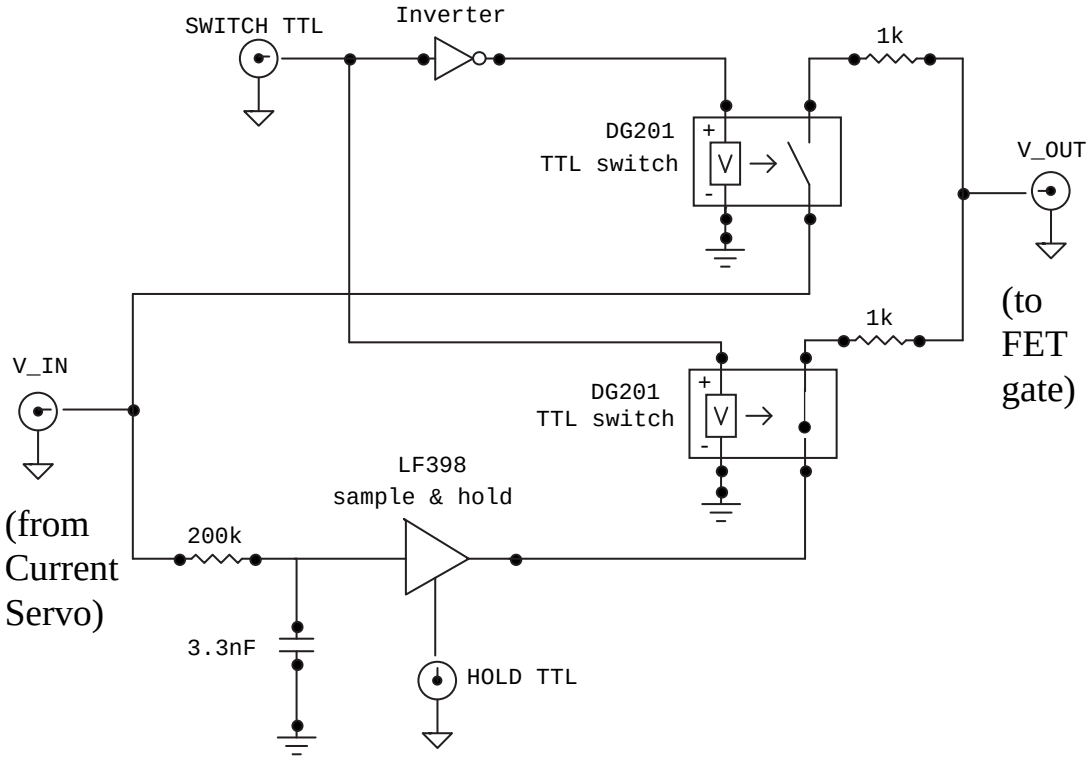

Figure 3.11: Schematic diagram of the sample-and-hold circuit. The circuit is shown in the HOLD configuration, so the trap servo is effectively disconnected from the FET. Both the BB and bias coil current servos have a sample-and-hold circuit like this one.

by the Hall current flowing through a resistor R_{Hall}=33.5 Ω. The fractional uncertainty in this calculation is roughly 20% due to uncertainty in measured values of R and z.

We tested this prediction with two different experiments. In the first experiment, we connected the auxiliary coil to a DC power supply and used a fixed 16 A current. We then loaded atoms into the magnetic trap and removed them with rf radiation from the rf coil. The rf frequency was smoothly ramped downward to cut away more and more atoms until none remained. We recorded the final rf frequency required to remove all of the atoms as a function of the auxiliary coil power supply current and converted the rf transition frequency to magnetic field using the Breit-Rabi equation. This procedure gave an auxiliary coil calibration of -3.696(2) G/V_{Hall}, which agrees quite well with the rough estimate given above.

We obtained a second calibration of the auxiliary coil using short rf pulse spectroscopy (discussed in section 3.3). Two 10 μs rf radiation pulses were applied at different time delays during the auxiliary coil pulse. The short rf pulse calibration was -2.26 G/V_{Hall}, which is only 60% of the "DC" calibration discussed previously. The reason for the discrepancy is the difference in induced currents for the two different calibration experiments. With a steady current flowing through the auxiliary coil, there are no induced currents in other coils or pieces of metal near the atom cloud. However, when we apply a short, high current pulse to the auxiliary coil, there is a tremendous change in magnetic flux through the other coils, leading to significant induced magnetic fields that oppose the auxiliary coil B-field. The presence of the induced currents limited the maximum ramp speed of the *total* field to ∼1 G/μs.

To compensate for the effects of induced currents, we had to first measure their time-dependence. As displayed in Figure 3.12, we used short rf pulses to map out B(t) for a trapezoidal auxiliary coil current pulse. In this experiment, the current remains constant during the hold time, t_{hold}. Although the auxiliary coil magnetic field, B_{aux}, must therefore be constant during t_{hold}, we observe that the total field decreases with

time, which means that the induced B-field is decreasing in magnitude (Lenz's law predicts that the induced B-field is opposite in sign to that of the auxiliary coil). Clearly, in the limit that $t_{hold} \rightarrow \infty$, the induced fields should decay to zero and the auxiliary coil calibration must return to its DC value of -3.696 G/V_{hall}.

By tailoring the reference voltage waveform, we changed the time-dependence of B_{aux} until the *total* B-field was approximately constant during t_{hold}. In most cases the required correction is a linear "droop" of the auxiliary coil current, as in Figure 3.12. We adopted an iterative procedure and found this linear slope empirically because a detailed model of the coupled coil system would be very complex. Figure 3.13 shows the measured dependence of the droop rate of the induced magnetic field on the auxiliary coil pulse height. This plot proved very useful for many of our BEC experiments, where a constant evolution B-field was important.

3.5 Improved BEC diagnostics

To conduct the experiments described in this thesis, we developed new methods to measure the number and temperature of the condensed sample. Accurate knowledge of these properties (especially the number of atoms) is crucial for studying the dynamics of the BEC when subject to changes in the magnetic field and scattering length. In our number and temperature measurements, we made extensive use of the Feshbach resonance to change the ground state size of the BEC wavefunction in a very highly-controlled fashion. Our manipulation of the wavefunction via the tunable scattering length in the ^{85}Rb condensate can be viewed as an example of quantum engineering, where the detailed quantum-mechanical characteristics of a system may be changed at will. Basically, we can use the well-understood mean-field interaction that depends on a to either expand or shrink the BEC wavefunction, allowing us to count the condensate number or measure its temperature. We then use these techniques to study the condensate dynamics in regimes that are *not* well-understood, such as the collapse of an

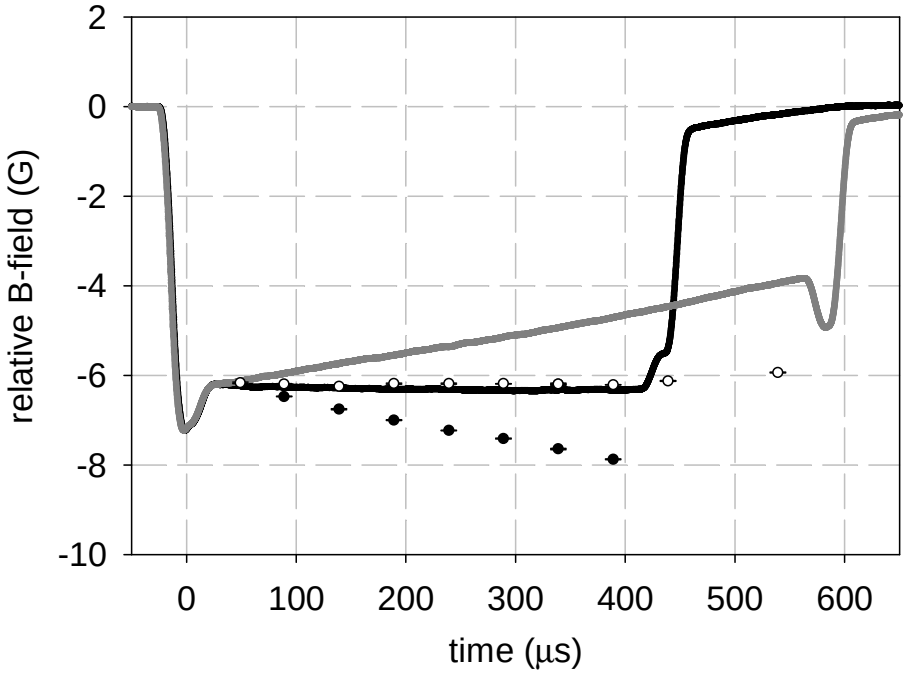

Figure 3.12: Compensating for induced currents. The black line shows the auxiliary coil B-field calculated from the Hall probe with the calibration -2.26 G/V. In this case, the auxiliary coil current was roughly constant during the hold time. The Hall probe voltage was filtered with a 2 μs averaging window. Black points with error bars are measurements of the total magnetic field experienced by the atoms from rf pulse spectroscopy (pulse length=22 μs) corresponding to the conditions of the black line. The decrease in total B-field is related to the droop in the induced magnetic field. The grey line shows the auxiliary coil magnetic field when a linear correction is applied to the servo reference voltage. The white points are the rf pulse B-field data corresponding to the grey line. By precisely adjusting the auxiliary coil current, we made the total magnetic field constant to within 30 mG for over 400 μs.

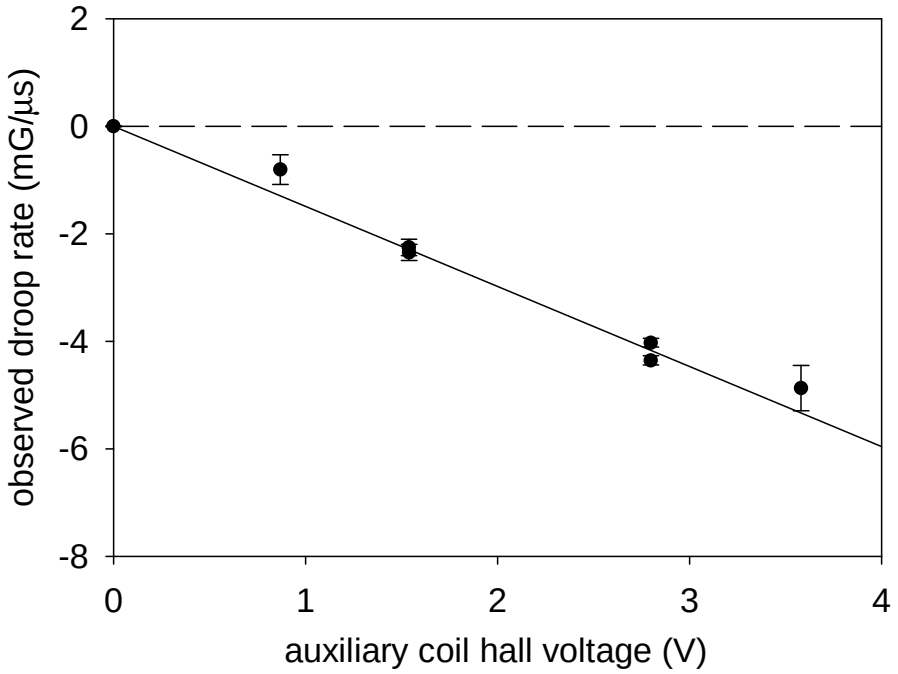

Figure 3.13: Dependence of induced B-field decay rate on auxiliary coil pulse height. The black points with error bars are obtained by fitting a straight line to a series of consecutive magnetic field measurements, as in Figure 3.12. The induced B-field is calculated to be the difference between the total magnetic field (measured by the rf pulse spectroscopy) and the auxiliary coil magnetic field, $B_{aux}(t)$=-2.26 G/$V_{Hall} \times V_{Hall}(t)$. The pulse height of the auxiliary coil current pulse, which is used on the x-axis, is defined as the initial value of the Hall probe voltage after the completion of the first rapid B-field ramp(s). We used this plot as a look-up table for adjusting the auxiliary coil droop rate to make the total magnetic field constant for a particular value of magnetic field, B_{hold}.

initially stable BEC (Chapter 4) or the non-adiabatic mixing of atomic and molecular states (Chapters 5 and 6).

3.5.1 Absorption imaging

All of our measurements of BEC properties depend on absorption imaging of the atom cloud. We illuminate the cloud with an on-resonant laser beam and then image the shadow onto a CCD camera. The "darkness" of the shadow gives information about the number of atoms casting the shadow. To obtain the most sensitive and accurate measurements of number, we find that the magnetic trap must be turned off and the condensate spatial size must be significantly larger than the 7 μm resolution limit of the optical system. Turning off the magnetic trap is important to maximize the number of photons scattered by each atom, which improves the signal-to-noise ratio of the shadow images.

The detection of the BEC number by absorption imaging is necessarily a destructive measurement because of the photon scattering and the trap turn-off. The BEC atoms are dramatically heated by the recoil momenta of the scattered photons, effectively destroying the ultracold condensate. Even if the photon heating could be reduced by turning down the laser intensity, turning off the magnetic trap would also destroy the condensate because when B$\rightarrow$0, the scattering length changes sign and magnitude ($a \rightarrow$ -470 a_0). This leads to a strong attractive self-interaction in the BEC, which should cause the condensate to self-destruct by collapsing (see Chapter 4).

To count the number of atoms in the BEC, we use the well-known relationship between the amount of absorption (the optical depth) and the number [1]. We typically fit the shadow image to a Gaussian function and then calculate the number of atoms from the fit parameters. Although the Gaussian function does not always fit the images perfectly, it provides a good approximation for most cases. A more robust way to estimate the number of atoms is to calculate the total optical depth by summing all of

the pixels in the shadow image. The number of atoms is directly proportional to this optical depth summation. One advantage of the pixel sum method is its insensitivity to the density distribution of the atoms that determines the precise spatial shape of the shadow image. Even non-standard density profiles or multi-component spatial distributions of atoms can be accurately counted using the pixel sum. We also developed more specialized fitting routines that combine Gaussian fitting and pixel sums for the dynamics experiments described in Chapters 4,5, and 6.

3.5.2 Motivation for expanding the BEC

There are a number of systematic effects that plague the experimenter attempting to measure the number of atoms in his ^{85}Rb BEC. The student cannot simply use the "standard" approach of turning off the magnetic trap, waiting for the condensate to expand for a few milliseconds, then finally taking a picture. In fact, there are a number of unusual features of the ^{85}Rb BEC that render the standard procedure given above quite useless. Some of the unusual features of the ^{85}Rb BEC system are the small spatial size of the BEC (comparable to the finite resolution limit of the optical system), the relatively low kinetic energy of the BEC owing to the weak magnetic trap confinement, the large density-dependent losses experienced by the condensate as the B-field crosses the Feshbach resonance [1, 26], and the large negative scattering length of ^{85}Rb at zero magnetic field (a=-470 a_0).

Fortunately, one can avoid all of these potential problems by expanding the BEC while it remains in the magnetic trap. Expanding the wavefunction above the resolution limit removes any systematic effects due to imaging a small object. Also, by expanding the condensate in the magnetic trap, we can dramatically reduce the density before crossing the Feshbach resonance at the trap turn-off. Finally, we have found that a low-density, rapidly expanding BEC does not collapse at B=0, despite the large negative scattering length.

3.5.3 Increasing repulsion to expand the wavefunction

We devised a simple method to expand the BEC wavefunction that utilizes the tunable scattering length in ^{85}Rb. We ramp the B-field to quickly increase the scattering length and excite a large amplitude collective oscillation of the BEC. In this case, the energy imparted to the condensate comes directly from the changing magnetic field, which is provided by a changing current in a Hewlett-Packard power supply.[2] After increasing the mean-field repulsion, the BEC does not expand indefinitely in the trap; the confining potential provides a restoring force that causes large amplitude breathing mode oscillations. The period for the radial oscillation is roughly $1/(2\ \nu_r) = 29$ ms. We therefore turn off the magnetic trap well before the condensate reaches the outer turning point of its radial oscillation, as shown in Figure 3.14. We set the timing of the expansion ramp to maximize the outward expansion velocity of the condensate at the moment that the trap turns off. This allows the condensate to continue to expand quasi-ballistically at B=0 (a=-470 a_0), despite the strong attractive mean-field interaction. For the conditions of Figure 3.14, the expansion velocities of the BEC radial and axial widths were measured to be $\sim$1 mm/s, corresponding to an average kinetic energy per atom of 5 nK.

As the BEC expands, the volume of the atom cloud increases and takes on a roughly spherical shape. The density of the BEC decreases, so that the probe beam used in absorption imaging becomes less heavily absorbed. The decrease in absorption occurs because a given laser photon has a lower probability of encountering an atom as it passes through the BEC. We typically expand our N=16000 atom condensates until the on-resonant optical depth of the cloud decreases to approximately unity. This corresponds to a volume increase of the BEC of a factor of 1600, assuming that the

[2] The change in energy is really very small: for an average excitation energy of 5 nK per atom, the total energy of an expanding 16000 atom BEC is $\sim$80 μK or 10^{-8} eV. As a side note, it is quite interesting to think about the way that the energy is transferred from power supply to atoms — the transfer is ultimately mediated by atomic collisions!

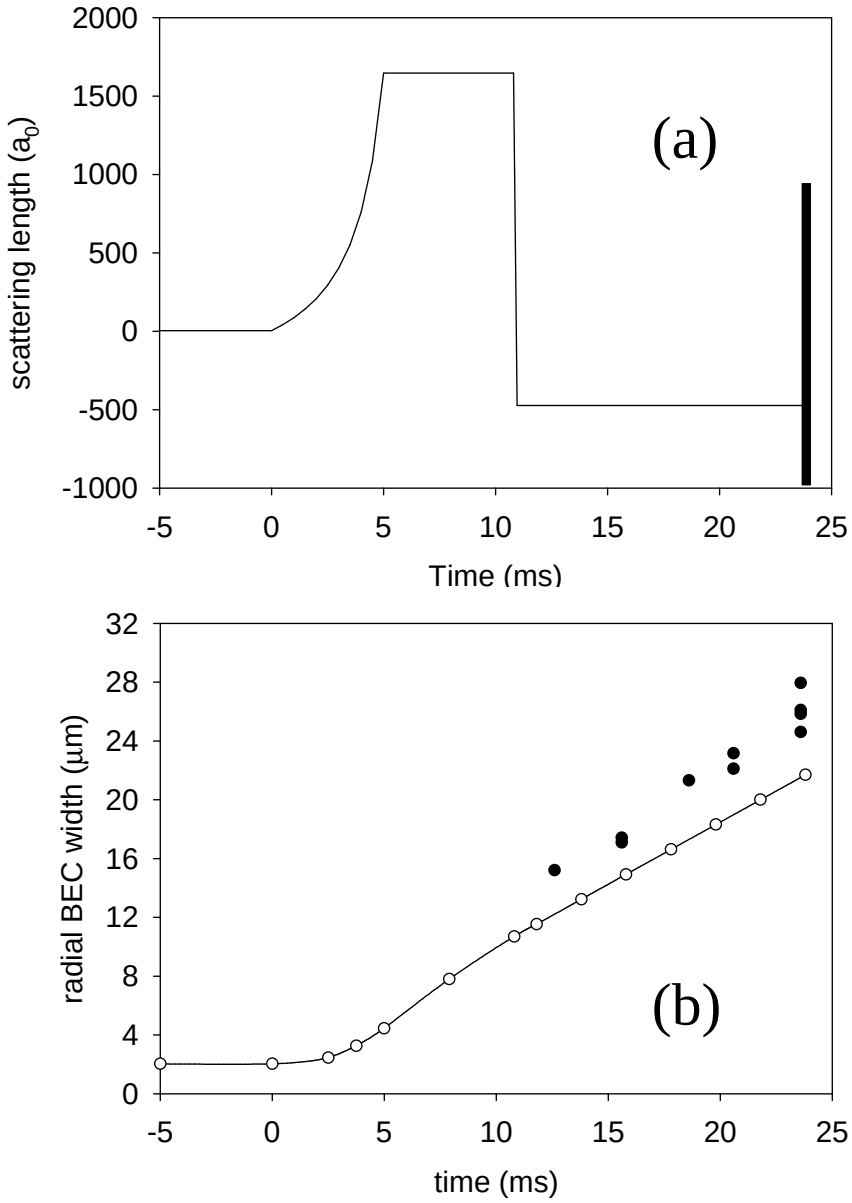

Figure 3.14: Increasing the repulsion to expand the BEC. **(a)** The scattering length versus time is shown as the thin solid line. The magnetic trap is turned off near 11 ms, when the scattering length changes sign. The thick black line represents the probe laser pulse for the absorption image, for a particular choice of expansion time. **(b)** Here we compare the observed expansion of the BEC to the prediction of the PG model. Black points show the measured rms radial width of the BEC versus time, as determined from a Gaussian fit. The white points connected by a line show the PG model prediction for the BEC rms width during the scattering length ramp shown in **(a)**. The small disagreement between the data and theory is likely due to a systematic underestimate of the width in the PG model due to the Gaussian approximation for the BEC wavefunction. We estimate this effect to be of order 15% when the scattering length is large enough that the BEC is in the Thomas-Fermi limit.

BEC starts near zero scattering length. To emphasize the effect of the expansion on the absorption imaging, we show an actual image of an expanded condensate in Figure 3.15.

For a simple intuitive explanation of the BEC expansion resulting from the change in scattering length, one can use a mean-field picture. The equilibrium BEC radius along a given direction is determined by a balance of forces consisting of outward quantum pressure due to the curvature of the confined wavefunction, a repulsive mean-field force that is proportional to the gradient of the atom density, and the confining force of the harmonic trap. When we quickly jump the scattering length to a larger value, the BEC wavefunction retains its shape immediately after the jump, but now the repulsive mean-field force is much larger. Although the mean-field force increases due to the jump, the confining force from the trap potential remains constant. Thus, the repulsive and attractive forces no longer balance one another and the BEC will begin to expand in size. Expansion continues until the trap force dominates the mean-field repulsion and causes the BEC to contract. As a function of time, a periodic oscillation occurs in the BEC radius, which is called a breathing mode oscillation [5].

To obtain a quantitative understanding of the BEC expansion, we use a model developed by Pérez-García et al. [27], hereafter referred to as the "PG model". This model involves an analytic variational solution to the nonlinear Gross-Pitaevskii (GP) equation using a Gaussian trial wavefunction. When adapted to our cylindrical trapping geometry, the PG model yields a pair of coupled nonlinear ordinary differential equations for the condensate widths in the radial and axial directions. We numerically solve these equations in Maple to predict the BEC expansion (or contraction) for an arbitrary scattering length ramp. A comparison of the results of the PG model with the observed BEC expansion rate is given in Figure 3.14. In addition to modelling condensate excitations, we also utilize the PG model for predicting the equilibrium size and density of the condensate for different values of the scattering length.

It is important to note that the PG model is limited to the conditions of appli-

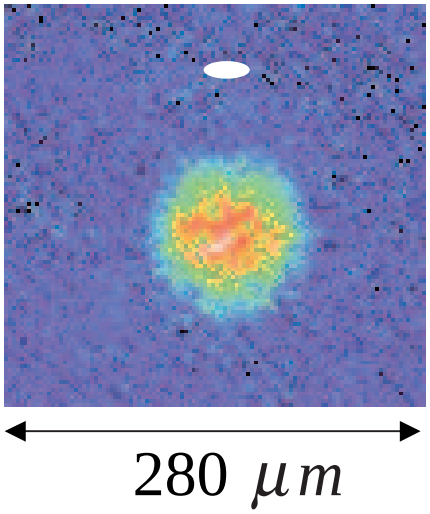

Figure 3.15: Absorption image of an expanded condensate. Here we used the scattering length ramp in part **(a)** of Figure 3.14 to expand the BEC. The false color image indicates the optical depth as a function of position in the expanded condensate. The white ellipse represents the equilibrium size of a 16000 atom condensate after formation at 162.3 G (210 a_0), as calculated with the PG model (see text). The principal axes of the ellipse are equal to $4 \times \sigma_i$, where σ_i is the Gaussian rms width along a particular direction. Comparing the BEC to the ellipse, we see how the signal-to-noise ratio of the number measurement can be improved by expansion because of the increased number of pixels in the absorption image. The area of the BEC image is 22 times larger than that of the ellipse.

cability of mean-field theory because the model is based on the GP equation. Another limitation of the model is the assumption of a Gaussian wavefunction for the condensate, which leads to a systematic error in the predicted BEC radii for the strongly repulsive interaction limit (Thomas-Fermi limit). Nevertheless, the PG model provides a useful and accessible analytic theory that can interpolate reasonably well between the non-interacting and strongly interacting limits. One can even model the attractive interaction regime for the condensate fairly well, as long as the BEC is not on the verge of collapse.

3.5.4 Low temperature calorimetry: shrinking the BEC

Since evaporative cooling to form Bose-Einstein condensates cannot remove all of the entropy from the atom cloud, there will always be a significant number of "thermal" atoms that do not occupy the ground state. The ratio of the number of thermal atoms, N_{therm}, to the total number of atoms, $N_{total} = N_0 + N_{therm}$, provides a measure of the temperature of the sample. Thus, we need to determine both N_{therm} and N_{total} in a given experiment. Unfortunately, the mean-field expansion described in the previous section only provides a method to accurately measure N_{total}; the expansion method does not distinguish between BEC atoms and thermal atoms. In fact, the thermal cloud is probably not static during the mean-field expansion due to coupling between thermal atoms and the expanding BEC. We observe that the thermal cloud and the condensate have significant spatial overlap in the absorption images of expanded BECs.

To separate the two components of our BEC samples and accurately measure N_{therm}, we again make use of the tunable self-interaction of the condensate. In this case, we shrink the BEC wavefunction by slowly decreasing the scattering length toward zero. As a approaches zero, the condensate wavefunction shrinks inward (while the thermal cloud remains unaffected) until the BEC radii match the harmonic oscillator lengths of the trap ($a_{ho,\,radial}$=2.6 μm, $a_{ho,\,axial}$=4.2 μm). After dividing these widths by $\sqrt{2}$ to

account for the difference between the widths of the BEC wavefunction and the observed BEC density profile, one finds that the BEC widths are 5 to 8 times smaller than the corresponding radii of a 10 nK thermal cloud. We can therefore spatially resolve the BEC from the surrounding thermal cloud "halo". Our low-temperature calorimetry procedure and the data from an example absorption image are given in Figure 3.16.

There is a small gloss in the above description of the N_{therm} determination. Shortly after the completion of the adiabatic decrease in the scattering length to shrink the BEC, we also impart a small outward velocity to the condensate before we turn off the magnetic trap. Although this seems counter-productive for the goal of spatially separating the two components, it turns out that a small amount of BEC expansion is very useful for two reasons. First, the expansion velocity decreases the density before we cross the Feshbach resonance and this reduces density-dependent losses and burst production (see Chapter 5). Second, the outward velocity of the BEC prevents the condensate from collapsing at B=0, which also produces a burst of hot atoms (Chapter 4). Whether the burst atoms are generated during the magnetic trap turn-off or during the brief delay time at B=0, the presence of the burst atoms can potentially distort the the determination of N_{therm}.

In practice, we determined the parameters of the expansion ramp by finding the best compromise between minimum spatial size of the BEC and minimum number of burst atoms created. The best expansion ramp consisted of a 1 ms linear B-field ramp to 161.5 G ($a \simeq$290 a_0) followed by a 2.4 ms hold. The trap was then turned off and an absorption image was taken 1.6 ms later. This ramp was used to obtain the image shown in part **(b)** of Figure 3.16 (to avoid confusion and because of its short duration, the ramp was not shown in part **(a)**). Our sensitivity limit to thermal atoms with the condensate shrinking technique is very low — roughly 500 thermal atoms.

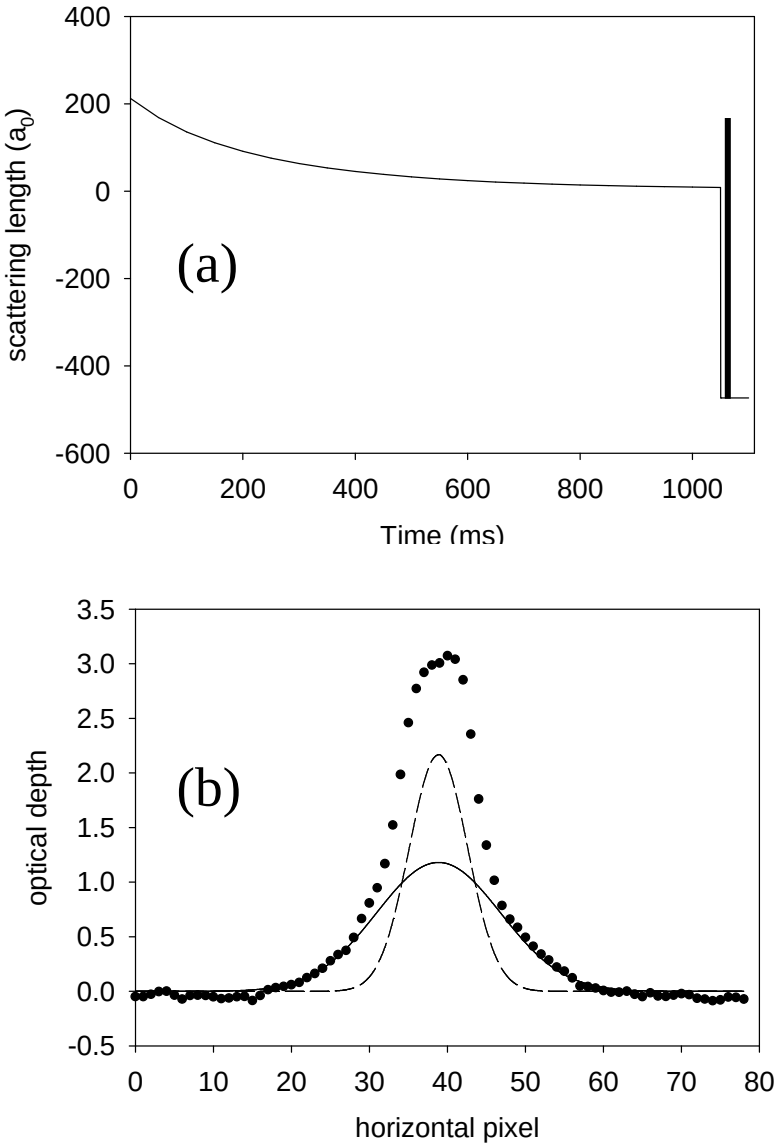

Figure 3.16: Shrinking the BEC to extract the thermal fraction. **(a)** Scattering length versus time and probe laser pulse. The scattering length is adiabatically (∼0.5 s) ramped down to a value near zero, then the magnetic trap is turned off. We take an image after a short delay of 1.6 ms to allow induced currents to die away. The slow decrease in a causes the BEC to contract as the mean-field repulsion vanishes. **(b)** Absorption image axial cross-section for a BEC plus thermal cloud after the scattering ramp shown in **(a)**. Black points are the measured optical depth versus pixel position on the camera. One pixel length equals 2.54 microns. The dashed line and solid line are simultaneous Gaussian fits to the condensate and thermal cloud, respectively. From the thermal cloud fit, we find $N_{therm} \simeq 5000$ atoms. The condensate fit is subject to systematic effects (resolution limit and optical depth ceiling), so we do not use this to determine N_0. When we combine the accurate N_{therm} measurement with a subsequent measurement of $N_{total} \simeq 16000$ as in section 3.5.3, the BEC temperature is quite well-known.

3.5.5 Making bigger and better condensates

As a result of our clever schemes to manipulate the BEC wavefunction, we have been able to produce larger condensates with smaller thermal fraction than we could previously [1]. The ability to accurately measure both N_{total} and N_{therm} for each cloud of atoms enabled us to re-optimize the final stages of evaporative cooling. We adjusted the trajectory of the rf frequency versus time to minimize the thermal number while maximizing the total number in the condensed sample. As a result, in our day-to-day experiments we typically work with N_{total}=16,000 and $N_{therm} \leq$500, which corresponds to a condensed fraction of 97 %. This represents a dramatic improvement over our earliest BEC experiments in August 1999, when the optimum value for the condensed fraction was roughly 10 %. The very best condensates created in our experiment had N_{total}=30,000 with fewer than 500 thermal atoms. As we have not been able to reproducibly obtain such low temperature condensates, we suspect there may have been a particularly advantageous planetary alignment at that time.

Chapter 4

Dynamics of collapsing and exploding ^{85}Rb Bose-Einstein condensates

4.1 Introduction

This Chapter presents a description of our experiments with ^{85}Rb BEC in the attractive self-interaction regime, where the condensate may become unstable and undergo a "collapse" if the attraction is sufficiently strong. The first part of the Chapter provides some background information about BEC collapse physics, including our early experiments to study them. We move on to a detailed description of the response of the BEC when the sign of the scattering length is quickly switched from positive to negative. At the end of the Chapter, we compare our data to recent theoretical models for the collapse dynamics.

The ^{85}Rb BEC system is an ideal candidate for studying the collapse instability because of the condensate's tunable interactions. By ramping the magnetic field, we can easily change the sign and magnitude of the scattering length (and interaction strength). As discussed in Chapter 2, the BEC self-interaction is repulsive when the scattering length is positive, and attractive when a is negative. The existence of the ^{85}Rb Feshbach resonance, which leads to a magnetic-field-dependent scattering length, allowed us to gain tremendous insight into the collapse physics.

Before our experiments in ^{85}Rb, condensates with attractive interactions had received only limited study in a ^{7}Li BEC system with fixed negative scattering length. The early ^{7}Li BEC studies [28] showed evidence for an instability, but the data did

not allow for stringent tests of theory. More recent experiments in ^{7}Li have focused on the collapse process in a high temperature condensate, where the BEC was continually replenished by a cold thermal cloud, leading to a sequence of growth and collapse cycles [29, 30]. In contrast, our ^{85}Rb BEC experiments were conducted with nearly thermal-atom-free condensates, and we took full advantage of our experimental control of the scattering length to extract more information about the collapse process.

4.1.1 Stability condition for BEC with a<0

A stable, harmonically trapped condensate with negative scattering length has a maximum or critical allowed number of atoms, N_{crit}. When the number in the condensate exceeds the critical number, $N_{BEC} > N_{crit}$, the attractive self-interaction dominates the repulsive zero-point energy of the confined condensate wavefunction. The stability condition for the BEC is defined as

$$\frac{N_{crit}|a|}{a_{ho}} = k_{collapse}, \tag{4.1}$$

where $a_{ho} = \sqrt{\hbar/(m\overline{\omega})}$ is the mean harmonic oscillator length of the trap potential (with mean frequency $\overline{\omega} = \sqrt[3]{\omega_r^2\omega_z}$) and $k_{collapse}$=0.55 is a constant [31]. One can also view equation (4.1) as defining a critical value for the magnitude of the negative scattering length, a_{crit}, if the number of BEC atoms is assumed to be fixed. The stability condition expressed in equation (4.1) was determined by studying the ground state of the GP equation as a function of the product $N|a|$ [31, 32]. When this product exceeds the stability condition, then no stable solution can be found for the ground state. Thus, one expects an initially stable BEC that experiences a change in scattering length such that $(a_{init} > 0) \rightarrow (a_{final} < a_{crit})$ to become unstable and collapse in some fashion.

In our early experiments [33], we found that an initially stable BEC undergoes a dramatic ($\sim 50\%$) number loss some time after the scattering length is decreased below a critical value. Typically, we label this number loss as the BEC "collapse". By measuring

the critical number of atoms for collapse at several different values of negative scattering length, we verified the functional form of equation (4.1). We also determined the value of $k_{collapse}$, which was significantly lower than the prediction of existing theory [32]. However, our more recent high-precision measurement of the Feshbach resonance parameters (see Chapter 7) has allowed us to revise our previous estimate of $k_{collapse}$. The new value is completely consistent with theory [31].

The collapse of the condensates was an all-or-nothing process. We never observed partial collapses; a given BEC would either collapse at negative a or remain stable, depending on whether or not the number exceeded N_{crit}. We saw no evidence for a macroscopic quantum tunneling phenomenon in the collapse process, as some theory work had suggested(see Ref. [34] and references therein). In fact, collapse process turned out to be so reproducible that we could use it to precisely measure the magnetic field. We accomplished this by first measuring N_{crit} and a_{crit} and then using our knowledge of the variable scattering length due to the Feshbach resonance.

On a daily basis, we found the initial magnetic field using a fairly simple procedure. We first prepared a stable BEC at some initial value of B-field that corresponded to a positive scattering length. We then ramped the B-field to change the sign and magnitude of the scattering length to a negative value near a_{crit}. We observed the resulting BEC number and noted which final magnetic fields (final scattering lengths) caused large BEC number loss. After determining N_{crit} and a_{crit} in this way, we found the absolute magnetic field using equation (4.1) in combination with the known dependence of scattering length on magnetic field. We extrapolated from B_{crit} to B_{zero}, the field where the scattering length vanishes (corresponding to $N_{crit} = \infty$). The value of B_{zero} provided us with a useful calibration point.

Utilizing the BEC collapse to measure the magnetic field proved to be a rapid and precise technique. We repeated the experimental cycle with different B-field ramps until N_{crit} and a_{crit} were known. In a period of about one-half hour, we could determine

the initial magnetic field to a ∼5 mG precision. Precise knowledge of B_{init} and a_{init} was quite useful for a variety of other experiments described in this thesis.

4.1.2 Overview of collapse dynamics

Although our early BEC experiments in the attractive self-interaction regime verified the stability condition and showed that condensate collapse involves number loss, our data actually raised more questions than they answered. For instance, we could not initially determine the fate of the atoms that left the BEC. We had other unanswered questions regarding the details of the number loss: how quickly were the atoms going away and what was setting the timescale of the collapse? Furthermore, what exactly happened to the BEC wavefunction during the collapse process?

At the time of our experiments, existing theories of BEC collapse [35, 36, 37] predicted that an unstable BEC would implode on itself. The contraction of the BEC would presumably take place on the time scale of a trap oscillation, and the density would sharply increase after $T_{rad}/4 \simeq 14$ ms, where T_{rad} is the radial trap period. As a result of the density growth, 3-body recombination losses were expected to cause a rapid depletion of the BEC, preventing the formation of a true singularity in the density of the atom cloud.

To explore the dynamics of the collapse process and check the validity of the proposed theoretical pictures, we took full advantage of the variable scattering length of ^{85}Rb condensates. We changed the sign of a and observed the time-dependent response of the BEC. We were quite surprised by the complexity of the BEC collapse. Various phenomena were observed — an initial gradual contraction was followed by a supernova-like explosion of hot atoms. At the end, a small remnant condensate was left behind in an excited oscillatory state, and much of the initial condensate had completely disappeared from view. In the rest of this chapter, we detail the prominent features of the collapse process as well as the methods used to study them.

4.2 Preparing and manipulating the condensate

The first stage in our experiment was to form a stable ^{85}Rb condensate[26]. A standard double magneto-optical trap (MOT) system[19] was used to collect a cold sample of ^{85}Rb atoms in a low-pressure chamber. Once sufficient atoms had accumulated in the low-pressure science MOT, the atoms were loaded into a cylindrically symmetric cigar-shaped magnetic trap with frequencies $\nu_{radial} = 17.5$ Hz and $\nu_{axial} = 6.8$ Hz. Radio-frequency evaporation was then used to cool the sample to $\sim$3 nK to form pure condensates containing >90% of the sample atoms. The final stages of evaporation were performed at 162.3 G where the scattering length is positive and stable condensates of up to 20,000 atoms could be created. After evaporative cooling, the magnetic field was ramped adiabatically to 166 G, where the scattering length was near zero. This provided a well-defined initial condition — the BEC would shrink to approach the size and shape of the harmonic oscillator ground state (see section 3.5.4). We note that in a few cases, the initial scattering length was chosen to be significantly different from zero; this allowed us to vary the initial density of the condensates over a wide range.

We developed various different magnetic field ramps into useful tools for studying the BEC collapse dynamics. The B-field control allowed us to adjust the mean-field interactions within the BEC to a variety of values on time scales as short as 0.1 ms. The obvious manipulation was to jump to some value of $a < a_{crit}$ to trigger a collapse, but the tunability of a also greatly aided in imaging the sample. Usually the condensate size was below the resolution limit of our imaging system (7μm FWHM). However, we could ramp the scattering length to large positive values and use the repulsive interatomic interactions to expand the BEC before imaging, thus obtaining information on the pre-expansion condensate shape and number. A typical $a(t)$ sequence is shown in Figure 4.1. We have used a variety of such sequences to explore many aspects of the collapse and enhance the visibility of particular components of the sample.

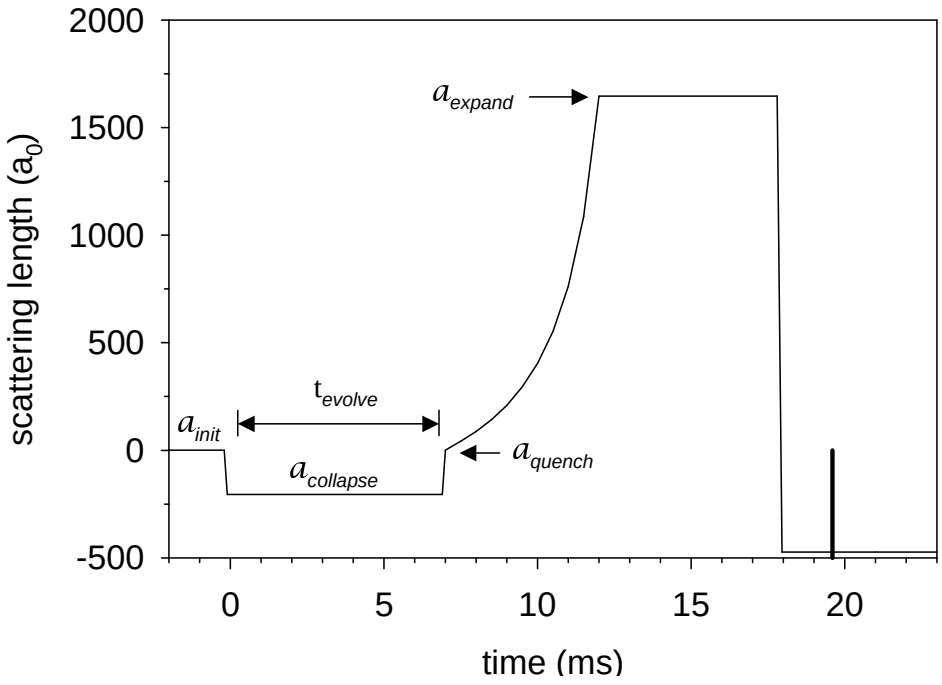

Figure 4.1: An example of experimental control of the scattering length. The thin solid line is the time dependent scattering length while the thick vertical line indicates the timing of the probe laser pulse for absorption imaging. We used a variety of $a(t)$ sequences similar to what is shown here to study the dynamics of the BEC collapse. To determine $a(t)$, we first calculated the magnetic field using a calibrated current sensor on the magnetic trap coil. Then we converted the B-field into scattering length using equation (2.2), the Feshbach theory expression for $a(B)$.

In Figure 4.1, the scattering length is jumped at $t = 0$ in 0.1 ms from $a_{init} \simeq 0$ to $a_{collapse} < 0$, where the BEC evolves for a time t_{evolve}. We carefully control the B-field so that magnetic field noise translates into fluctuations in $a_{collapse}$ on the order of $\sim 0.1\ a_0$ in magnitude. After the time t_{evolve}, the BEC collapse process is then interrupted with a jump to a_{quench}, and the field is ramped in 5 ms to a large positive scattering length which makes the BEC expand. After 7.5 ms of additional expansion, the trap is turned off in 0.1 ms and 1.8 ms later the density distribution is probed using destructive absorption imaging with a 40 μs laser pulse (indicated by the vertical bar in Figure 4.1). In some instances, we increased the expansion time after the trap turn-off to further expand the BEC wavefunction.

As discussed in section 3.5.3, the increase in a from $a_{collapse}$ to a_{expand} is far too rapid to allow for the BEC to expand adiabatically. On the contrary, the smaller the BEC before expansion, the larger the cloud at the moment of imaging. Thus we can readily infer the relative size of the BEC wavefunction just prior to the jump to a_{quench}. After the mean-field expansion, the density of the expanded BEC is so low that the rapid transit of the Feshbach resonance [38] during the trap turn-off and the subsequent time spent at $B = 0$ ($a = -470\ a_0$) both have a negligible effect.

4.3 BEC number loss

4.3.1 BEC number versus t_{evolve}

When the scattering length is jumped to a value $a_{collapse} < a_{crit}$, the BEC kinetic energy no longer provides a sufficient barrier against collapse. After making such a scattering length jump, we observed a delayed and abrupt onset of number loss from the condensate. As a function of the time spent at $a < 0$, the BEC number remained steady for a while, then dropped exponentially with a time constant τ_{decay}. This trend is illustrated by Figure 4.2, which is a plot of the condensate number N_{BEC} versus the

evolution time, t_{evolve} at a negative scattering length. Here the observed delay time before the onset of number loss is defined as the collapse time, $t_{collapse}$. The exponential number decay finally leveled off at a value N_{rem}, which we define as the remnant BEC number. N_{rem} was typically $\simeq 40\%$ of the initial number, N_{init}.

Although N_{BEC} was constant for a short time after the jump to $a_{collapse}$, we did observe some slight changes to the expanded condensate radius during t_{evolve}. These radius changes indicated that the BEC was contracting during the evolution time. Since the pre-expansion BEC was smaller than our resolution limit, we could not observe the contraction directly; however, we could infer the extent of the contraction by observing the degree of mean-field expansion. In fact, the BEC expanded more and more during the expansion ramp of Figure 4.1 as it contracted more and more during t_{evolve}. We actually observed that the post-expansion condensate widths changed very little with time t_{evolve} before $t_{collapse}$. For the data in Figure 4.2, the expanded radial BEC width increased by only 10% as t_{evolve} increased from 0 ms to 3.5 ms. The axial BEC width showed even less of a change.

From this we infer that the cloud of condensate atoms did not contract dramatically before loss began. To obtain a quantitative estimate for the amount of contraction, we use the equations in Ref. [27]. The PG model results provide a fairly good match to the observed expanded BEC shape over a moderate range of $a_{collapse}$ and time before collapse. We can therefore have some confidence in using the equations of Ref. [27] to estimate the density before collapse. Surprisingly, we find that the predicted contraction corresponds to only a 50% increase in the average density (to 2.7×10^{13} cm^{-3}) before the beginning of the number loss. Using the inelastic collision rates for ^{85}Rb that we measured in Ref. [39], this density predicts a loss time that is far longer than what we observe ($\tau_{inelastic}$ $\sim$2.5 s) and does not have the observed sudden onset. Thus, our simple estimates of the BEC contraction and inelastic loss do not jibe with the observed behavior in Figure 4.2. The disagreement implies that the conventional simple picture

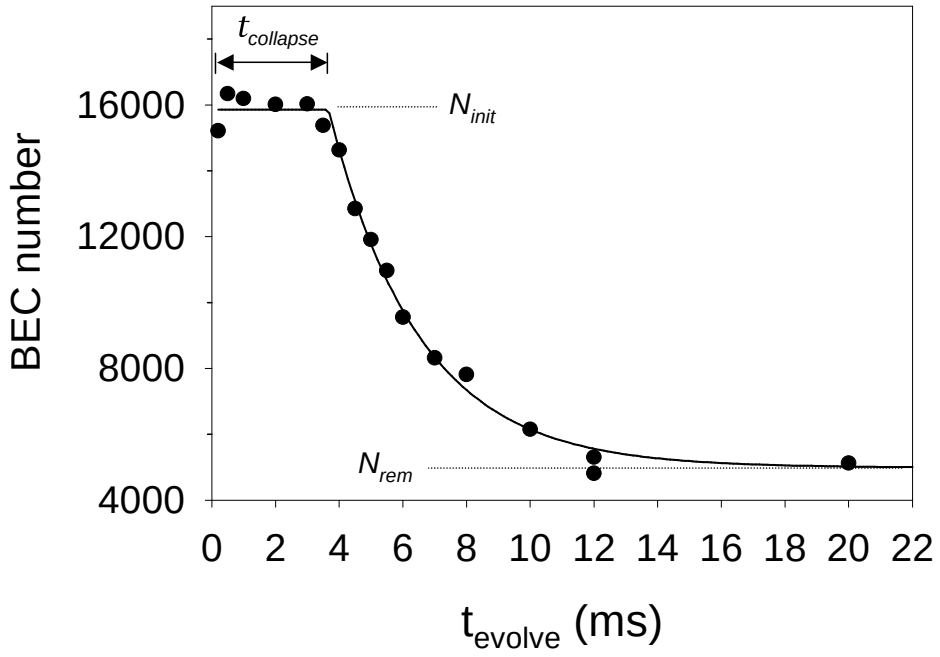

Figure 4.2: The condensate number versus time after a jump to a negative scattering length. Points are the number of atoms remaining in the BEC versus t_{evolve} at $a_{collapse} = -36\ a_0$. The initial scattering length before the jump was $a_{init} = +8\ a_0$ and the initial number of condensate atoms was N_{init}=16,000. These conditions produced an estimated average initial density of $1.8 \times 10^{13}/\mathrm{cm}^3$. We observed a delayed and abrupt onset of loss from the BEC number. The solid line is a fit to the data using a delayed exponential function with a best fit value of $t_{collapse} \simeq 3.7(5)$ ms for the delay. The number of atoms remaining in the condensate after the end of the decay process is $N_{rem} \sim 5000$.

of the collapse as a global implosion of the entire BEC wavefunction is incorrect. We will provide additional discussion of this point in section 4.5.3.

For the data in Figure 4.2 and most other data presented in this Chapter, we jumped to $a_{quench} = 0$ in 0.1 ms after a time t_{evolve} at $a_{collapse}$. We believe that the number loss stopped immediately after the jump. This interpretation is based on the surprising observation that the quantitative details of curves such as that shown in Figure 4.2 did not depend on whether the collapse was terminated by a jump to $a_{quench} = 0$ or $a_{quench} = 250\ a_0$. Presumably, if there were a significant amount of loss occurring after the "quenching" ramp, then quantities such as N_{rem} and $t_{collapse}$ should depend on the precise value of a_{quench}; however, this was not the case.

4.3.2 Variations in $t_{collapse}$

We have measured number decay curves like that in Figure 4.2 for many different values of the negative scattering length. The measured collapse time versus $|a_{collapse}|$ for fixed initial density is presented in Figure 4.3. As we increased $|a_{collapse}|$ from 7 a_0 to 65 a_0, the collapse time decreased by more than one order of magnitude. The data display a nearly perfect inverse dependence on the magnitude of the scattering length, as shown by the solid line.

We also studied the dependence of $t_{collapse}$ on the initial BEC density. By reducing N_{init}, we decreased the initial density from $\langle n_{init} \rangle = 2.8 \times 10^{13}$ cm^{-3} to $\langle n_{init} \rangle = 1.1 \times 10^{13}$ cm^{-3} (a factor of ~ 2.5). This change caused the collapse time to lengthen by a factor of 2.4(8) at $a_{collapse}$=-8 a_0. We verified that $t_{collapse}$ was truly proportional to density and not only to N_{init} by reducing the density through a volume change to the initial condensate. Holding N_{BEC} fixed at roughly 16,000 atoms, we decreased the initial density by a factor of 3.5 (with a corresponding increase in volume) by setting $a_{init} = +105\ a_0$ instead of our more typical value, $a_{init} = +8\ a_0$. At $a_{collapse}$ = -15 a_0, the volume-induced density change caused $t_{collapse}$ to grow by roughly a factor of 3.

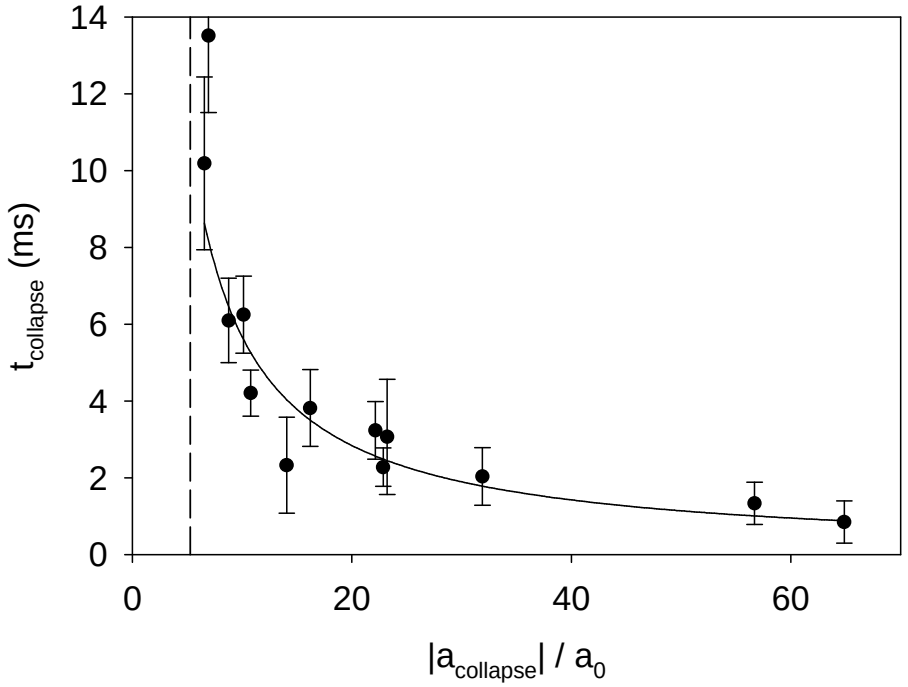

Figure 4.3: The collapse time versus $a_{collapse}$ for 6000 atom condensates. Points with error bars are the measured values of $t_{collapse}$. The solid line is a weighted fit to the function: $t = Q/a_{collapse}$, with Q=57(6) ms a_0. The vertical dashed line indicates a_{crit} for $N_0 = 6,000$. The data were acquired with $a_{init} = a_{quench} = 0(2)$ a_0, so that the initial BEC density was $\langle n_{init} \rangle = 3(1) \times 10^{13}$ cm^{-3}. The average BEC densities given here were computed using the PG model (section 3.5.3) to determine the volume of the BEC wavefunction for a given value of the initial scattering length. We found that the PG model accurately predicts the mean density over the entire range of repulsive interactions, from the Thomas-Fermi limit of strong interactions to the non-interacting limit.

The observed dependences of the collapse time on scattering length and density indicate that there is some critical condition that must be reached before the onset of number loss. The time to reach the critical condition becomes smaller as we increase $\langle n_{init} \rangle$ and $|a_{collapse}|$. All of our evidence supports the idea that $t_{collapse}$ is inversely proportional to the magnitude of the attractive mean-field interaction: $E_{mf} \propto \langle n \rangle a$. This dependence seems reasonable since the rate of implosion of the BEC should depend on E_{mf}.

In contrast to $t_{collapse}$, the atom loss time constant τ_{decay} depended only weakly on $a_{collapse}$ and $\langle n_{init} \rangle$. For the range of $a_{collapse}$ shown in Figure 4.3, τ_{decay} did not depend on $a_{collapse}$ or $\langle n_{init} \rangle$ by more than the $\sim$20% experimental noise in the τ_{decay} determination. On average, τ_{decay} was 2.8(1) ms. For the very negative value of $a_{collapse} \simeq -290\, a_0$, however, τ_{decay} did decrease to 1.8 ms for $N_{init} = 6,000$ and 1.2 ms for $N_{init} = 15,000$.

4.4 Energetic burst of atoms

Thus far we have not explained what happens to the atoms after they exit the condensate during a collapse. As displayed in Figure 4.2, a large fraction of the atoms leave the BEC during the exponential decay. There are at least two components to the expelled atoms. One component (known as the "missing atoms") is not detected in the absorption images. The other component emerges as a burst of detectable, spin-polarized atoms with energies much greater than the initial condensate's energy but much less than the magnetic trap depth. The bizarre properties of the burst and its surprising formation during the BEC collapse prompted Carl Wieman and Eric Cornell to name it a "Bosenova", in analogy with a supernova. In our attempts to understand the origins of the burst, we have studied the details of the burst atom distribution under a wide range of conditions. The average energy and number of the burst atoms depend in a complex manner on $a_{collapse}$ and N_{init}. Although the details are complicated, we present them here because they provide a stringent test of collapse theories.

The angular kinetic energy distribution with which the burst atoms are expelled from the condensate can most accurately be measured by observing the harmonic oscillations of the atoms in the trap, as illustrated in Figure 4.4**(a)**. For example, one-half of a radial period after the expulsion ($T_{rad}/2$), all burst atoms return to their initial radial positions. At times significantly before or after this radial "focus", the burst cloud is too dilute to be observed. Fortunately, at the radial focus, the oscillation trajectories along the axial trap axis are near their outer turning points. Therefore the axial energy can be found from the length of the stripe of atoms along the axial direction. The radial energy can be found with an identical procedure in an axial focus.

One can also define the "sharpness" of the burst focus as the minimum width in the narrow dimension. The harmonicity of the magnetic trap potential ensures that the sharpness of the burst focus should only depend on the duration of time that burst atoms are expelled from the BEC (the length of the explosion) and the initial spatial distribution of the atoms before the explosion. In principle we can therefore determine the formation time for the burst atoms by measuring the narrow width of the burst focus. However, this technique only allows us to set an upper limit on the burst creation time because of significant broadening of the images from our finite optical resolution limit. The upper limit from the burst focus sharpness is consistent with a direct measurement of the burst generation time ($\sim$1.2 ms) in section 4.4.1.

Figure 4.4**(b)** shows an image of a radial focus. The size scales for the burst focus and the remnant were always well separated since the latter was not expanded when we imaged the burst. Figure 4.4**(c)** shows axial cross sections of the image in part **(b)** and the fit cross sections for the burst and thermal clouds. The burst spatial distribution was well fit by a 2-D Gaussian function whose width in the long dimension corresponded to the average energy of the burst atoms.

Since the burst atom cloud extended far out into the edges of the absorption images and the optical depth was fairly low in the outer wings of the atom distribution,

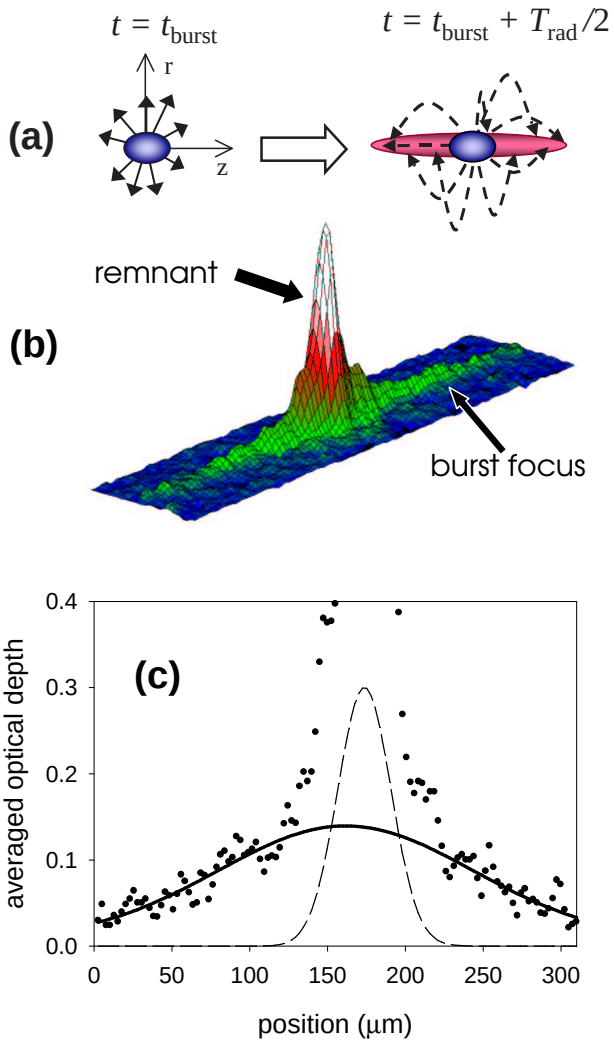

Figure 4.4: A burst focus. **(a)**. Conceptual illustration of a radial burst focus. **(b)** An image of a radial burst focus taken 33.5 ms after a jump from $a_{init} = 0$ to -36 a_0 for $N_0 = 15,000$. Here $T_{rad}/2 = 28.6$ ms, which indicates that the burst occurred 4.9(5) ms after the jump. The average axial energy for this burst was $\langle E_{burst,axial} \rangle = 62$ nK. The image dimensions are 60×310 μm. **(c)** Radially averaged cross section of the image in **(b)** along with a Gaussian fit to the burst spatial distribution. The central 100 μm were excluded from the fit to avoid fitting distortions from the condensate remnant and the thermal cloud. The rms widths of the BEC remnant and thermal cloud were $\sigma = 9\mu$m and $\sigma = 17\mu$m, respectively. A small cloud of thermal atoms is present in the pre-collapse sample due to the finite temperature; these atoms appear to be unaffected by the collapse. The dashed line indicates the fit to this initial thermal component. There is a clear offset between the centers of the burst and the remnant. This offset varies from shot to shot by an amount comparable to the offset shown.

we utilized an image-processing tool to reduce background noise and improve the image signal-to-noise ratio. Much of the "noise" in the absorption images is actually due to interference fringes from the coherent probe laser beam. We could therefore improve the fitting procedure by removing the periodic stripes from the images. The removal was done by calculating the spatial Fourier transform of the optical depth data, then removing the probe laser stripes from the image, and finally transforming back to real space. In this way, we could obtain reliable measurements of the average burst atom energy along the radial and axial directions.

The average energy was generally different for the two trap directions. The burst energy fluctuated from shot to shot by up to a factor of 2 for a given $a_{collapse}$. This variation is far larger than the measurement uncertainty or the variation in initial number (both $\sim 10\%$), and its source is unknown. The burst energy and the dependences of $\langle E_{burst} \rangle$ on N_{init} and $a_{collapse}$ will be described in section 4.4.2.

4.4.1 $\mathbf{N}_{burst}$ versus $\mathbf{t}_{evolve}$

One of the most interesting aspects of the burst behavior was the increase in N_{burst} during the collapse process. When we interrupted the BEC collapse with a jump back to $a_{quench} = 0$ (see section 4.3.1), we also interrupted the growth of the burst. The "interrupted" burst atoms still refocused after sitting at $a = 0$ for the requisite one-half of a trap period. We found the energy of the atoms in the interrupted bursts to be the same, but the number of atoms was smaller than in the uninterrupted case. By changing the time at which the collapse was interrupted we could measure the time dependence of the creation of burst atoms.

The increase in the burst number with t_{evolve} is illustrated in Figure 4.5. The number of burst atoms N_{burst} grows exponentially with a time constant of 1.2 ms, starting at t_{evolve}=3.5 ms and reaching an asymptotic final number of $\sim$2500 atoms for all times $\geq$7 ms. N_{burst} also levels off at roughly the same time as the remnant BEC

number displayed in part **(b)** of the figure. Despite the observed large variations in the burst number, the average energy of the burst atoms ($\sim$ 85 nK) does not change significantly over the range of t_{evolve} shown in Figure 4.5.

The interrupted burst data clearly show that the growth of the burst with time at negative scattering length mirrors the decay of atoms from the condensate — the time dependences for these two processes are quite similar. However, by comparing parts **(a)** and **(b)** of Figure 4.5, one can see that the number of burst atoms is far smaller than the number of atoms leaving the BEC — there are at least $11000 - 2500 = 8500$ missing atoms. At present, the fate of the missing atoms has not been determined by experiment. The prevailing hypothesis is that the missing atoms are due to 3-body recombination into molecules, where the molecular binding energy is converted into kinetic energy that is shared by the collision partners. We discuss the scattering length dependence of the missing fraction of atoms in section 4.5.2.

Somewhat surprisingly, the number of atoms in the burst did not depend on the scattering length, $a_{collapse}$. Although N_{burst} varied randomly by $\sim$20% as $|a_{collapse}|$ increased from nearly 0 a_0 to 350 a_0, on average the fraction of atoms going into the burst remained fixed at roughly 20% of the initial BEC number. Larger initial condensates produced larger bursts in direct proportion, so that the burst fraction remained constant as a function of N_{init}.

4.4.2 $\langle E_{burst} \rangle$ versus $a_{collapse}$

We carefully examined the scattering length dependence of the burst energy as one part of our collapse dynamics experiment. Although the burst energies were seen to vary from shot to shot, the average value for the energy was well defined and showed large-scale trends that dominated the shot-to-shot variations. We show the axial and radial burst energies versus $a_{collapse}$ in Figure 4.6**(a)** and 4.6**(b)** for $N_{init} = 6,000$ and 15,000, respectively.

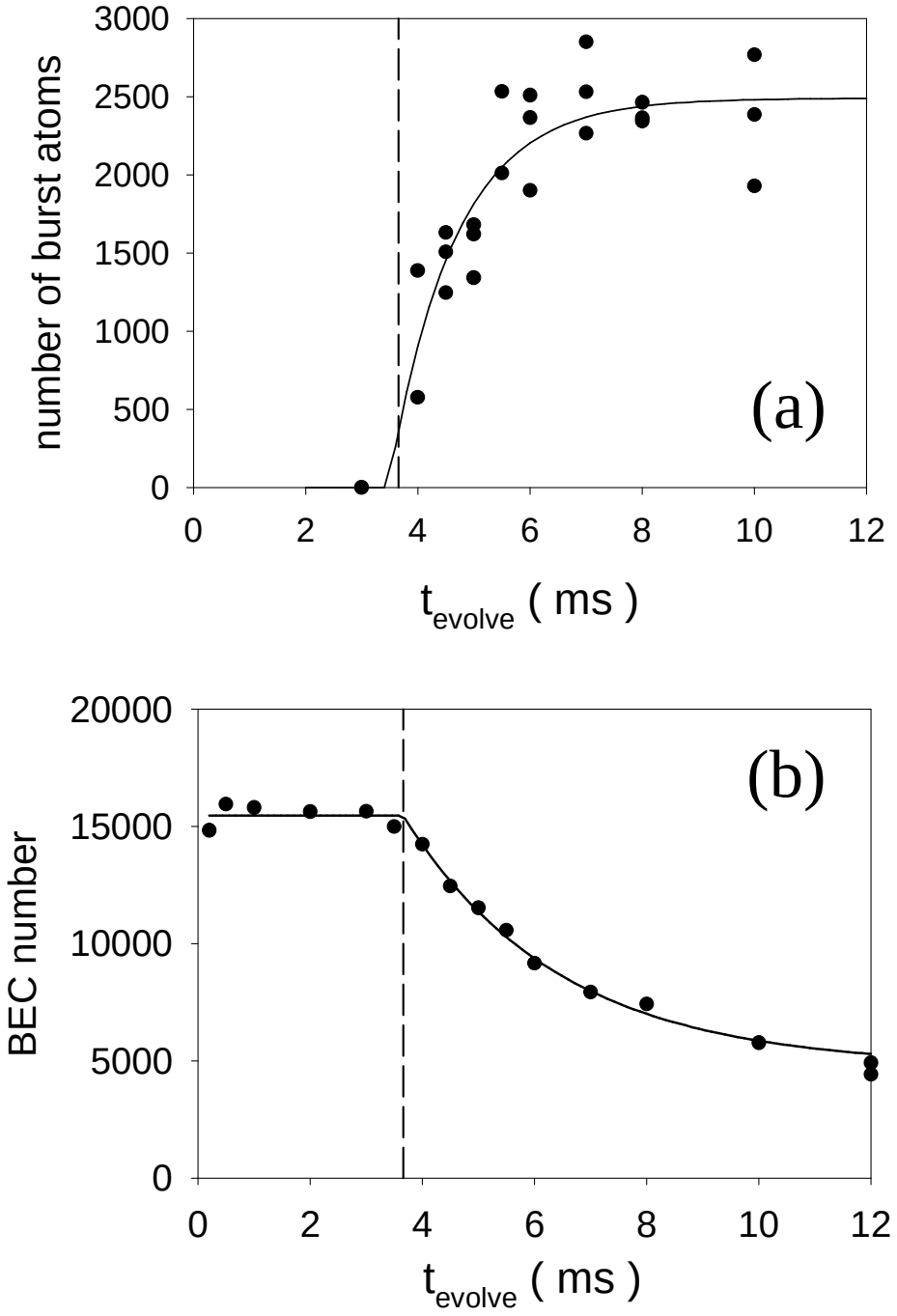

Figure 4.5: Growth of burst number with t_{evolve}. The data were collected under the same conditions as for Figure 4.2. **(a)** The points are N_{burst} versus evolution time at $a_{collapse}$=-36 a_0. The solid line shows the best fit of the data to a rising exponential function with time constant τ=1.2(3) ms. The dashed vertical line indicates the best fit value for $t_{collapse}$ from a fit to the BEC loss data in part **(b)**. Figure **(b)** displays the BEC number decay for comparison to the burst growth data. The burst growth begins and ends at about the same time as the condensate loss. The time constants for BEC loss and burst growth are also comparable: τ_{BEC}=2.7(3) and τ_{burst}=1.2(3) ms.

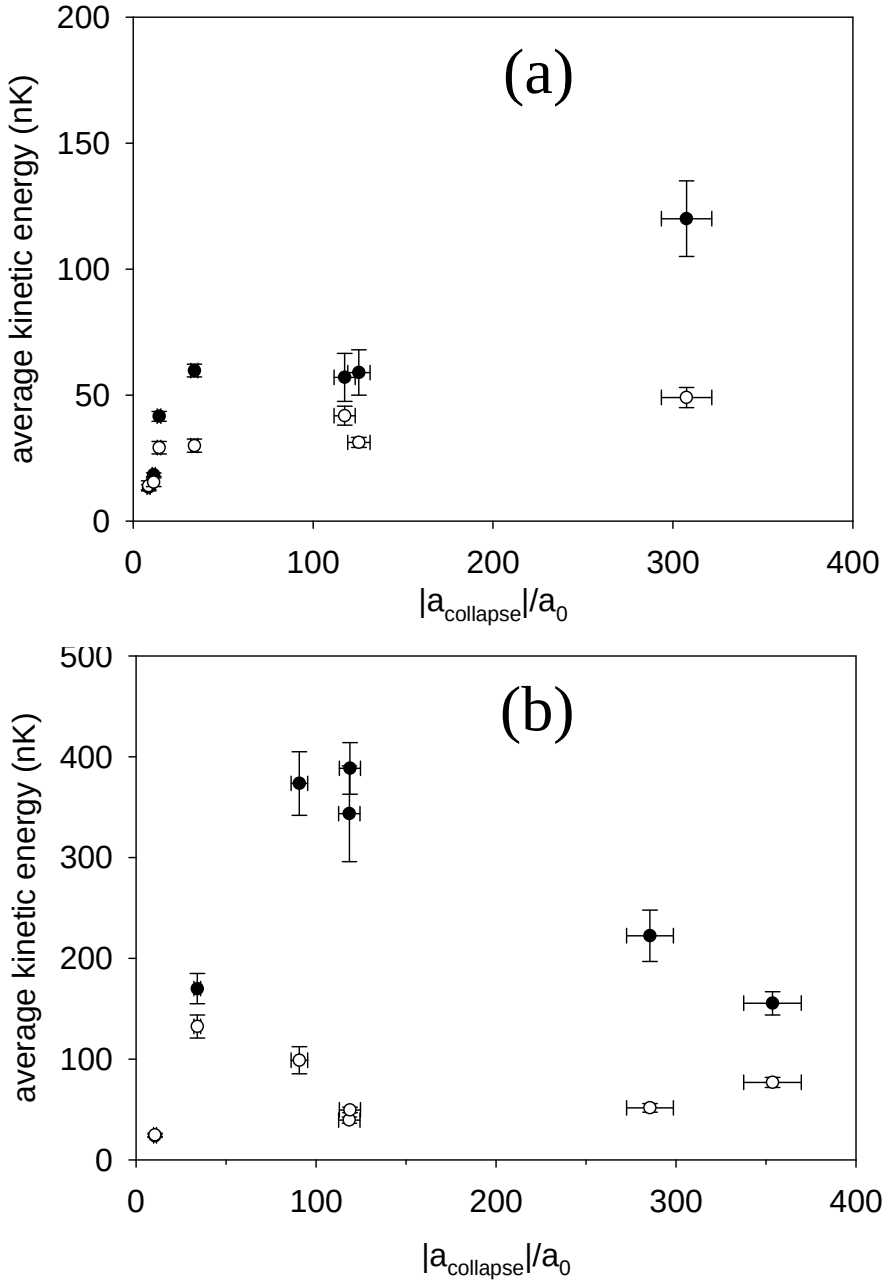

Figure 4.6: Average burst atom energy versus scattering length. **(a)** and **(b)** show the average axial and radial burst energies versus $|a_{collapse}|$ for $N_{init} \simeq 6,000$ and $N_{init} \simeq 15,000$, respectively. Filled points are the radial burst energies; open points are the axial energies. The average energy is calculated from the rms width, σ, of the 2-D Gaussian fit to the data as shown in Figure 4.4. For a given dimension, the average energy is $\langle E_{burst,i} \rangle = m\omega_i^2\sigma^2/2$, where ω_i is the trap frequency in the i$^{\text{th}}$ dimension. On average, ten burst focuses were measured for each trap direction at each value of $a_{collapse}$ studied. The vertical and horizontal error bars indicate the standard error of the measurements and the uncertainty in $a_{collapse}$ arising from the magnetic-field calibration, respectively. For some of the points, the uncertainties are comparable to the symbol size.

The most striking feature of the data is the strong dependence of the average energy on the number of condensate atoms. Comparing **(a)** and **(b)**, one sees that for fixed $|a_{collapse}| \simeq 30$ a$_0$, the radial and axial burst energies increase by a factor of $\sim$3 as the initial condensate number increases by 2.5$\times$. In fact, the energies were higher for the larger N_{init} condensates over the full range of $a_{collapse}$ studied. An additional observation is the overall trend of increasing energy with increasing $|a_{collapse}|$ in the low N$_{init}$ data (Figure 4.6**(a)**). However, the high N$_{init}$ data in part **(b)** display much more complex behavior that is not monotonic with $a_{collapse}$.

We also note that over much of the scattering length range shown in Figure 4.6 there is a significant anisotropy in the burst energy. The radial energy is always greater than or equal to the axial energy. We discovered that the burst energy anisotropy depended on N_{init}, $a_{collapse}$, and a_{init}. The anisotropy showed a peaked behavior for 15000 atom condensates, with maximum near $|a_{collapse}| \sim$100 a$_0$. For values of $|a_{collapse}|$ only slightly larger than $|a_{crit}|$, the burst was isotropic for both $N_{init} \simeq 6,000$ and $N_{init} \simeq 15,000$. At larger values of $|a_{collapse}|$, condensates with larger number gave rise to stronger anisotropies.

We cannot rule out a possible dependence of the burst energy anisotropy on the initial aspect ratio of the cloud, λ. We define λ as the ratio of the axial and radial rms widths of the BEC: $\lambda = \sigma_z/\sigma_r$. For the data with $N_{init} = 6000$, the initial scattering length was $a_{init} \simeq 0$ a$_0$, leading to $\lambda = 1.6$. In contrast, the high number data with $N_{init} =$ 15,000 had $a_{init} \simeq +8$ a$_0$ and $\lambda = 2$. When instead we started at $a_{init} = +100$ a$_0$ (N$_{init}$=15,000), the BEC was initially more anisotropic ($\lambda = 2.4$), but the burst became more isotropic, with $\langle E_{ax} \rangle$ going up by $\sim$40% and $\langle E_{rad} \rangle$ dropping by $\sim$60% at $a_{collapse} = -100$ a_0. These various results for the burst energy and the energy anisotropy are clearly very complicated. It is impossible to say how much of the observed differences between the low number and high number data in Figure 4.6 are due to the change in N$_{init}$ because we also changed the initial scattering length between

these two data sets. Nevertheless, the measured burst energy dependences can be used to test the validity of several mean-field models that were recently proposed to explain our results (see section 4.7).

4.5 Remnant BEC

4.5.1 $\mathbf{N}_{rem}$ exceeds $\mathbf{N}_{crit}$

After each collapse, a "remnant" condensate containing a fraction of the atoms survived with nearly constant number for more than one second. The remnant BEC oscillated in a highly excited collective state with the two lowest breathing modes at $\nu \simeq 2\nu_{axial}$ and $\nu \simeq 2\nu_{radial}$ being predominantly excited. The measured frequencies were $\nu = 13.6(6)$ Hz and $\nu = 33.4(3)$ Hz. To find these oscillation frequencies, we measured the widths of the condensate as a function of the time spent at $a_{collapse}$. As usual, we utilized a mean-field expansion of the BEC to measure the widths. While the expansion leads to large increases in the widths, it does not distort their periodic modulation in time.

The number of atoms in the remnant depended on $a_{collapse}$ and N_{init}, and in general was not limited by the critical number, N_{crit}. Although the stability condition in equation (4.1) certainly determined whether or not the condensates experienced a collapse event [33], the number of atoms left behind was often significantly larger than N_{crit}. This behavior is shown in Figure 4.7, where we plot the remnant number as a function of scattering length.

In Figure 4.7, the 6000 atom data do mostly lie on or below the line showing the value of the critical number. In fact, for $N_{init} = 6,000$ and $|a_{collapse}| < 10\ a_0$, more atoms were lost than the number required to lower N_{rem} below N_{crit}. Since we did not take the large N_{init} data until much later, we initially believed that N_{crit} truly did constrain $N_{remnant}$. However, the agreement observed in the N_{init}=6000 data

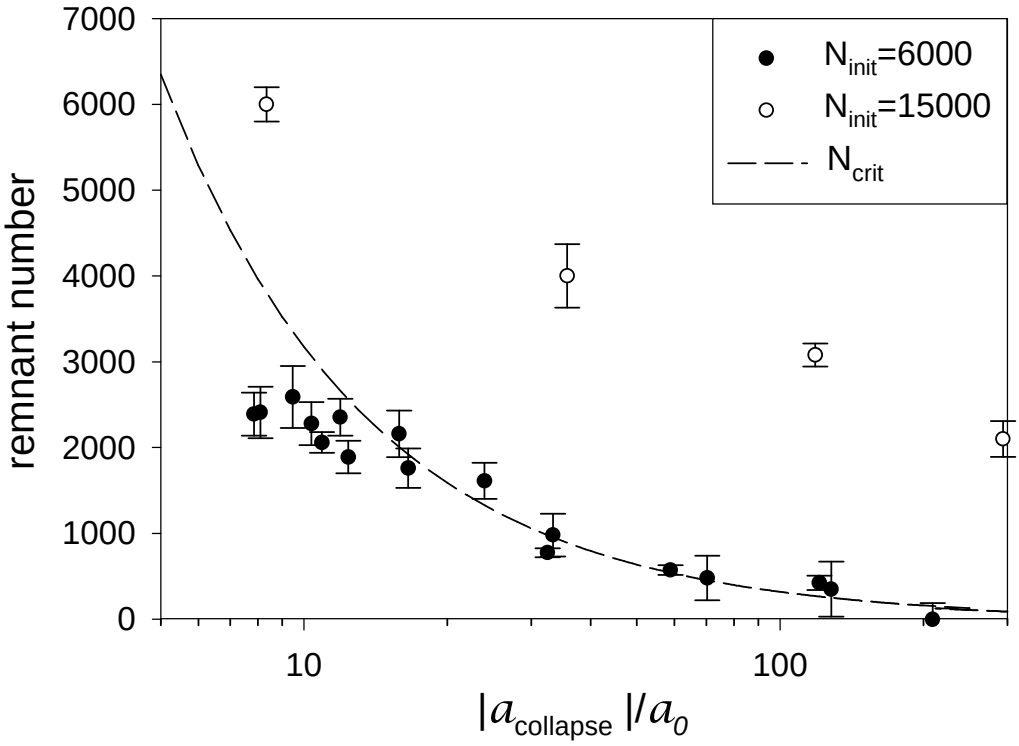

Figure 4.7: Remnant BEC number versus initial BEC number. The dashed line is the critical number of BEC atoms as calculated from the stability equation (4.1) with $k_{collapse}$=0.55 [31]. The black points and white points are the values of N_{rem} for different initial number, as explained in the legend. Note that the N_{init}=6000 remnant data (black points) correspond to the data we used for determining the collapse time as a function of scattering length in Figure 4.3.

turned out to be entirely coincidental; when we increased the initial number to ∼16,000 atoms, the remnant number always exceeded N_{crit} for the entire range of $|a_{collapse}|$ that we investigated. The fraction of initial number of atoms that went into the remnant decreased with $|a_{collapse}|$, and was ∼40% for $|a_{collapse}| < 10\ a_0$ and ∼50% for $|a_{collapse}| > 100\ a_0$.

We found that a fixed fraction of N_{init} went into the BEC remnant independent of the value of N_{init}, so that smaller condensates often ended up with $N_{rem} < N_{cr}$, but larger condensates rarely did. After discovering this surprising result, we studied the remnant dependence on initial number in the condensate. Figure 4.8 demonstrates the direct proportionality between N_{rem} and N_{init} for fixed scattering length. Increasing the value of $|a_{collapse}|$ merely shifts the proportionality constant downward — the linear dependence remains.

The observation that the remnant number routinely exceeded the critical number is surprising, but not impossible to explain. One reason that we might expect this behavior is the highly excited state of the remnant. Due to the excitations and large number losses, it is difficult to know the proper temperature of the cloud. It is possible that the remnant is not actually a condensate, although the observed mean-field expansion of the atom cloud indicates that the phase space density is comparable to unity. Another possible explanation for N_{rem} exceeding N_{crit} is an inherent stabilizing nature of the excitations. Pattanayak et al. [40] have shown that a BEC with a particular type of collective excitation known as a quadrupolar shape oscillation can impart enough angular momentum the BEC to provide a centrifugal barrier to collapse. The excitation can stabilize a condensate by creating an additional quantum pressure beyond that provided by the confining trap potential. However, Ref. [40] also predicts that radial breathing mode excitations should *destabilize* a BEC with attractive interactions. Since we have observed breathing mode oscillations in the condensate widths, the Pattanayak et al. mechanism for stabilization is unlikely to explain our results. It would be inter-

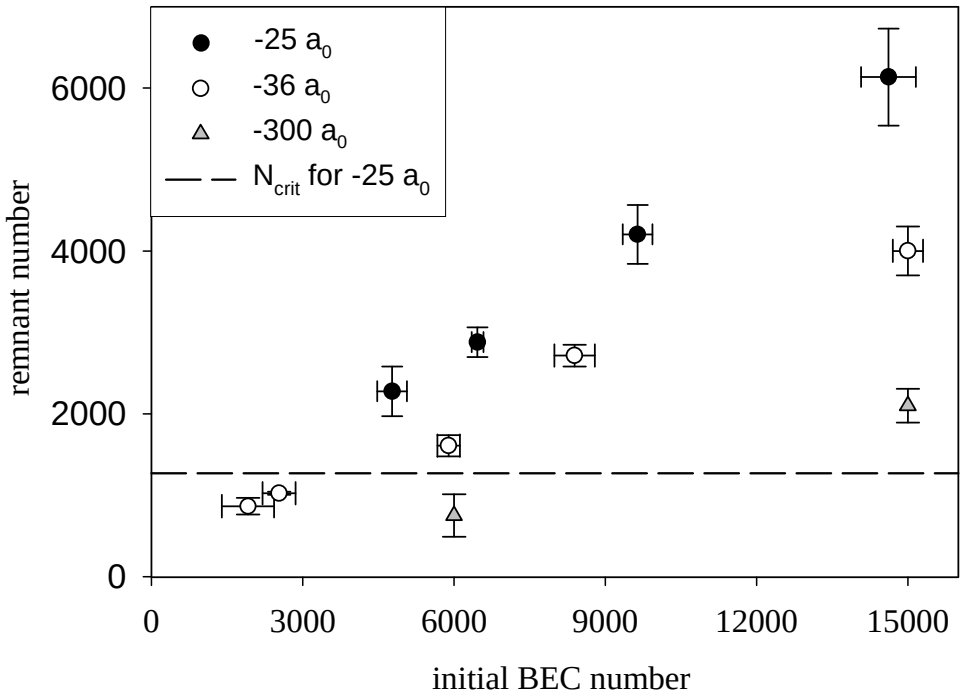

Figure 4.8: Dependence of remnant number on initial BEC number. The points are the measured values of N_{rem} versus N_{init}. The legend lists the various different values of $|a_{collapse}|$ that were used. The dashed line shows the critical number for the smallest relevant value of $|a_{collapse}|$=25 a_0. Most of the data clearly lie above this stability line. For the data with $|a_{collapse}|$=25 a_0, we found no discernible dependence of N_{rem} on initial scattering length when a_{init} was varied between -1 a_0 and $+6$ a_0.

esting to return to the issue of the BEC excitations and the apparent stabilization of the remnant in the future. One observable that might give useful information, but was not yet studied carefully is the excitation amplitude of the remnant cloud. Perhaps we could determine whether the oscillation amplitude is bigger for the collapse events in which N_{rem} greatly exceeds N_{crit}.

4.5.2 Missing atoms

In the collapse process, a large fraction of the initial BEC disappears. The missing atoms do not show up in the absorption images of the post-collapse BEC. Although we cannot yet say what happens to these expelled atoms, we are able to discuss the dependence of the missing atoms on scattering length and initial number because we know the corresponding trends for the burst and remnant numbers. Since N_{burst} was independent of $|a_{collapse}|$ but N_{rem} decreased with $|a_{collapse}|$, the number of missing atoms grew larger with $|a_{collapse}|$.

Interestingly, the absolute number of missing atoms also increased with N_{init}. The increase was proportional to the initial number so that the missing fraction dependence on $|a_{collapse}|$ was identical for both $N_{init} = 6,000$ and $N_{init} = 15,000$. For $|a_{collapse}| < 10\ a_0$, we measured a missing fraction of $\sim$40%, while the fraction was $\sim$70% for $|a_{collapse}| \geq 100\ a_0$. The missing atoms were presumably either expelled from the condensate at such high energies that we could not detect them ($> 1\ \mu$K), or they were transferred to untrapped atomic states or undetectable molecular states.

We made an attempt to test the hot atom hypothesis for the missing atoms by turning off the magnetic trap immediately after a collapse and then recapturing the atoms in the MOT. Because the MOT trap depth of order $\sim$1 K is much deeper than that of the magnetic trap ($\sim$100 μK), the recapture process should collect atoms with much higher energy than we could ever observe with absorption imaging. An additional advantage of the MOT is its large trap volume, which greatly exceeds the magnetic

trap volume. However, recapture in a MOT and subsequent fluorescence detection suffers from two major defects that we could not surmount. The first defect is the poor sensitivity of fluorescence detection versus absorption imaging. For small atom samples, there simply is not much light scattered by the atoms for detection. The sensitivity problem can be solved by careful design of a high-gain photodiode circuit. However, there is another problem with the MOT recapture, namely, the large background signal due to hot "Oort cloud" atoms in the magnetic trap. The Oort cloud is thought to form during the evaporative cooling process and to interact only very weakly (if at all) with the BEC [41]. In fluorescence detection, the Oort cloud atom signal swamps the BEC signal due to a difference in the numbers of atoms of many orders of magnitude. As a result, we could not make a quantitative search for the missing atoms with the magneto-optical trap.

4.5.3 Strange density patterns: jets

Under certain experimental conditions, we observed streams of atoms with highly anisotropic velocity distributions emerging from the collapsing condensates. Atoms in the "jets" possess distinctly different properties from the burst atoms. First, the jets have much lower kinetic energy than the burst (a few nK compared to ∼100 nK). The average velocity of the jet atoms is nearly purely radial, so that the energy anisotropy is at least 10. In addition, we have discovered that the jets appear only when the BEC collapse process is interrupted (i.e., by jumping to $a_{quench} = 0$) during the period of BEC number loss. When the collapsing condensate was allowed to complete the collapse process so that $N_{BEC} \rightarrow N_{rem}$, no jets were emitted from the BEC. In contrast to this behavior, the burst atom explosion always seemed spontaneous; bursts would form whether or not we quenched the collapse by quickly ramping to zero scattering length.

Examples of the strange jet density patterns we have observed are shown in

Figure 4.9 for different values of t_{evolve} and the same conditions as Figure 4.2. We observed that the jet size and shape varied from image to image even when all conditions were unchanged, and as many as three jets were occasionally emitted from the collapse of a single condensate. Surprisingly, the jets were not always symmetric about the condensate axis. We even observed that some jets were emitted at a slight angle with respect to the radial direction.

We hypothesize that the jets are manifestations of local "spikes" in the condensate density that grow while the BEC is imploding and then expand when the balance of forces is changed by quenching the collapse. If this interpretation is correct, we can estimate the size of the density spikes using the uncertainty principle. After a jump to $a_{quench} = 0$, the kinetic energy of the atoms in the resulting jet must be equal to the confinement energy that the spike had prior to quenching the collapse. If we assume a Gaussian density spike in the BEC wavefunction with a width σ, then the average kinetic energy of the jet atoms is related to the width of the spike by

$$\langle T \rangle = \frac{1}{2} m \langle v \rangle^2 = \frac{\hbar^2}{4m\sigma^2}. \tag{4.2}$$

In the context of the spike picture, the observed anisotropy of the jets indicates that the spikes from which they originated were also highly anisotropic, being narrower in the radial direction. From the calculated widths (using equation (4.2)) and the measured number of atoms in the jets, we can estimate the density in the spikes. We present plots of the number of jet atoms and the inferred spike density versus t_{evolve} in Figure 4.10. The jet data exhibited variability in energy and number significantly larger than the $\sim 10\%$ measurement noise.

The jets expanded with velocity $v \simeq 1$ mm/s, which corresponds to a kinetic energy of $\sim$5 nK and a radial pre-quench Gaussian rms width of ~ 0.5 μm. Since the axial size of the jets was below our optical resolution limit, we could not measure the axial

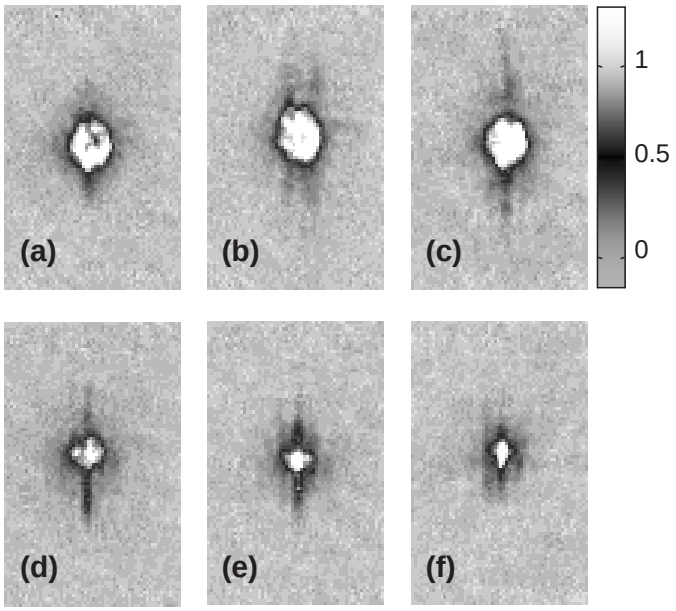

Figure 4.9: Jet images for a series of t_{evolve} values. The absorption images were taken with the conditions of Figure 4.2. The evolution times were 2, 3, 4, 6, 8, and 10 ms (from **(a)** to **(f)**). Each image has dimensions 150×255 μm. The shaded bar indicates the optical depth scale. For these data, we applied an expansion ramp to $a_{expand} = +250\ a_0$, so the jets are longer than for the quantitative measurements explained in the text. The jets were longest (i.e., most energetic) and contained the most atoms at values of t_{evolve} for which the slope of the number loss curve (Figure 4.2) was greatest. A tiny jet is barely visible for $t_{evolve} \simeq 2$ ms (image **(a)**), which is 1.7 ms before $t_{collapse}$. The central component of the images is the remnant BEC, which clearly decreases with time. The time between the application of a_{quench} and the acquisition of the images was fixed at 5.2 ms.

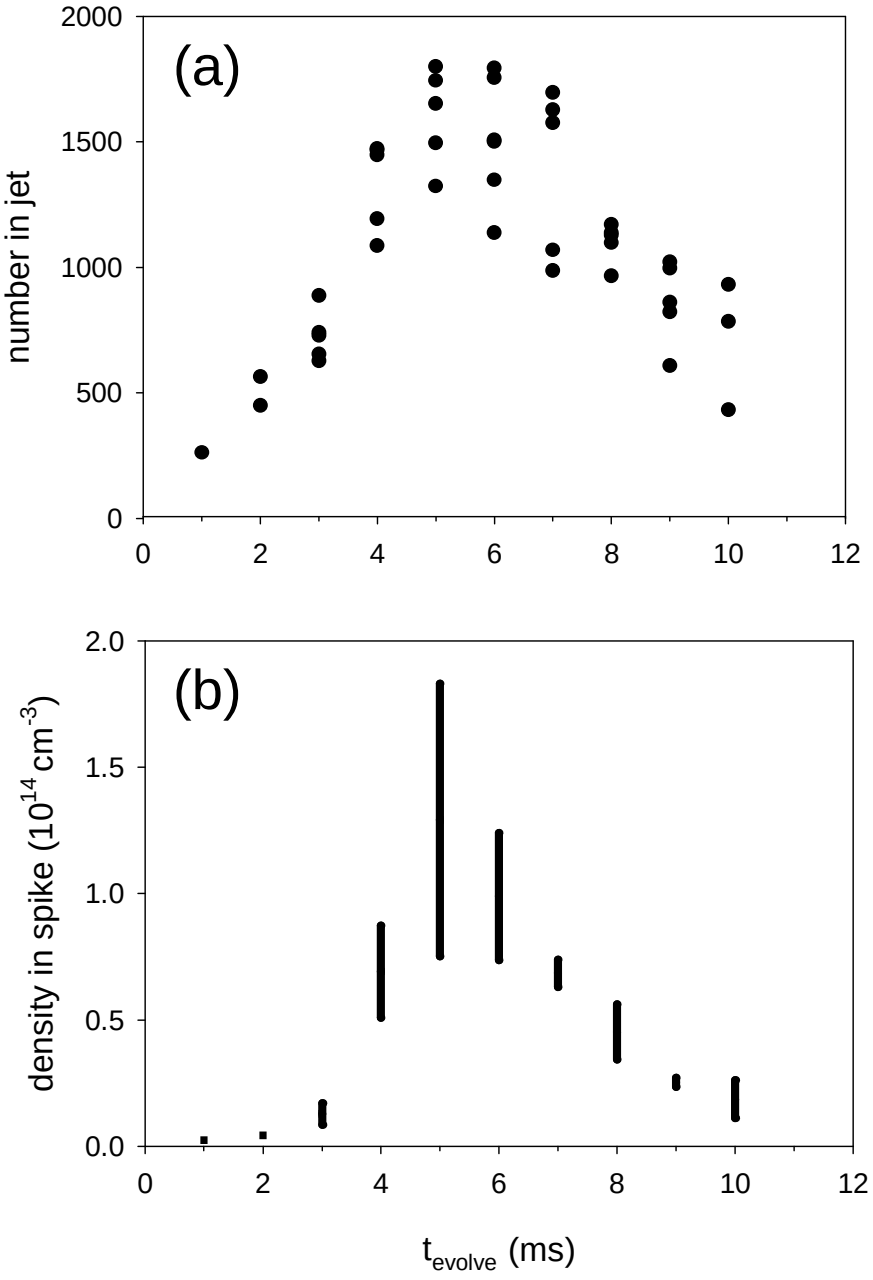

Figure 4.10: Quantitative jet measurements. **(a)** The number of atoms in the jets versus t_{evolve} for the conditions of Figure 4.2. **(b)** The spike density inferred from the kinetic energies of the jets. The vertical bars indicate the full range of shot-to-shot variability, which was rather high. For the analysis, we assumed the jets were disk-shaped since the magnetic trap has cylindrical symmetry. The images were taken perpendicular to the axial trap axis, corresponding to an edge-on view of the disks.

expansion rate. We therefore assumed an axial width equal to the harmonic oscillator length for estimating the spike density. The atom density in the spikes decreased for larger values of $|a_{collapse}|$, and was half as large for $a_{collapse} = -170\ a_0$ as for $-36\ a_0$.

The observation of jets in the collapsing condensates suggests that the collapse process involves a clumping of atoms into bunches. The implosion of the BEC probably cannot be simply characterized as an overall contraction with a single density peak at the center of the cloud [37]. In fact, we have evidence from mean-field expansion of the collapsing condensates (see section 4.3.1) that the overall density contraction is relatively small — with an average density increase on the order of 50%. So a more plausible picture of the collapse is one with internal structure, as suggested by more recent theoretical models. A discussion of the recent theory is given in section 4.7.

4.6 Collapse at B=0

In addition to the measurements described in this Chapter, it is potentially very interesting to examine the collapse of an ^{85}Rb BEC after turning off the magnetic trap. When the trap potential is switched off, we have the novel situation that the scattering length is large and negative ($\sim$-470 a_0 at B=0). We have not extensively studied the collapse dynamics at B=0 because most of the special techniques we have developed, such as mean-field expansion of the BEC and focusing the burst atoms, do not work at zero field.

However, when we quickly turn off the magnetic trap after forming a high density condensate, we do observe a burst of energetic atoms emerging from the BEC. At the same time, the number of condensate atoms decreases rapidly. Unfortunately, it is somewhat difficult to determine how much of the burst and number loss is due to collapse physics and how much is due to ramping the B-field across the Feshbach resonance (see Chapter 5). Nevertheless, the BEC collapse at B=0, and also at magnetic fields slightly below the Feshbach resonance, may provide an interesting avenue for future research.

4.7 Discussion of theoretical models

4.7.1 Overview of observations

Collapsing ^{85}Rb condensates display very dramatic and complex behavior. At the time that the data were collected, most of the observed details of the collapse could not be easily explained in terms of existing theoretical models for the collapse [36, 37, 42, 43, 44]. These theories were developed to describe ^{7}Li experiments, where the scattering length was fixed and the BEC interactions with a large thermal cloud proved very important. The peculiar and complex collapse behavior seen in our ^{85}Rb experiment prompted a number of theorists [45, 46, 47, 48] to adapt their models to our experimental conditions. To facilitate comparison of the prominent features of our data with the predictions of the theories, we can summarize our main observations.

(1) There is a delayed and abrupt onset of number loss from the condensate after $a \rightarrow a_{collapse}$.

(2) The delay time before the loss depends inversely on both the initial density and $|a_{collapse}|$.

(3) The loss decay constant τ_{decay} is independent of both N_{init} and $|a_{collapse}|$ for $|a_{collapse}| < 100\ a_0$, and only weakly depends on these quantities for larger $|a_{collapse}|$.

(4) Part of the BEC number loss is due to formation of an energetic burst of atoms. The average burst energy and energy anisotropy exhibit dramatic variations with initial condensate number and $|a_{collapse}|$.

(5) The number of cold remnant BEC atoms surviving the violent collapse varies between much less and much more than N_{crit}, depending on N_{init} and $a_{collapse}$.

4.7.2 Mean-field models for collapse

All of the papers that model the collapse dynamics experiments described in this Chapter [46, 47, 48] use a mean-field approach that includes density-dependent decay from the BEC. To account for 3-body recombination losses and also describe the attractive self-interaction in the BEC, the authors of Refs. [46, 47, 48] integrate a modified Gross-Pitaevskii (GP) equation that possesses an imaginary loss term [37].

Santos and Shlyapnikov [46] numerically integrate the modified GP equation for our anisotropic magnetic trap potential, using a particular value for the 3-body recombination loss coefficient, L_3. The authors choose L_3 to be within the limits set by our previous experiments [39], with a typical choice being $L_3 = 2 \times 10^{-26}$ cm^6/s. The model of Ref. [46] shows that 3-body recombination losses set an upper to the contraction of the collapsing BEC. The density should grow until the loss "burns" a small number of atoms in the dense central region, then the region is quickly refilled by surrounding atoms. Santos and Shlyapnikov observe a series of such intermittent collapses of the BEC, with each collapse destroying only a small number of the condensate atoms. As the number decreases due to the losses, the balance of forces controlling the condensate wavefunction changes. The attractive mean-field interaction becomes weaker and is overcome by a repulsive force from the tight compression of the BEC wavefunction. Thus, each intermittent collapse has a compression phase followed by a rapid expansion or explosion of BEC atoms.

The authors of Ref. [46] therefore identify the burst atoms observed in the experiment as excited condensate atoms produced during the intermittent collapses. Obviously then, the missing atoms are the atoms that are burned off by 3-body recombination. Santos and Shlyapnikov make quantitative predictions for several experimental quantities, including $t_{collapse}$, τ_{decay}, and $\langle E_{burst} \rangle$ in the axial and radial directions. The model reproduces several of the prominent features of the experimental data, including the

BEC loss characteristics (features (1)-(3) above) and the observed fact (5) that N_{rem} is often much greater than N_{crit}. There is no explanation given for $N_{rem} > N_{crit}$ in the model — the authors simply state that this is "expected"!

Santos and Shlyapnikov assert that the energetically expanding BEC atoms are the burst atoms. The calculated burst energies are predicted to scale with the ratio $a^2_{collapse}/L_3$. By allowing L_3 to vary with scattering length from $\sim 2 \times 10^{-27}$ cm^6/s at $a \simeq -30$ a$_0$ to $\sim 2 \times 10^{-25}$ cm^6/s at $a \simeq -250$ a$_0$, Santos and Shlyapnikov obtain good agreement with the experimental data for $\langle E_{burst} \rangle$ with N_{init}=6000 atoms. However, the agreement with the larger N_{init}=15,000 data is quite poor. Overall then, Santos and Shlyapnikov cannot model the full experimental burst behavior (feature (4) above), even when they allow the loss rate coefficient to vary by a factor of 100. While Ref. [46] has intuitive appeal and does qualitatively explain all of the observations, it is impossible to fully evaluate the validity of the theory without better knowledge of the 3-body decay rates in the negative scattering length regime.

Other theoretical models have been developed to explain the collapse dynamics [47, 48]. Most notably, Saito and Ueda [47] have proposed a mean-field model that is nearly identical to that of Ref. [46], with the only quantitative difference being a smaller choice for the 3-body decay rate coefficient ($L_3 = 2 \times 10^{-28}$ cm^6/s). Saito and Ueda also predict details of the BEC loss that agree with experiment and they observe a burst of energetic atoms. However, the authors make no attempt to model the burst energy because of the unknown L_3 dependence on scattering length. One unique prediction from Saito and Ueda regards the jets. The authors explain that the jets do not result from the released confinement energy of density spikes but instead are due to interference of matter waves emanating from different density clumps in the imploding BEC.

4.7.3 Beyond mean-field theory

Although the published theoretical models for the ^{85}Rb BEC collapse behavior are all based on conventional BEC mean-field theory, it is possible that the physics might require more complicated theories that go beyond the level of the GP equation. Murray Holland has expressed the opinion that the ^{85}Rb collapse is special because of the Feshbach resonance. He suggests that a quantum field theory that includes higher-order correlations between the atoms is necessary to fully explain our observations. In addition, T. Kohler and K. Burnett have also been pursuing a beyond-GP-equation approach to explain the burst atoms we observed during the collapse process (Ref. [46] contains a note about this). It will be interesting to see whether a full theory of resonant BEC can be developed to explain both the collapse experiments and the atom-molecule coherence experiments in Chapter 6.

On a related note, Jake Roberts has proposed an interesting experiment to study the collapse by changing the scattering length in a different way. We could use an RF π pulse to change the spin state of the atoms from $|2,-2\rangle$ to $|2,-1\rangle$. This state has a large negative scattering length and no nearby Feshbach resonance. Thus, by studying the collapse dynamics (especially the possible presence of burst atoms), one could potentially separate the physics of the collapse at fixed scattering length from the physics of resonant BEC.

Chapter 5

Microscopic dynamics in a strongly-interacting Bose-Einstein condensate

5.1 Introduction and motivation

This chapter describes experiments that explore the response of an ^{85}Rb BEC to rapid magnetic field variations. We begin by giving a motivation for the experiments. Next comes a detailed explanation of the experimental methods and data. Finally, we review some of the relevant theory for modeling the experiments.

In contrast to the negative scattering length experiments of Chapter 4, here we discuss BEC behavior in the positive a region near the ^{85}Rb Feshbach resonance, where the condensate self-interaction is large and repulsive. We used rapid magnetic field variations to probe the strongly interacting regime in the condensate. We changed the magnetic field to approach the Feshbach resonance from above, which causes the positive scattering length to increase. As na^3 becomes comparable to or larger than one, the customary mean-field description of the dilute gas BEC, which assumes no correlations between the atoms, breaks down. Correlations between the atoms become increasingly important and a BEC with sufficiently large na^3 will eventually reach a highly correlated state such as that found in a liquid. We are interested in the nature of this transition to a highly correlated state and the time scale for the formation of the condensate correlations. In a strongly-correlated BEC with large scattering length, it should be possible to discover effects that go beyond the standard mean-field theoretical

description.

In addition to such interesting physics, our time dependent experiments also allow us to investigate the possibility of collisional coupling between pairs of free atoms and bound molecules. Since the atomic and molecular BEC states are degenerate at the Feshbach resonance, a number of authors [14, 49, 50, 15, 51, 52, 53] have predicted that atom-molecule transitions can occur during a B-field ramp. These theories were mainly inspired by the Na BEC experiments at MIT [12, 38], in which very large number losses to the condensate were seen when the magnetic field was ramped through a Feshbach resonance. However, these observations always revealed that the more time spent near the Feshbach resonance, the greater the number loss. This time dependence is consistent with a basic mean-field description of the BEC that includes a density-dependent loss process, such as three-body recombination into molecules [54, 41]. Thus, the Na BEC experiments could neither prove nor disprove the hypothesis that coherent molecule creation was the cause of the observed BEC number loss.

We also observed BEC number loss due to ramping the B-field across the resonance. In fact, after producing ^{85}Rb condensates in 1999, our most important task was to determine the effect on the BEC of crossing the Feshbach resonance. Except in special cases, we always turn off the magnetic trap before imaging the BEC, which requires that we ramp the magnetic field quickly from $\sim$160 G to 0 G. Any perturbations to the condensate caused by crossing the Feshbach resonance at 155 G could potentially distort our measurements of BEC dynamics in the trap. In our early tests, we saw number loss from the BEC of up to 75% when we crossed the Feshbach resonance. The number loss became steadily smaller as we ramped more quickly to zero B-field, until the fastest ramp we could produce ($\sim$1 G/μs) caused N_0 to drop by less than 10% [26]. In later experiments, we found that the BEC number loss was density-dependent [1]; therefore, we could completely eliminate the loss by expanding the condensates in the magnetic trap before crossing the resonance (see section 3.5.2). These measurements stimulated

our curiosity. We wanted to discover how much of the number loss was due to ordinary inelastic collisions, which become increasingly frequent as one approaches the Feshbach resonance [39], and also whether any of the loss might be due to the coherent formation of molecules suggested by Refs. [14, 49, 50, 15, 51, 52, 53].

5.2 Experimental methods

5.2.1 Producing short B-field pulses

To understand time dependence of loss in our ^{85}Rb BEC, we examined the response of the condensate when we briefly approached the Feshbach resonance by applying a short magnetic field pulse (much shorter than the period for collective excitations). We initially generated these B-field pulses using a time-dependent current in the base-ball coil. From the outset, it was clear that the pulse had a dramatic effect on the BEC — depending on how closely we approached the resonance, we saw large number loss from the condensate and also a relatively hot ($\sim$150 nK) burst of atoms (this burst was similar in character to that produced during the collapse dynamics experiments in Chapter 4). The most obvious feature of the BEC response to the magnetic field pulse was a loss of atoms that increased when we made our pulses shorter, until the loss became very large for very short pulses. Since the BEC number loss occurred very quickly (pulse duration < 100 μs), we had to improve our B-field control to make very short pulses. We designed an auxiliary B-field coil (details given in Chapter 3) for generating precisely tailored pulses toward the Feshbach resonance, as shown in Figure 5.1.

Our ability to carefully control the B-field allows us to probe the effects of microscopic physics in the BEC. By applying a short B-field pulse, we obtain a remarkable separation of the time scales for microscopic versus macroscopic changes to the condensate. For instance, we can change the magnetic field by 10 G in a time of 10 μs, which is a factor of 10^3 shorter than the oscillation period of the atoms in the trap.

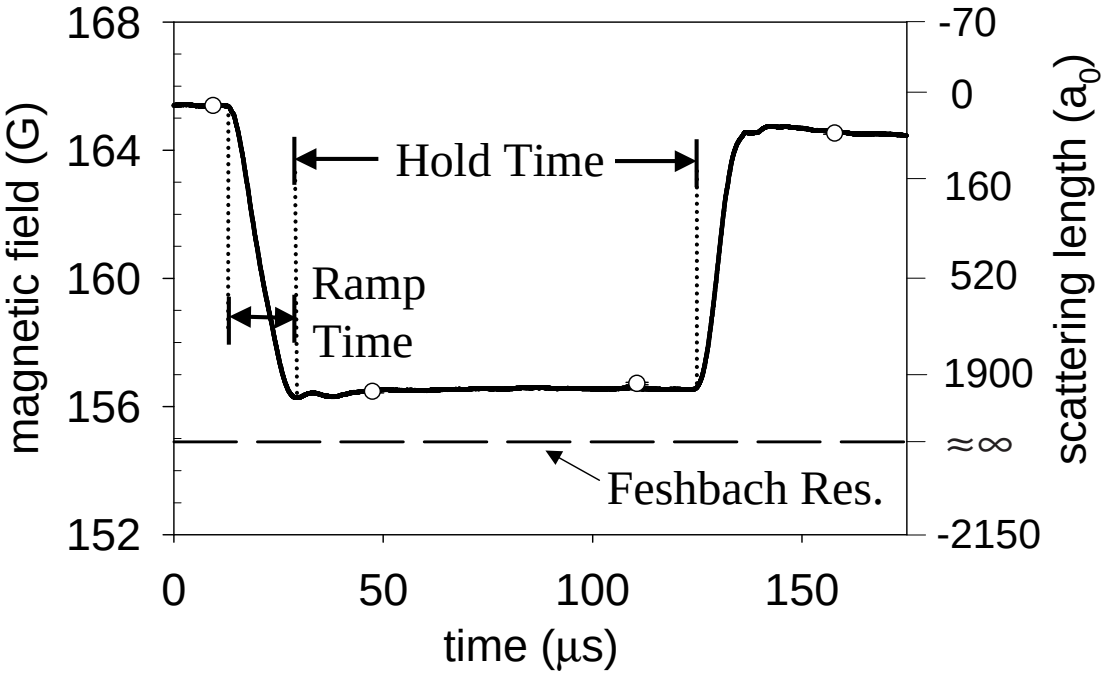

Figure 5.1: Magnetic field vs. time for a typical auxiliary coil pulse. The solid line is the field calculated from measurements with calibrated Hall-effect current sensors. On the right vertical axis, the corresponding variation in scattering length is shown. The open circles are independent measurements of the magnetic field obtained by determining the resonant frequency for a 10 μs RF radiation pulse that drives atoms to the m_F=–1 spin state (error bars are smaller than the points). The dashed line shows the position of the Feshbach resonance, where the scattering length becomes infinite. The field variation on the peak of the pulse was typically $\Delta B \lesssim 0.1$ G.

This means there is negligible motion of the atoms during a short pulse – the BEC wavefunction remains static for the pulse duration. In fact, the brevity of the pulse prevents any BEC expansion despite the fact that the repulsive self-interaction energy of the condensate typically increases during the pulse. We have verified this assertion by modeling the BEC density with the PG model (see section 3.5.3) for the pulses used in the experiment.

5.2.2 Counting the BEC atoms

To study BEC number loss we first form a ^{85}Rb condensate, following the procedure given in Ref. [26]. A sample of ^{85}Rb atoms in the F=2 m_F=–2 state is evaporatively cooled in a cylindrically symmetric magnetic trap (ν_{radial} = 17.5 Hz , ν_{axial} = 6.8 Hz). The magnetic field at completion of evaporation is 162.3 G, corresponding to a scattering length of 210 a_0. Typically, the cooled sample has N_0=16,500 BEC atoms and fewer than 1000 noncondensed atoms. The magnetic field is then ramped adiabatically (in 800 ms) to ∼166 G where the scattering length is positive but nearly zero [33], and the BEC assumes the shape of the harmonic trap ground state.

We next apply a short magnetic field pulse (duration < 1 ms) so that the field briefly approaches a value moderately close to the Feshbach resonance at ∼155 G, as displayed in Figure 5.1. We use destructive absorption imaging to look at the number of atoms remaining in the condensate. This experiment is repeated with a variety of differently shaped magnetic field pulses.

We find that the magnetic trap must be turned off and the condensate spatial size must be significantly larger than our resolution limit to obtain the most sensitive and accurate measurements of number (see section 3.5.2). To expand the BEC after the short pulse, we ramp in 5 ms to ∼157 G (a=2000 a_0), and then hold at that B-field for 7.6 ms. The mean-field repulsion during the ramp and hold times decreases the density by about a factor of 30 before the trap is turned off. The density decrease

avoids density-dependent losses that we have observed during the trap turn-off (see section 5.1). After turning off the trap, we allow the BEC to continue to expand for 12.6 ms at B=0 before taking an absorption image. From the absorption image of the expanded BEC we calculate the number of atoms remaining after a given auxiliary coil pulse.

5.2.3 Determining burst properties

The burst atoms generated by the B-field pulse have a very different energy distribution from the condensate, so we employ a different procedure to determine their properties. The best way to find the total number, N_{burst}, and average energy, $\langle E_{burst} \rangle$, of the burst atoms is to image them at a focus of their simple harmonic motion (see section 4.4). To focus the burst atoms onto the axial axis of the trap, we allow them to oscillate in the harmonic potential for 20.4 ms, which is more than one-half of a radial period ($T_{rad}/2$=29 ms). We obtain this delay without interfering with the BEC expansion ramp by adding a 7.8 ms delay between the end of the short B-field pulse and the start of the BEC expansion ramp. After 20.4 ms in the trapping potential, all of the burst atoms have an inward radial velocity. We then turn off the trap and the burst atom spatial distribution continues to contract ballistically until reaching a minimum radial size or focus 12.6 ms later.

A typical absorption image of the burst atom distribution superimposed on the BEC remnant is shown in Figure 5.2. This image was taken after preparing the sample of atoms according to the procedure given above. We use a 2-D Gaussian to fit the burst atom image, but we exclude the central region containing the condensate remnant from the fit. The excluded Gaussian fit easily separates the burst from the BEC remnant because of the large difference in the spatial extent of the two parts of the image.

The Gaussian fit parameters for a particular absorption image allow us to extract both N_{burst} and the value of $\langle E_{burst} \rangle$ for either the axial or radial direction. The focused

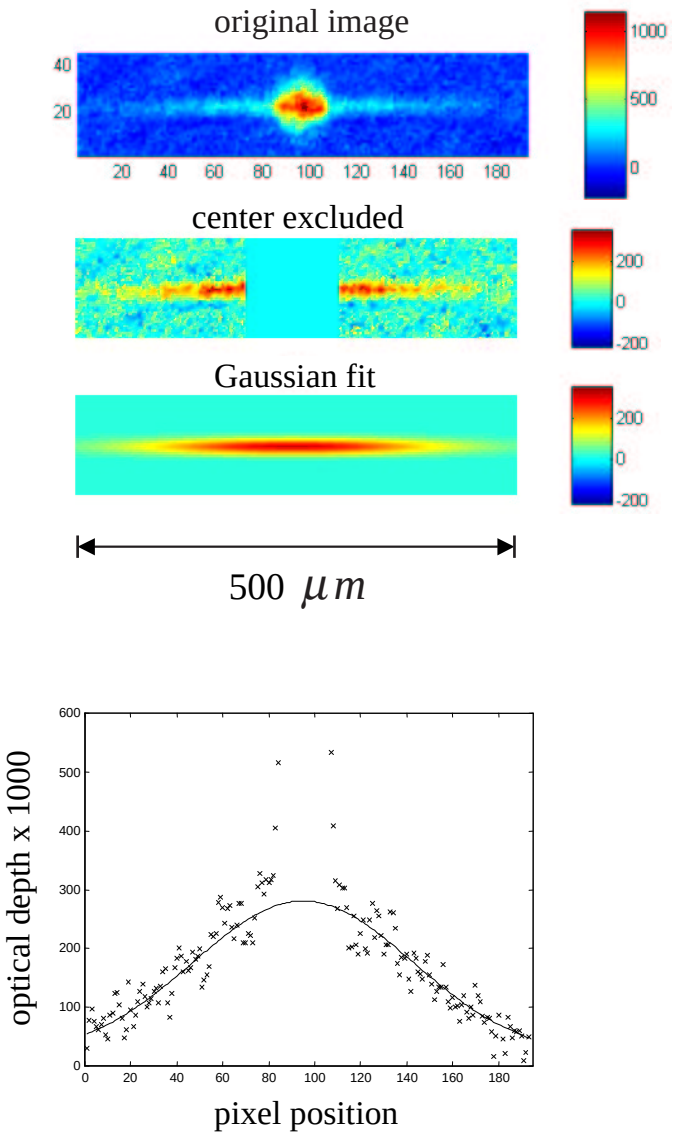

Figure 5.2: Determination of burst properties from an absorption image. At top we show a false-color absorption image taken after applying a short B-field pulse to the BEC, then expanding the condensate and focusing the burst as described in the text. Here we used a B-field pulse from B_{init}=165.5 G to B_{final}=157.1 G with ramp times of 13 μs and t_{hold}=30 μs. The images show the measured optical depth times 1000 versus spatial position on the camera pixel array (see colorbar). With the three images, we show how the central region of the image containing the BEC is excluded from the 2-D Gaussian fit. The excluded region size is chosen to be large enough so that the fit parameters are independent of the box size. At the bottom is an axial cross-section of the data and fit. Note the dramatic difference between the two spatial distributions, owing to the large difference in their mean energies ($\langle E_{burst} \rangle = 150\ nK \simeq 50 \times \langle E_{remnant} \rangle$).

burst looks like an elongated cigar with an aspect ratio of roughly 20. In a fit to the burst focus, the long dimension of the Gaussian (usually along the axial direction) gives an estimate of the rms energy of the burst atom distribution. The short dimension of the Gaussian is very narrow; we find that the observed size of the burst is limited by the finite resolution of our imaging optics. In principle, with perfect imaging optics and a truly harmonic potential, we could determine the burst formation time from the extent of the narrow focused dimension.

We can use the observed signal-to-noise (S/N) ratio in images such as Figure 5.2 to estimate our sensitivity to higher energy atoms in the burst. From the typical imaging S/N we believe there are no burst atoms with energy between 300 nK and 1 μK. Of course, it would be harder to see such atoms if there were two distinct components to the burst energy distribution, but this seems unlikely given the observed smooth spatial distribution that is fit very well by a Gaussian function.

To determine the BEC number from an image such as Figure 5.2, we first perform an excluded Gaussian fit to the burst atoms, then we subtract the Gaussian fit from the absorption image. The remaining image pixels due to the BEC remnant are then summed to find the total optical depth of the remnant. We compute the number of BEC atoms from the optical depth sum.

5.3 BEC number loss from short B-field pulses

In this section, we simplify the description of the BEC response to the magnetic field pulses by concentrating on the most obvious effect — the time dependent number loss from the condensate. We also observed that a significant fraction of the initial BEC number was converted into burst atoms by the short B-field pulses. However, the burst atoms did not account for all of the BEC number loss — there were also some undetected or missing atoms as in Chapter 4. Discussion of the burst atoms will be postponed until section 5.4.

5.3.1 BEC number loss versus pulse amplitude

One of our first experiments was to explore the amount of BEC loss as a function of the approach distance to the Feshbach resonance. We used triangular magnetic field pulses with variable amplitude and ramp time. The amplitude was varied to examine fields from 158.0 G (a=1200 a_0) to 156.0 G (a=4500 a_0). Here we list the corresponding scattering lengths that we have observed by slowly adjusting the magnetic field, as in Ref. [26]. The scattering length was calculated from the equation: $a(B) = a_{bg}(1-\Delta/(B-B_{peak}))$ with the Feshbach resonance parameters as given in section 7.3.3. For the range of magnetic fields examined here, the maximum value of the diluteness parameter for the BEC varied from $na^3 = 0.01$ for a=1200 a_0 to $na^3 = 0.7$ for a=4500 a_0.

The resulting BEC loss data are displayed in Figure 5.3. Here the dominant trend is an increase in the number loss as the pulses approach closer to resonance. For a fixed pulse amplitude, the BEC remnant number, N_{rem}, is largest at the shortest ramp time and then decreases with ramp time until it reaches a minimum. Then longer ramp times cause N_{rem} to increase over a time scale of tens of microseconds. The minimum in N_{rem} versus ramp time corresponds to a maximum in the number of lost atoms. The data in Figure 5.3 demonstrate that the ramp time that induces maximal loss becomes longer as the pulses approach the Feshbach resonance. In addition, the width of the minimum is largest for the pulses that come closest to resonance.

The triangular B-field pulses produce a very interesting and non-intuitive time dependent number loss. Under some conditions, we see that the loss increases for less time spent near resonance. Of course, the loss is not instantaneous; as the pulse lengths approach zero time, the loss time dependence reverses and the loss also goes to zero. Here it is useful to recall that conventional condensate loss is characterized by a rate constant for a density-dependent decay process, and thus the loss increases monotonically with time. In contrast, we measure an enhanced loss when the ramp time *decreases*, which

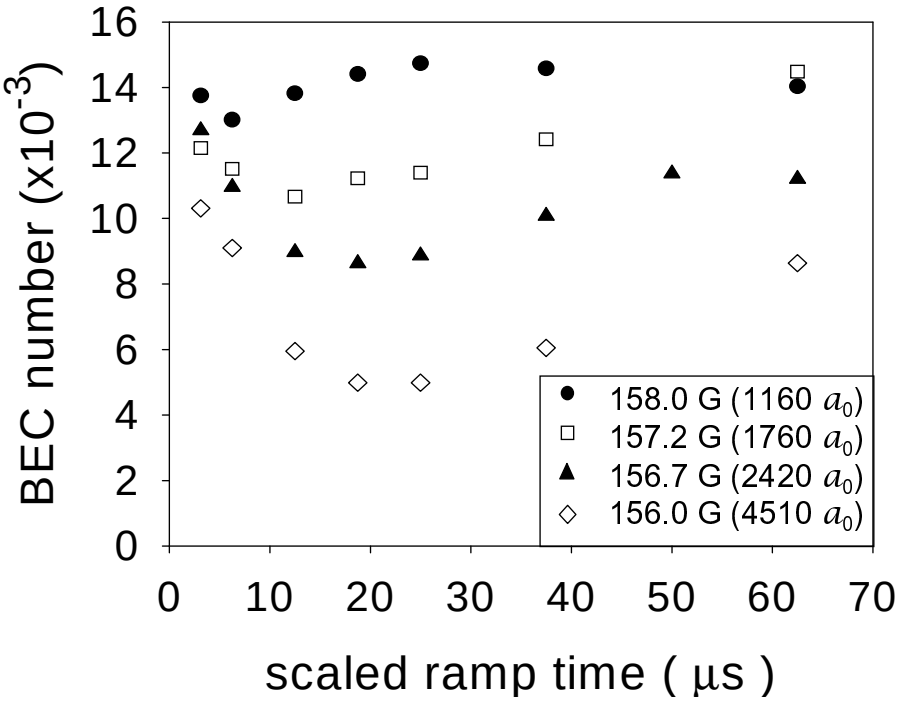

Figure 5.3: Ramp time dependence of BEC number for different triangular pulse amplitudes. The legend gives the magnetic field (and scattering length) at the peak of the pulse, which may be compared the Feshbach resonance B-field of 155 G. The BEC number and density at the beginning of the pulse were N_0=16,600 and $\langle n \rangle_0 = 1.9 \times 10^{13}$ cm^{-3}. The initial scattering length was a_{init}=7 a$_0$. The scaled ramp time on the x-axis is equal to the actual pulse ramp time divided by four, showing the time required to ramp from 75% to 100% of the pulse amplitude. This scaling reflects the observed fact that most of the loss occurred at fields closest to the Feshbach resonance. The pulse hold time was fixed at 1μs for these data. Data points are larger than the error bars.

suggests the presence of microscopic BEC physics such as non-adiabatic transitions to another state.

5.3.2 BEC loss versus pulse shape

We also measured how the BEC number loss depends on the ramp time of the magnetic field pulse for a variety of different pulse hold times. As shown in Figure 5.4, we varied the ramp time from 12.5 μs to 250 μs and changed the hold time at the pulse peak from 1 μs to 100 μs. For hold times $t_{hold} \leq 15$ μs, there is an initial decrease in N_{rem} as the ramp time increases. Then the slope changes and fewer atoms are lost for longer ramp times. Thus, the short hold time data show a distinct minimum in N_{rem} vs. ramp time, which shifts toward shorter ramp times as the hold time is increased. All of the hold time data display an upward slope in N_{rem} versus ramp time over some range of times, but the range is largest for the 100 μs hold time. This increase in remnant number for longer ramp time provides clear evidence that the loss is not conventional inelastic decay that is characterized by a rate constant.

Of course, the above interpretation of our data would be modified if the density of the BEC were changing due to the rapid increase in the mean-field interaction, but the characteristic time for such readjustments in cloud shape is far longer (of order $1/(2\nu_{radial})$=29 ms) than the time scales for the B-field pulses considered here. For example, using the analytic PG model (section 3.5.3), we calculate that for a 250 μs ramp to B_{final}=156.0 G (4500 a_0), the change in mean-field energy causes the BEC density to decrease by only 1% from its initial value. Thus, the observed dependences on ramp time must reflect microscopic physics in the BEC and not any macroscopic changes in the shape of the condensate.

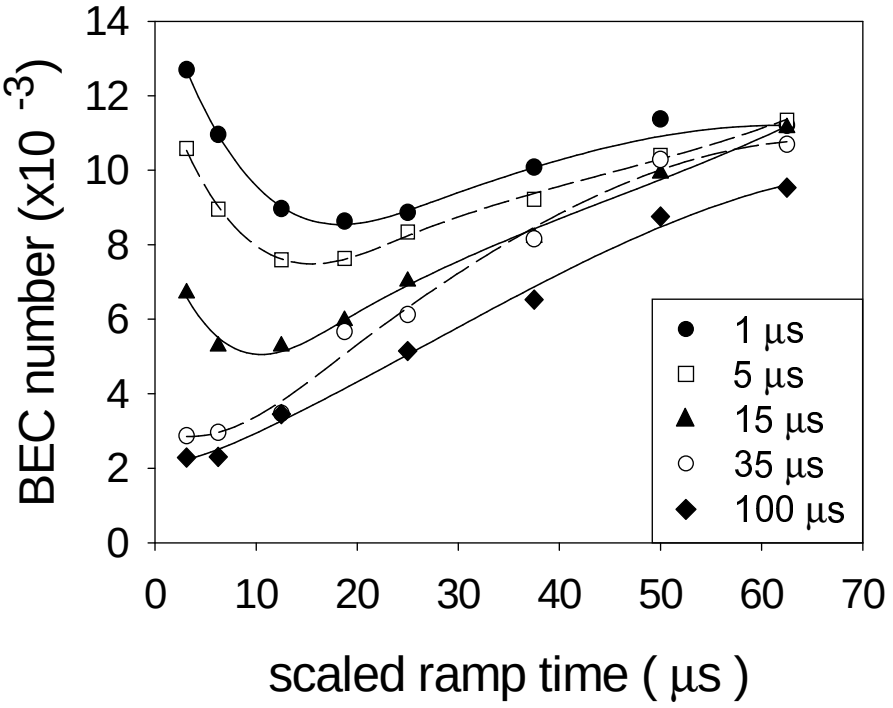

Figure 5.4: Dependence of remnant BEC number on pulse ramp time for various hold times (see legend) with N_0=16,500 ($\langle n \rangle_0 = 1.9 \times 10^{13}$ cm^{-3}). For the majority of the data points, the symbol is larger than the statistical error bar (not shown). The lines are spline fits to guide the eye. The ramp times were multiplied by a factor of 1/4 as in Figure 5.3. The magnetic field during the hold time was B_{hold}=156.7 G (2400 a_0).

5.3.3 Unconventional loss: Rabi-like oscillations

An alternative way to demonstrate the unconventional time dependence of the BEC number loss is by measuring the remnant BEC number as a function of hold time for the magnetic field pulse. For example, we can take the data from Figure 5.4 and plot N_{rem} versus t_{hold} for a B-field pulse with fixed ramp time. Using a linear ramp of 12.5 μs duration, we observed BEC number loss of 10-20% when the hold time was set to zero (corresponding to a triangular pulse). The number of BEC atoms then showed a smooth exponential drop as the hold time increased (see Figure 5.5).

At first glance, the exponential time dependence of the data in Figure 5.5 seems to support the hypothesis that the number loss came from density-dependent decay, as in Refs. [54, 41]. However, we showed that this was not true because the decay rate was insensitive to the initial BEC density. The BEC density before the short magnetic field pulse can be varied over a wide range by slowly changing the scattering length [26]. Surprisingly, when we used this method to reduce the initial BEC density by more than a factor of 2, the time constant for number decay was nearly unchanged. In addition, the low[high] density data exhibited a decay time constant that was over 2[1] orders of magnitude shorter than predicted by our previous inelastic loss measurements with cold thermal clouds [39].

To further explore the BEC number loss with hold time, we also varied the magnetic field at the peak of the pulse, B_{hold}. At B_{hold}=157.1 G, we observed a striking damped oscillation in N_{rem} versus t_{hold}. As displayed in Figure 5.6, the initial number loss actually reverses sign near t_{hold}=20 μs! Clearly this behavior cannot be explained in terms of a monotonic density-dependent number loss. To the contrary, the oscillation data suggest that the BEC number loss may involve coherent transitions to another state that are analogous to Rabi-flopping oscillations. However, the actual physical process appears to be more complex — there is a strong damping to the N_{rem} oscilla-

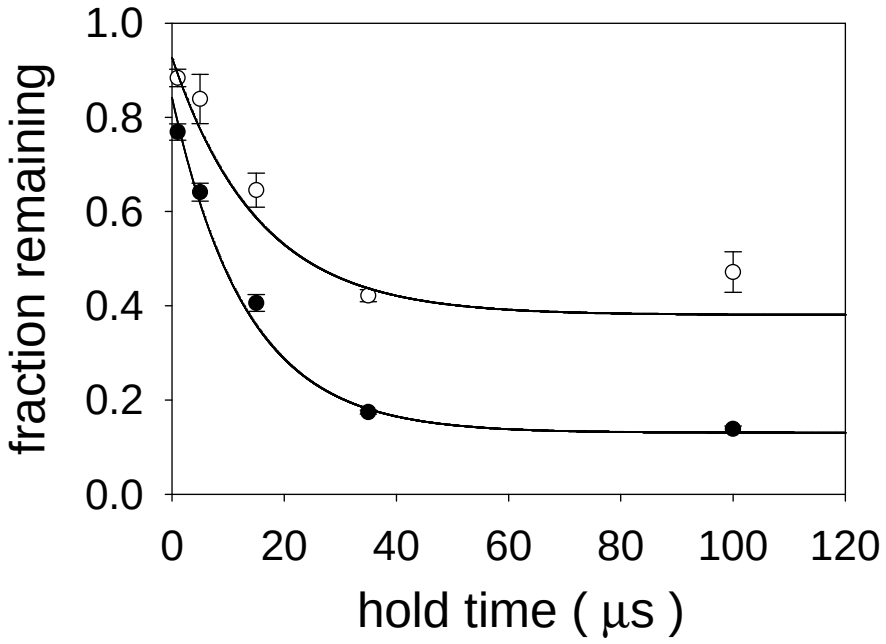

Figure 5.5: Fraction of BEC remaining versus pulse hold time. The pulse ramp times were 13 μs and the magnetic field during the hold was B_{hold}=156.7 G (2420 a_0). Number decay was measured for two different initial densities: $\langle n \rangle = 1.9 \times 10^{13}$ cm^{-3} ($\bullet$) and $\langle n \rangle = 0.7 \times 10^{13}$ cm^{-3} ($\circ$). Fitting the data to exponential functions (solid lines) gave time constants of 13.2(4) μs and 15.4(14) μs. Thus, reducing the density by a factor of 2.6 caused an increase of only 17(11)% in the decay time constant.

tions and there is an overall irreversible number loss from the BEC. From a damped sinusoidal fit to the data, we find an oscillation frequency of roughly 25 kHz, which is similar to the binding energy of the weakly bound molecular state associated with the Feshbach resonance. Attempting to extract the frequency precisely from the data is quite difficult, however, because of the rapid damping of the oscillations and the overall exponential decay of the BEC number.

Experimentally, the Rabi-like oscillations were quite difficult to observe and could only be seen with B_{hold} centered in a $\sim$0.1 G wide window of magnetic field around 157.1 G. We believe this narrow window results from a trade-off between being close enough to the resonance to have strong coupling with the molecular state and far enough from the resonance to have an oscillation period that is short compared to the overall BEC number decay time. We have discovered a way to avoid these limitations with an improved method for inducing atom-molecule oscillations. As described in Chapter 6, we use two magnetic field pulses separated in time to obtain Ramsey-like oscillations [24] in the BEC number.

5.4 Burst atoms created by short pulses

In our short pulse experiments, we always observed the formation of a relatively hot burst of atoms accompanying the disappearance of the BEC atoms. This section begins with an overview of the burst characteristics and then describes a more detailed experimental study of the burst.

5.4.1 Overview of burst characteristics

When we first realized that it was possible to generate an explosion or burst of atoms using a short magnetic field pulse toward the Feshbach resonance, we were shocked. The existence of this burst was very surprising because of its extremely rapid formation time of less than 20 μs. For comparison, the qualitatively similar burst

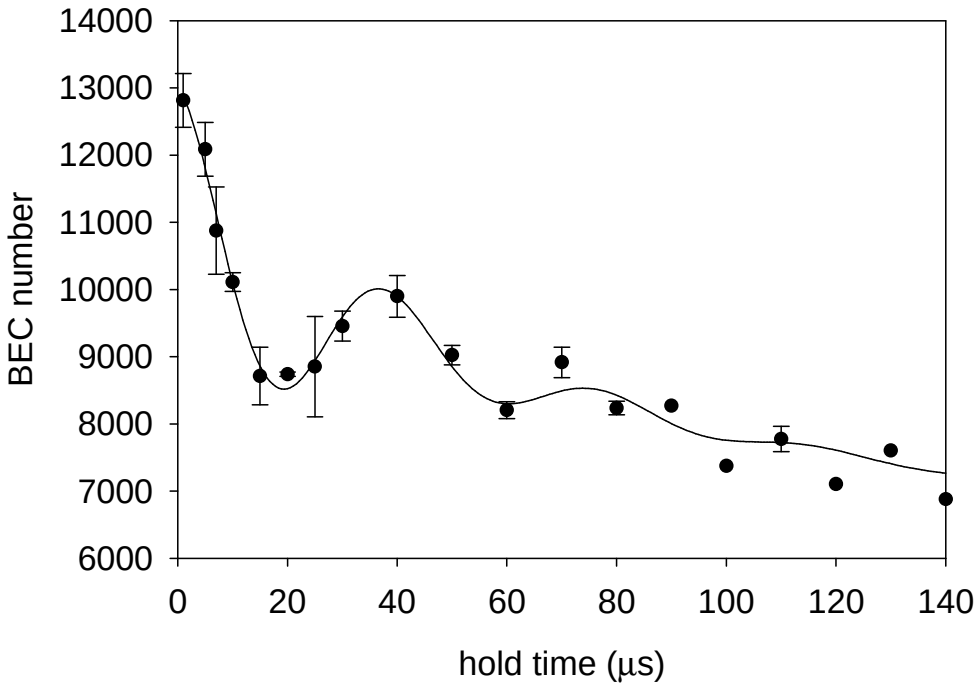

Figure 5.6: Rabi-like oscillation in the number of BEC atoms. Black points with error bars are the measured BEC number as a function of hold time for a trapezoidal B-field pulse. The ramp times for the pulse were fixed at 13 μs and the pulse decreased the B-field from the initial value of $\sim$165.5 G to the value B_{hold}=157.12 G (1840 a_0). The black line is a fit to the data using a damped oscillation superimposed on an exponential decay, with the functional form $N(t) = N_0 - \gamma \exp(-t/\tau) + A \exp(-\beta t) \sin(\omega_e t + \phi)$. For this fit, the BEC number decay time τ=110 μs is somewhat longer than the damping time for the oscillation, $1/\beta$=32 μs and the oscillation period $2\pi/\omega_e$=40 μs.

of atoms observed in the BEC collapse experiments (Chapter 4) was generated in a time of several milliseconds.[1] The BEC collapse process seemed to create burst atoms spontaneously during the slow implosion of the condensate at fixed magnetic field. In contrast to that scenario, we saw that short B-field pulses allowed us to generate an atom burst from a stable BEC and to influence the burst during its formation. In fact, we observed that the short-pulse burst characteristics were quite sensitive to the magnetic field pulse shape and amplitude, as discussed in section 5.4.2. Note that for the remainder of the Chapter, the short-pulse burst will simply be referred to as "the burst" or "the burst atoms".

Because the burst formation time is much less than the harmonic oscillation period of the magnetic trap, $T_r = 2\pi/\omega_r$=57 ms, the trap potential focuses the burst atoms onto a symmetry axis after a time t=$T_r/2$. The cylindrical anisotropy of the trap potential leads to radial and axial burst focuses at different delay times in the magnetic trap. Depending on whether the atoms form an axial or radial focus, we measure a different average burst atom energy, with the radial energy being roughly 2× the axial energy. Presumably this energy anisotropy results from the initial spatial anisotropy of the BEC before application of the short B-field pulse. We could study this by varying the initial condensate aspect ratio using the tunable scattering length, but we have not tried this yet.

It is interesting to note that the energy anisotropy of the burst atom distribution can persist indefinitely in the magnetic trap due to the absence of thermalizing collisions. The density of the burst atoms remains very low throughout their motion in the trap. Simply put, the burst atoms do not form an equilibrium distribution! We may therefore be able to use the observed energy anisotropy to glean information about the history of the burst, i.e., the mechanism for the burst generation.

[1] Despite the fact that it was created under very different conditions, the short-pulse burst atom distribution had comparable number (∼3000) and average energy (∼150 nK) to the collapse burst.

In addition to their energy, another important characteristic of the burst atoms is their spin-polarization. From the observed occurrence times and spatial locations of the burst focuses, we can infer that the oscillation frequency of the burst atoms corresponds to the $|F, m_F\rangle = |2, -2\rangle$ state, which is the same as that of the BEC atoms. We looked for any additional burst atoms in other spin states with comparable energies to those of the $|2, -2\rangle$ atom burst. This was done by reducing the total time delay before taking an absorption image to the rather short value of 2.1 ms. Since our absorption imaging is sensitive to all spin states of ^{85}Rb [1], the short delay time should allow us to count burst atoms *not* in the $|2, -2\rangle$ state before they could expand appreciably. We saw no evidence for any such "extra" burst atoms in other spin states — our experimental sensitivity was ∼500 atoms, or 8% of the $|2, -2\rangle$ burst number. This observation indicates that the burst generation mechanism does not involve Zeeman spin flip transitions.

We have found that the rapid magnetic field variations only create burst atoms from Bose-Einstein condensates and not from cold thermal clouds. We searched for burst atoms after subjecting a 40 nK thermal cloud with density $< n >= 7 \times 10^{11}$ cm^{-3} to a standard B-field pulse, but we did not observe any trace of a burst. The absence of the burst may have been due to a strong density-dependence in the burst formation process, or perhaps the burst cannot be formed from a thermal cloud at all. For instance, the observed burst formation from a BEC might depend on the fact that the atoms are initially all in the same ground state of the harmonic trap instead of being distributed over many trap states, as in a thermal cloud. Since we have not repeated the experiment with condensates that have similar density to the thermal cloud, we cannot presently distinguish between the two possibilities.

5.4.2 Burst dependence on pulse shape

As a complement to the experiments on BEC number loss described in Section 5.3, we carefully examined the dependence of the burst properties on magnetic field pulse

shape. We first studied the burst number and energy as a function of the B-field pulse length, as shown in Figure 5.7. Here we see N_{burst} smoothly grows with increasing t_{hold} before saturating at roughly 4000 atoms. During the same time period, the average axial energy of the burst atoms shows a significant decrease from 200 nK to 100 nK. We did not measure the radial energy of the burst atoms for these conditions, but we assume that this energy obeys a similar time dependence.

One possible mechanism for the burst energy that was initially quite appealing to us is the sudden increase in mean-field energy due to the change in scattering length during the fast B-field pulse. The idea is that the BEC suddenly finds itself far from equilibrium due to the dramatically increased repulsive interactions. After completion of the first magnetic field ramp, the BEC should therefore immediately start to expand as the increased mean-field energy (potential energy) converts into kinetic energy. Ramping back to the initial B-field before the expansion has proceeded very far should halt the process by removing the excess potential energy.

To investigate the validity of the mean-field impulse hypothesis, we again utilized the PG model. With the magnetic field pulse of Figure 5.7 as input to the model, we determined the time dependent scattering length and integrated the PG model equations. The prediction of the PG model for the amount of mean-field energy that is converted into kinetic energy is shown in the inset to part **(b)** of Figure 5.7. Not only is the magnitude of the predicted impulse energy far too small, but it also shows the opposite time dependence to that observed in the data. There is simply not enough time for the increase in mean-field potential energy to be converted into significant kinetic energy.

Although the changing mean-field energy of the BEC clearly cannot explain the hold time dependence of burst energy, the energy for burst formation certainly must be related to the time-varying magnetic field. For the data in Figure 5.7, the most energetic burst atoms are produced by the shortest values of t_{hold}, which correspond to the B-field pulses that are closest in shape to a spike or triangle pulse. Perhaps

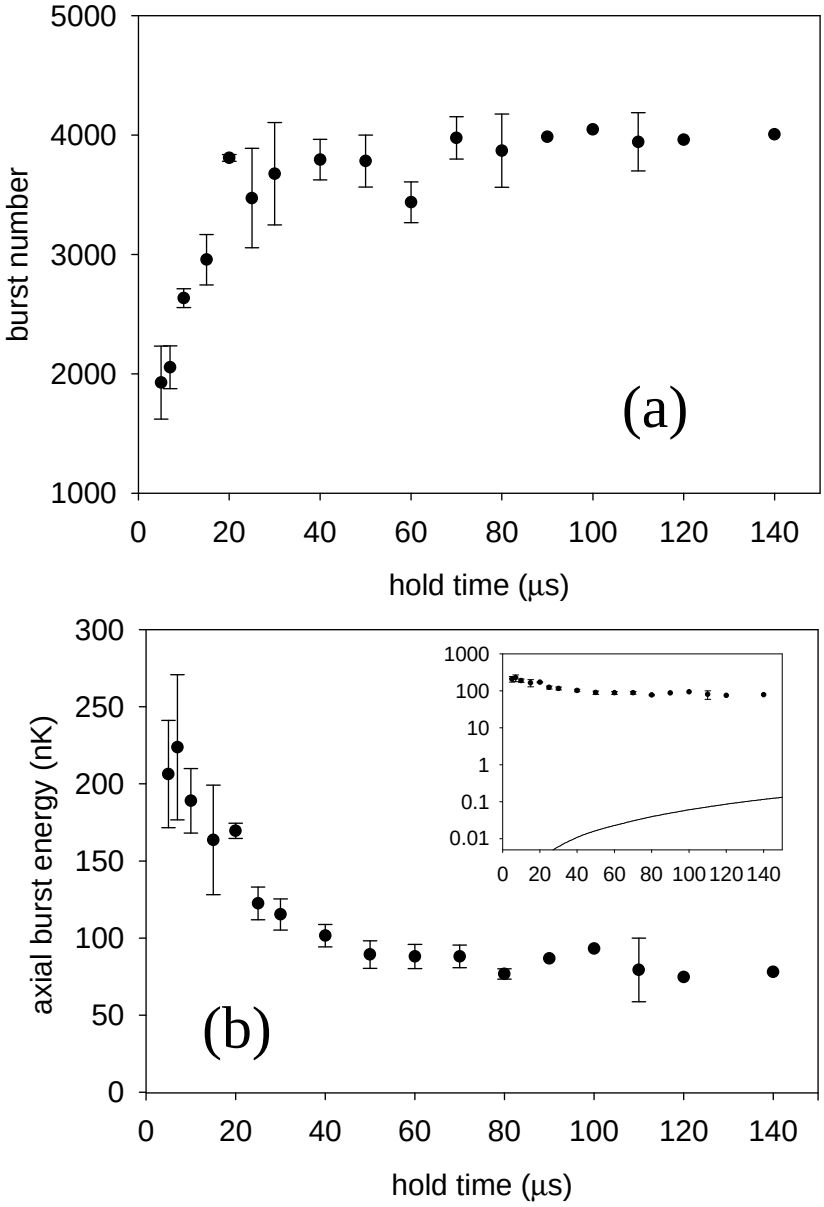

Figure 5.7: Dependence of burst characteristics on pulse length. **(a)** Burst number versus pulse length. Black points with error bars are the measured number of burst atoms versus hold time for a trapezoidal pulse. In this pulse, the magnetic field was ramped in 13μs from $\sim$165.5 G to B_{hold}=157.12 G (1840 a_0). After the completion of the hold time, the B-field was ramped back to roughly 165 G. **(b)** Burst energy versus pulse length. Black points with error bars are the measured average burst atom energy in the axial direction. The inset shows the same data plotted on a log scale for the y-axis. The black line is the PG model prediction for the mean-field impulse energy imparted to the BEC.

there is some relationship between the Fourier transform of the pulse and the energy imparted to the burst atoms. Murray Holland is conducting simulations to investigate this idea for the burst energy dependence on pulse shape [55] using a quantum field theory approach [56]. Some discussion of this theory will be given in section 5.5.4.

5.4.3 Burst dependence on pulse amplitude

The characteristics of the burst atoms produced by the magnetic field pulses also displayed a strong dependence on the pulse amplitude. Figure 5.8 gives the measured variation of both N_{burst} and average radial burst energy versus pulse height. In this figure, we combine data from two slightly different magnetic pulses. The black points were taken with a ramp time of 100 μs and hold time of 1 ms, while the white points had t_{ramp}=50 μs and t_{hold}=200 μs. We believe it is reasonable to plot the B-field dependent data for these two different pulse shapes on same graph because both pulses were sufficiently long so that the burst should have reached "steady state" values for the number and energy, as observed in Figure 5.7.

The burst number shows very little magnetic field dependence over most of the range given in part **(a)** of Figure 5.8. From ∼155 G to 159 G, the number of atoms in the burst remains fairly constant. However, N_{burst} decreases very sharply as B_{hold} rises above ∼159 G. For pulses with values of the hold B-field greater than 160 G, we did not observe any burst atoms.

In contrast to the saturating dependence of the burst number with B-field, the average radial energy grows in a linear fashion with increasing pulse amplitude (decreasing B_{hold}). This behavior continues all the way down to magnetic fields very near the Feshbach resonance at 155 G. It would be interesting to see whether the linear trend continues past 155 G, because this would imply that the burst formation has relatively little to do with the Feshbach resonance. We note that the average axial burst energy depends on magnetic field in a similar fashion to the radial energy, but the axial energy

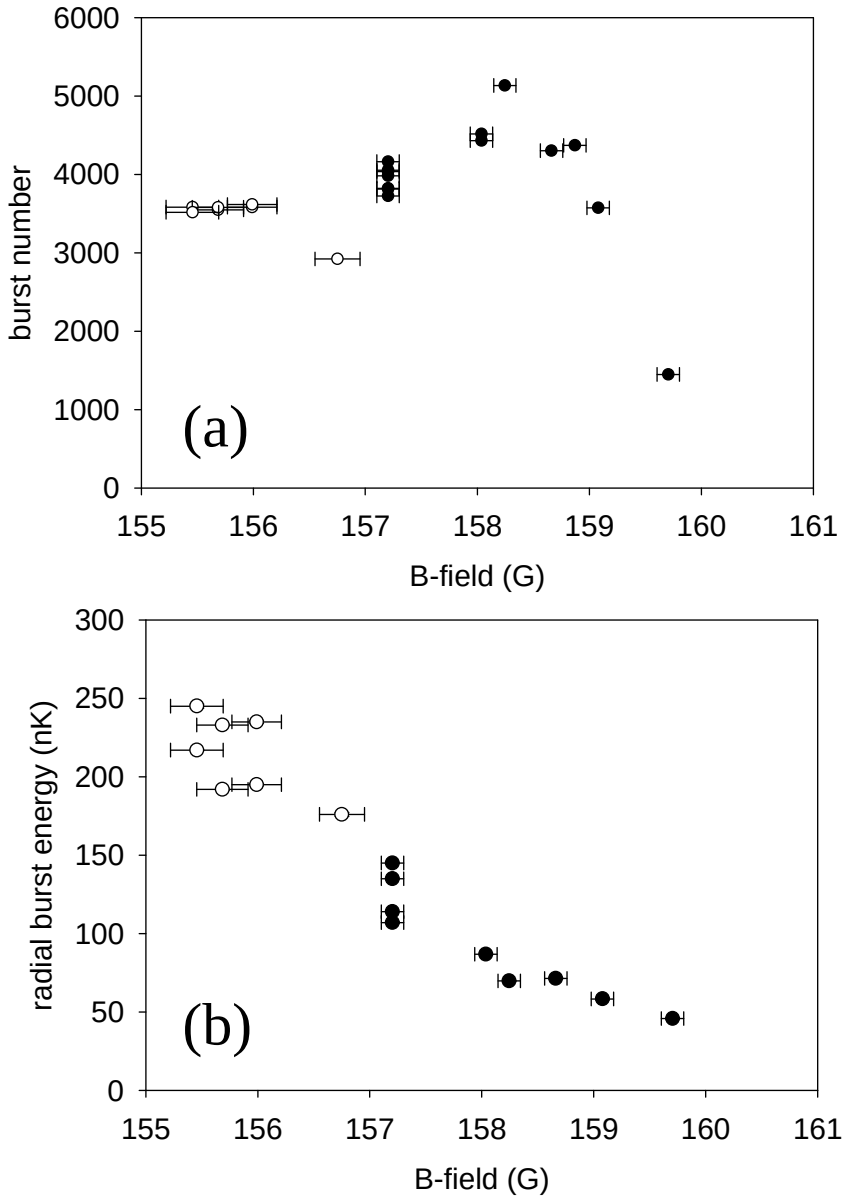

Figure 5.8: Dependence of burst properties on B-field pulse amplitude. **(a)** Number of atoms in the burst versus B_{hold} for an initial field B_{init} ∼166 G. Black points with error bars are the number of atoms measured in a radial burst focus after a trapezoidal pulse with t_{ramp}=100 μs and t_{hold}=1 ms. White points show the burst number generated by a slightly different B-field pulse shape with t_{ramp}=50 μs and t_{hold}=200 μs. **(b)** Average radial burst energy as a function of pulse amplitude, for the same B-field pulses as in part **(a)**.

is consistently about a factor of 2 smaller in magnitude (the axial energy data were omitted to improve the clarity of Figure 5.8).

5.4.4 Search for secondary collision mechanism

In an attempt to explain some of the observed burst properties, we looked for evidence that the burst atoms might be generated by secondary collisions with "super-hot" (∼0.1 to 1 mK) atoms. Beijerinck and co-workers [57, 58] have proposed that the energetic decay products of 2- and 3-body collisions might cause considerable heating of a BEC if these super-hot atoms collide with the near-stationary BEC atoms while exiting the cloud. The density-dependent inelastic decay rates are highest in the dense central region of a condensate, so the decay products usually must travel through a significant region of space containing many BEC atoms before escaping. If the cross-section for collisions with BEC atoms is high enough, there should be many secondary collisions during this time. The authors in Ref. [58] also suggest the possibility that the secondary collision products may also collide with the BEC atoms, leading to a sort of positive-feedback or avalanche effect.

Originally, these ideas seemed somewhat plausible to us. After the fast B-field pulses, we had observed missing atoms, burst atoms, and the BEC remnant. We suspected that the missing atoms might correspond to the super-hot inelastic decay products while the burst atoms could be created in secondary collisions. We believed that we should be able to test this possible burst generation mechanism by varying the elastic cross-section of the BEC atoms after producing a bunch of super-hot atoms.

To test the secondary collision hypothesis, we devised a special B-field pulse consisting of an initial brief triangular spike followed by a long plateau with an adjustable height (see Figure 5.9). The idea was to generate the hot 3-body recombination products during the brief spike toward the Feshbach resonance, then to alter the s-wave elastic cross-section, $\sigma_s = 8\pi a^2$, by changing the level of the plateau. If the burst atoms

were coming from secondary collisions, then we should be able to strongly influence the number and energy of the burst by varying the plateau scattering length.

Unfortunately, the BEC number loss and burst data resulting from the spike/plateau pulse did not allow for a conclusive test of the hypothesized burst generation mechanism. For instance, while N_{burst} did grow as the plateau scattering length was increased, the average burst energy was reduced. In addition, the total number of missing atoms increased with increasing plateau scattering length. This means that we cannot obtain a consistent secondary collision picture because it is impossible to say that the super-hot atoms were only generated during the initial brief spike part of the pulse. Also, the observed values for the burst energy $\langle E_{burst} \rangle \simeq 100$ to 200 nK seem far too small for the predictions of the secondary collision model. If the posited super-hot atoms really have energies of 100 to 1000 μK, then it is difficult to understand how they could impart such a tiny fraction of their energy to the burst atoms. Due to the difficulties with the secondary collision mechanism, we decided to abandon these studies. While there may be some 3-body recombination and subsequent secondary collisions occurring in our short B-field pulse experiments, we believe that most of the observations can be explained in terms of non-adiabatic transitions to another state, as described in section 5.5.

5.5 Modeling BEC loss and burst production

The observed time dependence of the BEC number loss from magnetic field pulses suggests the presence of non-adiabatic transitions to another state. In our case, the obvious candidate for this other state is the weakly-bound molecular state that causes the Feshbach resonance. At B-fields larger than the resonant value of 155 G, the molecular bound state lies just below the zero-energy threshold for two colliding BEC atoms. As one decreases the magnetic field to values below 155 G, the molecular state rises above threshold and becomes a quasi-bound state with a finite lifetime due to coupling with a continuum of scattering states with finite collision energy. These considerations suggest

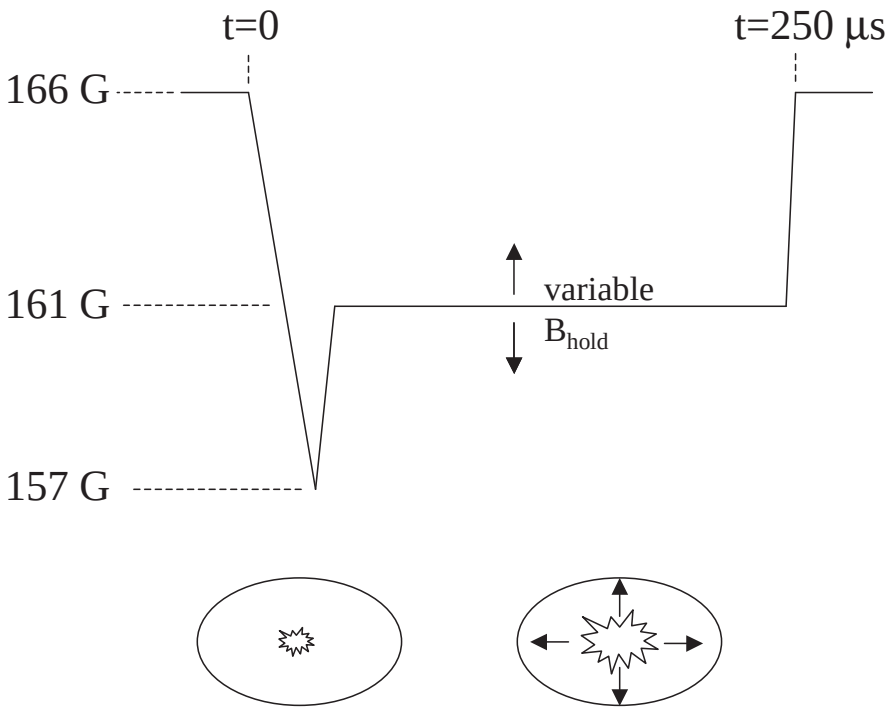

Figure 5.9: Schematic of the B-field pulse for testing the secondary collision mechanism. At top, we show the time-dependent magnetic field during the pulse. The total length of the spike part of the pulse is 50 μs and the plateau length is typically 200 μs. The lower part of the figure displays a simplified picture of the secondary collision mechanism proposed in the text. The ellipses show the condensate spatial extent. In the condensate at left, the explosion represents hot products of 3-body recombination. The next BEC picture shows the expansion of these decay products into the BEC volume during the B-field pulse plateau.

the possibility of modeling the Feshbach resonance as an avoided crossing of the atomic and molecular states, as in the well-known Landau-Zener (LZ) model. In this section, we discuss a simple "toy" model for the Feshbach resonance to gain some qualitative understanding of our experimental data. To improve upon the toy model, we also consider a more elaborate curve-crossing model from Josh Dunn and Chris Greene that includes many trap states. Finally, we give a brief review of published atom-molecule coupling theory as it applies to our data, including theory work from JILA (Servaas Kokkelmans and Murray Holland) and Oxford (Kohler, Gasenzer, and Burnett).

5.5.1 Toy Landau-Zener model for BEC loss

In an attempt to understand the BEC number loss in terms of non-adiabatic transitions, we developed a simple toy model for the Feshbach resonance. Although the model is totally useless for quantitative comparison with experiment, it does provide some insight into the time dependence of the BEC loss for various magnetic field pulses. By investigating the limitations of the toy model, one can learn more about the real physics of the Feshbach resonance. For instance, one major flaw of the toy model is its neglect of the burst atoms. In the toy model avoided crossing (see Figure 5.10), there are only two states – the initial colliding atom state and the molecular state. These states are coupled by an off-diagonal matrix element in the Hamiltonian so that transitions between the atomic and molecular states are possible. Using this model, one might postulate that the BEC number loss observed in the experiment is due to the formation of molecules (the "missing atoms"), but then how do the burst atoms fit into the picture? In fact, the burst atoms do not fit into a two-level picture at all! This point caused us considerable confusion when we first observed the burst atoms and were unable to identify them with a particular state of the 2-level toy model. The burst atoms can only be explained in terms of excited states with higher energy than the BEC ground state. The excited states may form a series of discrete levels of the harmonic

trap or a continuum of states if the trap is neglected.

Before calculating transition probabilities with the toy model from a pulsed magnetic field, it is illuminating to review the standard Landau-Zener theory. Let us assume that the initial state of the system is a stable BEC of atoms at a magnetic field above the Feshbach resonance. This initial condition corresponds to a probability of unity of being in the colliding atom state of the toy model (the upper dashed line to the right of the avoided crossing in Figure 5.10). For a single linear ramp through the avoided crossing, the probability of making a non-adiabatic transition from one adiabatic or dressed state to the other is [59, 60]

$$p = \exp\left(-2\pi\frac{\omega_0^2}{4\dot{\omega}}\right), \tag{5.1}$$

where ω_0 is the coupling matrix element divided by $\hbar$ and $\dot{\omega}$ is the time rate of change of the detuning between the uncoupled atomic and molecular states. The single-passage transfer probability becomes smaller as the ramp rate decreases, so that an infinitely slow ramp produces zero transition probability. In the toy model, this infinitely slow, adiabatic ramp causes the atomic state to smoothly change into the molecular state while gaining potential energy from the magnetic field. In contrast, a very fast ramp through the crossing leads to a large non-adiabatic transition probability p$\simeq$1, so the state of the system during the ramp is best described by the uncoupled atomic state, shown as the horizontal solid line in Figure 5.10.

For our pulsed magnetic field experiments, a much more relevant case to consider is that of a double passage through the avoided crossing, in which the field is ramped linearly from far above resonance to far below resonance, then back again. In the limit that the initial, intermediate, and final detunings are infinitely far away from resonance, the probability of making a non-adiabatic transition from the upper dressed state to the lower dressed state is

$$P_{double} = 2p(1-p), \tag{5.2}$$

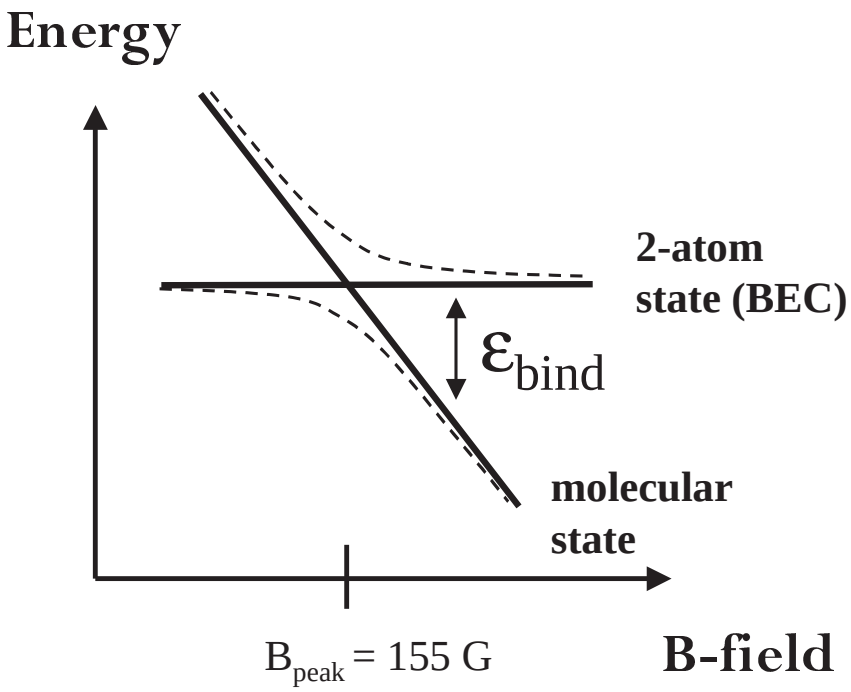

Figure 5.10: Toy model for ^{85}Rb Feshbach resonance. Here the resonance is represented as a simple avoided crossing of two states: the zero-energy state of two colliding BEC atoms and the molecular state (solid lines). The different magnetic moments of the two states cause them to cross at 155 G, but this degeneracy is broken by a weak coupling between the states. The adiabatic or dressed state eigenvalues of the total Hamiltonian are shown by the dashed lines.

where p is the single-pass transition probability from equation (5.1). The structure of this equation leads to a very different time dependence of the transition probability. For fast ramps (short magnetic field pulses), the single-pass probability is near unity, so that P_{double} is almost zero. The state of the system during the entire pulse is approximately that of the uncoupled or diabatic atom-atom state. The opposite condition of very slow ramps (long magnetic field pulses) causes p→0, which again leads to a vanishingly small value for P_{double}. In this case, the atoms "ride along" the adiabatic energy level during the pulse before coming back to where they started at the beginning. The only way to get a significant double-pass transition probability out of the initial state is to use intermediate ramp speeds such that p has an intermediate value between 0 and 1. In fact, the largest transition probability is obtained for p=1/2. The different time dependences for single- and double-passages through resonance are shown graphically in Figure 5.11 for a particular choice of the avoided crossing parameters.

5.5.2 Modifying the LZ model for triangular B-field pulses

After discussing the standard LZ model predictions in the context of the toy model for the Feshbach resonance, we are now in a position to explore the effect of *finite* B-field pulses. In the actual experiment, we mostly use magnetic field pulses that approach, but do not cross the Feshbach resonance B-field of 155 G. To predict the effects of such a pulse in the toy model, it is necessary to move beyond the simple LZ analytical expressions presented above. To do this, we use the concise formulation of a standard avoided crossing from Ref. [61]. We numerically integrate the coupled Schrodinger equations for the two-level system and calculate the non-adiabatic transition probability. The numerical integration allows us to simulate various differently-shaped B-field pulses subject to the initial condition that all of the probability resides in the atomic state corresponding to a pair of BEC atoms.

We observe that the behavior when the B-field approaches and then backs away

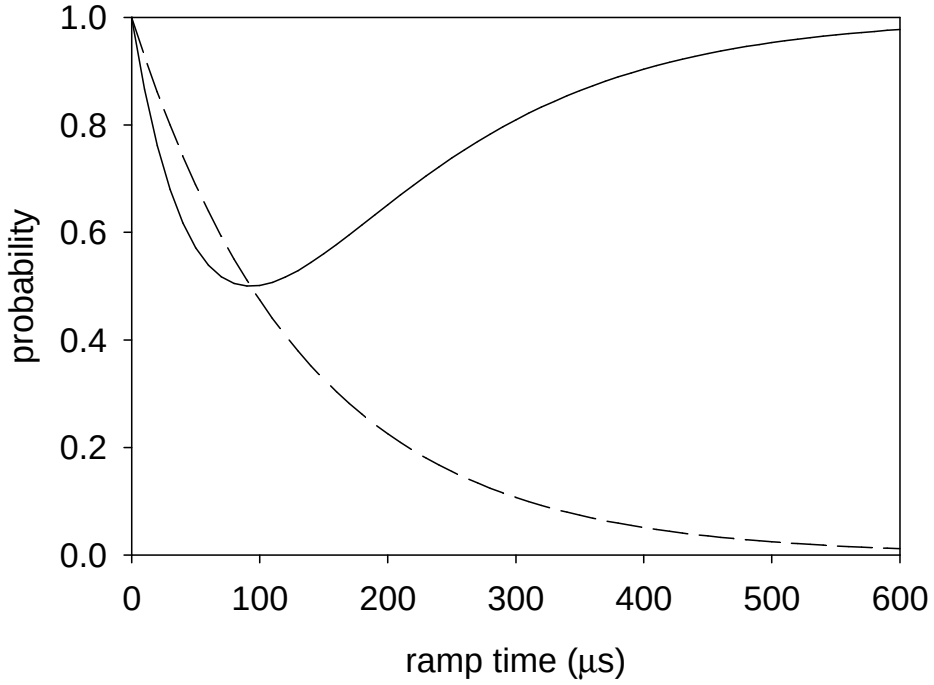

Figure 5.11: Comparison of the Landau-Zener model predictions for single- and double-passages through an avoided crossing. The dashed line is the non-adiabatic transition probability, p, as a function of ramp time for a single-passage through resonance. In the context of the toy model, the dashed line gives the probability of remaining in the atomic state after the ramp. The solid line is the quantity 1-2p(1-p), which corresponds to the probability of remaining in the atomic state after sweeping over resonance and coming back. Although both predictions show a decrease in probability as the ramp time increases from zero, the minimum in the double-passage probability versus ramp time leads to a strikingly different time dependence for longer, slower ramps. For both the dashed and solid line predictions, the B-field is swept so that the detuning changes by $|\Delta\omega| = 4.3 \times 10^8$ s^{-1} during the ramp time and the coupling strength is fixed at $\omega_0 = 1.4 \times 10^6$ s^{-1}.

from the crossing point with a triangular pulse is qualitatively similar to the more familiar double-passage case discussed previously.[2] As shown in Figure 5.12, the finite B-field pulses still produce a minimum in the probability remaining versus pulse ramp time. However, the depth of the probability minimum depends strongly on the approach distance to resonance and is generally less than for the infinite ramp case. This behavior can be understood in terms of the magnetic field width of the avoided crossing, defined as the ratio of the coupling strength to the slope of detuning with B-field: $\omega_0/(d\omega/dB)$. The transition probability goes up as the pulses penetrate more deeply into this strong coupling region. Another notable difference between the finite B-field pulse result and the infinite double-passage result is the ramp time at which the minimum occurs (Δt_{min}) . For finite pulses, the probability minimum occurs at a ramp time that is proportional to the inverse of the squared dressed state splitting at closest approach. The dressed state splitting decreases as one approaches resonance, so that Δt_{min} becomes larger. It is very interesting to observe these trends in the toy model because the same qualitative features are observed in the experimental data for triangular B-field pulses (see Figure 5.3). In those data, the number remaining in the condensate after a triangular pulse toward resonance has a clear minimum as a function of ramp time. The depth and position of the minimum vary with approach distance to resonance, as in the toy model.

Given the qualitative agreement between the toy model predictions and the triangle pulse experimental data, one might hope to make a quantitative comparison or even try to fit to the data. In principle, this would allow a determination of the appropriate Feshbach resonance coupling strength and relative magnetic moment between the atomic and molecular states. However, all of our attempts to fit the toy model to

[2] Even when the B-field pulse does cross resonance, there is one conspicuous difference between the numerical integration and the LZ prediction – the integration yields large amplitude, high frequency probability oscillations, called Stückelberg oscillations, as a function of the ramp time. The LZ model expression 2p(1-p) is a result of phase-averaging over these rapid oscillations. Stückelberg oscillations were never seen in the experiment.

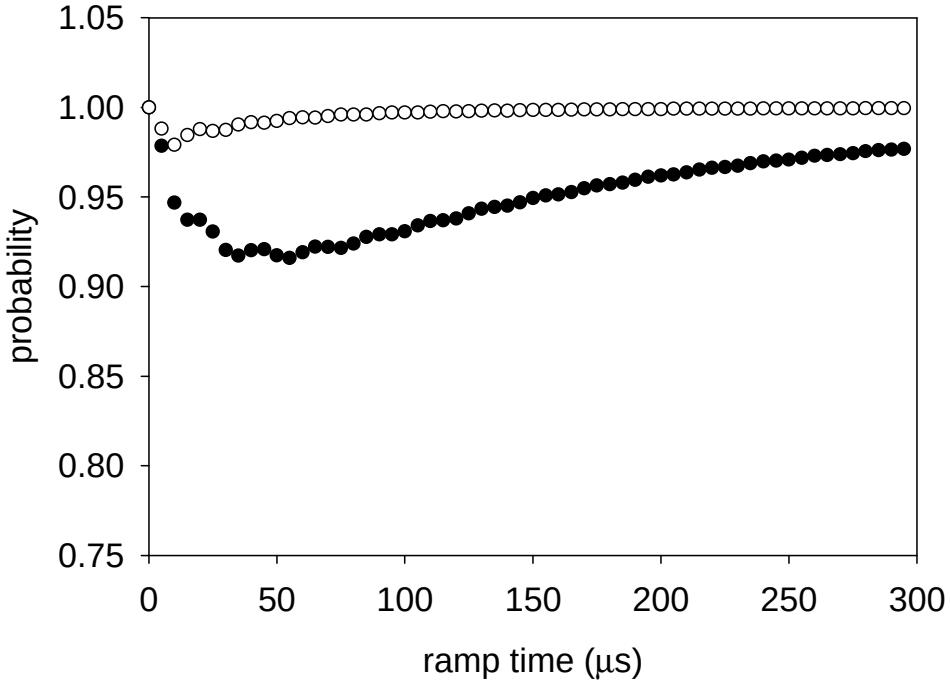

Figure 5.12: Toy model predictions for finite magnetic field pulses. The probability of remaining in the initial atomic state is shown versus ramp time for a triangular pulse. The conditions are B_{cross}=155 G, B_{init}=165.6 G, and B_{pulse}=158 G (white points) and 156 G (black points). The coupling strength and relative magnetic moment between the atomic and molecular states are (arbitrarily) set to be 11 kHz and 7.6 kHz/G, respectively. We are unable to obtain quantitative agreement with the experimental data of Figure 5.3 even when we allow these two parameters to float freely.

the data have failed. We find that the toy model does a rather bad job at reproducing quantitative features of the data, even when we allow the coupling strength and relative magnetic moment between the two states to be arbitrary parameters in the numerical simulation. In addition, the production of the burst atoms in the experiment cannot be explained by the two-level toy model. It is clear that a more sophisticated avoided crossing theory is needed to accurately model the real Feshbach resonance.

5.5.3 A better avoided crossing model

Josh Dunn, Chris Greene, and coworkers developed a fairly simple theory of the ^{85}Rb Feshbach resonance [62, 63] (see also Ref. [64] for related picture) that has several advantages over the toy model discussed above. They model the Feshbach resonance as a series of avoided crossings between the resonance state (molecular state) and the eigenstates of the harmonic trapping potential. In the context of the Dunn/Greene model, one can see how a B-field pulse toward resonance could generate burst atoms. Because the molecular state is coupled to *many* trap states, the molecular state can serve as an intermediate state for transitions from the lowest trap level (BEC) to the excited levels. This provides a potential mechanism for the production of burst atoms in the experiment. While this model has some appealing features, we have not successfully applied it to the Feshbach resonance data discussed in Section 5.3 and Section 5.4. Here we provide a brief discussion of the model and its limitations.

The Dunn/Greene theory is based on the exact quantum mechanical description of a pair of harmonically-trapped atoms that interact via a short range (δ function) potential characterized by the scattering length, a [65]. While the δ function potential is an approximation to the real one, this approximation is justified when the atoms collide at low energy so that their deBroglie wavelength greatly exceeds the range of the physical potential. This means that the scattering length is sufficient to describe the interaction between pairs of condensate atoms. For the atom pair, the total Hamiltonian

can be broken into two parts — one for the center-of-mass motion and one for the relative motion. Since the relative motion Hamiltonian describes the atomic collisions, this part contains the interaction potential that depends on the scattering length. The eigenvalues of the relative motion Hamiltonian are simply the standard harmonic oscillator levels, but shifted according to the sign and magnitude of a. At positive scattering length or repulsive atom-atom interaction the energy levels are shifted upward. The opposite is true for negative a. Because the Feshbach resonance causes a large variation in a with magnetic field, the eigenvalues of the atom pair show a pronounced B-field dependence, as shown by the solid lines in Figure 5.13.

The actual calculation of the energy eigenvalues of the interacting atom pair involves solving a transcendental equation containing the energy and B-field-dependent scattering length. One can solve the equation iteratively or graphically, but there is no analytic expression for the eigenvalues as a function of magnetic field. Since this is rather cumbersome for predicting transition probabilities when the B-field is ramped near resonance, the authors of Ref. [62] create an approximate model Hamiltonian in which the molecular state undergoes repeated avoided crossings with all of the harmonic trap states. The uncoupled molecular state energy is assumed to vary linearly with B-field and the coupling matrix elements to the excited trap states obey the Wigner threshold law [52] ($\omega_0 \propto \sqrt{E}$). By adjusting the parameters of the model Hamiltonian and diagonalizing it, one can obtain very good agreement with the exact eigenvalues over a small range of magnetic field close to the Feshbach resonance (see part **(a)** of Figure 5.13). However, the agreement becomes quite terrible as the B-field increases by a few tenths of a Gauss above the resonance. The disagreement clearly shows that the curvature in the molecular bound state energy is *not* due to a simple coupling with the trap states! In fact, the binding energy curvature is very strong even outside the B-field region where the trap states mix strongly with the molecular state. In the exact solution to the interacting atom pair, the binding energy curvature is determined by

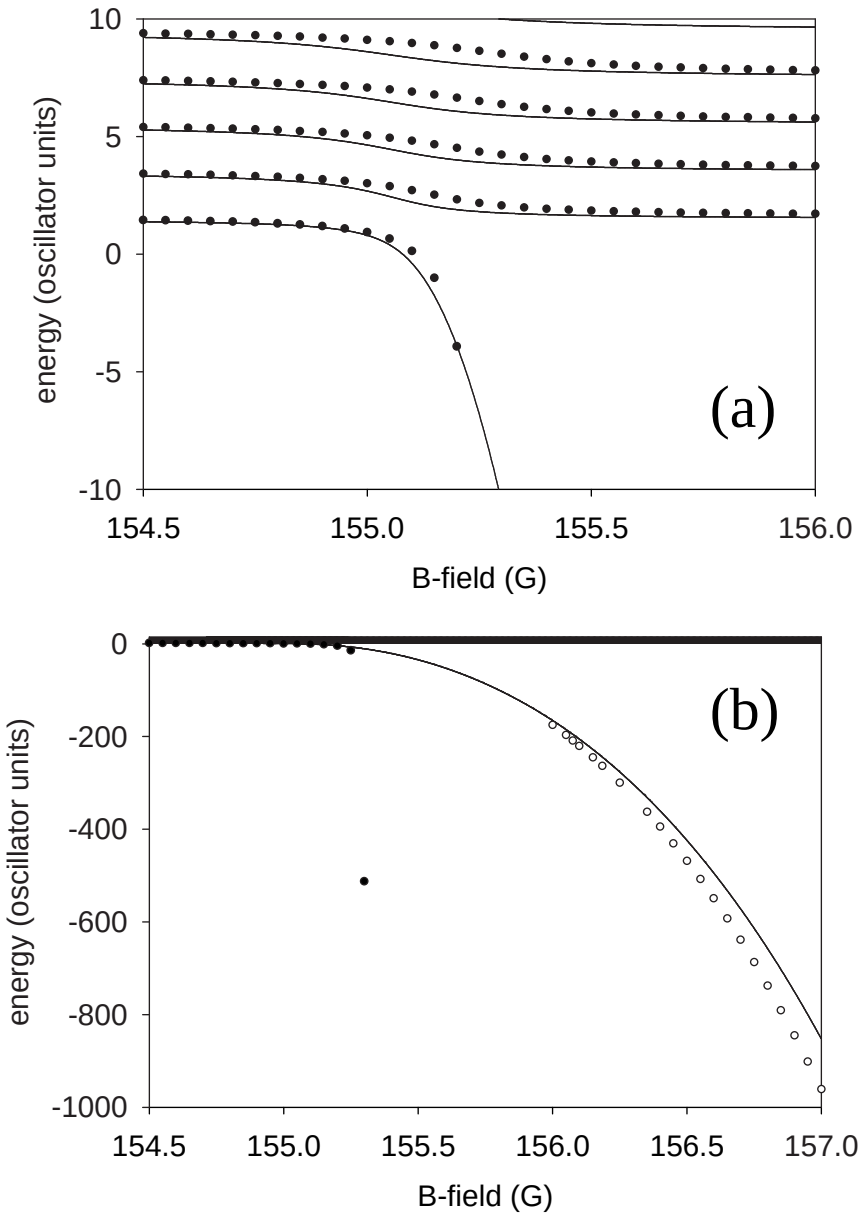

Figure 5.13: Energy eigenvalues versus B-field for an interacting atom pair near the Feshbach resonance. **(a)** Solid lines are the exact eigenvalues calculated by Josh Dunn. Black points are the eigenvalues of an approximate model Hamiltonian in which the diabatic bound state crosses zero energy at 155.3 G with a slope of -244,108 $\hbar\omega$/G. The coupling matrix elements are equal to (113 $\hbar\omega$) $\mathrm{n}^{1/4}$, where $n \geq 1$ is the quantum number of a given excited state. The agreement between the model Hamiltonian and the exact solution is quite good near resonance. **(b)** Same as in **(a)**, but with a larger energy and magnetic field range. Here the molecular bound state (solid line) lies well below the excited trap states, which are visible as a thick bar of black at the top. White points are the bound state energies from a coupled-channels calculation by Servaas Kokkelmans. These calculations agree quite well with the eigenvalues from the atom-pair model. However, the model Hamiltonian eigenvalues (black points) disagree very strongly with both the atom-pair model and the CC calculation over this B-field range.

the variation of scattering length with B-field.

Because of the failure of the model Hamiltonian to reproduce the molecular binding energy curve over the relevant magnetic field range, we have not attempted to model the effects of the experimental B-field pulses with the approximate Hamiltonian of the Dunn/Greene model. In the experiment, the pulses typically jump from ∼166 G to ∼156 G. This magnetic field range corresponds to the region where the model Hamiltonian from Ref. [62] fails to accurately describe the energy difference between the atomic and molecular states. Another potential obstacle to modeling the number loss and burst formation is the large number of trap states that we would need to include. Since the burst energy is of order 100 nK or 2 kHz, we expect that the number of trap states required would be roughly $\mathrm{E}_{burst}/\hbar\omega = 2\ kHz/12.7\ Hz \simeq 160$. However, calculating transition probabilities to a large number of trap states might not be necessary; one alternative is to reduce the number of states by changing the trap frequency used in the model (and adjusting the coupling matrix elements accordingly). We believe this would be justified because the exact structure of the harmonic trap potential should not affect the details of the non-adiabatic transitions, which occur on a time scale far shorter than an actual trap oscillation period. In the future, it may be possible to devise an improved model Hamiltonian that would allow one to predict the dependences of the experimental observables on the magnetic field pulses. Another possibility would be to find a way to integrate the Schrodinger equation using the exact eigenvalues from the transcendental equation in the Dunn/Greene model. Whether or not the BEC number loss and burst formation can be understood quantitatively in terms of simple 2-body interactions remains to be seen.

5.5.4 Modeling the resonance physics with quantum field theory

Servaas Kokkelmans and Murray Holland have developed a quantum field theory to describe the physics of near-resonant ^{85}Rb BEC [56, 9]. This theory has been highly

successful in describing the atom-molecule coherent oscillation experiments of Chapter 6, so it is reasonable to expect good agreement with the single pulse observations of the present Chapter. However, a detailed comparison between theory and single pulse data has not yet been made.

The Kokkelmans/Holland theory moves far beyond the level of the two-body scattering models discussed in the previous sections. In this theory, the BEC is described by a mean-field theory that includes pair correlations between atoms. Although all correlations between atoms are usually neglected in the standard Gross-Pitaevskii equation, the authors of Ref. [56] argue that the pair correlations are essential for understanding the BEC physics near a Feshbach resonance. The resonant two-body scattering physics is accurately contained in the effective field theory, where atomic and molecular field operators describe the open and closed channel states of the Feshbach resonance. The closed channel is coupled to a continuum of scattering states above the open channel threshold.

The effect of rapid B-field variations on the BEC can be determined by numerically solving the equations in Ref. [56]. As in the experiment, the model shows that a magnetic field pulse leads to number loss from the BEC. Most of the loss is due to formation of relatively hot noncondensate atoms (identified by Kokkelmans and Holland as the burst atoms). These noncondensate atoms are very strongly correlated because they are created as pairs of atoms with equal and opposite momenta ($\pm p$). Each pair of burst atoms can be viewed as a dissociated molecule. The model also predicts the creation of a fairly small number of bound molecules, which are assumed to be undetected or missing in the experiment. Focusing on the burst, the Kokkelmans/Holland theory predicts values for both the number and energy distribution of these atoms. The predictions for N_{burst} and E_{burst} agree quite well with the double magnetic field pulse experiments in Chapter 6 and we expect that the model will also accurately describe the single pulse experiments [55].

While the mean-field theory from Kokkelmans and Holland is conceptually much more complex than the avoided crossing models described previously, the field theory has the important advantage that it has successfully described the atom-molecule coupling in our double magnetic field pulse experiments. We will therefore provide more discussion of the Kokkelmans/Holland theory and its relationship to the experimental data in the next chapter.

A different quantum field theory for our BEC experiments was recently proposed by the Oxford theory group [16]. This theory shares some similar features with the Kokkelmans/Holland work, but the authors use a different method to incorporate the underlying two-body scattering physics into the many-body Hamiltonian. In addition, Kohler et al. examine the effect of a harmonic trapping potential on the physics of the atom-molecule coupling. Like the Kokkelmans/Holland theory, the theory of Ref. [16] yields a number of predictions that agree with experimental observables. More discussion of the Kohler et al. model will be postponed until Chapter 6.

Chapter 6

Atom–molecule coherence in a Bose-Einstein condensate

6.1 Introduction

The strange time dependence of BEC number loss described in Chapter 5 strongly suggested the presence of non-adiabatic transitions to an undetected molecular state. To further explore this loss process, we utilized a pair of carefully controlled magnetic field pulses, separated in time, in the vicinity of the Feshbach resonance.

The original motivation for the double B-field pulse sequence was to measure the BEC recovery time after a single pulse. We hypothesized that the first pulse would cause a large amount of 3-body recombination-induced number loss to the condensate. The abrupt increase in recombination should produce a multitude of tiny holes or voids in the BEC wavefunction. The sudden creation of voids would lead to condensate excitations because of the localized changes in the mean-field interaction potential [66]. One might ask the question of how long does it take for these voids in the BEC to refill as the surrounding atoms move in. Presumably the condensate recovery time could be determined by applying a second, identical B-field pulse shortly after the first one. One could increase the delay time between pulses until the 2nd pulse produced the same BEC loss as the first pulse; this delay time would define the recovery time and it should give information about the microscopic physics occurring inside the BEC. By measuring the BEC response on such short time scales, one might hope to find evidence for a breakdown in the predictions of mean-field theory.

However, the recovery time picture proved too simplistic. The main defect of this hypothesis lies in its assumption that the BEC number loss is incoherent; in contrast, we actually discovered that a significant part of the loss is due to coherent transfer to another state. We measured coherent oscillations in the BEC atom number as the spacing between the two magnetic field pulses was varied. The observation of coherent oscillations provides us with definitive evidence for coupling between the atomic and molecular states associated with the ^{85}Rb Feshbach resonance. These experiments demonstrate a remarkable quantum superposition between two distinct chemical species: free atoms and weakly bound molecules.

Although the single B-field pulse data from Chapter 5 also suggest that there is nonadiabatic mixing of the atomic and molecular states, these data were not as convincing as the results described here. The experiments discussed in this Chapter have led to a much more accurate theoretical picture of Feshbach resonances; in particular, the physical importance of the shallow s-wave bound state has become clear. As a result of our observations, the phenomenon of atom-molecule coupling and the role of the s-wave bound state in the dynamics of the near-resonant ^{85}Rb BEC have been explored recently by several theoretical groups [56, 16, 67, 68]. A discussion of the present agreement between experiment and theory will be given at the end of the Chapter.

6.2 Experimental methods

To study atom-molecule coherence, we first created ^{85}Rb condensates typically containing 16,500 atoms, with fewer than 1,000 non-condensed thermal atoms. The initial number, N_{init}, fluctuated from shot to shot by $\sim$500 atoms ($\sim$ 3% number noise). After producing a condensate at a B-field of 162.3 G, we ramped the magnetic field adiabatically to 165.5 G, corresponding to an initial scattering length $a_{init} \simeq 7\ a_0$. The spatial distribution of the atoms was Gaussian with a typical average atom density of $\langle n_{init} \rangle = 1.8 \times 10^{13}$ cm^{-3}. For some experiments where a lower initial density was

desired, the adiabatic ramp to 165.5 G was omitted so that the mean field repulsion at 162.3 G ($a_{init} \simeq 200\ a_0$) reduced the average initial density to $\langle n_{init} \rangle = 3.5 \times 10^{12}$ cm^{-3}.

After preparing the condensate, we applied a selected fast magnetic field pulse sequence by sending an appropriate time-dependent current through the auxiliary magnetic field coil. A representative set of double B-field pulses is shown in Figure 6.1. The sequence is composed of two nearly identical short trapezoidal pulses separated by a region of constant magnetic field (B_{evolve}). In our experiments, we varied the evolution time between pulses, t_{evolve}, from 0 to 400 μs, while B_{evolve} ranged from 162 G to 156 G. We determined the value of B_{evolve} between the two pulses using the short rf pulse technique described in section 3.3.3. We also found it useful to alter the initial magnetic field, B_{init}, to change the initial BEC density and distance from the Feshbach resonance. Usually, B_{init} was 162.3G or 165.5 G. We chose the B-field pulse amplitude so that the pulses always approached to within ∼2 G of the Feshbach resonance.

Upon completion of the fast-pulse sequence in Figure 6.1, we ramped the magnetic field from 165.5 G to ∼157 G in 5 ms and held the B-field constant for an additional 7 ms to allow the repulsive mean-field energy to expand the condensate (see section 3.5.3). Then we turned off the magnetic trap and used destructive absorption imaging 12.8 ms later to observe the condensate and burst atoms. Our detection scheme was not sensitive to atoms with kinetic energies larger than $\sim 2\ \mu$K nor to atoms in off-resonant molecular states.

As we observed for single pulses toward the Feshbach resonance, there were two distinct components of atoms visible in the absorption images and a third missing component that we could not detect. One of the observed components was a cold remnant BEC which was not noticeably heated or excited by the fast-pulse sequence (< 1 nK kinetic energy was imparted by the pulse sequence), while the other component was a relatively hot (∼200 nK) burst of atoms that remained magnetically trapped during the BEC expansion time. Using the PG model to simulate the mean-field expansion that

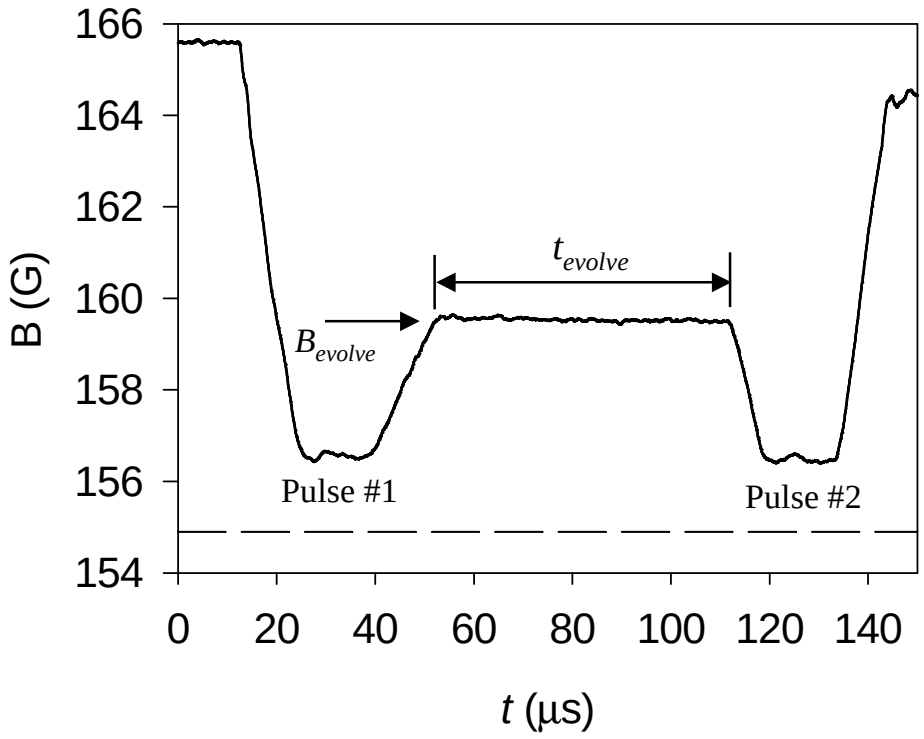

Figure 6.1: Magnetic field pulse shape. B-fields shown for pulses #1 and #2 correspond to scattering lengths of ∼3300 a_0, and the free precession field, B_{evolve}, corresponds to a scattering length of ∼600 a_0. The dashed line indicates the position of the Feshbach resonance, where the scattering length diverges to infinity. In the text, we refer to the free precession time as t_{evolve}. The average ramp time for most of the pulses was 14 μs.

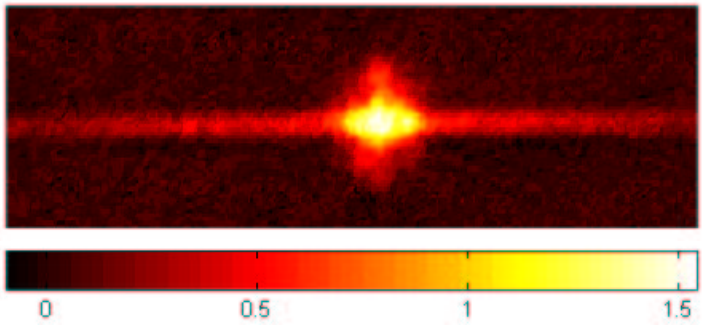

Figure 6.2: An absorption image taken after the fast magnetic-field pulse sequence and the mean-field expansion. The horizontal bar indicates the optical density. The horizontal and vertical directions coincide with the axial and radial axes of the trap, respectively. The dimensions of the image are 366×52 μm. The BEC remnant is the roughly spherical cloud at the center, while the burst atoms are focused into a thin line along the axial direction. There is a dramatic difference between the two spatial distributions, owing to the large difference in the mean energies of the burst and expanding BEC remnant ($\langle E_{burst} \rangle \simeq 50 \times \langle E_{rem} \rangle$).

we applied to the BEC remnant to measure its number, N_{rem}, we found that we should impart ≤ 3 nK expansion energy to the remnant before imaging. This estimate agrees well with the expansion velocity that we measured after the trap turn-off. Thus the remnant BEC was more than 60× colder than the burst. A typical absorption image of the atoms remaining after the double B-field pulses and time-of-flight expansion is shown in Figure 6.2.

To find the number of atoms in the remnant BEC and the number of burst atoms, we allowed the magnetic trap to focus the burst cloud before imaging. We fit the focused burst (which had a much larger spatial extent than the remnant) with a two-dimensional Gaussian surface, excluding the central region of the image that contained the remnant. This fit yielded the number of burst atoms, N_{burst}. Subtracting the fit from the image and performing a pixel-by-pixel sum of the central region of the image gave the remnant number, N_{rem}.

6.3 Observation of population oscillations

6.3.1 BEC and burst number oscillations versus $\mathbf{t}_{evolve}$

We observed large-amplitude oscillations in the number of BEC and burst atoms as we varied the delay time between magnetic field pulses. Representative number oscillation data for the condensate and burst atoms are displayed in Figure 6.3. The number oscillations were only visible after two B-field pulses; in fact, with only pulse #1 and the subsequent constant B-field but with no pulse #2, N_{rem} showed no variation except for a slow decay. The gradual decay rate of a few atoms per microsecond is consistent with the loss rate expected for a single pulse to the evolution magnetic field, as discussed in Chapter 5. Although we studied the oscillations under a wide variety of different conditions, we never observed the double-pulse value of N_{rem} to be larger than the single-pulse value, implying that each B-field pulse causes some incoherent or

irreversible loss to the BEC.

6.3.2 $N_{missing}$ oscillations

The BEC and burst atom oscillations in Figure 6.3 have very similar amplitudes and frequencies and they appear almost completely out of phase. N_{burst} grows larger when N_{rem} decreases, and vice versa. However, the measured phase shift between the two oscillations is actually 154(4)°, which is significantly different from 180°. Thus, the BEC and burst number oscillations do not exactly cancel out — if one calculates the total number of atoms, $N_{tot}=N_{rem}+N_{burst}$, this quantity also displays clear oscillations versus evolution time. As shown in Figure 6.4, the amplitude of the N_{tot} oscillations is significantly smaller than that of the other two number components.

Figure 6.4 clearly demonstrates that the time-averaged total number of atoms after the two B-field pulses does not equal the initial number of BEC atoms. There are a number of missing atoms, $N_{missing}$, and the measured oscillations in N_{tot} correspond to oscillations in $N_{missing}$. We therefore have evidence that some of the BEC atoms are oscillating into and out of a *different* state that is not detectable by the experiment. This phenomenon of oscillations to a state that is invisible to the detector may be compared to the well-known neutrino oscillations in astrophysics. We assume that the undetected state in our BEC experiment is the weakly bound molecular state of the Feshbach resonance.

As a side note, the data in Figure 6.4 were measured with fairly low-density condensates to minimize the number of missing atoms that do not oscillate and thereby allow for more atoms in the remnant BEC.[1] This improved the visibility of the remnant and the signal-to-noise ratio for the absorption images. To produce condensates with low density for these measurements, we altered the magnetic pulses somewhat from

[1] We observed that the B-field pulses always produce some missing atoms whose number does not oscillate with t_{evolve}. These atoms may or may not be converted into the weakly bound molecular state. In any case, we found that reducing the BEC density decreased the number of non-oscillating missing atoms. For further discussion of this point, see section 6.4.2.

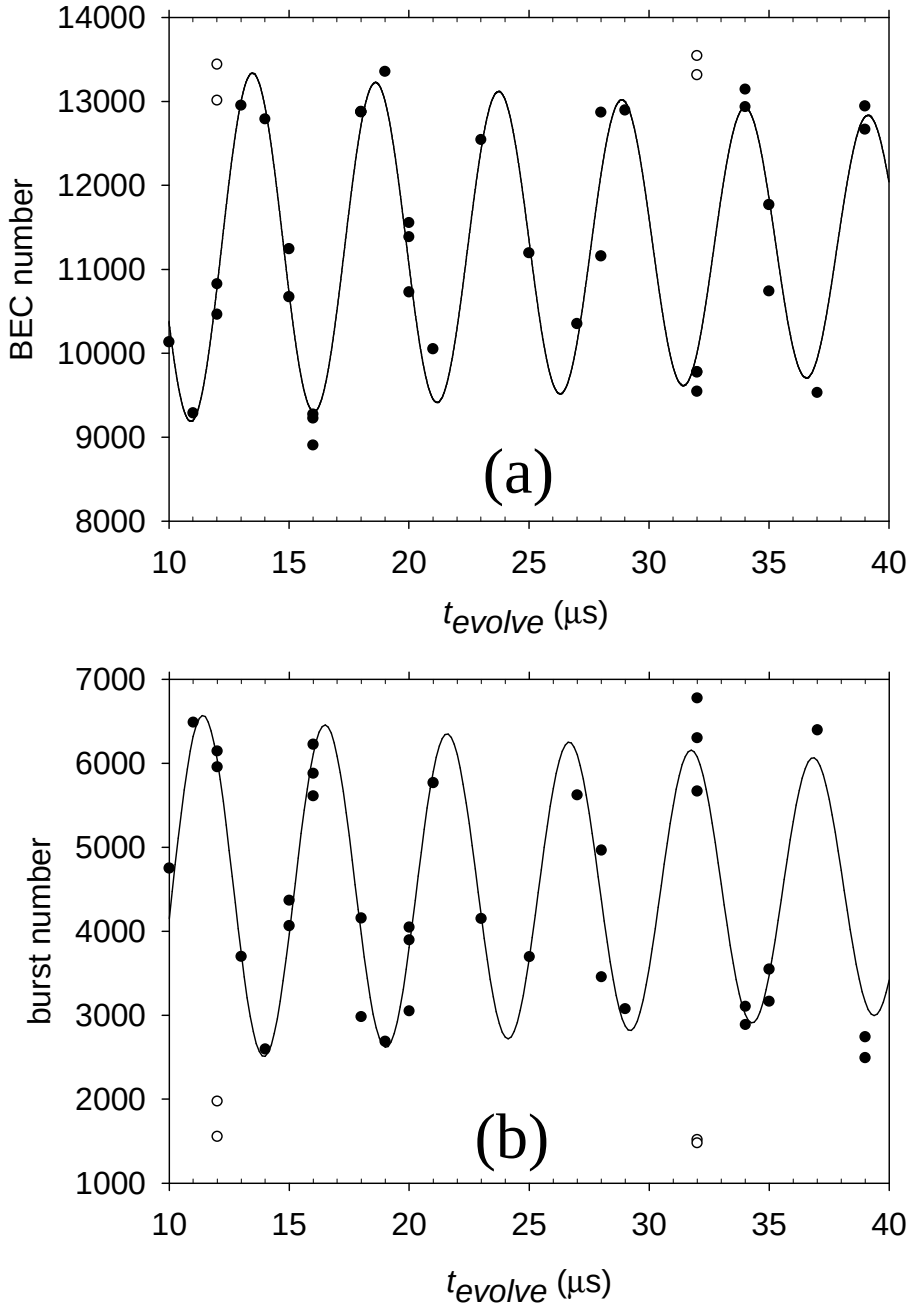

Figure 6.3: Coherent oscillations in BEC number and burst number. **(a)** Black points are the remnant BEC number, N_{rem}, versus evolution time, t_{evolve}, between the two magnetic field pulses. The solid line is a fit to the data using a damped sine wave with a frequency of 196(1) kHz and a damping rate of $11(4) \times 10^3$ s^{-1}. The open circles near $N_{rem} = 13000$ indicate the number remaining after only pulse #1 and t_{evolve} at 159.84 G. **(b)** Black points are the number of burst atoms versus t_{evolve}. The fit (solid line) yields an oscillation frequency and damping rate that are consistent with those from the fit to the BEC number in part **(a)**. The clear circles are the burst number measured after a single pulse plus a plateau at B_{evolve}. For the data in **(a)** and **(b)**, the initial BEC density was $\langle n_{init} \rangle = 3.5 \times 10^{12}$ cm^{-3} and B_{init}=162.25(5) G. The evolution B-field was B_{evolve}=159.84(2) G.

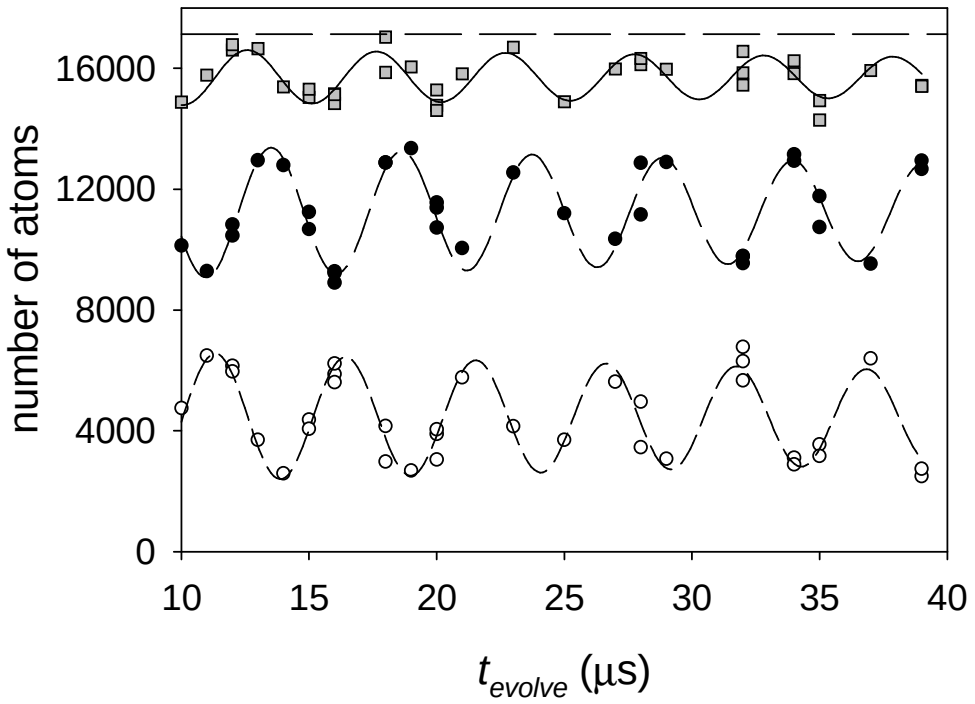

Figure 6.4: Number versus t_{evolve} for low density condensates ($\langle n_{init} \rangle = 3.5 \times 10^{12}$ cm^{-3}). From bottom to top, the data are N_{burst} (open circles), N_{rem} (filled circles), and the total number of observed atoms (gray squares). Each data set is fit by a damped sine wave as shown by the lines. Here the fitting function is $y = y_0 + A \exp(-t/\tau_{decay}) \sin(2\pi\nu_0 t + \phi)$, where ν_0 is the frequency and τ_{decay} is the decay time constant. The initial BEC number, $N_{init} = 17{,}100$, is indicated by the flat dashed line. The fit to the BEC remnant data gives an oscillation frequency of 196(1) kHz and $\tau_{decay} = 91(33)$ μs (the longer time data used to determine τ_{decay} are not shown).

the shapes shown in Figure 6.1. We set the initial magnetic field before the fast-pulse sequence to 162.25(5) G and reduced the amplitudes for pulses #1 and #2 to ∼7 G. The evolution B-field was B_{evolve} = 159.84(2) G. Under these conditions, the initial BEC density was relatively low: $\langle n_{init} \rangle = 3.5 \times 10^{12}$ cm^{-3}.

6.3.3 Oscillation frequency versus $\mathbf{B}_{evolve}$

Very strong evidence for the importance of the weakly bound molecular state to the observed BEC dynamics can be obtained from the magnetic field dependence of the number oscillation frequency. We have discovered that the oscillation frequency (ν_0) for the BEC, burst, and missing atom populations matches the binding energy of the molecular state: $h\nu_0$=$\epsilon_{\rm bind}$. We explored the B-field dependence of the oscillation frequency by applying different values of B_{evolve} during the evolution time between the magnetic field pulses. As shown in Figure 6.5, we mapped out ν_0 versus B-field over a ∼5 G range above the Feshbach resonance field of 155 G. The oscillation frequency varied by almost two orders of magnitude as B_{evolve} increased from 156.6 G to 162 G.

Along with the measured frequencies and magnetic fields, Figure 6.5 also displays theoretical predictions for the molecular bound state energy relative to the atomic state. One prediction, shown by the dotted line, comes from basic zero-energy scattering theory. In the regime where the scattering length is positive and much larger than the radius of the interatomic potential well, the bound state energy for an arbitrary attractive potential can be approximated by $\epsilon = -\hbar^2/ma^2$ [11], where $\hbar$ is Plank's constant divided by 2π, m is the atomic mass, and a is the scattering length. The same equation relates the bound state energy to the effective scattering length, which is calculated from the Feshbach resonance parameters through the relation $a = a_{bg} \times (1 - \frac{\Delta}{B - B_{peak}})$, where a_{bg} is the background scattering length, Δ is the width of the Feshbach resonance, and B_{peak} is the resonant magnetic field. The quantity $|\epsilon|/h$ is plotted with no adjustable parameters in Figure 6.5. The measured oscillation frequencies are in excellent agreement

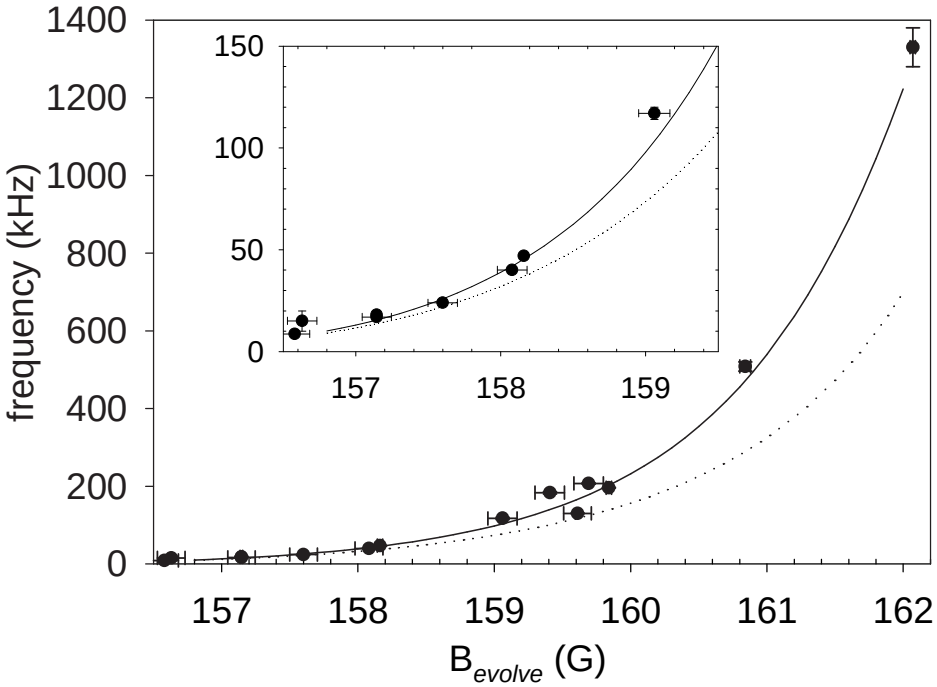

Figure 6.5: Oscillation frequency versus magnetic field. The points are the measured frequencies. The solid line is the energy difference between the atom–atom threshold and the bound molecular state found by S. J. J. M. F. Kokkelmans with a coupled-channels scattering calculation. The dotted line is a plot of $|\epsilon| = \hbar^2/ma^2$. The inset is an expanded view of the lower-frequency data. The magnetic-field measurements for the points with the smallest horizontal error bars were performed on the same days as the corresponding frequency measurements. The error bars for the points with larger field uncertainties were inflated by 100 mG to account for estimated day-to-day field drifts.

with this simple model over the range of magnetic fields where the model is expected to be valid.

The solid line in Figure 6.5 is a prediction of the binding energy from a coupled–channels (CC) scattering calculation by Servaas Kokkelmans. This calculation is based on the results of a recent determination of the rubidium collisional interactions from several high-precision data for ^{85}Rb and ^{87}Rb [69]. We see that the coupled-channels predictions for the binding energy are in excellent agreement with the oscillation frequency data over the entire range of magnetic field. It is important to emphasize that both the simple expression and the more sophisticated CC calculation provide predictions for the binding energy; they are not fits to the oscillation frequency data. The magnetic field dependence of ν_0 is discussed in greater detail in Chapter 7, where we use precision measurements of the frequency and B-field to tightly constrain the parameters of the Feshbach resonance.

6.3.4 Interpreting the oscillations

The fact that the population oscillations occur at exactly the frequency corresponding to the molecular binding energy clearly indicates that we are creating a coherent superposition of atoms and molecules with the sudden magnetic-field pulses. We suggest the following interpretation of our observations. Each magnetic field pulse provides a sufficiently rapid perturbation to result in coherent nonadiabatic transitions between the atomic and molecular states. The first B-field pulse produces an atom-molecule superposition state and the relative phase between the two states in the superposition evolves according to their relative energy difference during t_{evolve}. This energy difference is determined by the B-field-dependent binding energy at B_{evolve}. Because of the relative phase evolution, the final transition probability from the atomic state to the molecular state after the second pulse depends on t_{evolve}. The observed population oscillations are due to a quantum-mechanical interference between the transition am-

plitudes for pulse #1 and pulse #2. Another way to understand the oscillations is to consider that the 2nd pulse transfers some population from the molecular part of the superposition to the atomic state. This "new" probability amplitude in the atomic state can interfere with the amplitude that remained in the atomic state during t_{evolve}. The observed oscillation behavior is somewhat analogous to that seen in Ramsey's method of separated oscillatory fields [24], in which two microwave pulses, separated in time, drive transitions in a two-level atom.

Although our experiment possesses some similarities to the Ramsey 2-pulse experiment, there are also many differences. It is illustrative to explore these differences. For instance, we observe three distinct components of atoms oscillating as a function of evolution time, each with a different oscillation phase and amplitude. In contrast, the conventional Ramsey oscillations occur in a two-level system where the populations of the two states are always exactly out of phase with one another. An additional difference between our experiment and the Ramsey case is the precise nature of the coupling pulses. In the Ramsey experiment, the two states are coupled by a pair of rf or microwave radiation pulses that are nearly resonant with the transition frequency between the two states. Each radiation pulse has a duration that is much longer than the period of the rf or microwave radiation. Our coupling pulses, on the other hand, involve non-periodic time-variations of a magnetic field. We achieve coupling between the atomic and molecular states by briefly ramping down the relative energy difference between the states toward zero, as in a Landau-Zener experiment. In fact, our experiment is probably best pictured as a combination of Landau-Zener magnetic field coupling pulses separated by a Ramsey-like relative phase evolution between the atomic and molecular states.

The experimentally observed population oscillations in the BEC number indicate that we have produced a coherent superposition of atomic and molecular Bose-Einstein condensates. We propose a simple argument to justify our claim for the existence of

the molecular BEC (mBEC). First, we know from the phase coherence property of condensates that the initial atomic BEC possesses a common phase across the sample of atoms. After the double B-field pulses, we measure large contrast oscillations in the number of BEC atoms, which implies that there is a large fraction of the atomic BEC participating in the population oscillations. If a large fraction of the atomic BEC participates in the oscillations, then the atom/molecule superposition must exist at significantly different spatial positions within the original atomic BEC volume. Thus, we produce molecules that are distributed in space and are phase coherent — these are two important properties that identify a BEC! The creation of a molecular BEC is a remarkable achievement and should provide an abundance of avenues for future study.

6.3.5 Mechanisms for missing atoms

If our interpretation of the BEC number oscillations is correct, then one might ask how it is that we distinguish between the atomic and molecular states. In any interference experiment, there must be some way to discriminate between the two states that are interfering with one another. Since we find that some atoms are missing from the absorption images, we evidently do have a discriminating mechanism that is "built-in" to the experiment.

In our experiment, missing atoms could be created by at least two different mechanisms involving the molecular state. One possibility is that the molecules formed by the double B-field pulses are destroyed when we turn off the magnetic trap and cross the Feshbach resonance. A related idea is presented in Ref. [15]. By turning off the trap, we cause the molecular state to become unbound (the molecular state lies far above the colliding atoms threshold energy for B=0). The molecules could therefore dissociate into sufficiently high energy atoms during the trap turn-off ($> 1\ \mu$K) that we would not detect them in the absorption imaging.

Another mechanism for the generation of missing atoms is the possibility of in-

elastic molecule-atom or molecule-molecule collisions during the ∼30 ms time between the double pulse sequence and the magnetic trap turn-off. In principle the molecules should be confined in the magnetic trap because their magnetic moment is very similar to that of the $|2, -2\rangle$ atomic state for magnetic fields near the Feshbach resonance. During the time that a given molecule resides in the magnetic trap, if the molecule collides with an atom or another molecule, it may drop to a lower energy vibrational level, gaining substantial kinetic energy in the process. In this case, the deeply bound molecule would not experience a Feshbach resonant coupling to the atomic state and the molecule would remain a molecule after the magnetic trap turnoff. However, we would not see the molecule because of its large kinetic energy and low probability of scattering photons from the probe laser. It is important to note that the cross-sections and rates for collisions between highly-vibrationally-excited molecules and ultracold atoms have not been calculated for the heavy alkali atoms [51, 70], although some results have been obtained for He-H_2 collisions [71]. Measuring such a cross-section for Rb_2 would be a major experimental breakthrough.

To investigate the mechanism for missing atom generation, we attempted to measure the number oscillations by imaging the BEC in the magnetic trap. The goal was to look at the BEC immediately after the fast pulse sequence or even during t_{evolve} between the pulses. In theory, the presence or absence of oscillations in the data would then help us to identify how the missing atoms are removed from the sample under our normal operating conditions.

Unfortunately, our attempts to extract useful information from the in-trap imaging of the condensates proved inconclusive. Due to a number of systematic effects related to the small size of the unexpanded BEC, the large Zeeman shift of the trapped atoms, and optical pumping effects that reduce the number of photons scattered by each atom, the absorption images were difficult to interpret. For example, one consequence of not allowing the BEC and burst atoms to expand is the inability to distinguish between the

BEC and burst populations in the images. When we tried to circumvent this problem by expanding the BEC in the trap and then imaging the atoms, the data indicated that the missing atoms were still missing before the trap turn-off. However, this result should be considered preliminary and needs to be confirmed with more data. Although we may return to this experiment in the future, at present we have not definitively determined the mechanism for the missing atoms.

6.4 Controlling the oscillation characteristics

After making some preliminary measurements of the atom-molecule population oscillations, we made a detailed study of the oscillation characteristics. To learn more about the physics of this unique system, we explored the dependence of the oscillations on the initial BEC density as well as the particular shapes of the two magnetic field pulses. The behavior of the atom-molecule oscillations under a variety of different conditions is described in this section.

6.4.1 Amplitude of BEC number oscillations

The first property of the number oscillations that we studied was their amplitude. We desired to increase the amplitude as much as possible, both to increase the number of molecules created and also to improve the signal-to-noise ratio for determining other properties, such as the frequency and phase.

Keeping the pulse lengths fixed at 15 μs, we varied the double pulse amplitudes to change the approach distance to the Feshbach resonance. For pulses to $\sim$156.3 G, we measured a BEC number oscillation amplitude of roughly 1700 atoms. Increasing the pulse amplitudes to reach $\sim$155 G caused no change to the oscillation amplitude. The lack of a change is not surprising when one considers that the molecular binding energy has very little B-field dependence from $\sim$156.3 G to $\sim$155 G (see Figure 6.5) even though the scattering length increases from $\sim$3000 a_0 to more than 20,000 a_0. Since

the magnetic field dependence of ϵ_{bind} is nearly quadratic with B-field to the right of the Feshbach resonance, we expect that the population oscillations should dramatically decrease in amplitude for pulses that only approach to within 3 or 4 G from resonance. We did not attempt to study this expected decrease in oscillation amplitude. We felt that the single pulse data on BEC number loss versus pulse amplitude (see section 5.3) should be adequate for predicting the trend.

Based on the single pulse data for BEC loss, we suspected that varying the pulse lengths of the double pulses could substantially change the amplitude of the population oscillations. Although this proved to be true, nevertheless our original choice of 15 μs for the pulse lengths turned out to produce the largest number oscillations. We studied the pulse length dependence of the oscillation amplitude as the length was increased from 5 μs to 50 μs. The shortest pulses produced very little loss from the condensate, so the oscillation amplitude was small. In contrast, the longest pulses caused huge losses from the condensate (more than 50%), but the oscillation amplitude actually decreased. We found that simply increasing the overall number of missing atoms does not necessarily increase the missing atom oscillation amplitude, implying that there may be two parts to $\mathrm{N}_{missing}$. Some of the loss is coherent and leads to number oscillations while another part of the loss is incoherent. The incoherent number loss grows very rapidly with increasing magnetic pulse length.

6.4.2 Strong density dependence of $\mathbf{N}_{missing}$

In addition to the dependence of $\mathrm{N}_{missing}$ on pulse length for the double pulses, we also observed a strong dependence on the initial condensate density. When the BEC density was increased from $\langle n_{init} \rangle = 3.5 \times 10^{12}$ cm^{-3} by more than one order of magnitude, the missing fraction increased from $\sim$8% to $\sim$40% of the initial BEC number. In addition, the number of burst atoms increased dramatically. As a result, the average number of BEC remnant atoms was less than the average number of burst

atoms.

We show the three populations of atoms versus t_{evolve} for high initial BEC density in Figure 6.6. While the burst and condensate numbers apparently still oscillate at the same frequency for these data, the phases and amplitudes of the oscillations in N_{rem} and N_{burst} are such that the total number oscillations are not visible. Under these high density conditions, the number of missing atoms is huge — roughly 10,000 atoms! Here $N_{missing}$ exceeds the average value of N_{rem}, which is about 7000.

We took data similar to those shown in Figure 6.6 for several values of the BEC density and studied the resulting number of missing atoms. To isolate the density dependence of $N_{missing}$, we used fixed values of B_{evolve} and pulse length. We varied the initial density by two different techniques. In the first method, we changed the number of atoms in the BEC by holding the BEC in the magnetic trap for 5 to 10 s after completion of evaporative cooling. Density-dependent losses then reduced the number of BEC atoms without appreciably heating the condensate [1]. Our second method for changing the density was by adiabatically varying the initial magnetic field before the set of double pulses, thereby altering the repulsive self-interaction strength in the condensate. This caused the volume occupied by the BEC ground state wavefunction to vary with the magnetic field. In the latter method, we also adjusted the amplitude of the double pulses to ensure that they maintained the same approach distance to the Feshbach resonance.

The dependence of $N_{missing}$ on BEC density is illustrated in Figure 6.7. Over the range in the plot, the missing fraction rises from nearly zero to 0.4. For some reason, the smooth growth of the missing fraction with density saturates above $\langle n_{init} \rangle \simeq 2 \times 10^{13}$ cm^{-3}. Further investigation of the missing atoms is needed to understand this trend as well as the origin of $N_{missing}$.

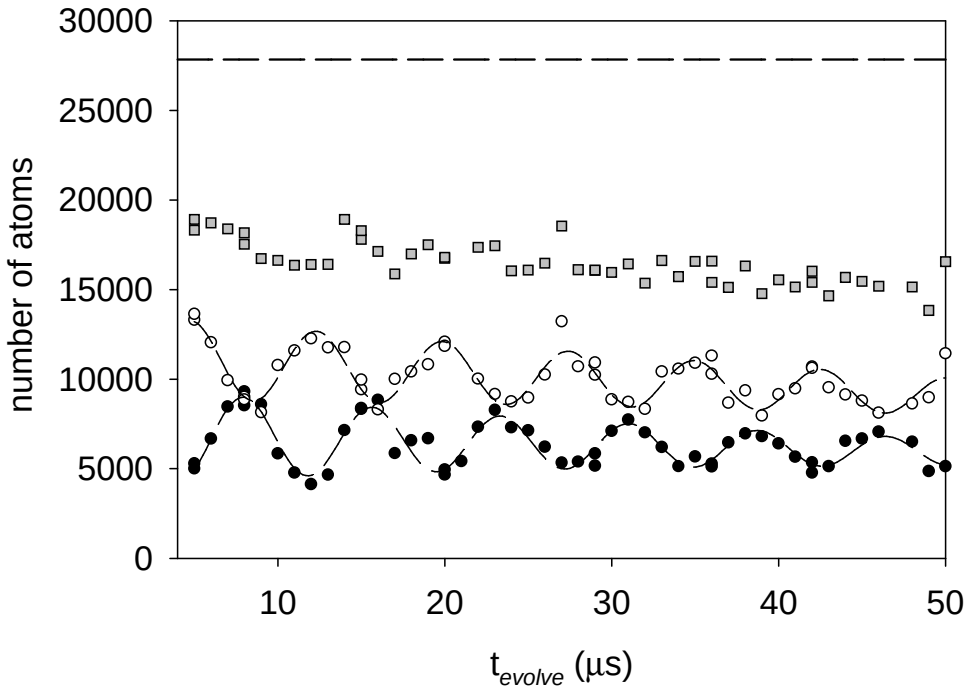

Figure 6.6: Number versus t_{evolve} for high density condensates ($\langle n_{init} \rangle = 4.4 \times 10^{13}$ cm^{-3}). As in Figure 6.4, we show N_{rem} (filled circles), N_{burst} (open circles), and the total number of observed atoms (gray squares). The lines are damped sinusoidal fits to the different populations of atoms. The initial BEC number, N_{init} = 27,800, is indicated by the flat dashed line. The fit parameters for the remnant oscillations are ν_0 = 133(1) kHz and τ_{decay} = 38(8) μs. We added an additional term to the fit function to account for an overall linear loss rate to the number. The fit gave a loss rate of -19(6) atoms/μs. The evolution B-field was B_{evolve} = 159.35(5) G. Because the initial magnetic field before the fast-pulse sequence was 165.71(15) G, we used pulse amplitudes of $\sim$10 G to closely approach the Feshbach resonance.

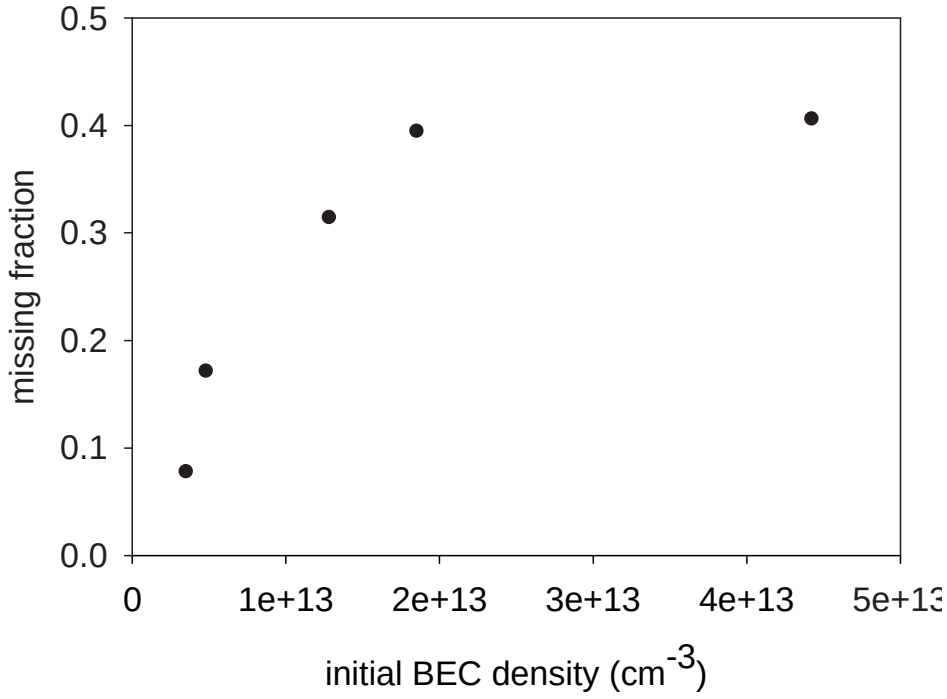

Figure 6.7: Fraction of missing atoms as a function of the initial BEC density. The missing fraction is defined as 1-$\langle N_{total}\rangle/\langle N_{init}\rangle$, where $\langle N_{total}\rangle$ is the average sum of the burst atoms and the BEC remnant atoms and $\langle N_{init}\rangle$ is the average number of BEC atoms before the double pulse sequence. We can determine the density by measuring the initial magnetic field (scattering length) and calculating the volume of the BEC using the PG model. After finding the volume, we use the measured value of $\langle N_{init}\rangle$ to calculate the average density. The typical uncertainty in this density determination is $\sim$20% due to uncertainty in the measured number of atoms and the initial scattering length used in the PG model.

6.4.3 Damping of N_{rem} oscillations

Damping of the number oscillations can be seen in most of the data that we collected. For values of B_{evolve} between 157 G and ∼161 G, the number oscillations are underdamped, so that the damping time is much longer than the oscillation period. To obtain a high precision measurement of τ_{decay} it is therefore necessary to measure the number oscillations over many cycles. One obvious method to obtain the damping time without requiring too many points is by taking closely-spaced data in windows that are separated by longer time intervals, $\Delta t >> 1/\nu_0$. Then one can fit the entire set to a damped sine wave that interpolates in the intervals between the data windows.

Unfortunately, we found this method did not work well in practice because of the presence of phase noise in the data. We observed shot-to-shot noise in the oscillation phase for different repetitions of the experimental cycle. The noise was bigger for longer t_{evolve}, indicating that the source of the noise was shifts to the oscillation frequency. The frequency noise was likely due to shot-to-shot magnetic field noise. We provide further discussion of this point in section 7.2.3.

To determine the damping rate despite the presence of phase noise, we adopted another technique for data measurement. We measured N_{rem} versus t_{evolve} in several windows having a length of one or two oscillation periods. The spacing between windows was chosen to be comparable to our estimated 1/e time for the damping. We analyzed the data by computing the maximum variation in remnant BEC number within each time window. We plotted ΔN_{max} versus t_{evolve} and fit the data to a decaying exponential function, as shown in Figure 6.8.

We discovered that the damping rate was quite insensitive to both initial BEC density and magnetic field in the B-field range from 157 G to ∼161 G. Recently, we have found that the rate ($1/\tau_{decay}$) actually increases rapidly as the magnetic field increases above ∼161 G, which is possibly related to the rapid variation in binding energy with

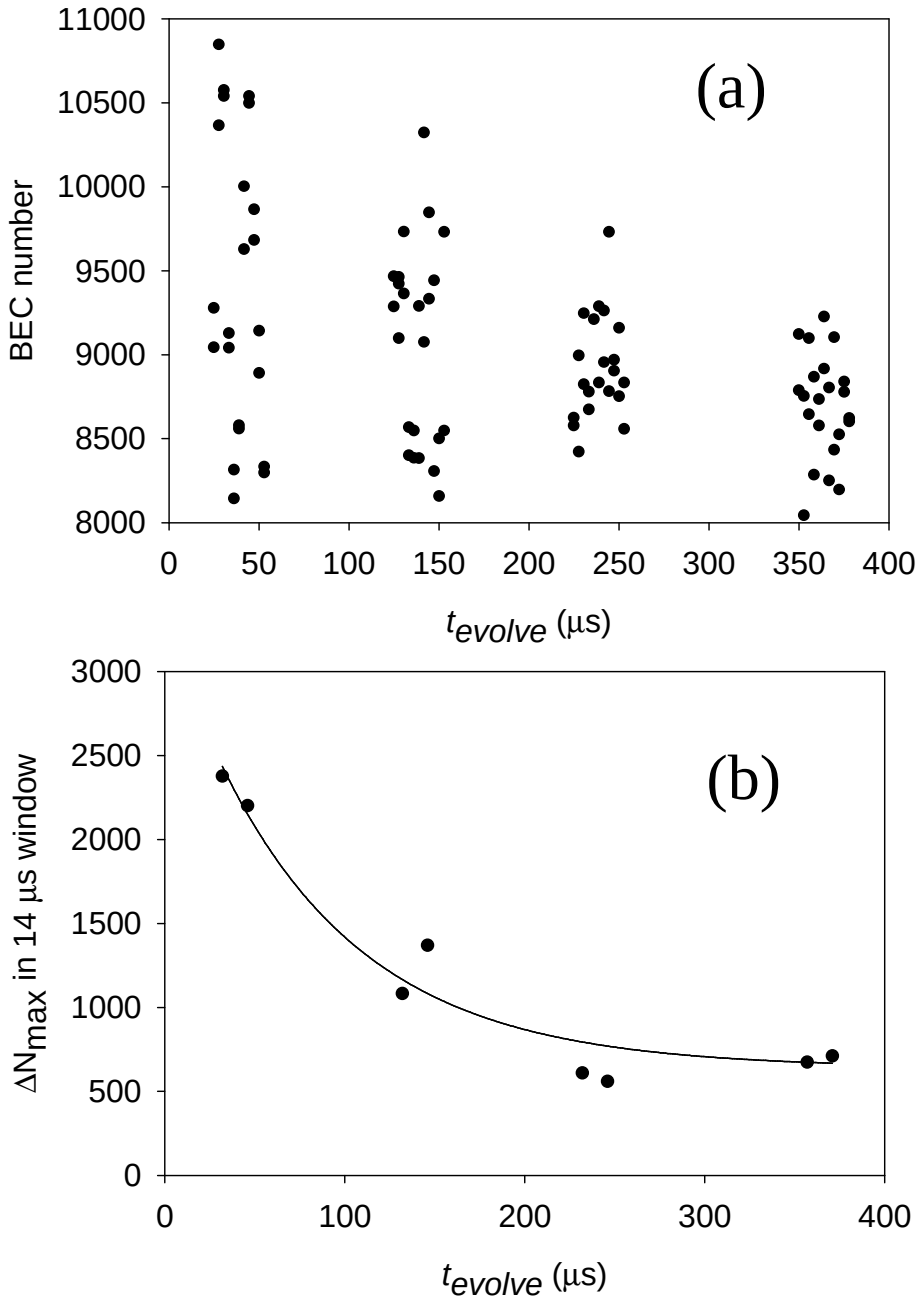

Figure 6.8: Damping of BEC number oscillations. **(a)** BEC remnant number (N_{rem}) versus t_{evolve}. The data are grouped into 4 windows with each window consisting of 2 oscillation periods. **(b)** Peak-to-peak variation in remnant number, ΔN_{max}, versus t_{evolve} (black points). ΔN_{max} is calculated for a single oscillation period, which is roughly 14 μs in length. The line is an exponential decay fit to the data, with the baseline fixed at the average of the four longest time data: N_{base}=640 atoms. The damping time from the fit is 82(14) μs (damping rate $\gamma = 12(2) \times 10^3$ s^{-1}). The baseline of 640 atoms is quite reasonable considering the peak-to-peak number noise observed during the measurement. Note that the peaks of the oscillations in part **(a)** decrease more rapidly than the troughs due to an overall loss of BEC atoms during t_{evolve}. We find that the loss is linear with time and occurs at a rate of -2.2(2) atoms/μs.

magnetic field. Both the B-field dependence and possible mechanisms for the damping are presently under investigation and will be the subject of a future publication by our group.

We also looked for a temperature dependence of both the damping and the oscillation frequency at $\nu_0 \sim 200$ kHz and did not see any. The high-temperature data were much noisier than the data for pure condensates, due to unexplained enhanced noise in the number of thermal atoms after the magnetic field pulses, but when the initial thermal fraction was increased from <5% to 30%, the data still displayed oscillations with frequency, amplitude, and damping consistent with what was observed with low temperature data. Since we changed N_{therm} by more than a factor of 6 and saw no effect, any dependence of the damping rate on temperature must be very weak.

6.4.4 Relative phase between N_{rem} and N_{burst} oscillations

A particularly intriguing aspect of our data is the observation of three distinct oscillations in the various number components visible from the absorption images. Because the relative phase between the BEC remnant and the burst oscillations does not equal 180°, there is a third oscillation visible in $N_{missing}$ (or N_{total}). We believe that the $N_{missing}$ oscillation amplitude may correspond to the number of molecules produced by the double pulse sequence.

For reasons that will be elucidated later in this section, we suspected that the number of molecules might be increased by ramping the B-field more slowly at the end of magnetic field pulse #2. We therefore examined the amplitude of the $N_{missing}$ oscillations as a function of the final ramp time of the second B-field pulse. As a result of changing this ramp time, there were variations in the relative phase between the BEC remnant and burst number oscillations, $\Delta\phi = \phi_{burst} - \phi_{BEC}$. The relative phase variations caused the $N_{missing}$ oscillation amplitude to change significantly. For example, increasing the final ramp time of pulse #2 from our default value of 11 μs to

160 μs caused the missing number oscillation amplitude to increase from 1000 atoms to nearly 2800 atoms. The number oscillations for the 160 μs final ramp time are displayed in Figure 6.9.

By comparing different data sets such as those shown in Figure 6.9, we observed that the relative phase shift , $\Delta\phi$, decreased as the final ramp time for pulse #2 became longer. The phase shift behavior was entirely due to a phase shift in the burst number oscillations; the BEC remnant phase remained fixed. As the final ramp time increased, the burst oscillation phase shifted in such a way that the lowest curve in Figure 6.9 moved smoothly to the right. We show the quantitative details of this trend in Figure 6.10. There $\Delta\phi$ is seen to decrease from $\sim$150° to $\sim$80° as the ramp time goes from 10 μs to 330 μs. After an initially rapid decline, the relative phase eventually levels out for slower and slower ramps.

After demonstrating that the relative phase shift could take on values very different from 180°, we scratched our heads and wondered about the origins of the shift. Since we had generally observed that fewer atoms in the BEC correspond to more atoms in the burst, we speculated that the phase shift between the N_{rem} and N_{burst} oscillations might originate in a time delay between the disappearance of the BEC and the creation of the burst atoms. To determine whether $\Delta\phi$ was a true phase shift or was simply a shift caused by a fixed time delay, we measured $\Delta\phi$ at two different values of the oscillation frequency. While holding the pulse #2 final ramp time fixed at 160 μs, we changed B_{evolve} to alter the oscillation frequency. Decreasing ν_0 from $\sim$200 kHz to 56 kHz caused the relative phase shift to change from 68(7)° to 88(9)°. The relative phase shift therefore increased by a factor of 1.3(2). However, if the phase shift were due to a fixed time delay, then decreasing the frequency by a factor of 4 should cause $\Delta\phi$ to drop by a factor of 4 also (so we would expect $68°/4 = 17°$ in this case). Thus, the time delay idea is clearly not correct.

Nevertheless, it remains true that the second magnetic pulse shape affects the

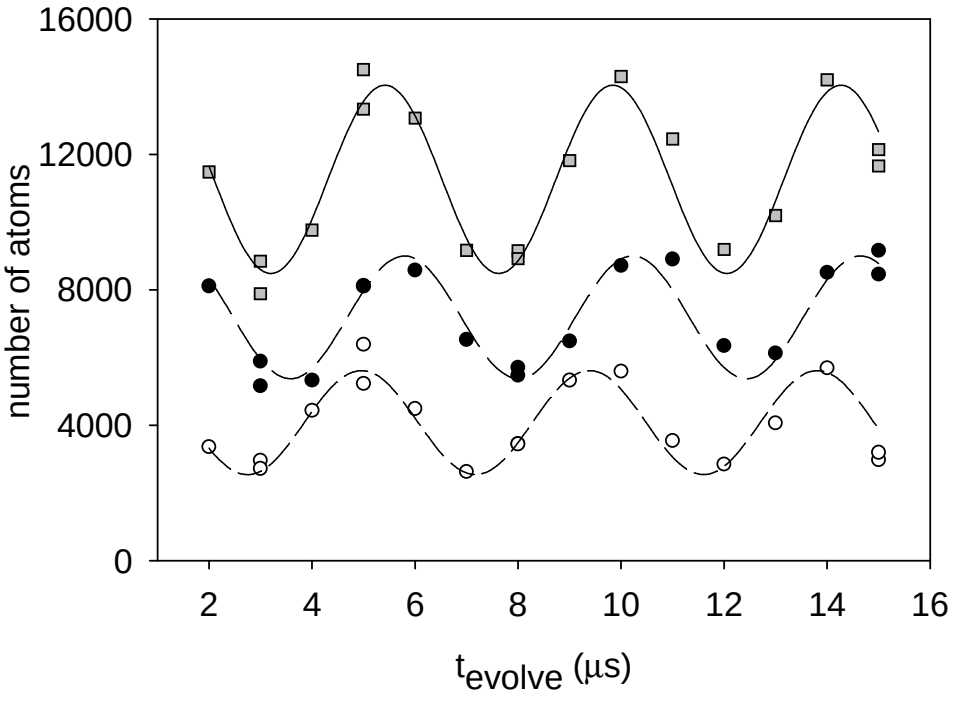

Figure 6.9: Enhanced $N_{missing}$ oscillations. Number versus t_{evolve} for a relatively long pulse #2 final ramp time of 160 μs. From bottom to top, the data are N_{burst} (open circles), N_{rem} (filled circles), and the total number of observed atoms (gray squares). The different data sets are fit by damped sine waves as shown by the lines. The relative phase between burst and remnant oscillations is $\phi_{burst} - \phi_{BEC}$=68(7)°, which is more than 2× smaller than the 147(8)° phase difference for our typical 11 μs final ramp time (see Figure 6.4 and related discussion in the text).

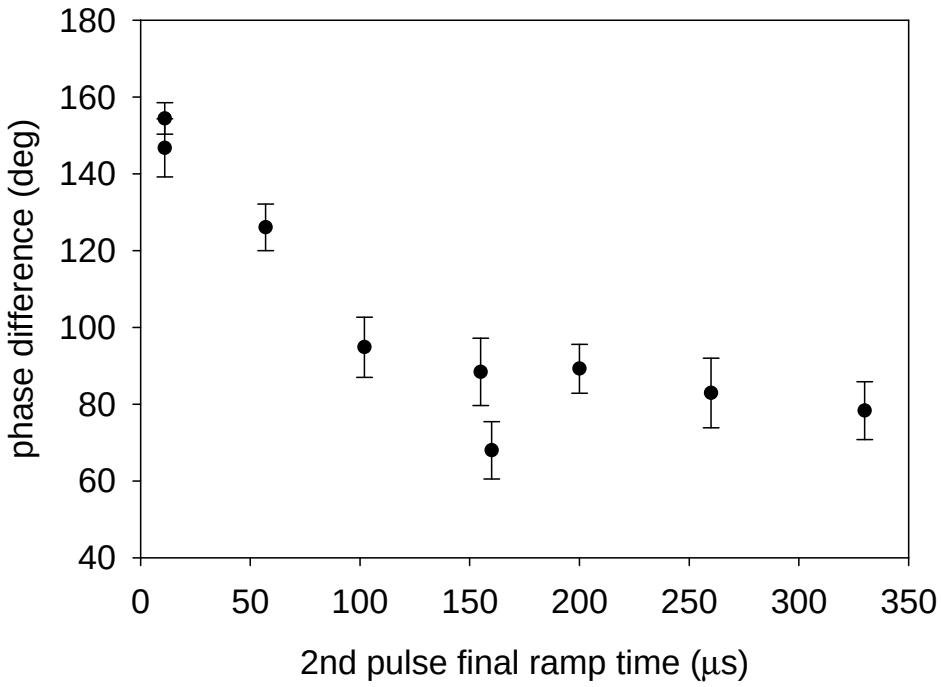

Figure 6.10: Relative oscillation phase versus final ramp time of 2nd B-field pulse. Black points with error bars are the phase difference $\phi_{burst} - \phi_{BEC}$. To calculate the phase difference, we first fit each population oscillation (remnant BEC atoms, burst atoms, and total number of atoms) to a sinusoidal function. From these three fits, we then compute the weighted average oscillation frequency. We next fit each component of atoms again, constraining the oscillation frequency for the fit to be equal to the weighted average value. This procedure allows us to determine the phase shift between the burst and remnant BEC number oscillations with improved precision.

ratio of BEC atoms to burst atoms at fixed evolution time. For instance, if we choose t_{evolve} such that N_{rem} is at a minimum or trough of the oscillation, then lengthening the 2nd pulse final ramp time causes the number of burst atoms to decrease and the missing number to increase. Another way to see this is to compare the phases of the oscillations in N_{rem} and $N_{missing}$. As the final ramp time becomes longer, the remnant oscillations become more and more out of phase with the missing number oscillations. Concurrently, the amplitude of the $N_{missing}$ oscillation grows larger.

These observations suggest that we preserve more molecules (more missing atoms) after pulse #2 by slowing down the final ramp. We believe that increasing the 2nd pulse final ramp time enhances the probability that the molecules formed during the coupling pulse survive the ramp back toward higher B-field ($\sim$166 G). The justification for this claim is based on the arguments of Chris Greene and Murray Holland. Since the radial wavefunction of the weakly bound molecular state has a size characterized by the scattering length (see Chapter 2), a longer pulse should allow a more gradual or adiabatic decrease in the size of the wavefunction toward smaller and smaller radius. In contrast, the shorter ramp times are more sudden and they lead to a higher probability that the molecule will simply dissociate into a pair of free atoms during the ramp. It is possible that the hugely extended molecules that are created near the Feshbach resonance are very fragile and they dissociate when the B-field jumps quickly back to small a. If this interpretation is correct, then the data imply that the dissociation of the molecular state can be influenced by the magnetic field ramp rate — with slower ramps leading to less dissociation.

One must take some care when talking in this way about the state of the molecule at a particular B-field (scattering length) because of the time variation of the field. During the double magnetic field pulses, the state of the system is far from equilibrium. We only observe the populations of the BEC remnant and burst atoms long after the atom-molecule coupling dynamics have ended.

While the "fragile molecule" hypothesis discussed above appears to have some validity, it is far too simple to describe all of the effects of changing the ramp time of pulse #2. In addition to the relative oscillation phase shifts and the oscillation amplitude of $N_{missing}$, we observed that several other observables depended on the 2nd pulse final ramp time. For example, the oscillation amplitude of N_{rem} and N_{burst} exhibited a slight decrease as the final ramp lengthened. There was also a decline in the average energy of the burst atoms for slower ramps. These trends have not been explained at the present time.

6.4.5 Burst energy oscillations

The final feature of the atom-molecule coherence experiments that we describe in this Chapter involves the energy of the burst atoms. We measured a periodic modulation of the average energy of the burst atoms as a function of t_{evolve}, as shown in Figure 6.11. The data in the Figure are the average energies corresponding to the burst atom number data that was plotted previously in Figure 6.6. For these data, number of burst atoms was the highest we ever observed, so that $N_{burst} > N_{rem}$. The large number of burst atoms in the absorption images facilitated the determination of the average energy of the distribution along the axial direction. As described in section 5.2.3, we fit each burst atom distribution to a 2-D Gaussian function and used the width of the Gaussian in the long dimension to calculate the average energy. In Figure 6.11, the observed variation in energy of $\sim$50 nK is equivalent to a modulation of $\sim$17 μm in the rms width of the focused burst atom cloud. The energy oscillations appear to damp out fairly rapidly until they become lost in the noise after $\sim$35 μs. Our measurements show that both the number of burst atoms and their energy distribution change with t_{evolve}.

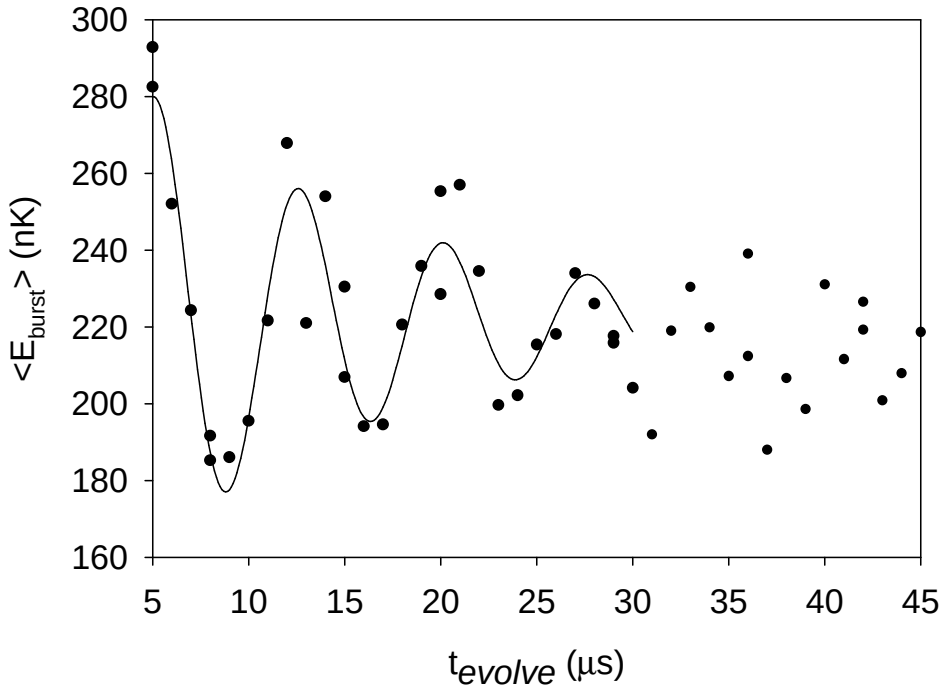

Figure 6.11: Average axial burst energy versus t_{evolve}. Black points are the average axial burst energy at different values of the evolution time between the double pulses. The line is a damped sine wave fit to the data for $t_{evolve} \leq 30$ μs. The fit yields the parameters: 222(2) nK average energy, 83(15) nK oscillation amplitude, 133(3) kHz oscillation frequency, and $70(16) \times 10^3$ s^{-1} damping rate. The oscillations in the average energy occur at the same frequency and phase as the burst number oscillations (see Figure 6.6), while the damping of the energy oscillations is roughly 3$\times$ faster than in the burst number oscillations.

6.5 Discussion of theoretical models

The observations of atom-molecule coherence described in this Chapter raise a number of outstanding questions. First, do the magnetic field pulses really produce molecules and if so, do the molecules form a molecular BEC? As discussed in section 6.3.4, the fact that we see an oscillation involving a large fraction of the atomic BEC strongly supports the existence of a molecular BEC. There are many remaining questions, however. For instance, exactly how many molecules can we produce and how can we increase this number by optimizing the shape of the B-field pulses? Another outstanding issue is the precise relationship between the burst atoms and the molecular state. Finally, what happens to the molecules after they are created? Are there collisions and/or mean-field interactions with the surrounding atoms [72]?

For a definitive experimental answer to these questions, we need to devise a method to directly detect the molecules and their spatial distribution in the magnetic trap. New experiments are currently being developed at JILA that should allow molecule detection by photo-ionization and subsequent detection of the molecular ions. However, many useful insights and possible answers to the questions raised by our data can be obtained from recent theoretical work. A number of theorists [9, 16, 67, 73, 68], inspired by our oscillation data, have studied the ^{85}Rb BEC system. Some of the theorists have developed models that capture most of the prominent experimental features, especially the existence of the different oscillating components of atoms that we observe. We describe the successes of some of the relevant theories in this section. We also point out areas that remain unexplored theoretically. At the end of the section, we use a table to present a concise comparison of the theories to the relevant experimental observables.

6.5.1 Kokkelmans and Holland model

Kokkelmans and Holland's theoretical description of the atom-molecule coupling experiments [9] was briefly described in Chapter 5. The authors emphasize that it is very important to properly incorporate the two-body scattering physics into their effective quantum field theory. The Feshbach resonance in the two-body atomic scattering can be described most accurately by a coupled-channels calculation, which predicts the B-field-dependent scattering length, the binding energy of the molecular state, and the bound state wavefunction (see Chapter 2). Kokkelmans and Holland show how to include the complex scattering physics into a simple effective Hamiltonian used in mean-field theory [56]. This effective Hamiltonian can then be used to predict the response of a near-resonant condensate to variations in magnetic field.

Kokkelmans and Holland solve a set of time-dependent equations for their effective Hamiltonian, which depends on magnetic field. Using the experimental B-field pulses, they integrate the equations for a homogeneous BEC. To model the inhomogeneous density distribution of the real condensates, Kokkelmans and Holland conduct their calculations for a range of densities, finally performing a Gaussian weighted average of their results. This corresponds to a local density approximation for the BEC. The authors assert that they can safely ignore any other physics due to the trapping potential because of the short time duration of the magnetic field pulses (much shorter than the magnetic trap oscillation period).

The theory successfully predicts a number of details of the experiment. Kokkelmans and Holland identify the condensate remnant as the atomic BEC field in their theory, while the burst atoms of the experiment correspond to noncondensate atoms that are created in strongly correlated pairs. The missing atoms are identified as a molecular BEC. Kokkelmans and Holland suggest that the reason the molecules turn into missing atoms in the experiment is because of inelastic collisions with BEC atoms

before the magnetic trap turn-off.

For a double pulse sequence beginning at B_{init}=162 G (low initial BEC density), the Kokkelmans/Holland theory predicts striking oscillations in the number of BEC and burst atoms, with an oscillation frequency that matches the binding energy of the molecular state. In the theoretical results, there is a phase shift between the remnant and burst oscillations that agrees with the experiment. In addition to these predictions, Kokkelmans and Holland find that the average energy of the burst atoms is similar to that observed experimentally.

There are only two important aspects of our experimental data that are not described by this theory. First, the theory does not contain any mechanism to cause the large numbers of non-oscillating missing atoms that we observe. We found in section 6.4.2 that increasing the BEC density caused the average value of $N_{missing}$ to increase dramatically. These missing atoms may be removed from the BEC by 3-body recombination, which is not contained in the Kokkelmans/Holland model. In the recombination process, two atoms spontaneously form a molecule during a collision with a third atoms. An alternative explanation to the recombination idea is that the non-oscillating missing atoms are in fact coherently formed molecules, but the Kokkelmans/Holland theory fails to predict their presence. An additional feature of the experiment that is not explained by the theory is the strong dependence of the relative phase, $\Delta\phi$, between burst and BEC remnant oscillations, on the final ramp time of the second B-field pulse. While Kokkelmans and Holland did observe a such a dependence, it was much weaker than in the data. Since we have interpreted the relative phase variation in terms of making more molecules, it would be interesting to further study the trend in the context of the Kokkelmans and Holland theory.

Overall, the success of this theory is remarkable. The Kokkelmans/Holland theory provides an explanation of the burst atoms — they are noncondensate atoms that develop strong pair correlations due to the B-field ramps near the Feshbach resonance.

According to the model, the burst atoms significantly outnumber the molecules due to the large spatial overlap of the weakly bound molecular state with the pairing field that describes the two-body correlations. For the B-field pulse and initial BEC density used in Ref. [9], the molecular fraction is predicted to be much smaller than the burst — only $\sim 2\%$ compared to $\sim 25\%$. In addition, the authors identify the oscillating population of missing atoms as a molecular BEC.

6.5.2 Kohler, Gasenzer, and Burnett model

Another theoretical paper describing our ^{85}Rb BEC experiments was recently produced by the theory group at Oxford [16]. In this work, Kohler, Gasenzer, and Burnett utilize a generalization of the mean-field theory leading to the well-known Gross-Pitaevskii equation. The theory goes beyond the GP equation by including first and second-order correlations between the atoms. This leads to a nonlinear Schrodinger equation for the atomic mean field (atomic BEC). The Schrodinger equation describes the relative motion of two colliding atoms through a time evolution operator. The operator and its related coupling function capture the full time-dependence of the magnetic field or scattering length in the experimental B-field pulses. The authors of Ref. [16] assert that their microscopic dynamics approach avoids any assumptions about the type of states involved in the system of colliding BEC atoms. They determine the state of the atoms after a double pulse sequence by projecting onto a given set of basis states, but the results are not dependent on the choice of the states. In addition, Kohler, Gasenzer, and Burnett examine the effect of including the magnetic trap potential. They compare their results for both a homogeneous gas and a trapped gas to learn more about the physics of the atom-molecule coupling.

Like the Kokkelmans/Holland effective field theory, the model of Ref. [16] predicts oscillations in the number of BEC atoms as a function of t_{evolve} between a pair of magnetic field pulses toward the Feshbach resonance. Kohler, Gasenzer, and Burnett

also identify a relatively hot component of noncondensate atoms in their theory with the burst atoms observed in the experiment. A population of bound molecules exists after the B-field pulses as well; according to the authors, these bound molecules correspond to the missing atoms in the experiment (no consideration is given as to how the molecules actually become missing atoms). The properties of the weakly bound molecular state near the Feshbach resonance are explored by the authors of Ref. [16] in a useful appendix to the paper.

For the case of a homogeneous BEC subject to a set of B-field pulses similar to those used in the experiment, the theory predicts that the BEC and burst populations oscillate slightly out of phase with one another, so that their sum, N_{total}, also oscillates. The amplitude of the N_{total} oscillations is reduced relative the that of the BEC and burst numbers, as was seen in experimental data.

When Kohler, Gasenzer, and Burnett include the magnetic trap in their simulations, they observe the same qualitative behavior in the number oscillations, but there are significant quantitative differences. The average number of burst atoms and missing atoms is seen to depend strongly on the presence of the trap potential. For instance, adding the trap potential causes the average burst fraction to increase from $\sim$15% to $\sim$40% while the average missing fraction decreases from $\sim$10% to $\sim$5%. However, the phases and frequencies of the population oscillations remain unchanged when the magnetic trap is included in the Schrodinger equation. The authors of Ref. [16] explain that the dependence of the quantitative details of the oscillations on the presence of the trap potential arises from the first B-field pulse toward the Feshbach resonance. During this pulse to 155.5 G, the magnitude of the scattering length approaches the harmonic oscillator length of the trap, which strongly affects the interactions of the atom pairs. Since the oscillator length does not appear in the homogeneous theory, it seems reasonable that the results should depend somewhat on the inclusion of the trap potential.

One interesting aspect of the theory is its explanation of the origin of the burst

atoms. The authors of Ref. [16] point out that the magnetic field pulses provide energy for the relative motion of the noncondensate atom pairs, but there is no transfer of momentum. Thus, the center-of-mass motion of the burst is unaffected by the magnetic field ramps.

In addition to providing energy for the relative motion of the burst atoms, the time-dependent B-field can remove energy from the system so that atom pairs can become bound together. Kohler, Gasenzer, and Burnett also predict the formation of a molecular BEC due to the B-field pulses. The authors state that after the pulse sequence, the mBEC remains overlapped with the atomic BEC while the burst atoms undergo a ballistic expansion. A density distribution for the molecular BEC is given in the paper.

There are some results of the experiments in this Chapter that remain unexplained by the Kohler, Gasenzer, and Burnett model. The large, density-dependent fraction of missing atoms that do not show an oscillating population are not predicted by this model. In addition, there is no modeling of our observed phase shift dependence on second B-field pulse final ramp time. Presumably this could be done and compared to data to further test the applicability of the theory; however, as in the model of Ref. [9], heavy numerical work is required to evaluate the predictions of the Kohler, Gasenzer, and Burnett theory. It is difficult for experimentalists to apply this model to the data to gain further intuition about the observed trends. For instance, we would like to use one of these successful theoretical models to investigate the dependence of the $N_{missing}$ oscillation amplitude on the second pulse final ramp time. Of course, it is not really fair to complain that the theory is too complicated because an accurate description of the physics probably does require an effective field theory.

6.5.3 Overview of experiment and theory

To clarify the comparisons between theory and experiment described here, we summarize them in Table 6.1. Here we list the experimental observables and trends and a brief note on the current status of agreement with theory.

Table 6.1: Comparison of experimental observables and trends with the two theoretical models described in this section.

Observation	Kokkelmans/Holland	Kohler/Gasenzer/Burnett
N_{rem}, N_{burst} osc. amplitude	calculated; agrees with expt.	calculated; agrees with expt.
$\langle N_{rem} \rangle$, $\langle N_{burst} \rangle$ avg. values	calculated; agrees with expt.	calculated; agrees with expt.
$N_{missing}$ oscillations	calculated; agrees with expt.	calculated; agrees with expt.
$\Delta\phi = \phi_{burst} - \phi_{BEC} \simeq 150^\circ$	calculated; agrees with expt.	calculated; agrees with expt.
$\Delta\phi$ vs. $t_{ramp,\,final}$ of pulse #2	calculated; does not agree	not yet calculated
$\nu_{osc} = \epsilon_{\rm bind}/h$	calculated; agrees with expt.	calculated; agrees with expt.
Damping of N_{rem} osc.	not yet calculated	not yet calculated
$N_{missing}$ vs. $\langle n_{init} \rangle$	calculated; does not agree	not yet calculated
$\langle E_{burst} \rangle$	calculated; agrees with expt.	calculated; agrees with expt.
$\langle E_{burst} \rangle$ oscillations	not yet calculated	not yet calculated

In addition to the theoretical models described here, there are several other papers that study the atom-molecule coupling in ^{85}Rb [67, 73, 68]. In particular, the predictions of Mackie et al. [67] bear some similarities to the observations of the experiments. However, the agreement is not particularly good. Since the Kokkelmans/Holland and Kohler, Gasenzer, and Burnett models have been so successful in describing our experiments, we do not include discussion of the other theories here.

Chapter 7

Very high precision bound state spectroscopy near a ^{85}Rb Feshbach resonance

7.1 Atom-molecule coherence as a novel Feshbach resonance probe

7.1.1 Introduction

The phenomenon of a Feshbach resonance in ultracold collisions of alkali atoms has received much theoretical and experimental interest in recent years and has sparked interest in the subject of resonant Bose-Einstein condensates (BEC). In addition to providing the subject matter for this thesis, Feshbach resonances were used to control elastic and inelastic collisions in ultracold gases [74, 75, 76, 77] and for tuning the self-interaction in BEC [12, 26, 2] by changing the magnitude of an external magnetic field.

The magnetic field controls the self-interaction in the BEC by affecting the s-wave scattering length, a. Close to resonance, the scattering length varies with B-field according to

$$a = a_{\rm bg}\left(1 - \frac{\Delta}{B - B_{\rm peak}}\right), \tag{7.1}$$

where $\mathrm{B_{peak}}$ is the resonance position and is defined to be the magnetic field where the magnitude of a becomes infinite, $a_{\rm bg}$ is the background scattering length, and $\Delta = B_{\rm zero} - B_{\rm peak}$ is the resonance width where $B_{\rm zero}$ is the B-field where the scattering length crosses zero. Measurements of Feshbach resonance positions and widths have

been used in a variety of alkali atoms to improve the determination of the interatomic potentials. These potentials have then been used to precisely calculate a multitude of important properties for trapped atomic gases [75, 78, 79, 13, 77, 69].

In ^{85}Rb, our recent production of an atom-molecule superposition state has allowed us to dramatically improve an existing determination of the Feshbach resonance position and width. The phenomenon of atom-molecule coherence was described in detail in Chapter 6. By inducing periodic oscillations in the number of condensate atoms, we obtain a direct, high precision measurement of the molecular bound state energy. Exploiting the resonance, we tune the molecular state very close to threshold — to our knowledge, this is the most weakly bound state ever observed.

This chapter discusses the experimental techniques for mapping out the B-field dependence of the molecular binding energy and how the data were fit to a theoretical model based on 2-body scattering theory. As a result of the fitting, there was a substantial improvement in the determination of the Feshbach resonance parameters. The strengths and limitations of the present method for studying the Feshbach resonance are emphasized. The final section of the chapter discusses our search for many-body effects, which manifest themselves in a mean-field shift to the observed oscillation frequency.

7.1.2 Sensitivity of binding energy to Feshbach resonance parameters

The atom-molecule coherent oscillation frequency, ν_0, is directly related to the molecular state binding energy by $\epsilon_{\rm bind}$=ν_0/h. Since the magnitude of this binding energy depends strongly on the distance from the Feshbach resonance, one can use measurements of the binding energy and corresponding magnetic field to constrain the Feshbach resonance parameters, such as the position (B_{peak}), width (Δ), and background scattering length (a_{bg}). To understand the close relationship between $\epsilon_{\rm bind}$ and the Feshbach resonance parameters, it is useful to consider the approximate expression

$$\epsilon_{\rm bind} = -\hbar^2/(ma^2), \tag{7.2}$$

which is valid when the scattering length, a, is large and positive.[1] Substituting equation (7.1) for a versus B-field into equation (7.2) leads to an equation relating the oscillation frequency to the Feshbach resonance parameters:

$$\nu_0 = \frac{\hbar}{2\pi m a_{bg}^2} \frac{(B - B_{peak})^2}{(B - B_{zero})^2}. \tag{7.3}$$

For magnetic field changes near resonance ($B \geq B_{peak}$), the numerator of equation (7.3) varies much more rapidly than the denominator and the B-field dependence is nearly quadratic. To first approximation, a plot of binding energy versus B-field is simply a parabola centered at B_{peak} and with a curvature that depends on $1/a_{bg}^2$. Clearly, one can obtain information about the Feshbach resonance parameters from the magnetic field dependence of ϵ_{bind}, as indicated schematically in Figure 7.1.

One of the best uses we found for equation (7.3) was to determine the optimal data-gathering strategy for precisely determining a given Feshbach resonance parameter. For example, if we hold other parameters fixed, B_{peak} can be best determined by measurements of high oscillation frequencies, where the slope $\Delta\nu_0/\Delta B$ is large. Using simple error propagation and making reasonable assumptions for experimental uncertainties in a typical (B, ν_0) measurement, we estimated that we should be able to measure B_{peak} to a precision of 0.047 G and a_{bg} to a precision of 4.5 a_0. Although these estimates turned out to be fairly conservative (see section 7.3.3), they motivated us to pursue the measurement because such precision would represent a dramatic improvement over that obtained in earlier experiments (0.4 G for B_{peak} and 21 a_0 for a_{bg} [1]).

Although the present discussion of equation (7.3) provides motivation for precise measurements of the binding energy, the actual theoretical analysis used to model the data was considerably more complex. Servaas Kokkelmans collaborated with us to model the binding energy data. He utilized a highly accurate coupled-channels scattering model to fit the experimental data and extract the Feshbach resonance parameters,

[1] In fact, equation (7.2) only underestimates the actual binding energy by $\sim$30% for $a \simeq 300$ a_0 ($B \simeq 161.5$ G).

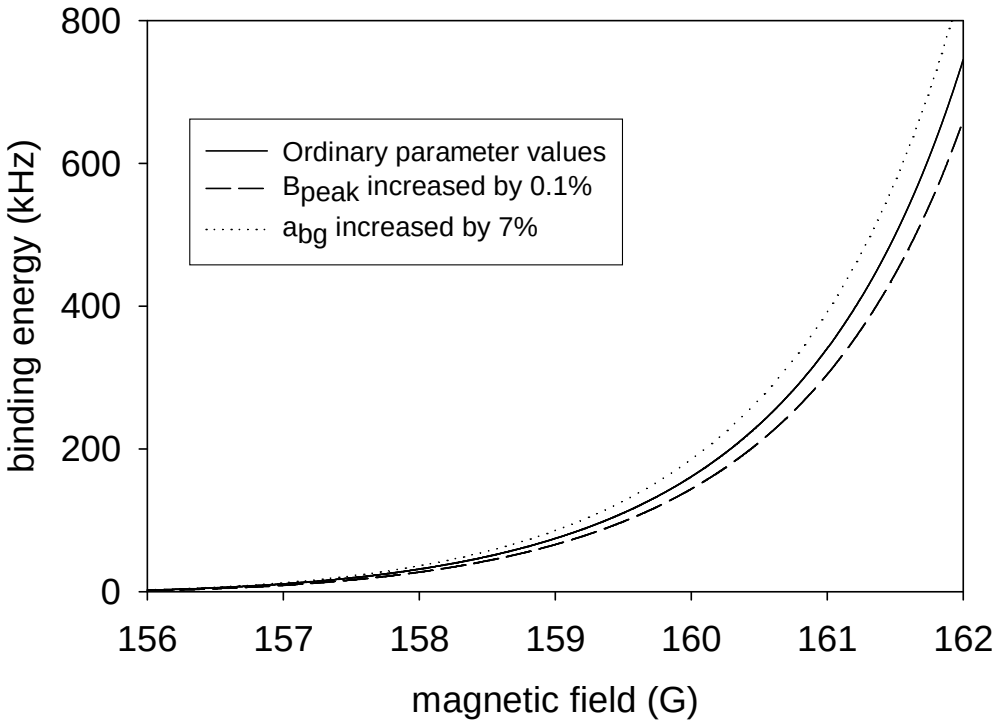

Figure 7.1: Sensitivity of binding energy to Feshbach resonance parameters. The solid line is the binding energy versus magnetic field as calculated from the approximate equation (7.3), with our current best determinations for the Feshbach resonance parameters (section 7.3.3). The dashed line shows the effect of increasing the value of B_{peak} by 0.1% (0.15 G), while the dotted line corresponds to a reduction in $|a_{bg}|$ by 7%. The relative difference in sensitivity to the different parameters can be understood from a simple Taylor expansion of equation (7.3).

providing strong constraints on the exact shape of the interatomic potential.

7.1.3 Advantages of the present method over previous ones

The present method for studying the Feshbach resonance through atom-molecule oscillations offers all of the many inherent advantages of a frequency measurement, including the possibility of high measurement precision, a lack of sensitivity to errors in the absolute atom number calibration, and a simple interpretation of the oscillation frequency in terms of the relative energy difference between the atomic and molecular states. When these advantages are combined with an improved method for magnetic field calibration [3], the present technique for probing the Feshbach resonance is much more precise than previous experiments that examined such Feshbach resonance observables as variable rethermalization rates in a trapped cloud of atoms [75, 13], enhancements of photoassociation rates [74] and inelastic loss rates near the resonance [80], and variations of the mean-field expansion energy of a BEC [12]. In particular, the present atom-molecule coherence experiments have exposed a systematic error in our previous determination of the background scattering length, a_{bg}, as discussed in section 7.3.4. Our new measurement of a_{bg} agrees with the value obtained from an analysis of several other high precision experiments with ultracold rubidium [69].

7.1.4 Improved determination of B_{zero}

To complete the precise characterization of the Feshbach resonance, we also made an improved measurement of B_{zero}, the magnetic field where the scattering length vanishes. This experiment is very similar to our previous work [1, 13, 33], where we determined the a=0 field by measuring the critical number (N_{cr}) for collapse of a BEC. For a given magnetic field (scattering length), there is an upper limit to the number of atoms the condensate can contain before becoming unstable. To measure this critical number, we prepare a large ($N_0 \sim$16000) condensate with fewer than 5% thermal fraction. The

condensate is formed at a B-field where the scattering length is positive (a ∼200 a_0. We next apply an adiabatic magnetic field ramp to change the sign of the scattering length from positive to negative, then we slowly increase the B-field until the condensate collapses, which causes an abrupt drop in the number of atoms. From the measured value of the collapse B-field ($B_{collapse}$) and the known slope of $1/N_{cr}$ versus magnetic field [33] we can extrapolate to the magnetic field where N_{cr} would be infinite, thereby determining the value of B_{zero}. We have improved the measurement precision of B_{zero} by about a factor of 4 by improving our magnetic field calibration and using a larger number of condensate atoms to measure the collapse. We find B_{zero}=165.750(13) G.

7.2 Measuring the B-field dependence of oscillation frequency

7.2.1 Production of BEC and measurement of total number

The procedure used to generate atom-molecule oscillations in ^{85}Rb Bose-Einstein condensates has been described in chapter 6, so we merely outline the method here. After creating condensates with initial number of atoms N_0 ≃16000 at a magnetic field B≃162 G, we apply two short B-field pulses (∼40 μs duration) that approach and then recede from the Feshbach resonance at B_{peak} ≃155 G. The intermediate value of magnetic field between the pulses, B_{evolve}, and the time spacing between pulses, t_{evolve}, are variable quantities. The double pulse sequence is followed by a slow change in the B-field to expand the BEC [2], then the trap is switched off (B→0) and destructive absorption imaging is used to count the number of atoms remaining in the condensate.

7.2.2 Atom-molecule oscillations

As in Ref. [4], periodic oscillations in the BEC number were observed as a function of t_{evolve} (see Figure 7.2). We fit the BEC number oscillation to a damped harmonic

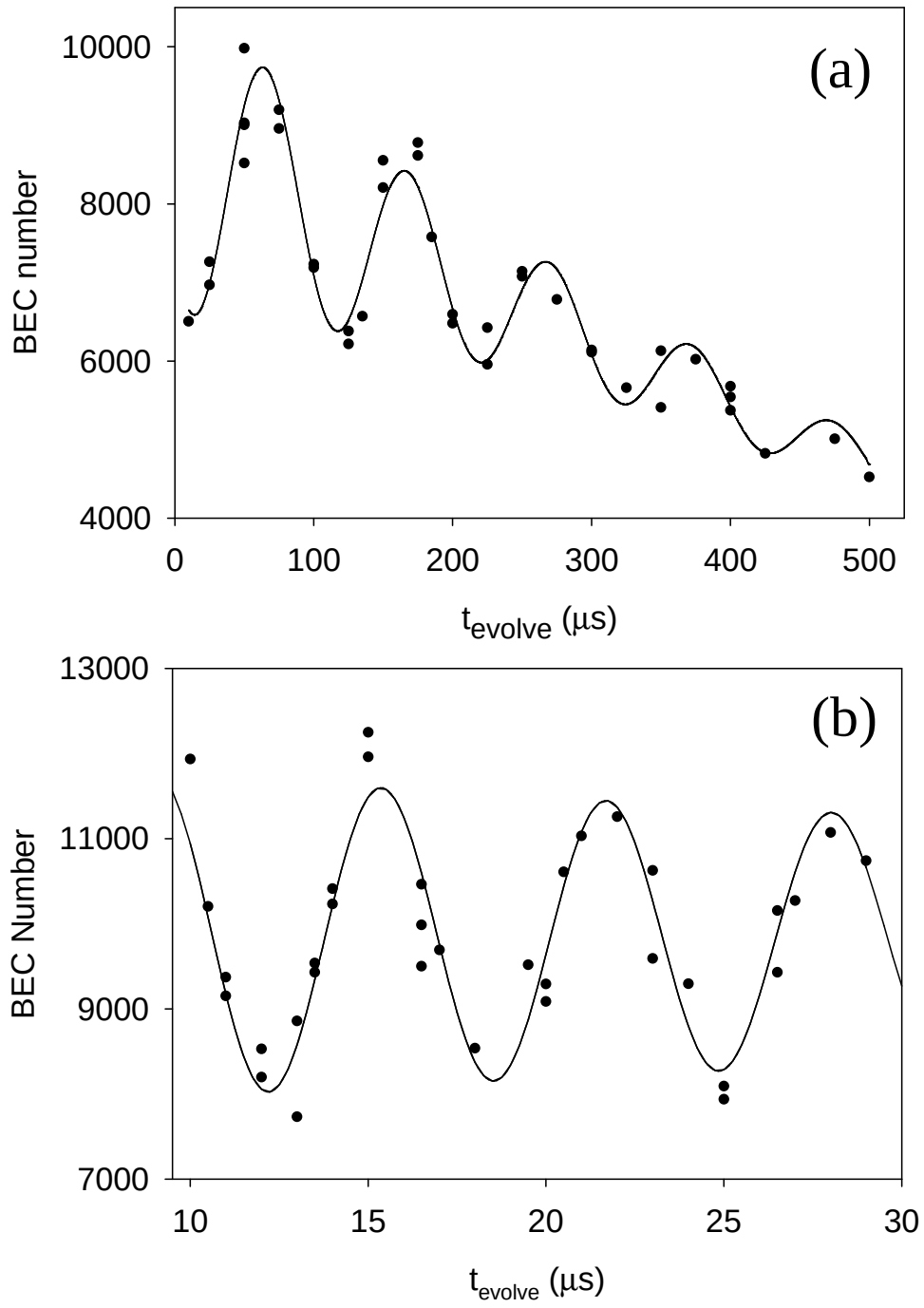

Figure 7.2: BEC number versus pulse spacing t_{evolve}. **(a)** B_{evolve}=156.840(25) G. At this magnetic field, which is relatively close to resonance, the oscillation frequency is very low (ν_0=9.77(12) kHz) so that the damping and atom loss significantly affect the observed time dependence (here β=3640(750) s^{-1} and α=7.9(4) atoms/μs). **(b)** B_{evolve}=159.527(19) G. Farther from resonance, the time dependence of the BEC number is dominated by the higher oscillation frequency of ν_0=157.8(17) kHz. Damping of the oscillations and atom loss are negligible in the relatively short time window used to determine ν_0.

oscillator function with an additional linear loss term:

$$N(t) = N_{avg} - \alpha t + A \exp(-\beta t) \sin(\omega_e t + \phi), \tag{7.4}$$

where N_{avg} is the average number, A is the oscillation amplitude, α and β are the number loss and damping rates, respectively, and $\omega_e = 2\pi\sqrt{\nu_0^2 - [\beta/(2\pi)]^2}$. The quantity of interest here is ν_0, the natural oscillator frequency corresponding to the molecular binding energy, $\nu_0 = \epsilon_{\rm bind}/h$.

We measured the oscillation frequency for values of $B_{\rm evolve}$ from 156.1 G to 161.8 G. Over this range, the frequency varies by over 2 orders of magnitude (10-1000 kHz), but the linear loss rate changes very little. The damping rate shows a significant B-field dependence, increasing from $\beta \simeq 2\pi \times 0.8$ kHz near 156 G to $\beta \simeq 2\pi \times 22$ kHz near 162 G. We find no significant density dependence to the damping at $B_{\rm evolve}$=158.60(5) G; increasing the total atom density by a factor of 4.3(5) leads to a damping rate increase of only a factor of 1.3(3). Atom loss from the BEC is well described by a linear rate of -2 to -7 atoms/μs over the field range of interest. The rate is consistent with previous measurements of number loss due to a single B-field pulse toward the Feshbach resonance, although we have not determined the mechanism for this loss [3].

7.2.3 Limits to precision of frequency measurement

The oscillation frequency measurements have a typical fractional uncertainty of 1%. In principle, the precision of the oscillation frequency determination could be improved indefinitely by increasing the integration time, t_{evolve}. However, there are several effects that prevent us from simply increasing t_{evolve} without limit. First, time variation in the applied magnetic field limits the number of oscillations we can observe. Since we destroy the condensate each time we measure the number of atoms, any variation in B-field from one shot to the next causes the B-field-dependent oscillation frequency to

shift slightly. This frequency shift manifests itself in the BEC number oscillations as a phase shift. If the phase shift between successive measurements is large enough, then the oscillations "wash out" and become impossible to measure. Because the phase shift is proportional to t_{evolve}, our sensitivity to phase noise increases for longer integration time. Evidence for phase noise can be seen in the BEC number oscillations displayed in Figure 7.3.

Another limitation to the precision of the oscillation frequency determination is the finite coherence time for the oscillations. The oscillation amplitude decays with time until the amplitude becomes similar in size to the experimental noise on the number measurement. We typically find that the effects of phase noise dominate over decoherence in limiting the precision of a given frequency measurement, except for the lowest frequency data taken near resonance, where the oscillations damp out on the same time scale as the oscillation period (see section 7.5.1).

In addition to shot-to-shot B-field variations, it is possible to have time variation of the magnetic field during t_{evolve} that is reproducible from shot-to-shot. For example, if the magnetic field from the auxiliary coil is not adjusted to properly compensate for eddy current effects (described in section 3.4.6), the B-field may change as t_{evolve} increases. This variation leads to an oscillation frequency variation or "chirp". Such a chirp significantly complicates the process of accurately determining the oscillation frequency as a function of magnetic field.

7.2.4 Magnetic field determination

To characterize the Feshbach resonance it is necessary to know B_{evolve} precisely as well as the oscillation frequency. As described in section 3.3, we measure B_{evolve} by transferring atoms to an untrapped spin state by driving $\Delta m=+1$ spin flip transitions with an applied pulse of rf radiation (pulse length=5$\rightarrow$25 μs). The spin flip frequency is determined from the rf lineshape for the loss of atoms from the magnetic trap. After

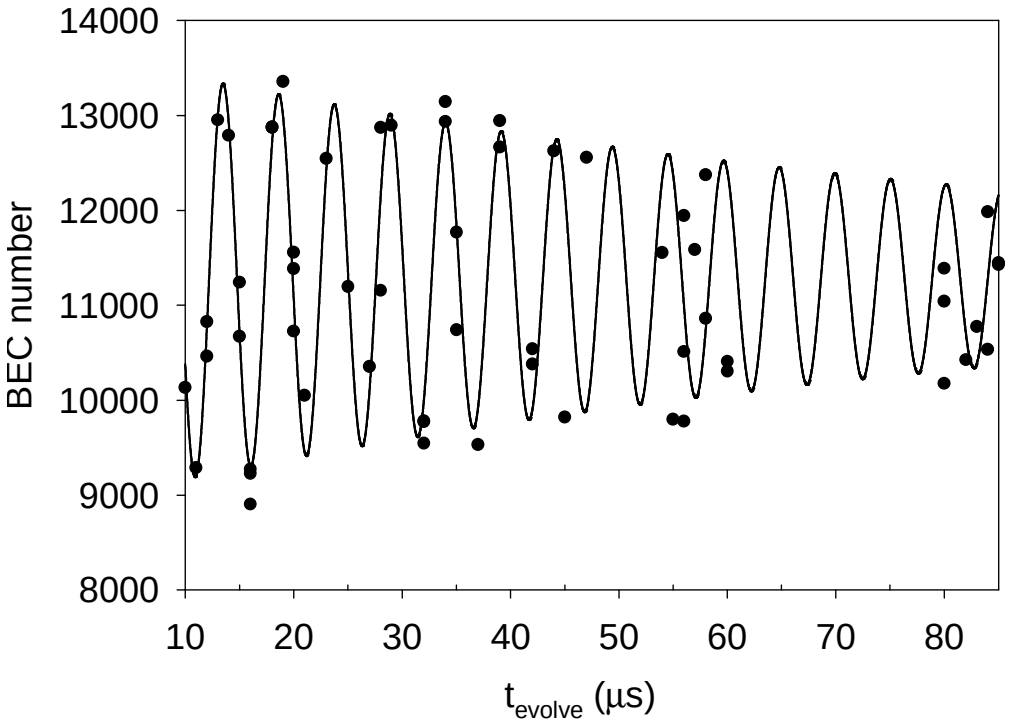

Figure 7.3: Phase noise in BEC number oscillations. Black points are the measured number of BEC atoms versus t_{evolve} while the black line is a fit to the short time data $t_{evolve} \leq 42$ μs. The scatter in the data near 50 μs and 80 μs indicates phase noise that is at least π radians in magnitude. From the observed phase noise and the known dependence of frequency on magnetic field, $\Delta\nu_0/\Delta B$, one can estimate the minimum amount of magnetic field noise required. The data near 50 μs imply shot-to-shot B-field noise of 0.05 G (peak-peak). Because $\Delta\nu_0/\Delta B$ increases rapidly as the B-field increases above the Feshbach resonance, the higher magnetic field (and higher oscillation frequency) data are more susceptible to phase noise.

measuring the rf transition frequency, we invert the Breit-Rabi equation to obtain the corresponding B-field. To ensure that the magnetic field is sufficiently constant during t_{evolve}, we map out $B(t)$ using rf pulses with lengths short compared to t_{evolve}. Due to interference of the rf radiation with the magnetic field control circuitry, there is a small systematic shift of the field as a function of the rf power used. The uncertainty for each magnetic field determination is the quadrature sum of the uncertainty due to the lineshape measurements (10→15 mG) and the uncertainty in the extrapolation to zero rf power(∼20 mG). Typically, the total uncertainty in the average B-field was ∼25 mG and was dominated by the rf power shift. Although we were aware of the rf power shift when we gathered the data, at that time we did not realize how the power shift would dominate all other uncertainties in the magnetic field determination. Only after extensive analysis did this become apparent. In the future, it should be possible to reduce the effects of rf interference in the experiment by adding shielding at appropriate places in the auxiliary coil circuit.

7.3 Coupled-channels analysis of data

7.3.1 Coupled-channels theory

To accurately model the nonlinear magnetic field dependence of the binding energy near the Feshbach resonance, a coupled-channels (CC) scattering theory is required. Coupled-channels scattering theory was first applied to ultracold alkali atom collisions by Verhaar and coworkers [81, 8]. This theory offers a full quantum mechanical description of the 2-body scattering process, including the hyperfine and Zeeman Hamiltonians of the separated atoms as well as the short-range molecular interactions and long-range van der Waals interactions. The CC theory can be used to predict the energy and magnetic field dependence of various quantities, such as the phase shift, scattering length, and the energy of molecular bound states. In principle, the accuracy of the CC calcula-

tions is limited only by the incomplete knowledge of the precise shape of the interatomic potentials, which cannot be calculated *ab initio* [82].

The coupled-channels model presented here for ^{85}Rb was developed by Servaas Kokkelmans, who collaborated with us to analyze the magnetic field dependence of the molecular binding energy [83]. Servaas' model is based on the coupled-channels analysis of van Kempen, Kokkelmans, Heinzen, and Verhaar (KKHV) [69], in which several high-precision data for ^{85}Rb and ^{87}Rb were combined to perform an inter-isotope determination of the rubidium interactions with unprecedented accuracy. The predictive power of the KKHV analysis can be seen from Ref. [4], where the initial data on the atom-molecule coherence were already in good agreement with the predicted binding energy of the molecular state. Another example of the accuracy of the KKHV analysis is its agreement with more than 40 Feshbach resonances recently discovered in ^{87}Rb [84].

7.3.2 Fitting the CC model to the data

The measured oscillation frequencies and magnetic fields are listed in Table 7.1 and plotted in Figure 7.4. For the purposes of the coupled-channels fitting, we choose B-field as the independent variable and assume the magnetic field uncertainty, σ_B, is zero. We then increase the frequency error to include the B-field uncertainty according to the formula [85]:

$$\sigma_{\nu,tot} = \sqrt{\sigma_\nu^2 + (\sigma_B \frac{\partial \nu}{\partial B})^2}, \tag{7.5}$$

where $\frac{\partial \nu}{\partial B}$ is the slope of binding energy versus magnetic field and σ_ν and σ_B are the actual measured uncertainties, as given in Table 7.1. For most of the data, the total frequency error ($\sigma_{\nu,tot}$) is dominated by the second term under the square root because of the magnitude of σ_B. This B-field uncertainty comes mainly from a systematic uncertainty related to the rf power shift (section 3.3.4). In fact, the magnetic field error becomes even more significant for the highest oscillation frequency data, where a given

B-field uncertainty corresponds to a much larger frequency uncertainty due to the steep slope of binding energy with B-field (see Figure 7.4). After determining the appropriate uncertainties, we fit the binding energy data and the zero-crossing field B_{zero} to the CC model with a numerical nonlinear regression in Mathematica.

Table 7.1: Measured values of magnetic field and oscillation frequency. The data were combined with a recent measurement of the magnetic field where a=0 (B_{zero}=165.750(13) G). We fit the combined data set with a coupled-channels scattering theory.

B (G)	σ_B (G)	ν (kHz)	σ_ν (kHz)
156.840	0.025	9.77	0.12
158.211	0.025	47.4	1.0
158.655	0.010	73.6	1.1
159.527	0.019	157.8	1.7
160.529	0.021	383.1	3.7
160.887	0.025	509	12
161.771	0.017	1072	11

7.3.3 Extracting Feshbach resonance parameters from best fit

The authors of Ref. [69] used the best known values [13] for the resonant magnetic field B_{peak} and zero crossing B_{zero}. In our analysis, we ignore the relatively imprecise value of B_{peak} from Ref. [13], and instead use the measured dependence of binding energy on magnetic field along with the new B_{zero} measurement given above to determine the interaction parameters. We observe that the fitting procedure is mainly sensitive to only three parameters: the van der Waals dispersion coefficient, C_6, and the non-integral vibrational quantum numbers at dissociation, v_{DS} and v_{DT}, which determine the position of the last bound state in the singlet and triplet potentials, respectively. Varying the additional parameters C_8, C_{10}, ϕ_T^E (the first-order energy-dependence of the phase of the oscillating triplet radial wave function), and J, the strength of the exchange interaction, does not improve the fitting because these changes can be absorbed in small shifts of v_{DS}, v_{DT} and C_6. Therefore, we take the mean values for these four

parameters [86] from the most recent determination in Ref. [84].

The best fit to B_{zero} and the seven highest frequency data points yields a reduced χ^2=0.30 for 5 degrees of freedom. This value of χ^2 is improbably low due to the fact that the uncertainty in the data is dominated by the systematic uncertainty in magnetic field related to the magnitude of the rf power shift. Figure 7.4 shows the resulting theoretical binding energy as a function of the magnetic field together with the experimental values. From the fit, we find substantially improved values for the Feshbach resonance position B_{peak}=155.041(18) G, width Δ=10.71(2) G, and background scattering length a_{bg}=-443(3) a_0. These results may be compared to previously obtained results B_{peak}=154.9(4) G and Δ=11.0(4) G [13], and a_{bg}=-450(3) a_0 [87]. Our best interaction parameter values are C_6=4707(2) a.u., v_{DS}=0.00918(17), and v_{DT}=0.94659(29). Here the error bars do not include systematic errors due to the uncertainties in other interaction parameters that are not constrained by our data. To compare our values with those of Ref. [69], we determined the sensitivity of our three interaction parameters to systematic shifts in the other parameters, as shown in Table 7.3.3. Using the fractional uncertainties in C_8, C_{10}, ϕ_T^E, and J from KKHV, we find C_6=4707(13) a.u., v_{DS}=0.0092(4), and v_{DT}=0.9466(5). All of these values agree with those given in KKHV: C_6=4703(9) a.u., v_{DS}=0.009(1), and v_{DT}=0.9471(2). Our value for v_{DS} is more precise than that of Ref.[69], while v_{DT} and C_6 are slightly less precise. However, if future experiments allow improvements to the other interaction parameters, then our results will also become more precise since the systematic errors are comparable to or larger than our statistical errors from the fit.

To understand the strong parameter constraints we obtain with our bound state spectroscopy, it is important to consider the nonlinear dependence of the binding energy on magnetic field. The magnetic field dependence of ϵ_{bind} as it approaches the collision threshold depends sensitively on the exact shape of the long range interatomic potentials, which are mainly characterized by the van der Waals coefficient, C_6. At

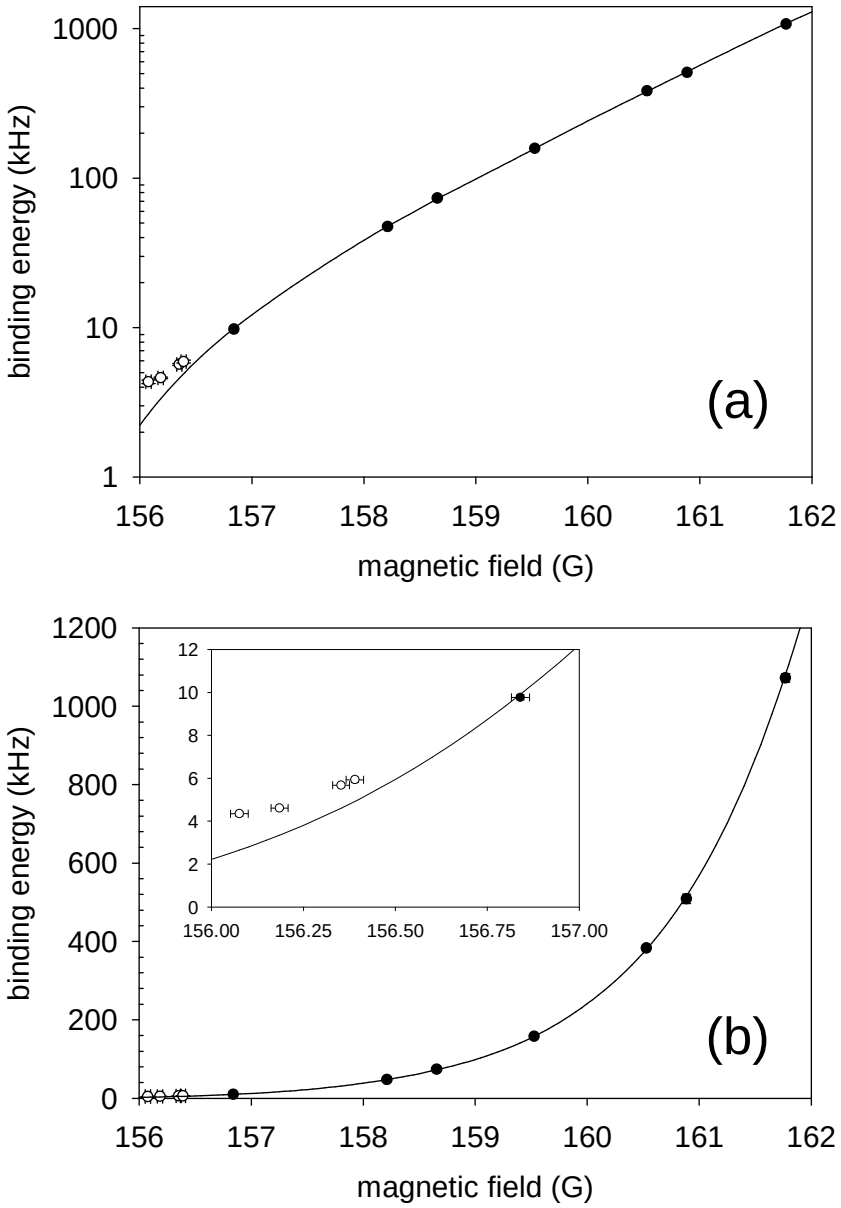

Figure 7.4: Molecular binding energy versus magnetic field, B_{evolve}. **(a)** The points are measured values of the atom-molecule oscillation frequency, ν_0, while the solid line represents the molecular binding energy, which we fit to the data by adjusting the parameters of a coupled-channels scattering theory. Only black points were included in the fit; white points were excluded because they experienced a statistically significant mean-field shift. To improve visibility, the points are larger than the error bars. **(b)** Same as in **(a)**, but with a linear scale for the vertical axis. The inset shows the deviation of the lowest frequency data from the fit to the rest of the data.

Table 7.2: Sensitivity of the determined interaction parameters v_{DS}, v_{DT} and C_6 to fractional uncertainties in C_8, C_{10}, ϕ_T^E and J. For instance, the systematic error in C_6 due to a 10% uncertainty in C_8 is $123 \times 0.10 = 12.3$ a.u.

	$\Delta C_8/C_8$	$\Delta C_{10}/C_{10}$	$\Delta\phi_T^E/\phi_T^E$	$\Delta J/J$
Δv_{DS}	-1.53×10^{-4}	-6.80×10^{-5}	-2.59×10^{-3}	1.72×10^{-3}
Δv_{DT}	-4.14×10^{-4}	-1.39×10^{-4}	2.31×10^{-3}	1.71×10^{-3}
ΔC_6	123	33.4	-47.8	19.3

magnetic fields far from resonance, the bound state wave function is confined to short internuclear distance and the binding energy varies linearly with magnetic field. The linear dependence on B-field gives relatively little information about C_6. As the B-field approaches resonance, the detuning decreases until the bound state lies just below threshold. Now the bound state wave function penetrates much deeper into the classically forbidden region, which causes ϵ_{bind} to curve toward threshold as a function of magnetic field. Because the energetically forbidden region stretches out as C_6/r^6, the observed curvature depends sensitively on the C_6 coefficient. One can show [17] that an analytical Feshbach model that includes the correct potential range and background scattering processes [56] can reproduce the binding energy curve over the full range of magnetic field.

7.3.4 Revised stability prediction for condensates with $a < 0$

As a result of the improved determination of the ^{85}Rb Feshbach resonance parameters, we find that our new value for the off-resonant or background scattering length, a_{bg}=-442.9(23) a_0, is inconsistent with the value given in Ref. [13], where a_{bg}=-380(21) a_0. The most plausible explanation we can find for disagreement is that the theoretical expression used to relate measured rethermalization rate to cross section [1] is insufficient for the requisite level of accuracy. However, the new value for a_{bg} allows us to revise our previous estimate for the stability condition of a BEC with negative scattering length [33]. We use equation (7.1) to obtain the linear slope of scattering

length versus B-field near B=B_{zero}. We then find the stability coefficient for BEC collapse, $k_{collapse}$, by combining the value of $\Delta a/\Delta B$=-39.86(22) a_0/G with the measured slope of $1/N_{crit}$ versus magnetic field [33] of 0.00128(3) (atoms G)$^{-1}$. Thus, we obtain the revised value $k_{collapse}$=0.547(58), where the error is dominated by a 10% systematic uncertainty in the determination of N_{crit}. The present determination agrees with the theoretical value of 0.55 [88].

7.4 Search for collective effects: mean field shifts

7.4.1 Inadequacy of 2-body scattering theory

The coupled-channels theory used in this work applies to 2-body scattering; therefore, this theory cannot account for many-body effects in the atom-molecule BEC system, such as a mean-field shift to the observed oscillation frequency [9, 68]. Any such mean-field shift must be fractionally largest near the Feshbach resonance, where the coupled-channels theory predicts that the binding energy approaches zero while the atom-atom scattering length increases to infinity. We searched for a mean-field shift to the oscillation frequency when B_{evolve} was decreased to ∼156 G. As shown in Figure 7.4, the lowest magnetic field data display a clear frequency shift with respect to the coupled-channels theory prediction. As B_{evolve} approaches resonance, the observed shift increases to 1.7 kHz, which significantly exceeds a simple estimate for the average atom-atom mean-field shift in the BEC: $4\pi\hbar^2\langle n\rangle a/m \simeq 0.5$ kHz at B_{evolve}=156.1 G. We expect the mean-field shift to depend on the density of atoms (and molecules), but we have not yet studied the density dependence. In practice, the initial BEC density can be changed by adiabatically varying the initial scattering length before the rapid magnetic field pulses as discussed in section 5.3.3.

7.4.2 Statistical method for determining mean-field shifts

Since the lowest frequency data show evidence for a mean-field shift, we exclude these points from the (2-body) theory fit. We determine the cutoff magnetic field for the excluded region by the following procedure. First, we fit the data set that includes all frequency measurements satisfying $\nu_0 \geq 73$ kHz. For these data, the expected fractional effect of any mean-field shift is negligible; for example, the average mean-field interaction energy in the atom BEC is $\leq$0.1 kHz, and we expect atom-molecule interactions to be similar in magnitude. After fitting this minimal data set, we add the next lower frequency/B-field measurement to the data set and repeat the theory fit. Finally, we compare the two fits according to their minimum χ^2 values. As long as the increase in χ^2 that results from addition of a new data point is reasonable (on the order of unity), we conclude that there is no significant mean-field shift associated with the frequency measurement.

Table 7.3: Total χ^2 and B_{peak} as a function of the number of included data points in the coupled-channels fit. The abrupt jump in χ^2 and B_{peak} as the data set increases from 7 to 8 points indicates the presence of a mean-field frequency shift in the 8th point. The mean-field shift magnitude increases as the added points approach closer to the Feshbach resonance; since the shift is non-statistical, χ^2 increases very rapidly as more points are added to the set.

Included pts.	Total χ^2	B_{peak} from fit
5	0.42	154.971
6	0.77	154.994
7	1.3	155.042
8	10.0	154.965
9	15.4	154.922
10	24.4	154.885
11	41.7	154.847

In Table 7.3 we give the variation of total χ^2 and B_{peak} as a function of the number of points included in the fit. Both χ^2 and B_{peak} shift abruptly when the number of points increases from 7 to 8 (corresponding to a decrease in B_{evolve} from 156.840 G

to 156.390 G). The observed behavior seems sensible since we expect mean-field shifts to increase rapidly as one moves toward resonance (see Figure 7.4). Our χ^2 exclusion criterion allows us to fit the data in a manner that avoids systematic errors in the Feshbach resonance parameters. By extrapolating the coupled-channels binding energy prediction to lower magnetic fields, we determine the magnitude of the mean-field shifts, which are listed in Table 7.4.

Table 7.4: Measured values of magnetic field and corresponding mean-field shifts to the molecular binding energy. The mean-field shifts were determined by subtracting the extrapolated coupled-channels binding energies from the lowest oscillation frequency data. The shift error, σ_{mf}, is simply the error from the frequency measurement.

B (G)	σ_B (G)	$\Delta\nu_{mf}$ (kHz)	σ_{mf} (kHz)
156.076	0.024	1.69	0.12
156.185	0.023	1.26	0.06
156.352	0.023	1.07	0.08
156.390	0.024	1.00	0.13
156.840	0.025	−0.15	0.12

7.5 Low frequency oscillations: a simple model

7.5.1 Damping of oscillations: experiment and theory

The low frequency oscillations that show evidence for a mean-field shift are quite strongly damped, so only one or two wiggles are observed before the signal-to-noise ratio approaches unity. In addition, the number loss rate, $\alpha \simeq 7$ atoms/μs, causes a significant decrease in the average number of BEC atoms during t_{evolve}. The combination of these effects leads to a rather complicated time dependence of the measured BEC number, as shown in Figure 7.5.

We use a simple model to explain part of the observed damping as due to inhomogeneous dephasing from a density dependent mean-field shift. This idea was suggested to us by Murray Holland and Servaas Kokkelmans [9]. Assuming that the atom-molecule

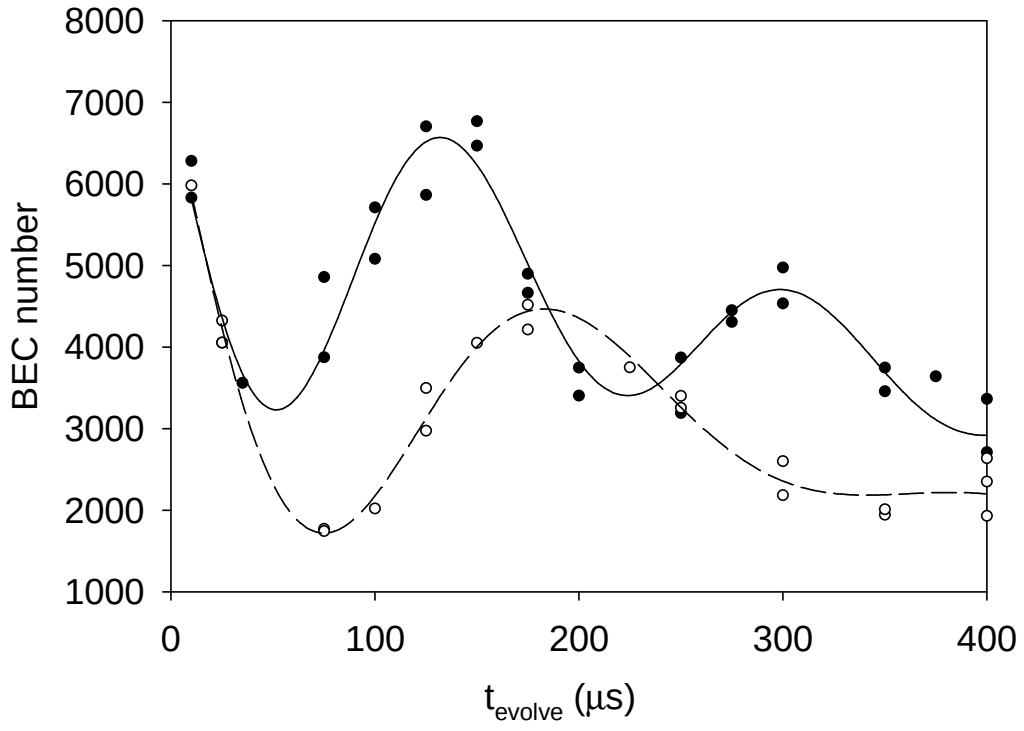

Figure 7.5: Low frequency BEC number oscillations. Black points correspond to B_{evolve}=156.390(24) G; white points were at a lower magnetic field of B_{evolve}=156.076(24) G. The solid line is a fit to the black points using equation (7.4) with ν_0=5.93(13) kHz, β=4500(1200) s^{-1} and α=6.1(8) atoms/μs. The dashed line fit to the white points gives parameter values of ν_0=4.34(12) kHz, β=7600(1000) s^{-1}, and α=6.4(5) atoms/μs.

oscillation frequency depends on the local density in the sample, we have

$$\nu(\vec{r}) = \nu_{bare} + An(\vec{r}), \tag{7.6}$$

where ν_{bare} is the "bare" oscillation frequency at zero density (i.e., the molecular binding energy), A is the (positive) frequency shift per density and is determined empirically, and $n(\vec{r})$ is the local density in the BEC cloud. For simplicity, we assume that the density distribution of the condensate has an isotropic parabolic form:

$$n(\vec{r}) = \begin{cases} n(0)[1 - r^2/R^2] & r \leq R \\ 0 & r > R \end{cases} \tag{7.7}$$

where $n(0) = \frac{15N}{8\pi R^3}$ is the peak density, N is the total number of atoms, and R is the radius of the parabolic condensate. Although we neglect the anisotropy of the BEC, this is a fairly reasonable approximation since the aspect ratio is at most 2.5 in the Thomas-Fermi limit (we approximate a football-shaped object by a sphere). The Thomas-Fermi approximation of a parabolic density distribution is well satisfied by the condensates since we typically prepare them at the evaporation magnetic field of 162.3 G, corresponding to $a \sim$200 a_0. For this scattering length, the ratio of mean field interaction energy to kinetic energy in the BEC is Na/a_{ho}=55, which is far into the Thomas-Fermi limit.

Using the above density distribution, we next obtain the probability distribution of the atoms in oscillation frequency space. We simply find the probability of being in a given spherical shell of constant density (constant frequency). The probability per unit frequency is

$$P(\nu) = \frac{2\pi R^3}{NA} \frac{(\nu - \nu_{bare})}{\Delta\nu_{max}} \sqrt{1 - \frac{(\nu - \nu_{bare})}{\Delta\nu_{max}}}, \tag{7.8}$$

where $\Delta\nu_{max} = An(0)$ is the maximum frequency shift corresponding to the peak density in the sample and $P(\nu)$ is normalized so that $\int_0^{\nu_{bare}+\Delta\nu_{max}} P(\nu)d\nu = 1$.

After obtaining the probability distribution in equation (7.8), we numerically calculate the Fourier transform of $P(\nu)$ and study the oscillation amplitude versus time.

One can then look for the effects of density-dependent dephasing in the oscillations.

7.5.2 Comparison of dephasing model to data

In Figure 7.6, we plot the theoretical oscillation amplitude as a function of time for two choices of the quantities ν_{bare} and $\Delta\nu_{max}$. We chose these values based on empirical estimates for the mean-field shift — we estimated the average shift by extrapolating the coupled-channels prediction for ϵ_{bind} and then calculating the difference between this prediction and the measured oscillation frequency.

The dephasing model predicts damped oscillations that are qualitatively similar to the experimental measurements, as can be seen by comparing Figures 7.5 and 7.6. To make a more quantitative test of the dephasing model predictions, we show the mean-field shift and damping rate versus magnetic field in Figure 7.7. Here the observed oscillation frequency shifts and damping rates can be directly compared to the predictions of the dephasing model. Figure 7.7 demonstrates that the damping rates predicted from the dephasing model are significantly smaller than those observed in the experimental data. There appears to be an additional B-field-independent damping mechanism in the experiment. The most obvious additional source of damping is the observed loss of BEC atoms during the evolution time between magnetic field pulses. This loss has no apparent B-field dependence over the range of magnetic fields in Figure 7.7. Although the mechanism for the loss is unknown, the process must be distinct from that of the inhomogeneous dephasing discussed here and should lead to a loss of coherence in the oscillations.

7.5.3 Additional damping from atom loss

To predict the expected damping rate due to the measured atom loss rate, we assume that the only the atomic state in the atom-molecule superposition experiences decay of population. One can show [89, 90] that if the number of atoms decreases at

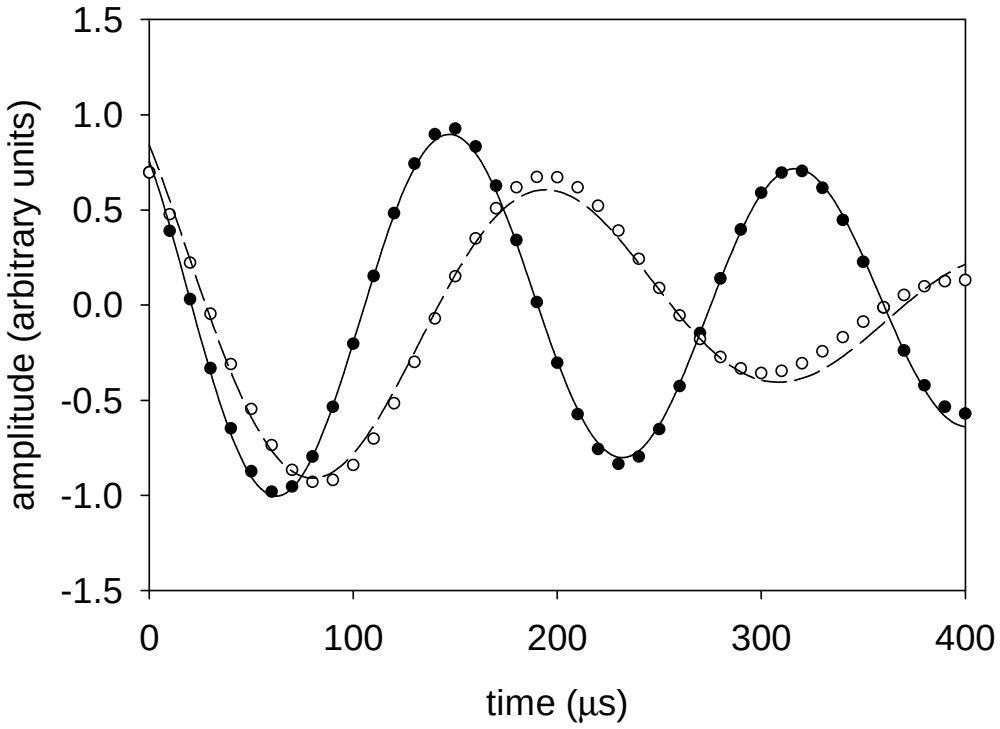

Figure 7.6: Theoretical model for density-dependent dephasing. Points are the calculated Fourier transform of the frequency probability distribution in equation (7.8) versus time. A phase shift of 0.8 rad was added to the Fourier transform to better approximate the initial phase in the experiment (see Figure 7.5). The black points correspond to a bare oscillation frequency of ν_{bare}=4.9 kHz with an average mean-field shift of $\Delta\nu$=0.99 kHz. The white points had ν_{bare}=2.7 kHz and $\Delta\nu$=1.7 kHz. The solid and dashed lines are fits to the two different model data sets. From these fits, we extract values for the oscillation frequency of an equivalent damped oscillator, ν_0 (see equation(7.4)), and its damping rate, β. The fits yield ν_0=5.90(1) kHz and β=2250(120) s^{-1} (solid line) and ν_0=4.42(3) kHz and β=3560(220) s^{-1} (dashed line). The fits allow us to compare the dephasing model directly to the data.

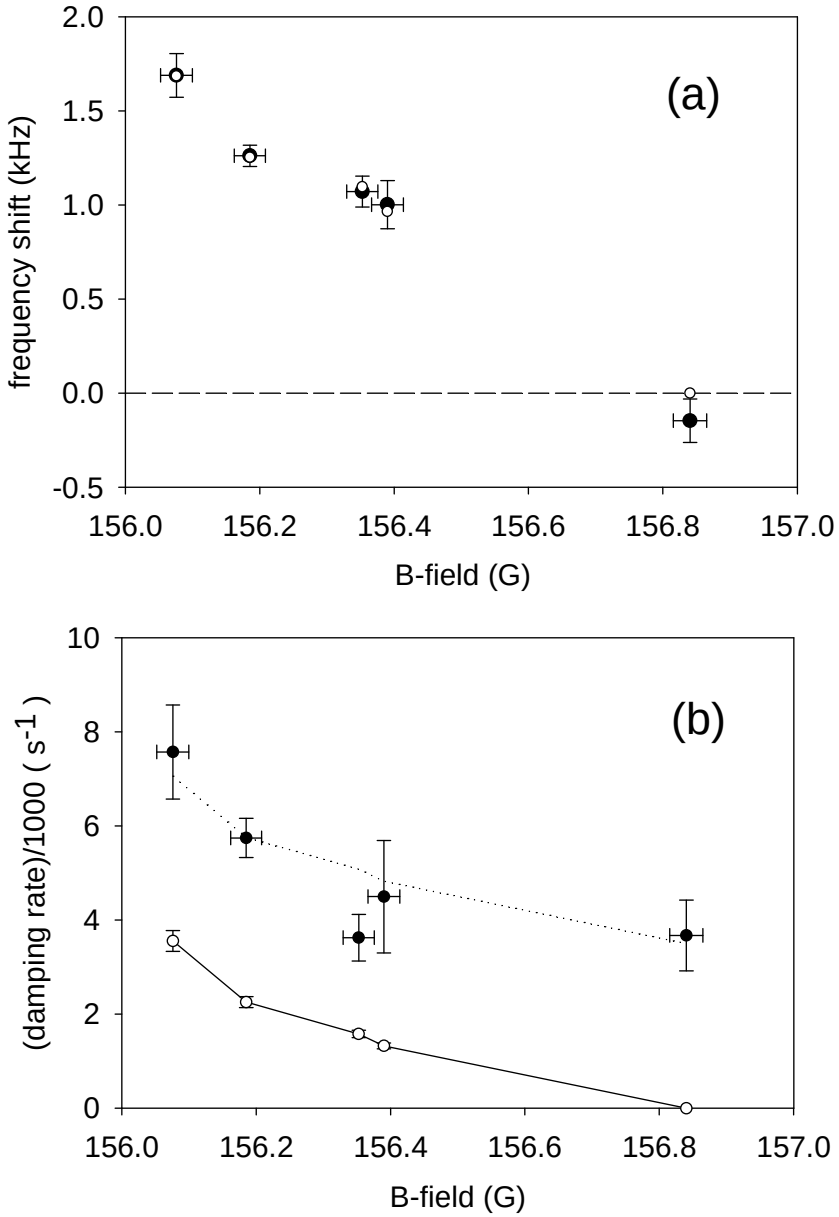

Figure 7.7: Comparison of data and theory for oscillation damping rates versus B-field. **(a)** Mean-field shift of the oscillation frequency as a function of magnetic field. Black points with error bars are empirically determined values of the mean-field shift, as discussed in the text. White points are the values of the mean-field shift used in the dephasing model. **(b)** Damping rates versus B-field. Black points with error bars are damping rates from fitting the BEC number oscillation data, as in Figure 7.5. White points connected by straight lines are the predicted damping rates due to inhomogeneous dephasing from the mean-field shifts in part **(a)**. The dotted line shows the effect of adding a constant rate of 3500 s^{-1} to the dephasing model prediction.

an exponential rate, $N_a = N_0 \exp(-\gamma t)$, the amplitude for population oscillations will decay according to $\exp(-\gamma t/2)$. In the magnetic field range of interest (from 156-157 G), we observed a roughly linear loss rate from the atom BEC of -α=-7.2 atoms/μs. To convert this linear loss rate into an effective exponential decay rate, we determine the time interval required to decrease the total number of BEC atoms by a factor of $1/e$. The initial average number of BEC atoms at our shortest evolution times ($t_{evolve} \simeq 0$) was 6000, so the time to reach $6000/e$=2210 with a linear loss rate of -7.2 atoms/μs is 527 μs. This $1/e$ time corresponds to an effective number decay rate of γ=1900 s^{-1}, so we expect the atom-molecule oscillations to decay at the rate $\gamma/2$=800 s^{-1}.

As can be seen from Figure 7.7, the additional damping rate due to atom number loss is too small to explain the discrepancy between the data and the simple dephasing theory. In fact, to explain the observations, there must be an additional damping rate of $\sim$3500 s^{-1}, which is more than 4 times larger than the expected damping from decay of the BEC number. There may be other sources for decoherence in the system, including a possible loss from the molecular state during t_{evolve}. Whatever the source of the additional damping, our data suggest that this damping is not strongly sensitive to magnetic field. We also have evidence that the additional damping rate is insensitive to density — at B_{evolve}=158.60(5) G, where the mean-field shift is negligible, we find that increasing the BEC density by a factor of 2.5(3) leads to a damping rate increase of only a factor of 1.24(25). Future investigation of the mean-field shifts and damping rates should improve our understanding of the physics of atom-molecule decoherence near the Feshbach resonance.

7.5.4 Magnitude of mean-field shifts

The magnitude of the mean-field shift shown in Figure 7.7 increases as the magnetic field approaches the Feshbach resonance. Over the 1 G range shown in this figure, the shift increases from 0 to 1.7 kHz. The shift for the lowest magnetic field data is

significantly larger than one would expect from a simple estimate of the average mean-field energy in the BEC, based on the GP equation: $4\pi\hbar^2\langle n\rangle a_{\rm evolve}/m \simeq 0.5$ kHz at $B_{\rm evolve}$=156.1 G. The observed shift also exceeds a recent calculation for the equilibrium mean-field shift using an effective quantum field theory [68] (<0.1 kHz). One intriguing possibility for the discrepancy is that there is a positive mean-field shift due to atom-molecule (or molecule-molecule) interactions. We believe that the current data are interesting and suggestive, but we have really only touched the tip of the iceberg in this area.

Since a mean-field shift must depend on the density of atoms and molecules, it would be desirable to study the density dependence. Ideally, one would like to change the density of atoms and molecules independently to identify the source of the shift(s). At the present time, we have not measured any density dependence to the mean-field shifts.

7.5.5 Limitations of current method and possible future experiments

As discussed above, the observed time dependence of the BEC number arises from the interplay between the bare atom-molecule oscillation frequency and a density-dependent frequency shift. The data suggest the presence of highly interesting many-body physics, but the information we can glean from the oscillation data is limited. For example, as we decrease the magnetic field to approach closer to the Feshbach resonance, we observe that the oscillations rapidly damp out due to increased dephasing. Eventually the damping rate becomes comparable to the oscillation frequency and it becomes impossible to reliably extract the underlying frequency because the system is critically damped. One way to avoid this limitation would be to measure the atom-molecule oscillations as a function of position in the condensate. If we could "bin" the cloud into different spatial regions, then we could avoid the effect of inhomogeneous dephasing [89]. However, our present method of measuring the BEC number involves a large

time-of-flight expansion before imaging, which effectively blurs any spatial information about the pre-expansion condensate (see section 3.5.3).

Another practical limitation of our experiment comes from the finite amount of charge stored in the capacitor bank used to control the magnetic field (see section 3.4.3) The finite amount of charge prevents us from holding the magnetic field constant for more than $\sim$1 ms, so we cannot observe an atom-molecule oscillation with a period longer than this limit.

However, we are investigating novel techniques to determine mean-field shifts to the atom-molecule system near the Feshbach resonance. For example, it may be possible to use rf pulse spectroscopy, as discussed in section 3.3.5, to measure the mean-field energy. Such a method allows one to probe the energy of the system on shorter timescales and has proven useful in studies of ^{40}K Feshbach resonances [91].

Bibliography

[1] J. Roberts, Ph.D. thesis, University of Colorado at Boulder, 2001, available at http://jilawww.colorado.edu/www/sro/thesis/.

[2] E. A. Donley, N. R. Claussen, S. L. Cornish, J. L. Roberts, E. A. Cornell, and C. E. Wieman, Nature **412**, 295 (2001).

[3] N. R. Claussen, E. A. Donley, S. T. Thompson, and C. E. Wieman, Phys. Rev. Lett. **89**, 010401 (2002).

[4] E. A. Donley, N. R. Claussen, S. T. Thompson, and C. E. Wieman, Nature **417**, 529 (2002).

[5] F. Dalfovo, S. Giorgini, L. P. Pitaevskii, and S. Stringari, Rev. Mod. Phys. **71**, 463 (1999).

[6] E. Tiesinga, B. J. Verhaar, and H. T. C. Stoof, Phys. Rev. A **47**, 4114 (1993).

[7] A. Moerdijk, B. J. Verhaar, and A. Axelsson, Phys. Rev. A **51**, 4852 (1995).

[8] H. T. C. Stoof, J. M. V. A. Koelman, and B. J. Verhaar, Phys. Rev. B **38**, 4688 (1988).

[9] S. J. J. M. F. Kokkelmans and M. J. Holland, Phys. Rev. Lett. **89**, 180401 (2002).

[10] J. J. Sakurai, Modern Quantum Mechanics (Addison-Wesley, Reading, Massachusetts, 1994).

[11] R. G. Newton, Scattering Theory of Waves and Particles (Springer, New York, 1982).

[12] S. Inouye, M. R. Andrews, J. Stenger, H. J. Miesner, D. M. Stamper-Kurn, and W. Ketterle, Nature **392**, 151 (1998).

[13] J. L. Roberts, J. P. Burke, Jr., N. R. Claussen, S. L. Cornish, E. A. Donley, and C. E. Wieman, Phys. Rev. A **64**, 024702 (2001).

[14] E. Timmermans, P. Tommasini, M. Hussein, and A. Kerman, Phys. Rep. **315**, 199 (1999).

[15] F. A. van Abeelen and B. J. Verhaar, Phys. Rev. Lett. **83**, 1550 (1999).

[16] T. Köhler, T. Gasenzer, and K. Burnett, cond-mat/0209100 (2002).

[17] S. J. J. M. F. K. *et al.*, to be published .

[18] P. Julienne, private communication .

[19] C. Myatt, N. Newbury, R. Ghrist, S. Loutzenhiser, and C. Wieman, Opt. Lett. **21**, 290 (1996).

[20] K. Lindquist, M. Stephens, and C. E. Wieman, Phys. Rev. A **46**, 4082 (1992).

[21] B. DeMarco, Ph.D. thesis, University of Colorado at Boulder, 2001.

[22] K. L. Corwin and *et al.*, Appl. Opt. **37**, 3295 (1998).

[23] I. I. Rabi, S. Millman, P. Kusch, and J. R. Zacharias, Phys. Rev. **55**, 526 (1939).

[24] N. F. Ramsey, Molecular Beams (Clarendon Press, Oxford, 1956).

[25] J. H. Moore, C. C. Davis, and M. A. Coplan, Building Scientific Apparatus: A Practical Guide to Design and Construction (Addison-Wesley, Reading, MA, 1989), p. 203.

[26] S. L. Cornish, N. R. Claussen, J. L. Roberts, E. A. Cornell, and C. E. Wieman, Phys. Rev. Lett. **85**, 1795 (2000).

[27] V. M. Pérez-García, H. Michinel, J. Cirac, M. Lewenstein, and P. Zoller, Phys. Rev. A **56**, 1424 (1997).

[28] C. Bradley, C. Sackett, and R. Hulet, Phys. Rev. Lett. **78**, 985 (1997).

[29] C. Sackett, H. T. C. Stoof, and R. Hulet, Phys. Rev. Lett. **80**, 2031 (1998).

[30] C. Sackett, J. Gerton, M. Welling, and R. Hulet, Phys. Rev. Lett. **82**, 876 (1999).

[31] A. Gammal, L. Tomio, and T. Frederico, Phys. Rev. A **66**, 043619 (2002).

[32] P. Ruprecht, M. Holland, K. Burnett, and M. Edwards, Phys. Rev. A **51**, 4704 (1995).

[33] J. L. Roberts, N. R. Claussen, S. L. Cornish, E. A. Donley, E. A. Cornell, and C. E. Wieman, Phys. Rev. Lett. **86**, 4211 (2001).

[34] J. L. Bohn, B. Esry, and C. H. Greene, Phys. Rev. A **58**, 584 (1998).

[35] R. Dodd, M. Edwards, C. Williams, C. Clark, M. Holland, P. Ruprecht, and K. Burnett, Phys. Rev. A **54**, 661 (1996).

[36] Y. Kagan, E. Surkov, and G. Shlyapnikov, Phys. Rev. Lett. **79**, 2604 (1997).

[37] Y. Kagan, A. Muryshev, and G. Shlyapnikov, Phys. Rev. Lett. **81**, 933 (1998).

[38] J. Stenger, S. Inouye, M. R. Andrews, H. J. Miesner, D. M. Stamper-Kurn, and W. Ketterle, Phys. Rev. Lett. **82**, 2422 (1999).

[39] J. L. Roberts, N. R. Claussen, S. L. Cornish, and C. E. Wieman, Phys. Rev. Lett. **85**, 728 (2000).

[40] A. K. Pattanayak, A. Gammal, C. A. Sackett, and R. G. Hulet, Phys. Rev. A **63**, 033604 (2001).

[41] C. J. Myatt, Ph.D. thesis, University of Colorado at Boulder, 1997.

[42] M. Ueda and K. Huang, Phys. Rev. A **60**, 3317 (1999).

[43] H. Saito and M. Ueda, Phys. Rev. A **63**, 043601 (2001).

[44] H. Saito and M. Ueda, Phys. Rev. Lett. **86**, 1406 (2001).

[45] R. A. Duine and H. T. C. Stoof, Phys. Rev. Lett. **86**, 2204 (2001).

[46] L. Santos and G. V. Shlyapnikov, Phys. Rev. A **66**, 011602 (2002).

[47] H. Saito and M. Ueda, Phys. Rev. A **65**, 033624 (2002).

[48] S. K. Adhikari, Phys. Rev. A **66**, 013611 (2002).

[49] E. Timmermans, P. Tommasini, R. Côté, M. Hussein, and A. Kerman, Phys. Rev. Lett. **83**, 2691 (1999).

[50] P. D. Drummond, K. V. Kheruntsyan, and H. He, Phys. Rev. Lett. **81**, 3055 (1998).

[51] V. Yurovsky, A. Ben-Reuven, P. Julienne, and C. Williams, Phys. Rev. A **62**, 043605 (2000).

[52] F. H. Mies, E. Tiesinga, and P. S. Julienne, Phys. Rev. A **61**, 022721/1 (2000).

[53] M. Holland, J. Park, and R. Walser, Phys. Rev. Lett. **86**, 1915 (2001).

[54] E. Burt, R. Ghrist, C. Myatt, M. Holland, E. Cornell, and C. Wieman, Phys. Rev. Lett. **79**, 337 (1997).

[55] M. J. Holland, private communication .

[56] S. J. J. M. F. Kokkelmans, J. N. Milstein, M. L. C. R. Walser, and M. J. Holland, Phys. Rev. A **65**, 053617 (2002).

[57] H. C. W. Beijerinck, Phys. Rev. A **62**, 063614 (2000).

[58] J. Schuster, A. Marte, S. Amtage, B. Sang, G. Rempe, and H. C. W. Beijerinck, Phys. Rev. Lett. **87**, 170404 (2001).

[59] L. D. Landau, Phys. Z. Sowjetunion **2**, 46 (1932).

[60] C. Zener, Proc. R. Soc. London Ser. **A137**, 696 (1932).

[61] J. R. Rubbmark, M. M. Kash, M. G. Littman, and D. Kleppner, Phys. Rev. A **23**, 3107 (1981).

[62] J. W. Dunn, C. H. Greene, D. Blume, B. E. Granger, and M. J. Holland, physics/0208031 (2002).

[63] D. Blume and C. H. Greene, Phys. Rev. A **65**, 043613 (2002).

[64] E. L. Bolda, E. Tiesinga, and P. S. Julienne, Phys. Rev. A **66**, 013403/1 (2002).

[65] T. Busch, B.-G. Englert, K.Rzazewski, and M. Wilkens, Found. Phys. **28**, 549 (1998).

[66] D. Guéry-Odelin and G. Shlyapnikov, Phys. Rev. A **61**, 013605 (1999).

[67] M. Mackie, K. A. Suominen, and J. Javanainen, cond-mat/0209100 (2002).

[68] R. A. Duine and H. T. C. Stoof, cond-mat/0210544 (2002).

[69] E. G. M. van Kempen, S. J. J. M. F. Kokkelmans, D. J. Heinzen, and B. J. Verhaar, Phys. Rev. Lett. **88**, 093201 (2002).

[70] V. Yurovsky, A. Ben-Reuven, P. Julienne, and C. Williams, Phys. Rev. A **60**, 765 (1999).

[71] R. C. Forrey, V. Kharchenko, N. Balakrishnan, and A. Dalgarno, Phys. Rev. A **59**, 2146 (1999).

[72] R. Wynar, R. Freeland, D. Han, C. Ryu, and D. Heinzen, Science **287**, 1016 (2000).

[73] E. Braaten, H.-W. Hammer, and M. Kusunoki, cond-mat/0206232 (2002).

[74] P. Courteille, R. S. Freeland, D. J. Heinzen, F. A. van Abeelen, and B. J. Verhaar, Phys. Rev. Lett. **81**, 69 (1998).

[75] J. L. Roberts, N. R. Claussen, J. P. Burke, Jr., C. H. Greene, E. A. Cornell, and C. E. Wieman, Phys. Rev. Lett. **81**, 5109 (1998).

[76] V. Vuletić, A. J. Kerman, C. Chin, and S. Chu, Phys. Rev. Lett. **82**, 1406 (1999).

[77] T. Loftus, C. A. Regal, C. Ticknor, J. L. Bohn, and D. S. Jin, Phys. Rev. Lett. **88**, 173201 (2002).

[78] F. A. van Abeelen and B. J. Verhaar, Phys. Rev. A **59**, 578 (1999).

[79] P. J. Leo, C. J. Williams, , and P. S. Julienne, Phys. Rev. Lett. **85**, 2721 (2000).

[80] C. Chin, V. Vuletic, A. J. Kerman, and S. Chu, Phys. Rev. Lett. **85**, 2717 (2000).

[81] A. Lagendijk, I. F. Silvera, and B. J. Verhaar, Phys. Rev. B **33**, 626 (1986).

[82] J. P. Burke, Jr., Ph.D. thesis, University of Colorado at Boulder, 1999, available at http://jilawww.colorado.edu/www/sro/thesis/.

[83] N. R. Claussen, S. J. J. M. F. Kokkelmans, S. T. Thompson, E. A. Donley, and C. E. Wieman, in preparation .

[84] A. Marte, T. Volz, J. Schuster, S. Dürr, G. Rempe, E. G. M. van Kempen, and B. J. Verhaar, cond-mat/0210651 (2002).

[85] P. R. Bevington and D. K. Robinson, Data Reduction and Error Analysis for the Physical Sciences (McGraw-Hill, New York, 1992).

[86] For the ϕ_T^E value, which is not listed in Ref. [84], we used $\phi_T^E = 0.159(18)$ K^{-1} (E. G. M. van Kempen and B. J. Verhaar, private communication) .

[87] The value for a_{bg}=-450(3) a_0 was extracted from the KKHV analysis. We refer to this value (as we did also in Ref. [4]) instead of our earlier experimentally determined value of a_{bg}=-380(21) a_0 [13], which is less precise and less accurate .

[88] A. Gammal, T. Frederico, and L. Tomio, Phys. Rev. A **64**, 055602 (2001).

[89] H. Lewandowski, Ph.D. thesis, University of Colorado at Boulder, 2002, available at http://jilawww.colorado.edu/www/sro/thesis/.

[90] L. Allen and J. H. Eberly, Optical Resonance and Two-Level Atoms (Dover, New York, 1975).

[91] C. A. Regal, private communication .